ABSTRACT

NUMERICAL AND ANALYTICAL METHODS TO PREDICT BEHAVIOR OF REINFORCED DUCTILE CONCRETE COMPOSITES

by
Mandeep Pokhrel

Structural components constructed with ductile concrete composites, such as high-performance fiber-reinforced cementitious composites (HPFRCC), are known to perform exceptionally well under extreme mechanical and environmental loading conditions compared to traditional concrete. HPFRCC flexural components exhibit enhanced performance in terms of displacement ductility, energy dissipation capacity, and damage tolerance capacity. However, recent research suggests that the flexural behavior of reinforced HPFRCCs in terms of crack progression, reinforcement plasticity, and failure mechanism is significantly different than conventional reinforced concrete. Specifically, the failure mode of flexural members is found to be predominantly through the fracture of longitudinal reinforcement rather than compression crushing of HPFRCC matrix. Further, the influence of cross-section properties on the deformation capacity of reinforced HPFRCC beams has been found to be opposite to that in reinforced concrete beams.

To that end, an extensive numerical simulation study is carried out with variations in material and structural properties to identify the fundamental variables affecting deformation capacity and plasticity in reinforced HPFRCC beams. The results of the study indicate that increasing tensile strength of HPFRCCs can significantly decrease component deformation capacity. The influence of other factors such as reinforcement ratio, boundary conditions, and shear span-to-depth ratio are also investigated. Statistical analyses are performed to understand the relative impact of these factors on deformation capacity, and recommendations are given to

predict deformation capacity in reinforced HPFRCC beams under monotonic loading condition.

In the next phase of the research, an investigation of plastic hinge behavior in reinforced HPFRCC flexural members is performed. Variations in mechanical properties, boundary conditions, and geometric properties are considered. The reinforcement yielding region, plastic strain distribution region, and curvature localization region are particularly explored. New expressions are developed to compute the *equivalent plastic hinge length*, L_p, using variables such as shear-span, tensile strength of HPFRCC, reinforcement ratio, yield strength of the reinforcement, boundary condition, and loading scenario. A simplified mechanics-based approach is developed to compute flexural strengths and rotation capacities at multiple damage states. The proposed approach is validated using a large experimental database found in the literature for wide range of HPFRCC classes.

To further validate the robustness of the analytical framework, an experimental program is carried out using two reinforced HPFRCC beams with variation in fiber volume fraction. The experimental results show that the plasticity length in steel reinforcement bar increases with a decrease in fiber volume fraction from 2% to 1%. The plastic hinge region of the HPFRCC specimen with 2% fiber content has crack localization over a short region compared to the specimen with 1% fiber content. The analytical approach developed in the previous research phase is used to predict the flexural strengths and rotation capacities at different limit states.

While the research presented represents significant advancement in the numerical analysis and design of reinforced HPFRCC members, additional experimental work is necessary to further improve the framework presented herein. Therefore, an experimental program is outlined considering two variants of HPFRCCs under monotonic and cyclic loading.

NUMERICAL AND ANALYTICAL METHODS TO PREDICT BEHAVIOR OF REINFORCED DUCTILE CONCRETE COMPOSITES

by
Mandeep Pokhrel

A Dissertation
Submitted to the Faculty of
New Jersey Institute of Technology
in Partial Fulfillment of the Requirements for the Degree of
Doctor of Philosophy in Civil Engineering

John A. Reif, JR. Department of Civil and Environmental Engineering

May 2020

APPROVAL PAGE

NUMERICAL AND ANALYTICAL METHODS TO PREDICT BEHAVIOR OF REINFORCED DUCTILE CONCRETE COMPOSITES

Mandeep Pokhrel

Dr. Matthew J. Bandelt, Dissertation Advisor Date
Assistant Professor of Civil and Environmental Engineering, NJIT

Dr. Methi Wecharatana, Committee Member Date
Professor of Civil and Environmental Engineering, NJIT

Dr. Shawn A. Chester, Committee Member Date
Associate Professor of Mechanical and Industrial Engineering, NJIT

Dr. Matthew P. Adams, Committee Member Date
Assistant Professor of Civil and Environmental Engineering, NJIT

Dr. Bruno M. Goncalves da Silva, Committee Member Date
Assistant Professor of Civil and Environmental Engineering, NJIT

BIOGRAPHICAL SKETCH

Author:	Mandeep Pokhrel
Degree:	Doctor of Philosophy
Date:	May 2020

Undergraduate and Graduate Education:

- Doctor of Philosophy in Civil Engineering,
  New Jersey Institute of Technology, Newark, NJ, 2020
- Master of Engineering in Structural Engineering,
  Asian Institute of Technology, Pathumthani, Thailand, 2013
- Bachelor of Engineering in Civil Engineering,
  Pokhara University, Pokhara, Nepal, 2011

Major: Civil Engineering

Presentations and Publications:

M. Pokhrel, Y. Shao, S. L. Billington, and M. J. Bandelt. Effect of fiber content variation in plastic hinge region of reinforced UHPC flexural members. Submitted to *RILEM-fib X International Symposium on Fiber Reinforced Concrete (BEFIB 2020)*, Valencia, Spain, September 21–23, 2020.

M. Pokhrel and M. J. Bandelt. Plastic hinge behavior and rotation capacity in reinforced ductile concrete flexural members. *Engineering Structures*, 200:109699, 2019.

M. Pokhrel and M. J. Bandelt. Plastic hinge region and rotation capacity in reinforced HPFRCC flexural members at collapse level. In *Proceedings of the Seventh International Colloquium on Performance, Protection & Strengthening of Structures under Extreme Loading & Events (PROTECT 2019)*, Whistler, Canada, September 16–17, 2019.

M. Pokhrel and M. J. Bandelt. Predicting UHPC structural response at ultimate limit state through numerical simulation technique. In *Proceedings of the Second International Interactive Symposium on Ultra-High Performance Concrete (2IIS– UHPC)*, Albany, New York, USA, June 2–5, 2019.

M. Pokhrel and M. J. Bandelt. Material properties and structural characteristics influencing deformation capacity and plasticity in reinforced ductile cement-based composite structural components. *Composite Structures*, 224:111013, 2019.

M. Pokhrel and M. J. Bandelt. Predicting structural behavior of UHPC and ductile concrete materials with numerical simulations. *ACI Convention Spring 2019*, Quebec, Canada, March 24–28, 2019.

M. Pokhrel and M. J. Bandelt. Simulation of reinforced HPFRCC deformation capacity under flexure- and shear-dominated stress states. In *Proceedings of the Computational Modeling of Concrete and Concrete Structures (EURO-C 2018)*, Bad Hofgastein, Austria, February 26–March 01, 2018.

A. J. Strand, M. Pokhrel, M. P. Adams, M. J. Bandelt, D. Masceri, and N. Romano. The long term bridge performance program bridge portal. *Service Life Prediction of Concrete: The Third Corvallis Workshop*, Corvallis, Oregon, USA, July 16–19, 2017.

M. Pokhrel, A. J. Strand, M. J. Bandelt, and M. P. Adams. Influence of adhered mortar on recycled concrete aggregate cracking through numerical simulations. *ACI Convention Fall 2016*, Philadelphia, Pennsylvania, USA, October 23–27, 2016.

मेरो परिवार र मेरी श्रीमती - रोशनी भारतीलाई।
तपाईहरुको माया, साथ, र धैर्यताको लागि।

To my family and my wife – Roshani Bharati.
For your love, support, and patience.

ACKNOWLEDGMENT

I am extremely grateful and thankful towards my dissertation advisor Dr. Matthew J. Bandelt for his mentorship, advice, and incredible support throughout the doctoral study. This dissertation would not have taken the current shape and form, without his insights and intellectual stimulation. I was fortunate to get the opportunity to work under his guidance and be involved in various collaborative research projects with Federal Highway Administration, Rutgers University, and Stanford University. Dr. Bandelt has inspired me to become a better researcher, presenter, academic writer, and instructor. It has been a rewarding experience to conduct research under the supervision of such an intelligent, hardworking, and caring advisor.

I would like to express my thankfulness towards Dr. Methi Wecharatana, Dr. Shawn A. Chester, Dr. Matthew P. Adams, and Dr. Bruno M. Goncalves da Silva for kindly agreeing to serve in the dissertation committee and providing useful suggestions. I am immensely grateful towards Dr. Methi Wecharatana for admitting me into the PhD program at NJIT and providing a great platform to pursue doctoral study. I would also like to thank Dr. Matthew P. Adams, co-director of Material and Structures Laboratory (MatSLab) at NJIT, for involving me in various research projects and providing constructive comments during the MatSLab research presentations. I would also like to acknowledge the generous funding provided by the Department of Civil and Environmental Engineering (CEE) at the New Jersey Institute of Technology (NJIT) for the doctoral study.

I would like to thank Stephen J. George and Nasser M. Channaoui for being readily available to help, especially to setup the lateral actuator, fabricate the test setup, and construct the wooden formwork. Furthermore, I would also like to thank Dr. Taha Marhaba (CEE department chair) and Ms. Heidi Young (former administrative assistant to the chair) for providing a comfortable work space and

expediting various administrative works throughout my doctoral study. I am thankful to Michael Monaco and Aaron Strand for guiding me through the concrete mixing procedure, tests of fresh and hardened concrete properties, and large scale concrete specimen tests during the summer of 2016. I am thankful to all the members of MatSLab research group: Aaron Strand, Anuruddha Jayasuriya, Jin Fan, Hasan Tariq, Daniel Calabro, Marwa Ibrahim, Noah Thibodeaux, and Seyed Shirkhorshidi for providing help in the laboratory and being involved in several research discourse in the Graduate Student Office (Colton 421). I am grateful towards Yi Shao and Dr. Sarah Billington for collaborating on an experimental program and providing useful data to validate my numerical findings.

I would like to express sincere appreciation towards my Master's thesis advisor Dr. Pennung Warnitchai and research collaborator Dr. Teraphan Ornthammarath at the Asian Institute of Technology in Thailand. Thank you for introducing me to the field of research and inspiring me to pursue further research study.

I feel blessed to have made so many wonderful friends during my time at NJIT, namely: Likun Hua (Stuart), Wanyi Fu (Vanessa), Jin Fan, Anuruddha Jayasuriya, Di Zhang, Gayani Gunarathna, Shaini Dilsha, Hasan Tariq, Jitendra Kewalramani, Janitha Batagoda, Chintan Vora, and Nirmal Bharati. I will always cherish the memories we made during our birthday celebrations and dinners. I would like to express immense gratitude towards my mother (Urmila Pokharel), father (Guna Raj Pokharel), grandparents, uncle (Dr. Yagya Raj Pokharel), brother (Manish Aatreya), and sister (Manisha Hicks) for their unconditional love, life lessons, and unwavering support throughout my life. I am thankful to my in-laws for bringing more joy and happiness in my life over the years. Lastly, I am extremely grateful towards my wife, Roshani Bharati, without whom this journey would be difficult to complete — thank you for your love, support, and patience.

TABLE OF CONTENTS

TABLE OF CONTENTS
(Continued)

TABLE OF CONTENTS (Continued)

Chapter **Page**

TABLE OF CONTENTS
(Continued)

Chapter Page

LIST OF TABLES

LIST OF FIGURES

LIST OF FIGURES
(Continued)

LIST OF FIGURES
(Continued)

Figure **Page**

LIST OF FIGURES
(Continued)

Figure **Page**

LIST OF FIGURES
(Continued)

Figure **Page**

CHAPTER 1

INTRODUCTION

1.1 Motivation

Innovative materials that can improve the strength, ductility, resilience, carbon footprint, and life-cycle cost are being developed to advance the performance of traditional reinforced concrete materials and structures [1–4]. For example, advances in alternative and supplementary binder systems have been developed to improve the durability of concrete [5–8]. Recycled aggregates are being used to address the depleting supply of high-quality natural aggregate systems [9–11] and fiber-reinforced polymers are being used to replace conventional steel reinforcement to limit damage due to corrosion [12–15].

One such novel material that has been extensively studied and is being used increasingly by the construction industry as an alternative to conventional concrete is fiber-reinforced concrete [16–19]. There are several classes of fiber-reinforced concrete and among them, ductile concrete composites, also known as, high performance fiber-reinforced cementitious composites (HPFRCCs), exhibit a ductile response under direct tension test. The uniaxial tensile strain in HPFRCCs exceed the yield strain of a typical reinforcing steel ($\approx 0.2\%$) [18, 20]. This ductile behavior of HPFRCCs has made them distinct from other fiber-reinforced concrete materials that are characterized by strain-softening behavior after first cracking [18]. Materials engineers have been able to achieve high levels of ductility by tailoring the fiber properties (e.g., elastic modulus, tensile strength, diameter, length, and volume), interface properties (e.g., bond mechanisms) and matrix properties (e.g., elastic modulus, compressive strength, and fracture properties) [20].

In the past decade, studies with structural level application of reinforced HPFRCC flexural members (beams or columns), shear-dominated members (coupling beams or structural walls), beam-column joints, and infill panels have been conducted to understand proof-of-concept behavior for applications under extreme loading (e.g., seismic loading) [21–30]. These studies show that use of HPFRCC improves the strength, damage tolerance, ductility, energy dissipation capacity, and durability of components [31, 32] when compared to conventional reinforced concrete. Further, the 2014 ACI Building Code included a provision to acknowledge the increased shear resistance in fiber-reinforced concrete members by allowing fiber-reinforced concrete to replace the minimum shear reinforcement that is typically required by the code [33].

Experimental research has led to application of HPFRCCs in the built environment around the world. For example, HPFRCC coupling beams were used in a high-rise core-wall building (42 stories) in Seattle, Washington in 2011 [34]. Similarly, in Tokyo, Japan—one of the seismically most active region—precast Engineered Cementitious Composite (a type of HPFRCC) coupling beams were used in Nabeaure Yokohama Residential Tower (41 stories) in 2007, and as expected, the building experienced less damage during the 2011 M_w 9.1 Tohoku earthquake [35]. HPFRCC is also being used increasingly in infrastructure projects subjected to severe environmental and mechanical loading condition. For example, Ultra High Performance Concrete (another type of HPFRCC) was used, for the first time in North America, to construct a long span (33.5 m) precast-prestressed girder for a highway bridge in Wapello County, Iowa in 2006 [36]. Since then, this material has been used progressively in more than 180 highway bridges, as a deck overlay material, field-cast bridge element connector, and precast-prestressed bridge component [37].

Research investigations of HPFRCC in the past were primarily focused on characterizing the mechanical properties of HPFRCCs [38–40] and formulating material models for numerical simulation [41–44]. Further, proof-of-concept studies established the flexural and shear response of reinforced HPFRCC members compared with conventional reinforced concrete members [45]. Further, the interaction between reinforcement and HPFRCCs has been characterized through bond-slip [46–49] and tension stiffening experiments [50–52].

Recent experimental work conducted by Bandelt and Billington [53] investigated the flexural behavior of reinforced HPFRCC beams up to large displacements. Results showed that the failure of reinforced HPFRCC beams occurs by fracture of tension zone reinforcement rather than crushing of compression zone material which is the typical failure mechanism in reinforced concrete beams. The difference in behavior for reinforced HPFRCC beams was due to inelastic strain concentration over a short debonded length of longitudinal reinforcement. The phenomenon of strain concentration was first observed by Moreno et al. [50] in tension stiffening experiments of different types of HPFRCC composite sections under large displacements. It was found that the fiber bridging action restrained the formation of splitting cracks in HPFRCC materials which caused a strain concentration phenomenon to occur. Further, studies of bond behavior revealed that the bond strength of reinforced HPFRCCs is higher than normal reinforced concrete which restricts the formation of splitting cracks [46, 47].

In addition to identifying the failure mechanism of reinforced HPFRCCs, Bandelt and Billington's study [53] also showed that the deformation capacity of reinforced HPFRCC beams increased with higher reinforcement ratios. Further, the deformation capacity of reinforced HPFRCC beams under cyclic loading was found to decrease by 67% when compared with deformation capacity under monotonic loading. The influence of reinforcement ratio and loading on the component-level response (i.e., ultimate drift capacity, damage pattern, failure mode) are different than observed in traditional reinforced concrete flexural members.

Further, the component-level response of concrete structural members are directly associated with the formation and behavior of plastic hinge region. Over the past several decades, many experimental and numerical studies have been carried out to understand the behavior of plastic hinge region in traditional concrete components [54–59]; however, such studies have been limited, in number and scope, in the case of HPFRCC structural components [18, 60, 61]. The plastic hinge region (i.e., region near maximum bending moment) in HPFRCC structural components exhibits unique phenomenon such as *crack localization* and *strain concentration* [53, 62, 63]. The behavior of this region, ultimately governs component-level ductility and energy absorption capacity under extreme dynamic loading condition.

With the addition of modeling, analysis, and acceptance parameters for performance-based seismic design in the recently published ACI 318-19 Building Code [64], practicing engineers now have the opportunity to analyze and design new structures using nonlinear response history analysis. However, novel ductile concrete composites such as HPFRCCs, do not have well established nonlinear modeling parameters and acceptance criteria, required for performance-based seismic design. For example, most of the lumped plasticity-based modeling technique requires quantification of plastic hinge length or analytical prediction of moment-rotation behavior for a given HPFRCC class and geometric cross-section. Therefore, there is a need to accurately quantify the plastic hinge length and develop analytical methods to calculate strength & displacement parameters at various performance levels (e.g, collapse level) to aid in the nonlinear modeling of reinforced HPFRCC structural components subjected to seismic loadings. The work presented in this dissertation aims to address some of these research needs by developing robust modeling, analysis, and design methodologies to advance the use of ductile concrete composites in structural components of new structures.

1.2 Research Objectives and Scope

The research objectives of this study originate from the discussion presented in the preceding section. The overall objective is to investigate the wide variability in component-level deformation capacity of reinforced HPFRCC flexural members under large deformations. In addition to that, a study is conducted to understand the plastic hinge behavior of reinforced HPFRCC structural components, and experimentation is used to explore the impact of reduction in fiber content on deformation capacity and plastic hinge behavior.

The following are the specific objectives of this research study:

1. Identify dominant factors influencing the deformation capacity and structural response of reinforced HPFRCC flexural members through numerical simulation.
2. Understand the plastic hinge behavior and develop an analytical method to quantify flexural strength and rotation capacity of reinforced HPFRCC structural components.
3. Understand the impact of change in fiber volume fraction on plastic hinge region of reinforced HPFRCC structural components through physical experimentation.
4. Outline an experimental framework to investigate the effects of material and loading variation on deformation capacity and plastic hinge behavior of reinforced HPFRCC flexural members.

The scope of this research is to conduct numerical simulation, statistical analysis, mechanics-based analysis, and experimental investigation of structural response in three major classes of HPFRCCs. The scope is limited to investigating component-level deformation capacity at collapse level, plastic hinge mechanisms, and developing simplified analytical framework to compute specific control points of moment-rotation curve. Limited physical tests are conducted and an experimental framework is proposed for future research extension.

1.3 Organization of Dissertation

This dissertation is organized into seven chapters. Chapter 1 discusses the motivation behind the research, objectives, and organization of the dissertation. A brief review of the remaining chapters is provided below.

Chapter 2 provides a review of the development of HPFRCCs along with detailed descriptions of three types of HPFRCC used in this study. A summary of previous experimental studies on the behavior of reinforced HPFRCCs is presented. A discussion on variation in deformation capacity of reinforced HPFRCC flexural members based on currently available experimental data is presented. The concept of plastic hinge length is described, and the type of damage associated with the plastic hinge region of reinforced HPFRCC structural components is presented. A review of past studies on plastic hinge region of reinforced HPFRCC structural components is provided in Chapter 4 instead of Chapter 2. A discussion on numerical models formulated to simulate the behavior of reinforced HPFRCC structural components is presented.

Chapter 3 describes the work carried out based on an extensive numerical analysis used to investigate the influence of material and structural properties on the deformation capacity of reinforced HPFRCC beams. Thirty-six simulations were carried out with the variation in material properties, reinforcement ratio, boundary conditions, and shear span-to-depth ratio under monotonic loading. Important factors influencing the deformation capacity were identified and investigated based on the damage pattern and length of plasticity. Recommendations to predict deformation capacity based on the statistical analysis are presented. The results of the work presented in Chapter 3 were recently published in *Composite Structures* [65].

Chapter 4 presents an investigation to understand the plastic hinge mechanism in reinforced HPFRCC structural components. A new plastic hinge length expression is proposed using a combined numerical and statistical approach. Further, a mechanics-based approach is developed to compute flexural strengths and rotation capacities at various damage states in reinforced HPFRCC structural components. A comprehensive set of experimental database is utilized to demonstrate the predictability of the proposed approach in different classes of HPFRCCs under different boundary conditions and loading scenarios. The work presented in Chapter 4 was recently published in *Engineering Structures* [66].

Chapter 5 examines the impact of change in fiber volume fraction in plastic hinge region of reinforced HPFRCC structural components. An experimental study is conducted with variation in fiber volume fraction. The specimens are tested monotonically, under a four-point bending test setup. The variation in moment-drift response, reinforcement plasticity, curvature distribution, and crack pattern are discussed. The analytical method developed in Chapter 4 is validated using the experimental data obtained from this study. The work presented in Chapter 5 will appear in the *Proceedings of RILEM-fib X International Symposium on Fiber Reinforced Concrete (BEFIB 2020).*

Chapter 6 outlines a detailed experimental program to physically quantify the impact of variation in HPFRCC material type and loading condition on deformation capacity and plastic hinge length in reinforced HPFRCC flexural members. Two types of HPFRCCs are proposed to be used for construction of cantilever specimens, which will be tested under monotonic and cyclic load. A data acquisition plan consisting of digital image correlation and strain gages, among others, will be used to record strain variation in the plastic hinge region. The experimental findings of this future research work can be used to supplement the numerical and analytical results presented in Chapter 3 and 4.

Chapter 7 concludes the dissertation with a summary of the important research findings and scientific contributions. Research limitations are discussed and recommendations for future research extensions are provided.

Chapters 3 through 5 of this dissertation were written as stand-alone articles for publication purpose. Due to this, there is some repetition of background information in the dissertation.

CHAPTER 2

LITERATURE REVIEW

2.1 Background

The use of short, discontinuous, and randomly orientated fibers in construction material dates back to the early human civilization where straw was mixed with clay-based binding material for the construction of adobe [67]. The research involving the use of fiber in the form of wire steel in concrete was started by Romualdi and Mandel [68] and Romualdi and Batson [69] in the early 1960s. With the passage of time, fibers of different shapes (e.g., hooked end, twisted, indented, etc.), size (e.g., fiber length and diameter) and material (e.g., plastic, glass, carbon etc.) were used in concrete.

Although the use of fibers increases toughness of concrete in compression, researchers were not able to increase the ductility under tensile loading condition. The addition of larger quantity of fibers, to improve the tensile behavior, was restrictive due to workability issues. However, in the 1980s and 1990s, there was advancement in the development of fiber-reinforced composites through the improved understanding of the micro-structure of concrete and introduction of mineral (e.g., silica fume) and chemical additives (e.g., water reducing admixtures) into the mixture. As a result, various classes of fiber-reinforced composites such as Slurry Inflitrated Fiber Concrete (SIFCON), Slurry Inflitrated Mat Concrete (SIMCON), and Engineered Cementitious Composite (ECC) were developed for practical applications [16, 17, 20]. These composites possessed a common characteristic of strain-hardening response after first cracking, with distributed cracking under uniaxial tension test [20, 70, 71]. To distinguish these composites from other fiber-reinforced composites, Naaman and Reinhardt [40] proposed a simplified classification system. Two major categories were proposed based on the uniaxial tensile response: tensile strain-hardening and tensile strain-softening as shown in Figure 2.1. Fiber-reinforced composites with tensile strain-hardening behavior are referred to as “High Performance Fiber Reinforced Cement Composites” as per this classification. Generally, the critical fiber volume in HPFRCC mix is less than or equal to 2% for better workability and the peak tensile strain, ε_{pc}, of the HPFRCC material should be more than the yield strain, ε_y, of the mild steel to obtain a hardening response under flexural bending [40].

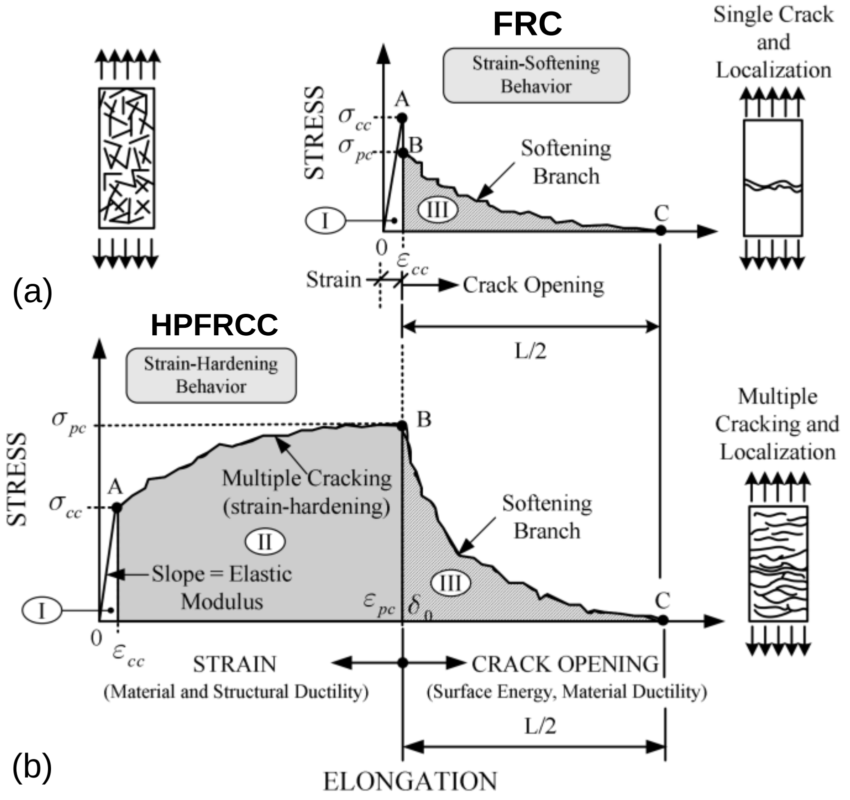

Figure 2.1 Typical Stress-strain curve under uniaxial tension (a) Fiber-reinforced concrete (FRC) composites with strain-softening behavior (b) HPFRCC with strain-hardening behavior.
Source: [18].

Over the last two decades, laboratory testing of large scale structural components were actively carried out to understand the structural behavior of reinforced HPFRCC components. Specifically, the seismic behavior of reinforced HPFRCC components such as coupling beams were investigated to quantify energy dissipation capacity, ductility, and damage tolerance capacity [22, 34, 72]. Further, the behavior of flexural members [23, 27, 53], bridge piers [21, 73], beam-column joints [28], and infill panels [26], among others, were also assessed. The physical tests showed improved performance of HPFRCC components over traditional concrete in terms of damage tolerance, strength, and ductility.

Studies to understand the composite behavior of steel reinforced HPFRCCs using tension stiffening experiments were also conducted [50, 52, 74], which showed the high resistance of HPFRCCs towards the formation of splitting cracks due to fiber bridging action. Bond behavior of HPFRCCs were also investigated, which revealed higher bond strength and requirement of smaller development length in reinforced HPFRCCs compared to conventional reinforced concrete [46–49]. With the improved understanding of the material behavior and component-level response, recent research is focused on developing constitutive models and numerical methods to predict the component-level behavior using finite element modeling approaches at the continuum level [42, 43, 75] and discrete level [41, 61].

2.2 Representative Classes of HPFRCCs

Researchers have engineered and developed numerous types of HPFRCCs based on a desired level of performance for various loading conditions (e.g., mechanical loading, thermal loading, etc.). In this study, three representative types of HPFRCCs were investigated, namely, a Ultra High Performance Concrete (UHPC), an Engineered Cementitious Composites (ECC), and a Hybrid Fiber-Reinforced Concrete (HyFRC). These three materials are all considered HPFRCCs because their tensile stress-strain curve exhibit strain hardening behavior (or elasto-plastic behavior) and have fiber contents below 2% by volume fraction of the mixture.

2.2.1 Ultra High Performance Concrete

2.2.1.1 Material Description. Ultra High Performance Concrete (UHPC) is an advanced class of cement-based composite material developed using optimal particle packing theory in the 1990s [76]. UHPC has a low water-to-cement ratio, usually less than 0.2, and is characterized by a dense cementitious matrix with a discontinous pore structure [37]. The presence of micro-steel fibers removes the intrinsic brittleness associated with high tensile and compressive strength of UHPC.

A typical mixture of UHPC consists of portland cement, fine sand (0.2 mm maximum particle size), silica fume, ground quartz, high-range water-reducing admixture (HRWR), accelerator, steel fibers, and water [77]. Coarse aggregates are used less frequently. UHPC generally contains 1% to 2.5% by volume fraction (V_f) of smooth, hooked, or twisted steel fibers with a fiber length (l_f) of 13 mm to 30 mm and a diameter (d_f) of 0.2 mm to 0.38 mm. The fibers used in UHPC usually have an aspect ratio (l_f/d_f) of 65 to 100 [36, 78]. The nominal tensile strength and stiffness of steel fibers is 2600 MPa and 205 GPa, respectively. The type of fibers, aspect ratio of fibers, and mixture constituents influence the mechanical response of UHPC mixture [78].

2.2.1.2 Mechanical Properties. The tensile stress-strain response of UHPC has been idealized by Graybeal [79] into four phases as shown in Figure 2.2 (a). Phase I represents the elastic response of a UHPC specimen under uniaxial a tension test. Phase II represents fine multiple distributed crack formation in UHPC matrix. Phase III represents debonding of the fibers from UHPC matrix and widening of the individual cracks. Localization of cracks occur in phase IV where fibers bridging a dominant crack break or start to pullout as shown in Figure 2.2 (b).

The maximum tensile strength (f_t) of UHPC under direct tension test ranges from 5 MPa to 11 MPa, whereas the maximum compressive strength ($f_c^{'}$) ranges from

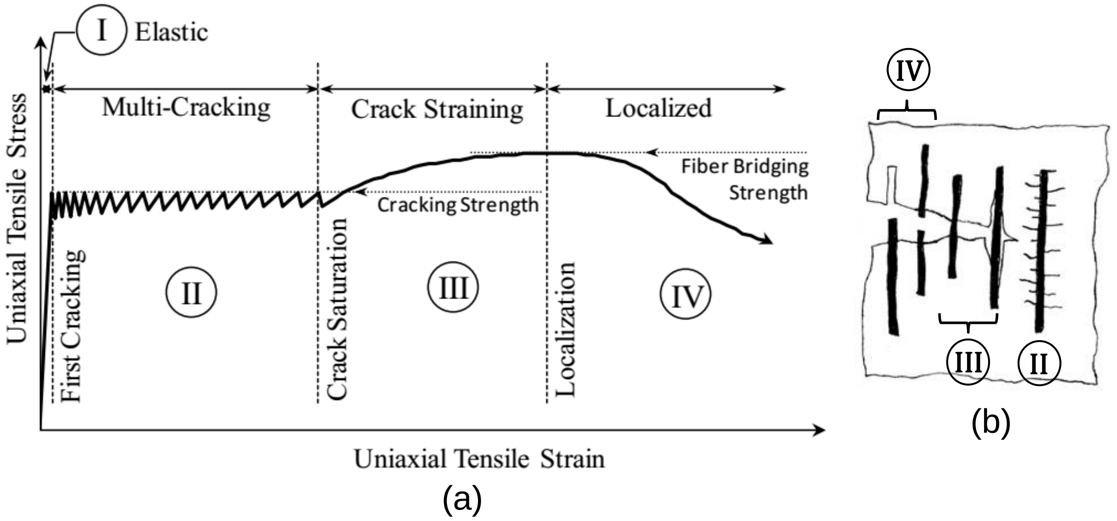

Figure 2.2 (a) Idealized tensile property of UHPC and (b) cracking mechanism. *Source*: [79].

120 MPa to 210 MPa under uniaxial compression test [77]. The static modulus of elasticity ranges from 40 GPa to 50 GPa and can also be computed using empirical equations found in the literature (e.g., $E = 4040\sqrt{f_c'}$ MPa) [77, 79]. The value of Poisson's ratio for UHPC ranges from 0.18 to 0.20 and flexural bending strength ranges from 25 MPa to 35 MPa [77].

2.2.2 ECC

2.2.2.1 Material Description. Engineered Cementitious Composites (ECC) were developed by tailoring fiber and matrix properties to obtain steady state cracking under uniaxial tension loads by Li [80]. The interaction between fiber, matrix and fiber-matrix interface was studied using micro-mechanics principles which relates to the fiber-bridging property of the matrix. The fiber-bridging property across a matrix crack is the most fundamental property of ECC material and is associated with the average tensile stress (σ) transmitted across a crack with uniform opening (δ) [2]. The tensile stress vs. crack opening (σ-δ) provides the linkage between material constituents and composite tensile ductility (Figure 2.3 (a)). The (σ-δ) curve can be thought of as a spring law, governing the behavior of bridging forces at the opposite sides of a crack.

The multiple distributed cracking and strain hardening behavior of ECC is achieved by satisfying two criteria. The first criteria is the strength criteria which requires that the matrix cracking strength should be less than the maximum fiber bridging stress. If this criteria is not satisfied, fiber bridging action cannot support the applied load. The second criteria is the energy criteria which is associated with the complementary energy (C) as shown in the shaded region of σ-δ curve, in Figure 2.3 (b). If the fiber-matrix interface is too weak, fibers pull out resulting in σ-δ curve with low bridging strength (σ_{cu}). And, if the fiber-matrix interface is too strong, fibers rupture resulting in a small crack opening δ_p. In both cases, complementary energy will be small. However, if the complementary energy is low, the crack will behave like a Griffith crack with maximum crack opening at the middle of the crack (not a desirable cracking mechanisms). If the complementary energy is high, the crack will remain flat with steady state crack opening and maintaining tensile load carrying capacity. The load can be transferred from this crack plane to the matrix causing formation of another crack. The repetition of this process forms multiple distributed crack in ECC material [2].

A typical mixture of ECC consists of Type II/V Portland cement, Class F fly ash, silica sand (0.13 mm maximum particle size), viscosity modifying admixture (VMA), high-range water-reducing admixture (HRWR), polyvinyl alcohol (PVA) fibers, and water [81]. ECC mixtures generally do not contain coarse aggregates. ECC commonly contains 2% by volume fraction of smooth polyvinyl alcohol (PVA) or polyethylene (PE) fibers with a length of $12-13$ mm and a diameter of $0.038-0.040$ mm. The nominal tensile strength and stiffness of PVA fibers is 1600 MPa and 43 GPa, respectively, whereas the tensile strength and stiffness of PE fibers is 2580 MPa and 117 GPa, respectively [27, 81, 82]. The fibers used in ECC usually have an aspect

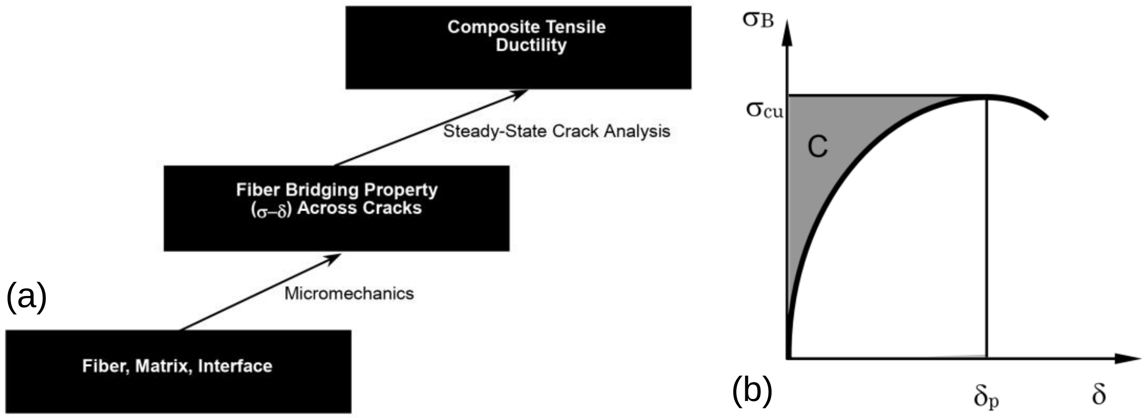

Figure 2.3 (a) Relationship of constituents, bridging property and composite tensile ductility and (b) Tensile stress vs. crack opening.
Source: [2].

ratio of 300 to 350. The types of fibers, their aspect ratios, and mixture constituents influence the mechanical response of ECC mixture [39].

2.2.2.2 Mechanical Properties. ECC exhibits ultra high tensile ductility, as high as 5%, under direct tension test as shown in Figure 2.4 [81]. The tensile stress-strain curve is similar to that of metal with an initial elastic portion followed by a plastic strain hardening portion. The specimen exhibits multiple distributed microcracking until it loses tensile load carrying capacity through crack localization. The peak tensile strain of ECC is greater than that of concrete by 2−3 orders of magnitude and the maximum width of microcracks is less than 100 μm [39]. These attributes lead to enhanced structural performance in terms of ultimate deformation capacity and energy dissipation capacity.

The maximum tensile strength of ECC under direct tension test ranges from 2.5 MPa to 5.0 MPa [39], whereas the maximum compressive strength ranges from 30 MPa to 90 MPa in uniaxial compression test [81]. The static modulus of elasticity ranges from 17 GPa to 34 GPa and flexural bending strength ranges from 10 MPa to 30 MPa [81, 82]. The value of Poisson's ratio for ECC is 0.15 [82].

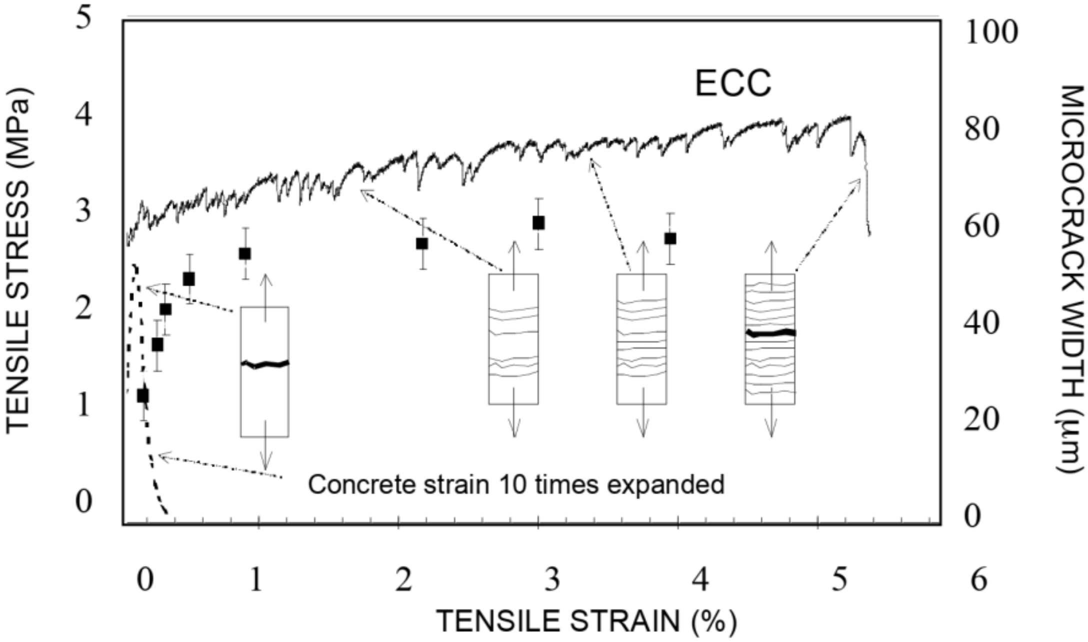

Figure 2.4 Uniaxial tensile property of ECC.
Source: [81].

2.2.3 HyFRC

2.2.3.1 Material Description. Hybrid Fiber-Reinforced Concrete (HyFRC) composite is called "Hybrid" due to the use of fiber hybridization technique in the mixture (i.e., the composite consist of steel macro-fiber and PVA micro-fiber with different lengths and diameter). HyFRC is believed to have better crack control due to fiber hybridization. This is illustrated in Figure 2.5 (b) where micro fibers are bridging micro cracks and once the micro cracks become large, they will be subsequently bridged by the macro fibers to resist propagation of cracks. However, as shown in Figure 2.5 (a), traditional FRC contains macro fibers only which are less effective in resisting rapid propagation of cracks. HyFRC also contains coarse aggregates which provides high elastic stiffness as compared to other HPFRCC materials.

Blunt and Ostertag developed a deflection hardening HyFRC mixture based on a performance-based approach [83]. The performance criteria was based on the average yield strain of mild reinforcement (0.002) and was used to design the composite. This

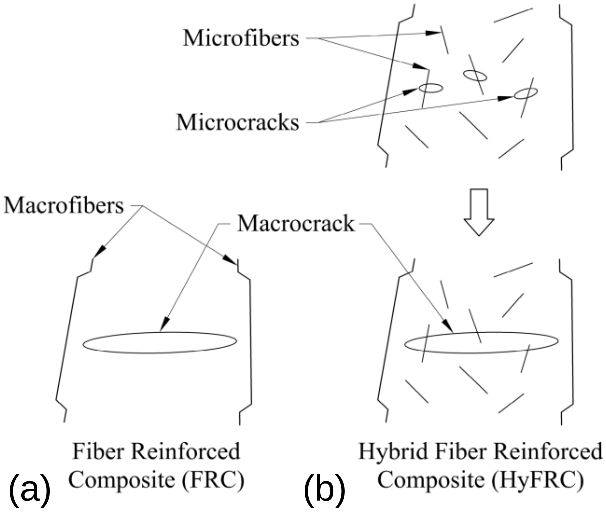

Figure 2.5 Fiber bridging in (a) FRC and (b) HyFRC.
Source: [32].

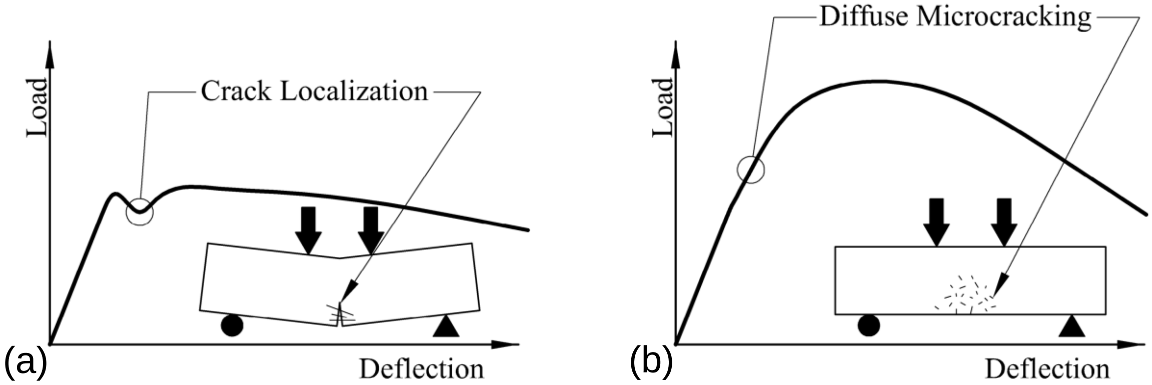

Figure 2.6 Load vs. deflection in (a) FRC and (b) HyFRC.
Source: [32].

resulted in a more durable cracking mechanisms in the composite. Figure 2.6 (a) shows the deflection softening behavior in traditional FRC due to crack localization and Figure 2.6 (b) shows deflection hardening behavior in HyFRC due to formation of multiple distributed fine cracks. HyFRC has been used in bridge approach slabs which resulted in less durability issues compared to concrete slabs. Further, the amount of reinforcement in HyFRC could be reduced without compromising the strength and serviceability performance leading to lower initial cost [32].

A typical mixture of HyFRC consists of Type I/II Portland cement, coarse aggregate with nominal maximum size of 9.5 mm, fine aggregate, high-range water-reducing admixture (HRWR), polyvinyl alcohol (PVA) fibers, steel fibers, and water [82, 83]. HyFRC consists of a hybrid combination of steel macro-fibers and polyvinyl alcohol micro-fibers with a volume fraction of 0.5%−1.3% and 0.2%−0.3%, respectively [82, 83]. PVA fibers are smooth with a length of 8−9 mm and a diameter of 0.038−0.040 mm. Steel fibers are hooked end with a length of 30−60 mm and a diameter of 0.55−0.75 mm. Macro-fibers in HyFRC mixtures generally have an aspect ratio of 55−80, whereas micro-fibers have an aspect ratio of 200−250 [82, 83].

The nominal tensile strength and stiffness of PVA fibers is 1600 MPa and 43 GPa, respectively, whereas the tensile strength and stiffness of steel fibers is 1100 MPa and 200 GPa, respectively [82, 83]. The types of fibers, their aspect ratios, and mixture constituents influence the mechanical response of HyFRC mixture.

2.2.3.2 Mechanical Properties. The synergistic action between macro- and micro-fibers results in a large tensile strain capacity in HyFRC compared to conventional concrete under uniaxial tension (Figure 2.7). The peak tensile strain capacity of HyFRC ranges from 0.2% to 1% [82, 83]. This tensile ductility and fiber hybridization makes HyFRC suitable for application under extreme environmental condition and seismic loading conditions.

The maximum tensile strength of HyFRC under direct tension test ranges from 1.5 MPa to 3.1 MPa [82, 83], whereas the maximum compressive strength ranges from 30 MPa to 45 MPa under uniaxial compression [50, 82]. The static modulus of elasticity ranges from 17 GPa to 34 GPa and flexural bending strength ranges from 10 MPa to 20 MPa [74, 84]. The value of Poisson's ratio for HyFRC is 0.15 [82].

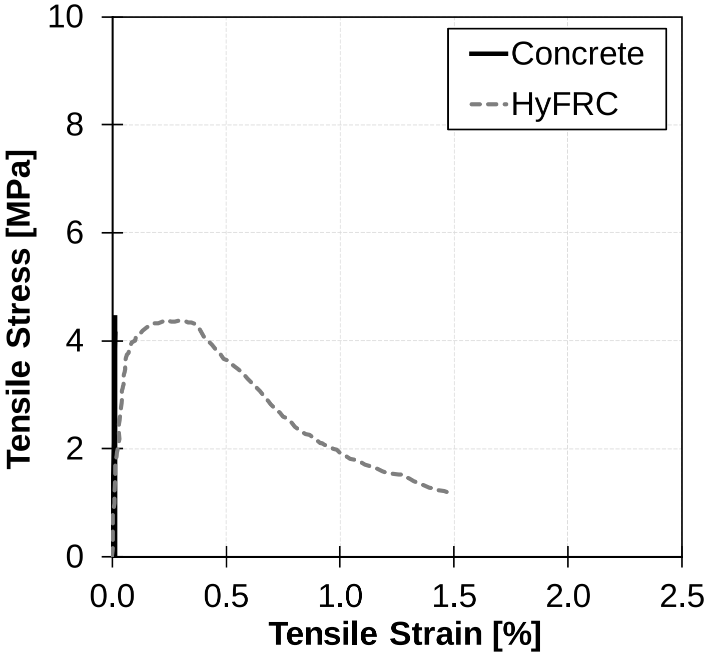

Figure 2.7 Uniaxial tensile property of HyFRC.
Source: [82].

2.3 Behavior of Reinforced HPFRCC Members

The behavior of reinforced HPFRCC members has been investigated by researchers through reinforced HPFRCC component level testing under various loading conditions and stress states. The component-level behavior has been reviewed and discussed in the sections below.

2.3.1 Flexural Behavior

The flexural behavior of three reinforced ECC cantilever specimens (S-2, S-3, S-4) and one reinforced concrete specimen (S-1) were studied by Fischer and Li [23]. The specimens had dimension ($l \times b \times h$) of 500 mm × 100 mm × 100 mm with same reinforcement ratio (1.73%) and were subjected to reversed cyclic loading. Two of the reinforced ECC specimens (S-3, S-4) did not contain transverse reinforcement. The reinforced concrete specimen failed by shear and compression failure of the concrete core at 9% drift level with ultimate strength of 13.8 kN. Two of the ECC specimens (S-2 and S-3) failed by reinforcement fracture at 14% and 15% drift level with ultimate lateral strength of 16 kN and 16.5 kN, respectively. One of the specimens (S-4) had an 80 kN axial load applied, and failed by the buckling of longitudinal reinforcement at 14% drift level with ultimate lateral strength of 19 kN. The drift capacity and lateral strength of reinforced ECC specimens were found to be greater than the reinforced concrete specimen. It was observed that the confinement of ECC was sufficient to prevent shear failure in ECC specimens. Based on the component hysteretic behavior, ECC specimens were found to have larger energy dissipation capacity than reinforced concrete specimens even without the use of transverse reinforcement (Figure 2.8).

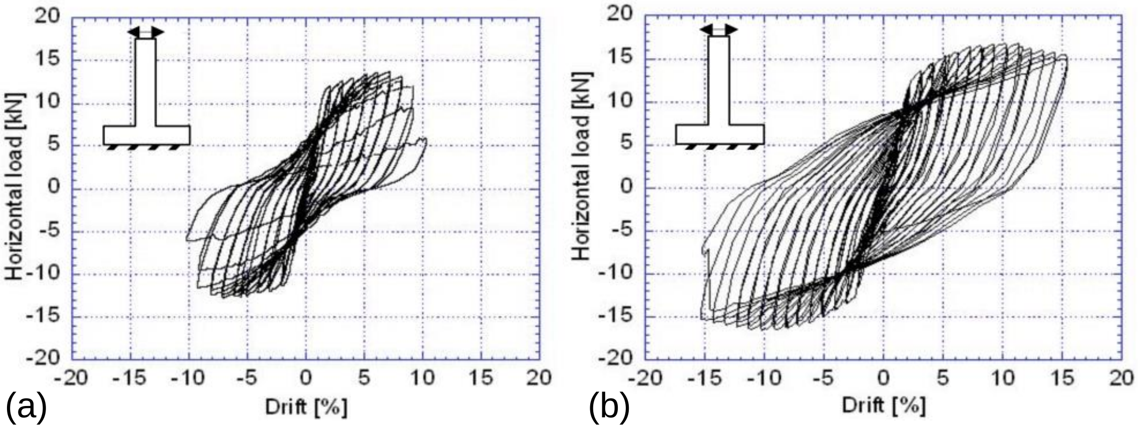

Figure 2.8 Load vs. drift response of (a) reinforced concrete specimen (S-1) (b) reinforced ECC specimen without stirrups (S-3).
Source: [23].

Bandelt and Billington [53] performed a series of experiments with reinforced ECC simply supported beams under monotonic and cyclic loading. One set of beams had a cross-sectional size ($b \times h$) of 130 mm × 230 mm with a reinforcement ratio of 0.54% (M-0.54 and C-0.54) and the other three sets had a cross-section ($b \times h$) of 130 mm × 180 mm with reinforcement ratios of 0.70% (M-0.70, C-0.70), 1.30% (M-1.30, C-1.30), and 2.0% (M-2.0 and C-2.0). Transverse reinforcement at $d/2$ spacing were provided in three sets of beams and at $d/4$ spacing for the set with reinforcement ratio of 2.0%. Seven out of eight beams failed by fracture of reinforcement which is in contrast with the flexural behavior of reinforced concrete where failure occurs through crushing of concrete (Figure 2.10). Failure by fracture was due to crack localization and strain concentration over a smaller length of longitudinal reinforcement compared to traditional concrete members. The deformation capacity of beams increased with increasing reinforcement ratio in the beams with a fracture failure mode. This behavior is also opposite to that of reinforced concrete beams. A comparison of the load-deformation response is shown in Figure 2.9 for beams under different loading conditions. Figure 2.9 shows that the cyclic response does not match the monotonic response curve for the same reinforcement ratio. The deformation capacity of beams under cyclic loading was found to range from 33% to 70% to that of monotonic loading for the same reinforcement ratio. The difference in the deformation capacity under different loading was found to be associated with the crack sizes and crack distribution.

Frank [85] recently conducted an extensive experimental study with three reinforced concrete cantilever beams having reinforcement ratios equal to 0.95% and eighteen reinforced ECC cantilever beams with a range of reinforcement ratios from 0.73% to 1.50%. The beams were tested under different reversed cyclic deformation histories using an unmodified FEMA 461 loading protocol [86], a modified FEMA 461 loading protocol with an initial small pulse of drift between 2.0%-2.5%, and modified FEMA 461 loading protocol with an initial large pulse of drift between 5.5%-7.0%. The result of the study shows that the ECC beams provided better damage tolerance compared to reinforced concrete beams under different loading histories. Concrete beams subjected to loading cycles with large pulse were found to have 42% lower deformation capacity compared to concrete beams with the same reinforcement ratio. Deformation capacity of ECC beams with lower reinforcement ratio (0.73%) was

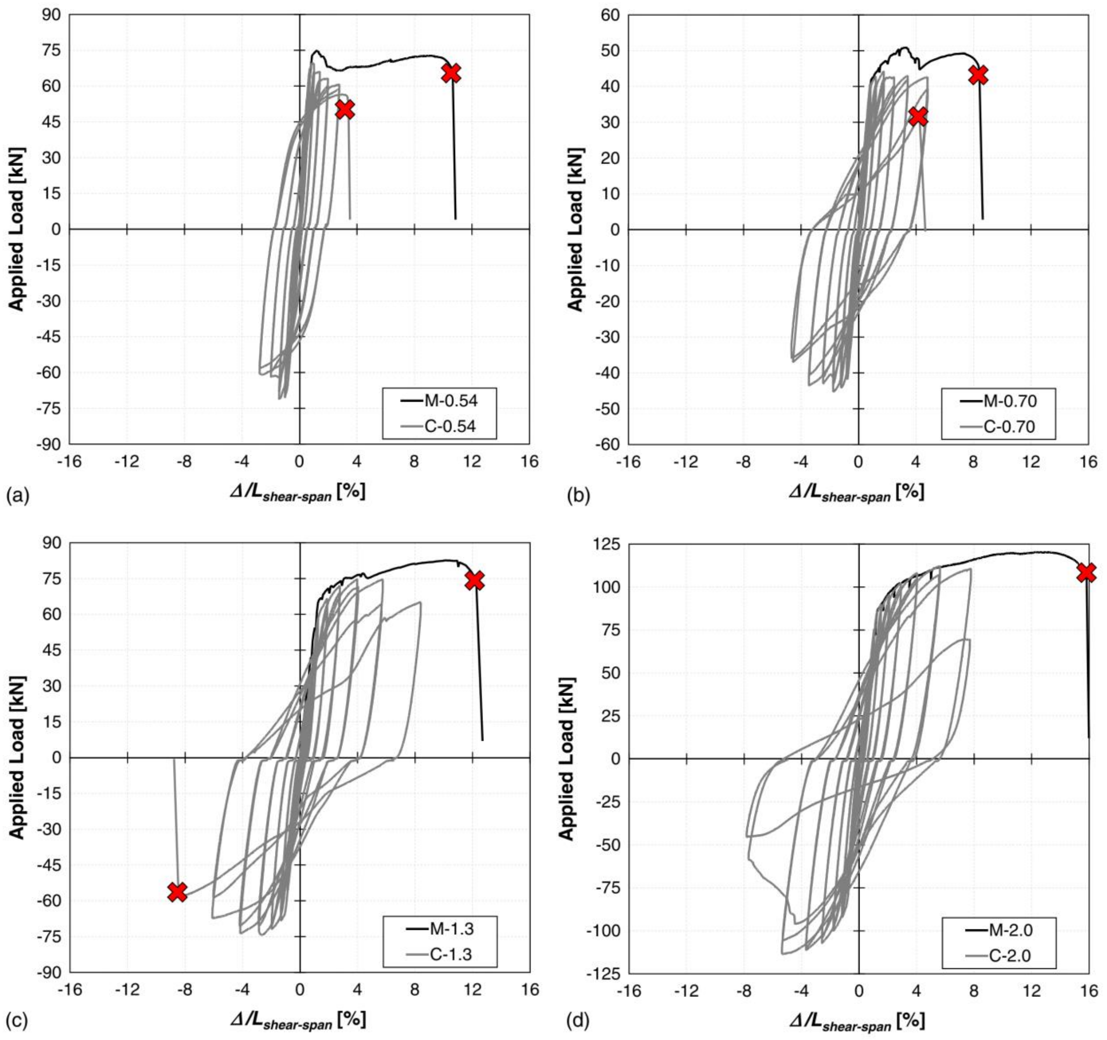

Figure 2.9 Load vs. deformation response of HPFRCC beams under monotonic and cyclic load for (a) $\rho = 0.54\%$, (b) $\rho = 0.70\%$, (c) $\rho = 1.30\%$, and (d) $\rho = 2.00\%$. *Source*: [53].

found to decrease with the presence and increase in size of initial pulse in the loading history.

2.3.2 Tension Stiffening Behavior

The tension stiffening behavior in reinforced ECC and reinforced concrete was studied by Fischer and Li [51] to understand the interaction between steel and cementitious material. The composite specimens were loaded under uniaxial tension up to a

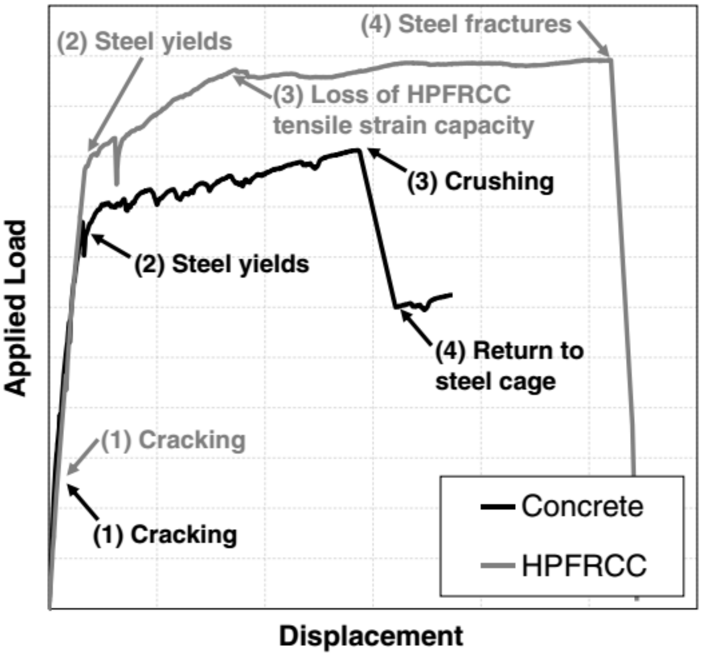

Figure 2.10 (a) Failure modes in HPFRCC specimens (b) flexural behavior of RC and HPFRCC beams.
Source: [53].

maximum strain of 0.5%. It was found that that ECC specimen achieved higher strength than concrete specimens because the ECC matrix significantly stiffened the specimen at uncracked sections. The crack patterns in concrete specimen contained splitting cracks whereas ECC specimens did not have any splitting cracks due to its matrix ductility. The steel and matrix material were found to deform compatibly up to a strain level of 0.005 in ECC specimens.

The tension stiffening behavior of concrete, ECC, SC-HyFRC, and HyFRC prismatic specimens (127 mm × 127 mm) with mild steel was studied by Moreno-Luna [82]. Moreno-Luna carried out the investigation up to large displacements under direct tension and compared the results to that of an earlier study done by Fischer and Li [51]. It was observed that the HPFRCC specimen had early strain hardening of the reinforcement due to the formation of dominant transverse cracks which led to lower deformation capacity than concrete specimens, as shown in Figure 2.11.

Splitting cracks of longer length were observed in concrete specimens whereas only transverse cracks were observed in the ECC specimens. Short splitting cracks were observed in SC-HyFRC and HyFRC specimens due to fiber bridge action (Figure 2.12). The absence of longer splitting cracks in HPFRCC specimens caused localization of strain over short de-bonded lengths resulting in early fracture of reinforcement compared to concrete specimens. It was also shown that the flexural strength of reinforced HPFRCC beams could be well predicted by accounting for hardening of reinforcement under bending.

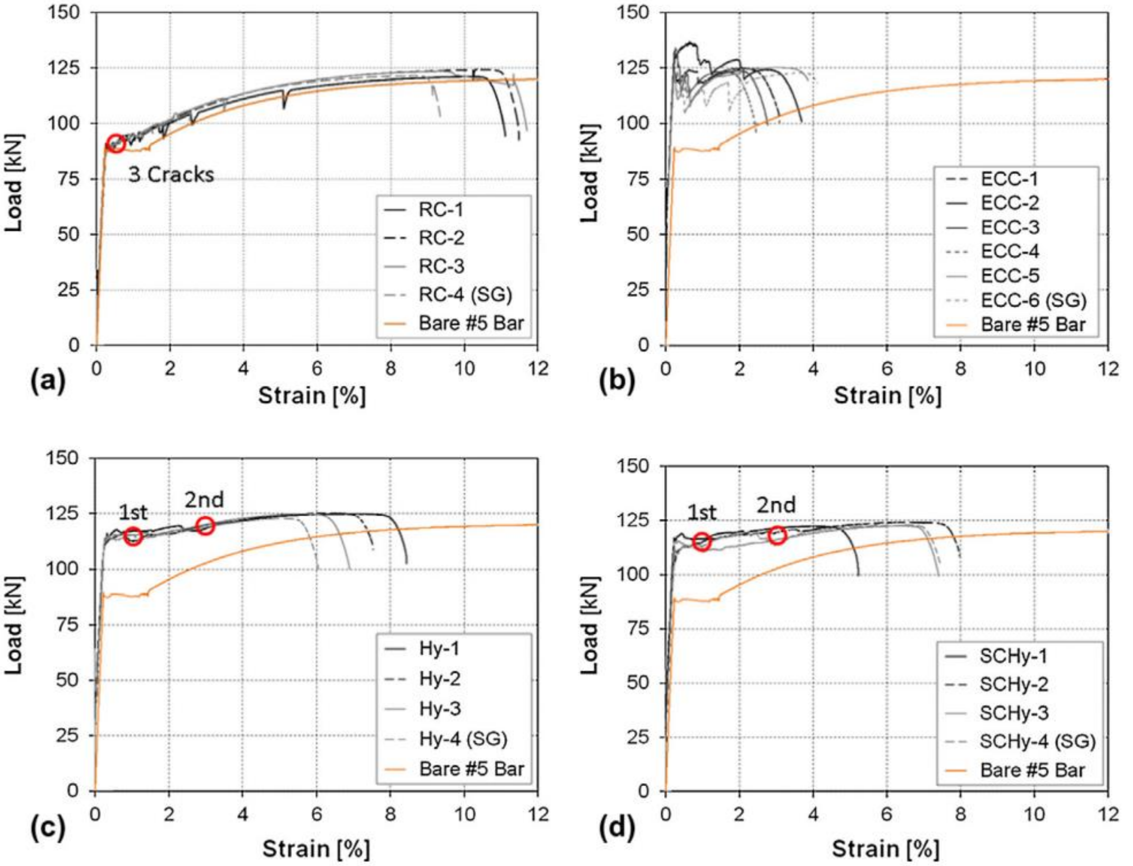

Figure 2.11 Load vs. strain in tension stiffening specimens of (a) concrete, (b) ECC, (c) SC-HyFRC, and (d) HyFRC with circle indicating formation of splitting crack.
Source: [50].

RC **[10.2%]** **ECC** **[3.5%]** **HyFRC** **[7.4%]** **SCHyFRC** **[7.4%]**

Figure 2.12 Crack pattern and deformation capacity before failure in tension stiffening specimens.
Source: [50].

2.4 Variation in Deformation Capacity

As performance-based seismic design is being widely adopted by the engineering community, it is more critical to have a fundamental understanding of deformation capacity of structural members at different performance levels (i.e., at cracking, yielding, and collapse level) [87, 88]. The exiting literature shows that there is a wide variation in the deformation capacity of reinforced HPFRCC members at the collapse level.

Table 2.1 shows a summary of the experimental studies carried out by various researchers in which failure occurred by fracture of reinforcement rather than crushing of cementitious material. All of the reported specimens had symmetrical reinforcement with no axial load applied on them and drift capacity was calculated at a residual strength of 75% or less. The reported data in Table 2.1 includes potential factors that can significantly affect the deformation capacity, such as loading type, tensile strength, reinforcement ratio, test setup, and shear span-to-depth ratio. The amount of variation in deformation capacity due to these factors is discussed in the sections below.

2.4.1 Loading Type

The type of loading significantly affects flexural response of the reinforced HPFRCC structural members compared to traditional reinforced concrete members. Bandelt and Billington [53] performed monotonic and cyclic test for four sets of simply supported beams with reinforcement ratios ranging from 0.54% to 2.0%. The beams were tested under monotonic load first using a displacement based load of 0.135 mm/s. The cyclic load was applied based on monotonic deformation capacity and increasing the displacement amplitude using FEMA 461 [86] loading protocol.

The load vs. deformation response shown in Figure 2.9 clearly shows that the cyclic response does not follow the monotonic response, whereas, in the case of a well-confined reinforced concrete member, the monotonic response forms the backbone of cyclic response. The deformation capacity of beams under cyclic loading were found to range between 33% and 70% to that of the monotonically loaded specimens for the same reinforcement ratios. The deformation capacity was significantly reduced in lower reinforcement ratios (0.54% and 0.70%) than in higher reinforcement ratios (1.30% and 2.00%). The difference in the deformation capacity was found to be associated with the crack sizes and crack distribution. Under cyclic loading, the beams with lower reinforcement ratios had fewer cracks compared to the beams with higher reinforcement ratios. Fewer cracks caused inelastic strain concentration over smaller length of reinforcement causing the failure of the beams by reinforcement fracture whereas a high number of distributed cracks caused uniform strain distribution over a longer length of reinforcement.

Table 2.1 Summary of Reinforced HPFRCC Experimental Study (Continued)

References	Specimen Name	Failure Mode	Loading Type	Tensile Strength [MPa]	Reinforcement Ratio [%]	Test Setup	Shear span to depth Ratio	Drift Capacity [%]
Fischer and Li [23]	ECC-0.57-0	RF	Cyclic	6.0	1.73	CLB	6.10	14.0
	ECC-0-0	RF	Cyclic	6.0	1.67	CLB	6.10	15.0
Parra-Montesinos and Chompreda [27]	PE2.0-0-0.6	RF	Cyclic	3.5	0.62	DCL	2.98	7.00
	PE2.0-0-1.1	RF	Cyclic	3.5	1.12	DCL	2.98	10.0
Olsen and Billington [26]	No. 2 P-Bar	RF	Cyclic	2.2	0.19	CLB	4.00	2.70
	V-Bar-2	RF	Cyclic	2.2	0.33	CLB	4.00	3.80
	Taper	RF	Cyclic	2.2	0.33	CLB	4.00	2.50
Yuan et al. [89]	S-4	RF	Cyclic	5.0	1.37	CLB	4.06	6.40
	S-5	RF	Cyclic	5.0	1.37	CLB	4.06	6.00
	S-6	RF	Cyclic	5.0	1.37	CLB	4.06	5.30
Tavallali et al. [90]	UC4-F	RF	Cyclic	4.4	1.23	DCL	3.00	12.0
	UC2-F	RF	Cyclic	4.1	1.23	DCL	3.00	11.0
Yoo and Yoon [62]	S13-0.94%	RF	Monotonic	5.8	0.94	SSB	5.02	5.80
	S13-1.50%	RF	Monotonic	5.8	1.50	4PS	5.07	5.70
	S19-0.94%	RF	Monotonic	8.5	0.94	4PS	5.02	5.60
	S19-1.50%	RF	Monotonic	8.5	1.50	4PS	5.07	7.30
	S30-0.94%	RF	Monotonic	8.0	0.94	4PS	5.02	8.90
	S30-1.50%	RF	Monotonic	8.0	1.50	4PS	5.07	8.10
	T30-0.94%	RF	Monotonic	9.5	0.94	4PS	5.02	7.30
	T30-1.50%	RF	Monotonic	9.5	1.50	4PS	5.07	9.10
Frank et al. [91]	ECC-1.30-M	RF	Monotonic	4.0	1.36	CLB	5.09	16.0
	ECC-1.30-MF	RF	Cyclic	4.0	1.36	CLB	5.09	11.9
Bandelt and Billington [53]	M-0.54	RF	Monotonic	2.2	0.54	4PS	3.26	11.0
	C-0.54	RF	Cyclic	2.2	0.54	4PS	3.26	3.40
	M-0.70	RF	Monotonic	2.2	0.70	3PS	4.28	8.40
	C-0.70	RF	Cyclic	2.2	0.70	3PS	4.28	4.80
	M-1.3	RF	Monotonic	2.2	1.30	3PS	4.32	12.0
	C-1.3	RF	Cyclic	2.2	1.30	3PS	4.32	8.50
	M-2.0	RF	Monotonic	2.2	2.00	3PS	4.36	16.0
Hung and Chueh [92]	B-2R-1SF	RF	Cyclic	6.2	1.98	CLB	5.98	8.00
	B-2R-2SF	RF	Cyclic	6.2	1.98	CLB	5.98	9.00
	B-1.4R-2SF	RF	Cyclic	6.2	1.32	CLB	5.98	7.00
	B-1.4R-2LF	RF	Cyclic	8.0	1.32	CLB	5.98	8.00

Table 2.1 (Continued) Summary of Reinforced HPFRCC Experimental Study

References	Specimen Name	Failure Mode	Loading Type	Tensile Strength [MPa]	Reinforcement Ratio [%]	Test Setup	Shear span to depth Ratio	Drift Capacity [%]
Frank et al. [63]	ECC-0.73-F	RF	Cyclic	4.0	0.73	CLB	5.00	11.9
	ECC-0.95-F	RF	Cyclic	4.0	0.95	CLB	5.00	11.9
	ECC-1-F	RF	Cyclic	4.0	1.00	CLB	5.00	11.9
	ECC-1.3-F	RF	Cyclic	4.0	1.30	CLB	5.00	11.9
	ECC-1.4-F	RF	Cyclic	4.0	1.40	CLB	5.00	16.9
	ECC-1.5-F	RF	Cyclic	4.0	1.50	CLB	5.00	16.7
	ECC-0.73-SP	RF	Cyclic	4.0	0.73	CLB	5.00	8.00
	ECC-0.95-SP	RF	Cyclic	4.0	0.95	CLB	5.00	11.9
	ECC-1-SP	RF	Cyclic	4.0	1.00	CLB	5.00	11.9
	ECC-1.3SP	RF	Cyclic	4.0	1.30	CLB	5.00	11.9
	ECC-1.4-SP	RF	Cyclic	4.0	1.40	CLB	5.00	16.9
	ECC-1.5-SP	RF	Cyclic	4.0	1.50	CLB	5.00	16.7
	ECC-0.73-LP	RF	Cyclic	4.0	0.73	CLB	5.00	6.00
	ECC-0.95-LP	RF	Cyclic	4.0	0.95	CLB	5.00	11.9
	ECC-1-LP	RF	Cyclic	4.0	1.00	CLB	5.00	11.9
	ECC-1.3-LP	RF	Cyclic	4.0	1.30	CLB	5.00	11.9
	ECC-1.5-LP	RF	Cyclic	4.0	1.50	CLB	5.00	16.7

Note: RF = Reinforcement fracture

CLB = Cantilever beam, DCL = Double cantilever beam

3PS = 3 Point Simply supported beam, 4PS = 4 Point Simply supported beam

It can be observed from Table 2.1 that besides the study by Bandelt and Billington [53], the rest of the experimental studies were conducted either monotonically or cyclically, so the deformation capacity under different loading scenario cannot be compared.

2.4.2 Tensile Strength

The sensitivity study conducted by Bandelt and Billington [75] shows that tensile properties such as, tensile strength and tensile fracture energy, significantly affect the load-deformation response under monotonic and cyclic loading. The authors found that the component deformation capacity was directly affected by the number of cracks which is a function of HPFRCC tensile strength. In cyclic loading, the use of damage fracture energy [38] was found to better capture the load-deformation response.

Figure 2.13 shows the scatter plot of drift capacity (%) vs. tensile strength (MPa) for the experimental data summarized in Table 2.1. It can be observed that there is no clear trend of increase or decrease of deformation capacity with change in tensile strength. Moreover, there is large dispersion in deformation capacity at particular tensile strengths. For example, at a tensile strength of 2.2 MPa, the drift varies from 3.4% to 16%. This large variation is due to the influence of other factors such as loading type and reinforcement ratio, among others. To quantify the influence of such factors, it is important to carry out a sensitivity analysis by varying one factor at a time and analyzing the response.

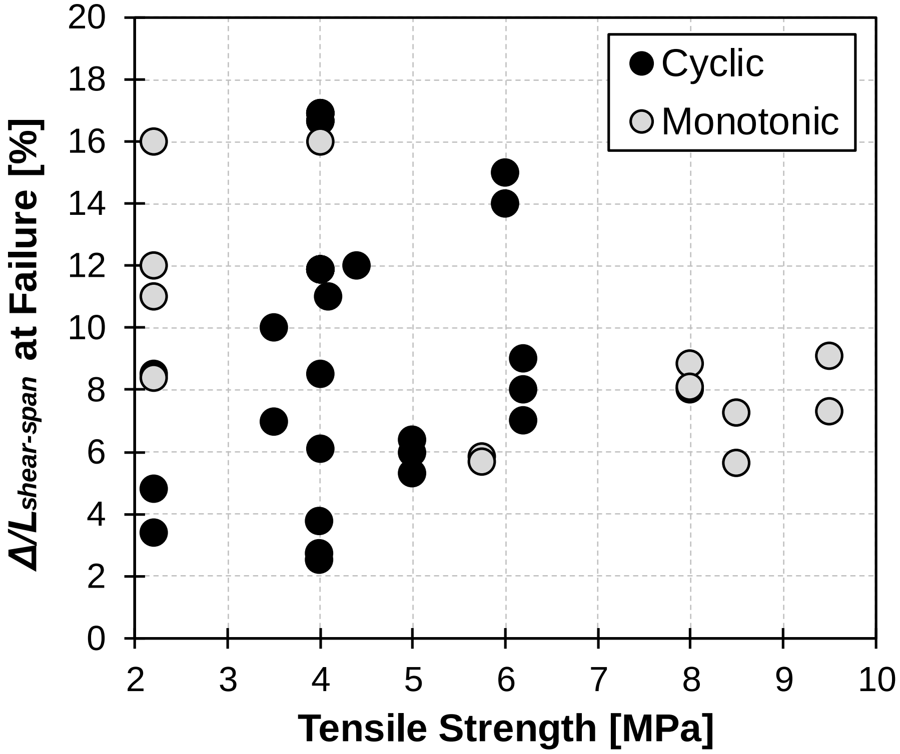

Figure 2.13 Drift capacity vs. tensile strength of reinforced HPFRCC specimens summarized in Table 2.1.

2.4.3 Reinforcement Ratio

Reinforcement ratio is another important factor affecting deformation capacity in reinforced HPFRCC members because the failure mode in HPFRCC members is governed by fracture of reinforcement. The experimental study by Bandelt and Billington [53] shows that deformation capacity increases with increasing reinforcement ratio, which contrasts the behavior of normal reinforced concrete beams where deformation capacity decreases with reinforcement ratio.

Figure 2.14 shows the scatter plot of drift capacity (%) vs. reinforcement ratio (%) taken from the study carried out by Bandelt and Billington [53]. It can be observed from the trend line that under cyclic and monotonic loading there is an increase in drift capacity with increasing reinforcement ratio. However, there is a large variation in deformation capacity, from 5% to 17%, at reinforcement ratios of 1.25%-1.50%. This large variation for a small range of reinforcement ratios might be due to the influence of a number of factors such as loading type, tensile properties, boundary conditions and shear span-to-depth ratio.

2.4.4 Test Setup

Different types of experimental test setups have been used to study the behavior of reinforced HPFRCC members, such as, cantilever [23, 63, 89], double cantilever [27], simply supported beams [53, 93], beam and column assembly [28], and beam and wall assemblies [72] etc. The deformation capacity of test members is affected by different boundary conditions imposed due to the use of these setups.

Figure 2.15 shows a scatter plot of drift capacity (%) vs. test setup for the experimental data summarized in Table 2.1. The summarized test data contained four types of setup, namely, cantilever beam setup (CLB), double cantilever beam setup (DCL), three-point simply supported beam setup (3PS), and four-point simply supported beam setup (4PS). It can be observed that there is a significant variation

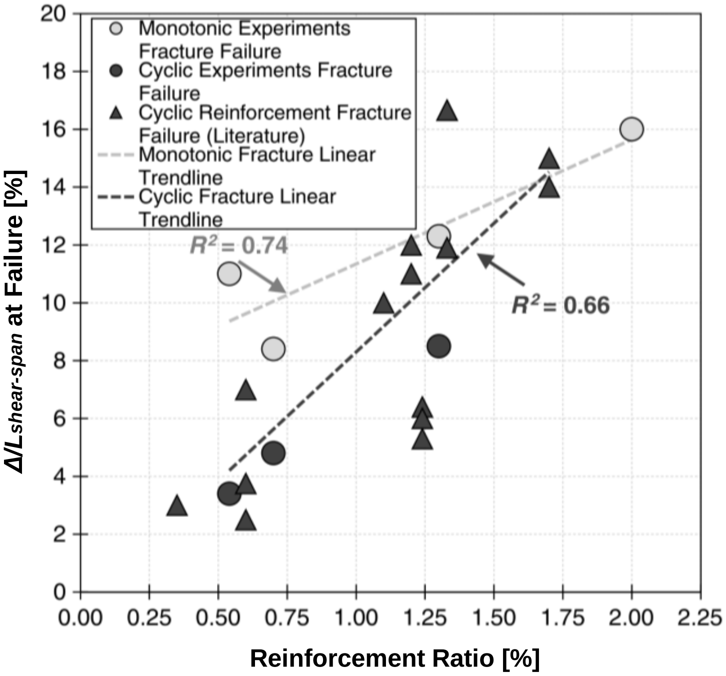

Figure 2.14 Variation of deformation capacity at different reinforcement ratios in HPFRCC beams.
Source: [53]

in deformation capacity for all types of test setups, and there is no clear relationship between drift capacity and test setup. To understand and quantify the variation of deformation capacity for a particular test setup, sensitivity analysis should be performed with all other factors being constant.

2.4.5 Shear Span-to-Depth Ratio

The behavior of short span beams (or deep beams), such as coupling beams, are generally shear-dominant whereas long span beams (or slender beams) generally have flexure dominant behavior [94]. The deformation capacity of short span beams are less than long span beams due to the early failure of such beams by the development of shear cracks.

Experimental research studies carried out in the past have been conducted with different shear span-to-depth ratio as listed in Table 2.1. Figure 2.16 shows the scatter

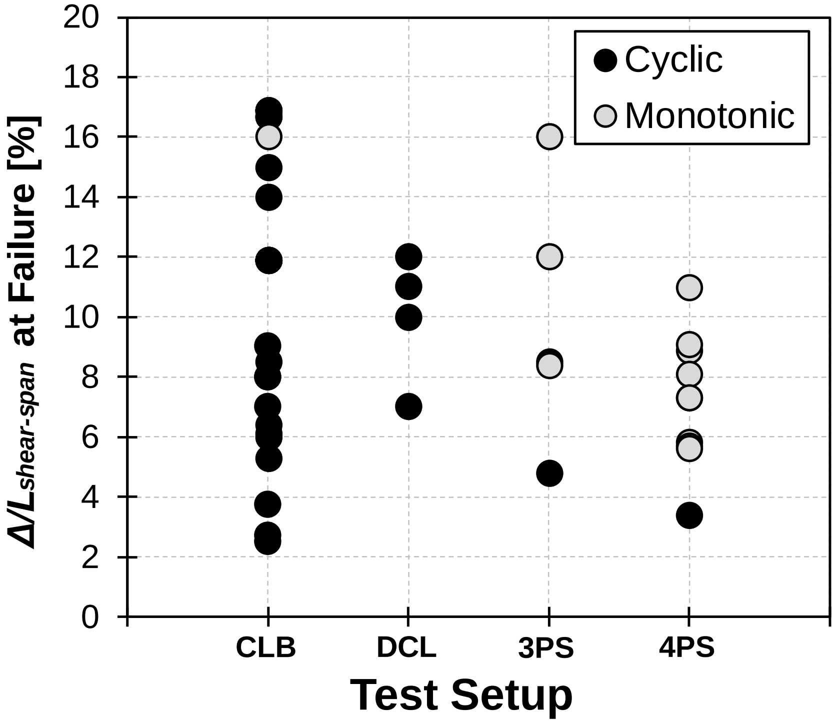

Figure 2.15 Drift capacity vs. test setup of reinforced HPFRCC specimens summarized in Table 2.1.

plot of drift capacity (%) vs. shear span-to-depth ratio for the experimental data summarized in Table 2.1. It can be observed that there is no clear trend of increase or decrease of deformation capacity with change in shear span-to-depth ratio. Moreover, there is large variation in deformation capacity for a given shear span-to-depth ratio. This large variation is due to the influence of other factors such as loading type, tensile property, reinforcement ratio, and test setup, among others. To quantify the influence of all such factors, it is important to carry out sensitivity analyses by varying one factor at a time and analyzing the response.

2.5 Plastic Hinge Region in Flexural Members

The region over which most of the inelastic damage occurs in a flexural member under the application of external loading is known as plastic hinge region. Over the past five to six decades there have been many experimental and numerical studies

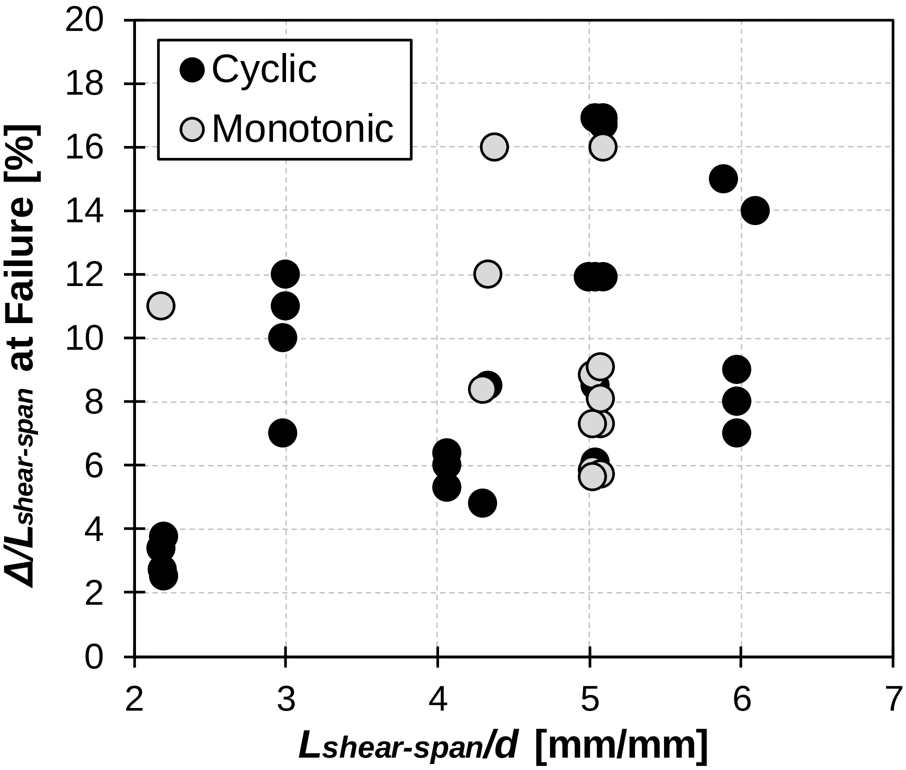

Figure 2.16 Drift capacity vs. shear span-to-depth ratio of reinforced HPFRCC specimens summarized in Table 2.1.

to understand the plastic hinge behavior in conventional reinforced concrete flexural members such as beams and columns [54–58, 95, 96]. The quantification of plastic hinge length in reinforced HPFRCC members are important for seismic detailing of the region which will be severely affected due to earthquake loading. Plastic hinge length is also necessary for discrete modeling of structural components in large structural systems [97].

The equivalent plastic hinge length, L_p, is a fictitious length near the maximum moment region of a structural member over which the plastic curvature is assumed to be constant, such that the area under the actual plastic curvature is equal to the area under the idealized plastic curvature [56]. This mathematical approach of concentrating the inelasticity in a small region is analogous to a mechanical hinge which rotates about a fixed point. This approach is widely used in the design industry in the form of lumped plasticity based modeling of structural components in buildings and bridges [98, 99]. Lumped plasticity based modeling provides a more realistic prediction of structural performance in terms of strength and/or displacement metrics under time variant extreme loading conditions, such as in structures subjected to severe pulse-like ground motions [100]. Further, the equivalent plastic hinge length implicitly accounts for the effect of tension shift due to shear cracking, bond-slip phenomenon, and tension-stiffening in the plastic hinge region and is the conventional way of calculating rotation parameters at collapse level (θ_u) for performance-based seismic design [87, 101].

2.5.1 Plastic Hinge Length

The theoretical formulation of L_p can be understood by considering a cantilever beam with a shear-span, L, subjected to a lateral load, P, as shown in Figure 2.17 (a). The moment diagram of the cantilever beam shows that critical section (i.e., region of maximum moment) lies near the fixed end (Figure 2.17 (b)). As the bending moment at any section is directly associated with curvature, the curvature distribution along the shear span is similar to the distribution of moment, until elastic limit. However, at large inelastic level of loading, the ultimate curvature distribution of the cantilever would be highly non-linear (Figure 2.17 (c)), with a significant portion of longitudinal reinforcement near the section of maximum moment exceeding the yield stress.

The plastic rotation capacity of the cantilever can be computed based on the inelastic curvature distribution at the ultimate level. Theoretically, the plastic rotation capacity, θ_p, of a member can be defined as [93]:

$$\theta_p = \int_0^{L_y} [\phi_u(x) - \phi_y(x)] dx \tag{2.1}$$

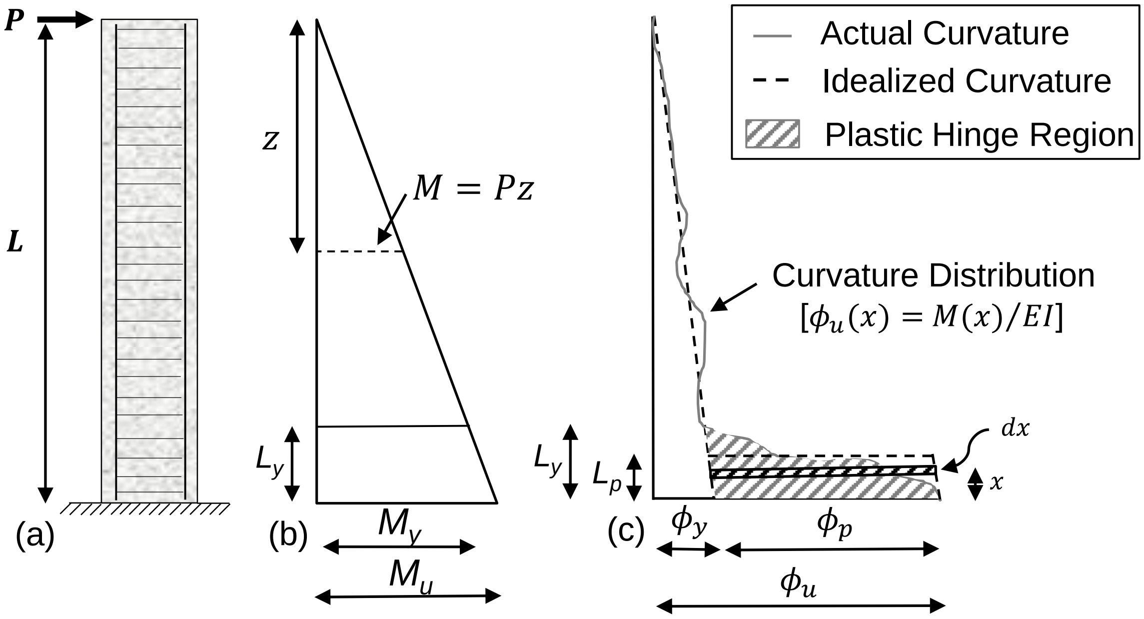

Figure 2.17 Cantilever beam with (a) applied load P, (b) schematic moment diagram, and (c) schematic representation of curvature.

In Equation 2.1, $\phi_u(x)$ and $\phi_y(x)$ are the yield and ultimate curvatures at a distance x from the critical section and L_y represents the length of the beam where reinforcement has yielded. The quantity under the integral sign is equal to the area of the shaded region in Figure 2.17 (c).

We can simplify the plastic curvature distribution in the shaded region to be uniform, such that $\phi_u - \phi_y = \phi_p$ (i.e., constant plastic curvature throughout equivalent plastic hinge length) [56]. Now, the equivalent plastic hinge length, L_p, can be calculated as

$$L_p = \frac{\theta_p}{\phi_p} = \frac{\theta_p}{\phi_u - \phi_y} \tag{2.2}$$

where, ϕ_u is the ultimate curvature at the collapse deformation and ϕ_y is the yield curvature at yield deformation.

Researchers have used this approach to quantify and propose empirical plastic hinge length expressions using experimental data and statistical analysis in reinforced concrete members [54–56, 96, 101]. More recently numerical analysis is being carried out with variations in large number of parameters to develop more robust plastic hinge length expressions [60, 102, 103]. A review of existing plastic hinge studies on reinforced HPFRCC structural components, list of various empirical equations developed for reinforced concrete members, and the significance of predictor variables used in those expression has been discussed in Chapter 4.

2.5.2 Damage in Plastic Hinge Region

HPFRCC structural components have better damage tolerance capacity compared to the traditional concrete components in the plastic hinge regions due to their mechanical behavior and fiber bridging action. Fischer and Li [23] studied structural behavior of three reinforced ECC flexural members along with a reinforced concrete member. The members were tested under reversed cyclic loading until failure. The amount of damage experienced by the concrete specimen (S-1) and the ECC specimen (S-3) at 10% drift level is shown in Figure 2.18. It can be observed that in the ECC specimen there was no spalling near the plastic hinge region and fiber bridging action provides sufficient confinement until 10% drift. However, the concrete specimen showed significant spalling of cover and shear cracks. The ECC specimen had fine flexural cracks without the development of any shear cracks, although shear reinforcement was absent from the ECC specimen. This type of damage mechanism in plastic hinge region of the ECC specimen led to a large ultimate drift capacity of 15%.

In an another study conducted by Frank et al.[104], three reinforced ECC cantilever specimens and three reinforced concrete specimens were tested under various cyclic deformation histories. The research showed that there was a significant difference in damage pattern in the plastic hinge region as shown in Figure 2.19. ECC specimen (ECC-F) showed narrow flexural cracks without any signs of spalling,

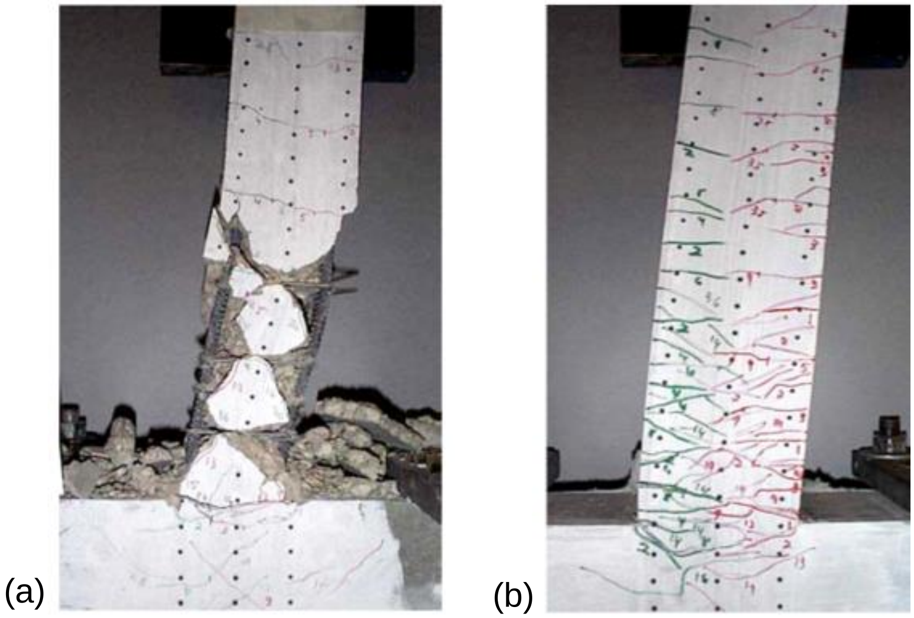

Figure 2.18 Damage in plastic hinge region of (a) reinforced concrete specimen (S-1) (b) reinforced ECC specimen without stirrups (S-3).
Source: [23].

whereas in the concrete specimen (RC-F) there was significant spalling with large cracking patterns. The crack widths in the ECC specimen were less than 0.1 mm except at the dominant crack location (i.e., at joint), but the number of cracks were as twice as compared to the concrete specimen. Further, the reinforcement strain recorded at 50 mm inside the joint at 4.7% drift level, indicated that there was more strain concentrated in the ECC specimen (2.7% strain) compared to the concrete specimen (1.3% strain). This was due to a shorter length of residual splitting crack in the plastic hinge region of the ECC specimen (13 mm) compared to the concrete specimen (30 mm). Therefore, the behavior of the plastic hinge region in reinforced HPFRCC components is different compared to traditional reinforced concrete in terms of crack pattern, number of cracks, crack length, reinforcement strain, among other factors.

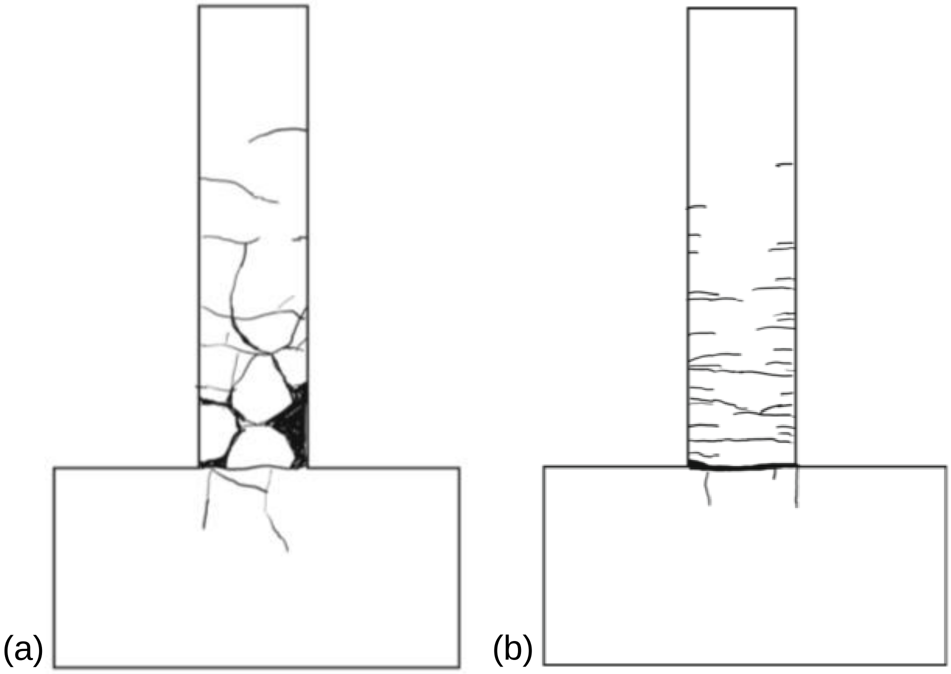

Figure 2.19 Damage in plastic hinge region of (a) reinforced concrete specimen (RC-F) (b) reinforced ECC specimen (ECC-F).
Source: [104].

2.6 Numerical Modeling of HPFRCC Structural Components

With the significant improvement in computing efficiency during the last two decades, research studies involving development and implementation of advanced numerical models to simulate the response of reinforced HPFRCC components has gained significant momentum. Modeling approaches at the microscale, mesoscale, macroscale, and structural scales can be used to investigate the behavior at HPFRCC components with different level of complexities. This dissertation mainly focuses on macroscale modeling using two-dimensional finite element simulation.

The majority of two-dimensional numerical models developed to simulate component-level response of reinforced HPFRCCs are based on plane stress formulation. Han et al. [42] implemented a total strain based rotating crack model developed by Feenstra et al. [105] to simulate cyclic response of reinforced ECC structural components [23]. The model overestimated the initial stiffness and total energy dissipation capacity; however, the overall global response was captured within a reasonable level of accuracy.

Hung and El-Tawil [43] improved the model proposed by Han et al. [42] by modifying the rotating crack model to a hybrid rotating/fixed crack model, which was able to better predict the crack pattern and crack orientation under reversed cyclic load. The model was shown to predict the force-deformation response including the pinching effect for shear-dominant components such as coupling beams and cantilever shear walls.

Gentruck and Elnashai [41] proposed a cyclic constitutive model for ECC materials and demonstrated its use on a full scale structural system using distributed plasticity modeling approach. The material model consists of twelve segments of loading, unloading, and reloading curves which aided to simulate the hysteretic response such as strength degradation and stiffness deterioration, pinching effects, and residual strain of reinforced ECC columns and structural frame within reasonable accuracy.

Bandelt and Billington [75] recently developed a bond-slip constitutive model to simulate the interaction between steel reinforcement and HPFRCC matrix in structural components. The model was shown to efficiently predict the fracture failure mode of reinforced HPFRCC components under both monotonic and cyclic loading conditions. The perfect-bond simulation results tend to underestimate the drift capacity compared to the bond-slip models as seen from the monotonic test result in Figure 2.20. The incorporation of bond-slip constitutive models aided in simulating strain concentration and crack localization effectively at large deformation levels. The failure criteria used to assess the collapse of components was based on strain being exceeded over 18% at three integration points of reinforcement. The fixed rupture strain value of 18% provides a convenient way of determining failure of reinforced HPFRCC components in two or three dimensional modeling approach.

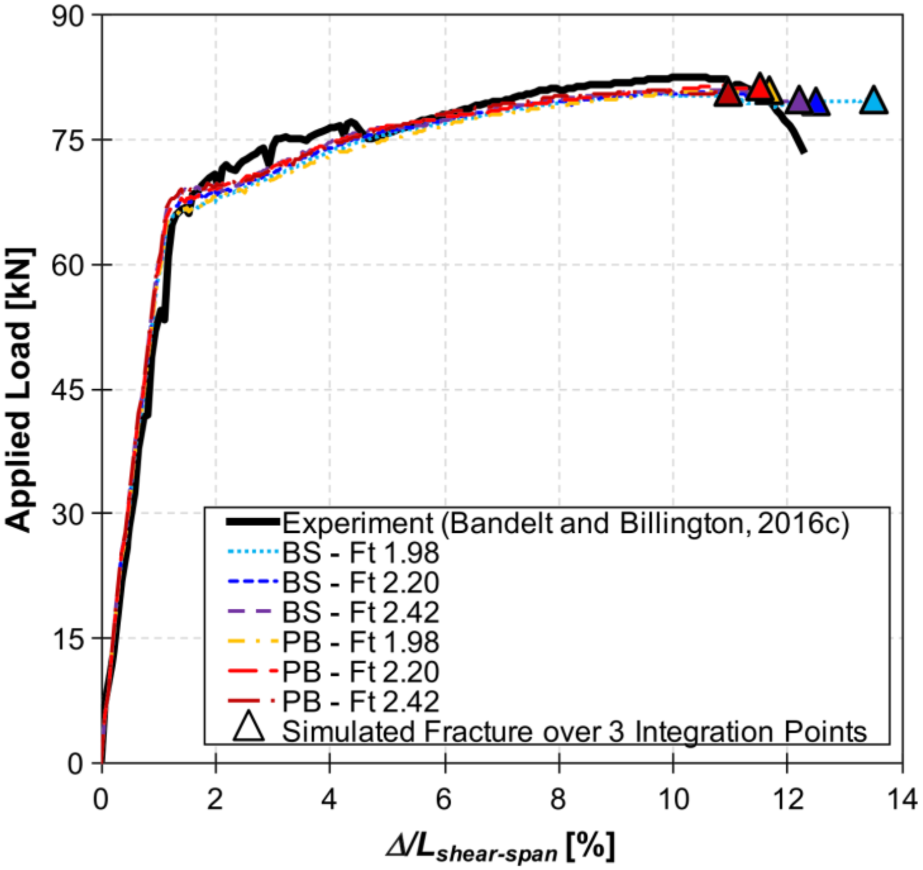

Figure 2.20 Comparison of experimental and numerical component-level response using new bond-slip model.
Source: [75].

Tariq et al. [61] developed a modeling strategy to simulate cyclic response of HPFRCC structural components using fiber-based fixed-length hinge model. The model was capable of simulating global force-deformation as well as hysteretic response of reinforced ECC beams. A plastic hinge length equation was proposed and cyclic modeling parameters of steel were recommended to calibrate this kind of hinge model. The comparison of experimental and numerical hysteretic response of a cantilever specimen ([23]) is shown in Figure 2.21 [61]. The modeling technique successfully simulated reinforcement fracture at ultimate drift levels and can be adopted to model structural component-level response in large scale structural systems.

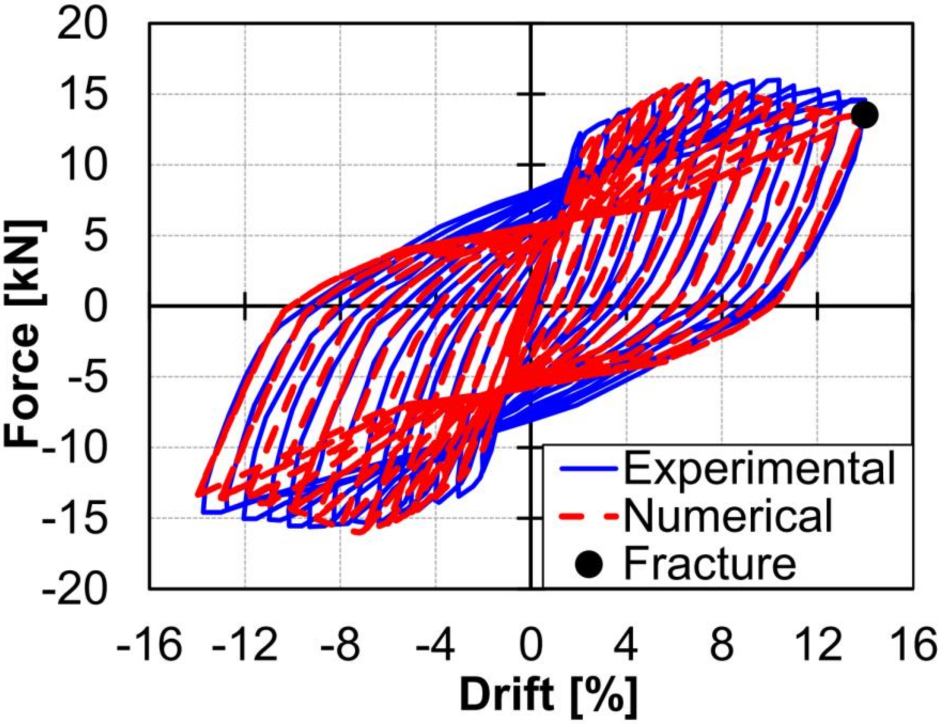

Figure 2.21 Comparison of experimental and numerical component-level response using fiber-based modeling technique.
Source: [61].

2.7 Summary and Research Needs

This chapter presented an overview on the development of HPFRCC materials since the 1960s. A detailed description of three representative classes of HPFRCCs and their mechanical behavior was presented. A summary of the flexural behavior and tension stiffening behavior of HPFRCCs was provided. A discussion on variation in deformation capacity of reinforced HPFRCC flexural members based on currently available experimental data was presented. The definition and formulation of the plastic hinge length in flexural members was described. The difference in the damage pattern in the plastic hinge region of reinforced concrete and reinforced HPFRCC was also discussed. A detailed review of past studies on plastic hinge region of reinforced HPFRCC structural components is presented in Chapter 4 instead of presenting it in this chapter. Lastly, a discussion on numerical models and methodologies currently used to simulate the behavior of reinforced HPFRCC structural components was reviewed.

Several research needs can be identified from the literature review presented in this chapter. There is a need to identify the important factors affecting the variability in the deformation capacity of reinforced HPFRCC flexural members. This will help practicing engineers and contractors to be able to optimally choose the material and structural properties required to achieve a specific performance objective. Chapter 3 addresses this research question through a numerical study involving three types of HPFRCCs. Furthermore, there is a need to develop an equivalent plastic hinge length expression for reinforced HPFRCC components by considering significant factors that affect plastic hinge behavior in HPFRCC components. Plastic hinge length expressions are required for inelastic modeling of HPFRCC components and computing plastic rotation capacity required for performance-based seismic design. Chapter 4 addresses this research need by performing a detailed numerical, statistical, and analytical study. Chapter 5 presents an experimental study designed to study the impact of fiber content variation on plastic hinge region and flexural behavior of highly reinforcement ratio HPFRCC beams. Finally, Chapter 6 presents an experimental framework to further validate the findings from Chapters 3 and 4.

CHAPTER 3

FACTORS INFLUENCING DEFORMATION CAPACITY AND PLASTICITY IN REINFORCED HPFRCC FLEXURAL MEMBERS

3.1 Introduction and Background

The material-level behavior of high-performance fiber-reinforced cementitious composites (HPFRCCs) is characterized by a multiple-cracking psuedo strain-hardening behavior in uniaxial tension [40, 80], and a gradual softening response, similar to that of well confined concrete, in compression [38, 74]. The high ductility and toughness of HPFRCCs make them an ideal substitute of traditional concrete in the design of primary structural components expected to undergo damage and dissipate energy in severe loading (e.g., seismic) conditions [45]. In design for severe loading, HPFRCCs have been studied in applications of walls [24], coupling beams [22, 72], flexural members [23, 27], bridge columns [21, 73], beam-column joints [28], and infill panels [26], among others. These experimental results of reinforced HPFRCCs have shown improved performance over traditional concrete in terms of damage tolerance, strength, and ductility.

Surprisingly, HPFRCC components reinforced with mild steel often fail due to reinforcement fracture as opposed to crushing of the concrete material, as is normal in reinforced concrete members [53]. Moreno et al. [50] conducted tension stiffening experiments of reinforced HPFRCCs where splitting cracks were prevented in HPFRCC specimens, leading to short de-bonded reinforcement lengths which then resulted in smaller deformation capacity as compared to traditional concrete in direct tension. Splitting cracks are suppressed in reinforced HPFRCCs because of the high bond resistance provide by the ductile cementitious material [46–48]. HPFRCC specimens with higher tensile strengths were also observed to fracture at lower specimen deformations as the tensile cracks localized once the fibers pulled out of the matrix [50].

Flexural testing of reinforced HPFRCCs under monotonic and cyclic deformation histories has shown that HPFRCC deformation capacity increases as a function of reinforcement ratio [53], whereas traditional reinforced concrete ductility decreases with increasing reinforcement ratio [106]. Deformation capacity increases with reinforcement ratio in HPFRCCs because members tend to fail due to reinforcement fracture, and the number of flexural cracks and the length of splitting cracks, both of which lead to more distributed reinforcement plasticity, increases with reinforcement ratio [53]. Further, cyclically loaded specimens had up to 67% lower deformation capacity than monotonic specimens as strain accumulated in the reinforcement with load cycles, leading to lower deformation capacity [53]. The deformation history, such as the presence of large pulses at the beginning of a cyclic deformation history, also influences the deformation capacity and damage progression [63]. Members with low reinforcement ratios are more likely to accumulate strain and fracture at lower deformations when specimens are subjected to large pulses early in the deformation history [63].

While the impact of reinforcement ratio, loading type, and deformation history have been quantified in terms of fracture of reinforced HPFRCCs, significant variability in deformation capacity is still not well understood. For example, cyclically loaded specimens made with the same HPFRCC mixture and reinforcement ratio have drift capacities (Δ/L) that have varied by a factor of 2.0 [47, 104]. Other factors that may contribute to deformation capacity, such as mechanical properties, stress state, and structural boundary conditions have been experimentally investigated, but not in a systematic manner to identify their impact on reinforcement fracture and deformation capacity. Recent enhancements in two dimensional finite element simulation techniques have been made, and numerical simulations can now predict reinforcement fracture with a large degree of accuracy by including effects such as bond-slip between the reinforcement and HPFRCC material [75]. These computational strategies allow for a broad investigation of the various factors that influence deformation capacity and plasticity.

The work presented in this chapter aims to (1) identify how tensile strength, boundary conditions, and span-to-depth ratio influence deformation capacity of reinforced HPFRCC beams through fracture of the reinforcement; (2) understand how these variables influence the progression of cracking and deformation capacity; and (3) characterize the relative slip and spread of plasticity in reinforcement in HPFRCC members. Numerical simulations are used to explore a wide variety of material properties and structural characteristics as recent advancements in modeling tools have shown that HPFRCC component damage and deformation can be simulated with a high level of accuracy [75, 107–109]. Specimens are simulated under monotonic loading to limit the added variability that occurs from cyclic loading. Finite element simulation results in terms of load-deformation behavior, damage pattern at different drift levels, longitudinal reinforcement strain, length of relative slip, and length of plasticity along the beams are explored to understand how these factors influence component level behavior of reinforced HPFRCCs.

3.2 Numerical Simulation

3.2.1 Finite Element Models

Two dimensional finite element models with different boundary conditions and shear span-to-depth ratios were simulated using DIANA FEA Version 10.2 [110]. Simply supported and cantilever beam setups were chosen as shown in Figure 3.1 and Figure 3.2, respectively. The test setup and specimen dimensions for the numerical simulations were selected because they are representative of reinforced HPFRCC component experiments tested to high deformations including fracture of

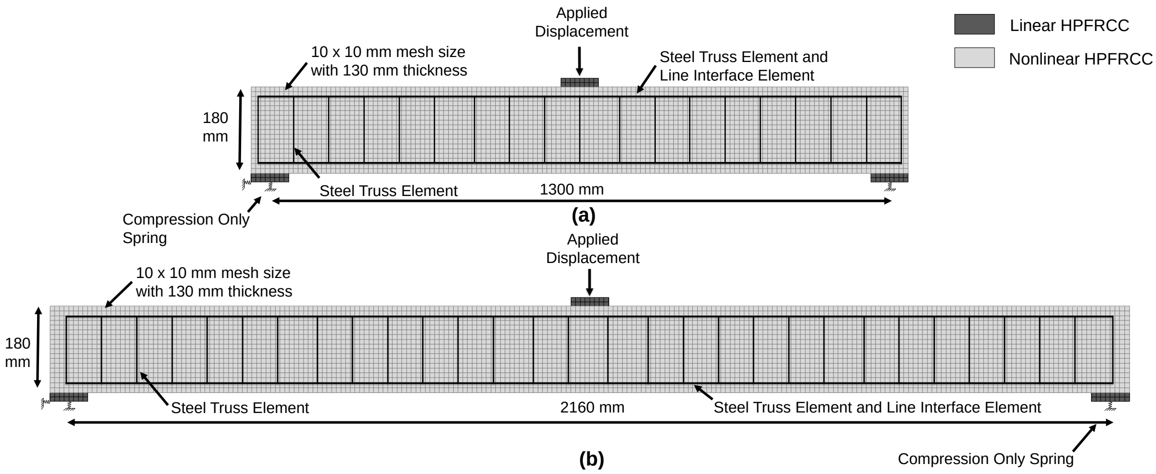

Figure 3.1 Finite element geometry of simply supported beams for (a) shear span-to-depth ratio 4.06 and (b) shear span-to-depth ratio 6.75.

the reinforcement [23, 53, 93, 104]. To investigate the deformation capacity under flexure and flexure-shear stress states, shear span-to-depth ratios of 4.06 and 6.75 were chosen [94]. Specimens with a shear span-to-depth ratio of 6.75 are considered to be dominated by flexural deformations; while specimens with a shear span-to-depth ratio of 4.06 are considered to have high contribution in deformation from both flexure and shear stresses.

In the case of the simply supported beam setup, the beam with a shear span-to-depth ratio of 4.06 had a clear span length of 1300 mm, and the beam with a shear span-to-depth ratio of 6.75 had a clear span of 2160 mm. Support plates with dimensions ($l \times b \times h$) of 80 mm × 130 mm × 20 mm were used at the two ends of the beams. A single loading plate with the same dimension as that of the supporting plate was used at the center of the beam to prevent local damage at the point of load application. The support plate and loading plate were assigned linear elastic properties. Vertical springs at the base of the support plates were modeled as elastic compression-only springs with a spring stiffness of 1.0×10^4 N/mm and the lateral springs were modeled with an elastic spring stiffness of 5.0×10^3 N/mm to replicate the softness of the plate supports in the experimental condition [75].

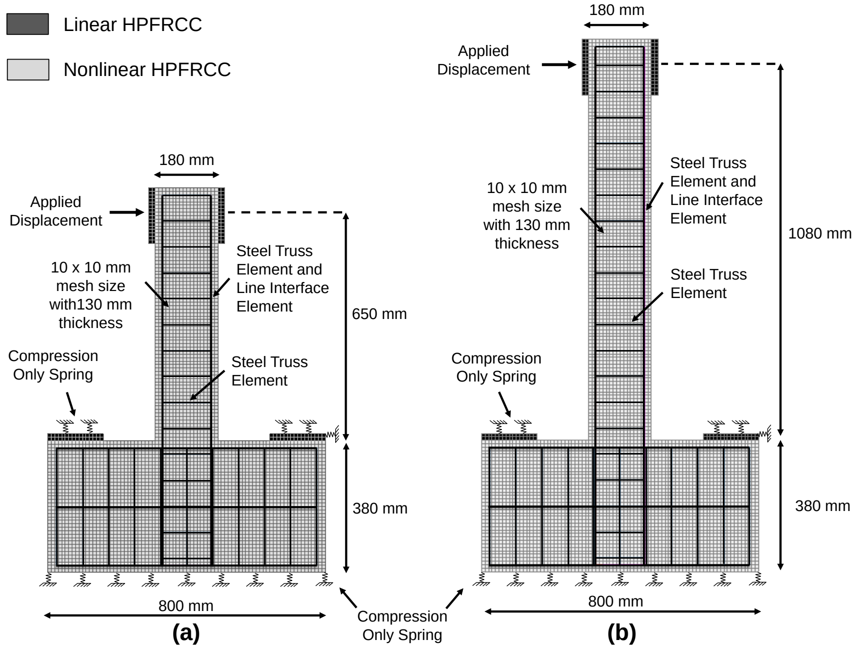

Figure 3.2 Finite element geometry of cantilever beams for (a) shear span-to-depth ratio 4.06 and (b) shear span-to-depth ratio 6.75.

For the cantilever beam setup, the beam with a shear span-to-depth ratio of 4.06 had a length (from the top of the beam foundation to the load application point) of 650 mm, and the beam with shear span-to-depth ratio of 6.75 had a length of 1080 mm. Foundation beams with dimension ($l \times b \times h$) of 800 mm × 130 mm × 380 mm were used as the fixed base support for the cantilever beams based on experimental testing conducted by Frank et al. [104]. Support plates with the dimension ($l \times b \times h$) of 160 mm x 130 mm x 20 mm were used at the two ends of the foundation beams. Loading plates with the same dimension as that of supporting plate was used at the free end of the cantilever beam for the application of load. Both the support plate and loading plate were assigned linear elastic properties. Vertical and lateral springs at the top of the support plates were modeled as elastic compression-only springs with a stiffness of 1.0×10^4 N/mm and the foundation springs were modeled with an elastic stiffness of 9.0×10^5 N/mm to reproduce the experimental conditions [85].

The cantilever and simply supported beam lengths were sized such that when a moment, M, was applied, the resulting shear demand, V, would be equal in the cantilever and simply supported beams. The selected dimensions makes the ratio of shear demand to applied moment (V/M) equal to 1.5 in short span beam, and 1.0 in long span beam. Under such condition, the only variable under investigation when comparing results between the two test setups will be the boundary condition. Thus, the effect of strain penetration in increasing the ductility of the cantilever member can be investigated without influence of any other factor.

The cross sectional properties of the finite element models are summarized in Table 3.1. These properties were based on the experimental study performed by Bandelt and Billington [53] and Frank et al. [104]. A total of 36 beams with variations in material properties, boundary conditions, shear span-to-depth ratio, and longitudinal reinforcement ratio were simulated in this study. The naming convention of the simulated beams were based on these variations. For example, UHPC-S-4.06-0.70 refers to a beam with mechanical properties of an Ultra-High Performance Concrete (UHPC) material, boundary conditions of a simply supported beam, a shear span-to-depth ratio of 4.06 and a longitudinal reinforcement ratio of 0.70%.

In this study, longitudinal reinforcement was symmetrical at the top and bottom of beams with areas of 142 mm^2, 258 mm^2, and 398 mm^2 corresponding to reinforcement ratios of 0.70%, 1.25% and 1.90%. It is recognized that increasing the area of compression steel limits the potential for damage on the compression side of the members; however, symmetrical reinforcement was selected to make comparisons to results from the literature in which members are generally symmetrically reinforced for seismic application. All of the beams were modeled with transverse reinforcement of 16 mm^2 with uniform spacing of 75 mm.

Table 3.1 Cross-Sectional Properties of Beams

Notation	Beam Setup	$L_{shear-span}/d$	Cross Section		Depth	Longitudinal Steel		Transverse Steel		
			b [mm]	h [mm]	d [mm]	d_b [mm]	Area [mm^2]	d_s [mm]	Area [mm^2]	Spacing [mm]
UHPC										
UHPC-S-4.06-0.70	SSB	4.06	130	180	160	10	142	3	16	75
UHPC-S-4.06-1.25		4.06				13	258			
UHPC-S-4.06-1.90		4.06				16	398			
UHPC-S-6.75-0.70		6.75				10	142			
UHPC-S-6.75-1.25		6.75				13	258			
UHPC-S-6.75-1.90		6.75				16	398			
UHPC-C-4.06-0.70	CLB	4.06	130	180	160	10	142	3	16	75
UHPC-C-4.06-1.25		4.06				13	258			
UHPC-C-4.06-1.90		4.06				16	398			
UHPC-C-6.75-0.70		6.75				10	142			
UHPC-C-6.75-1.25		6.75				13	258			
UHPC-C-6.75-1.90		6.75				16	398			
ECC										
ECC-S-4.06-0.70	SSB	4.06	130	180	160	10	142	3	16	75
ECC-S-4.06-1.25		4.06				13	258			
ECC-S-4.06-1.90		4.06				16	398			
ECC-S-6.75-0.70		6.75				10	142			
ECC-S-6.75-1.25		6.75				13	258			
ECC-S-6.75-1.90		6.75				16	398			
ECC-C-4.06-0.70	CLB	4.06	130	180	160	10	142	3	16	75
ECC-C-4.06-1.25		4.06				13	258			
ECC-C-4.06-1.90		4.06				16	398			
ECC-C-6.75-0.70		6.75				10	142			
ECC-C-6.75-1.25		6.75				13	258			
ECC-C-6.75-1.90		6.75				16	398			
HyFRC										
HyFRC-S-4.06-0.70	SSB	4.06	130	180	160	10	142	3	16	75
HyFRC-S-4.06-1.25		4.06				13	258			
HyFRC-S-4.06-1.90		4.06				16	398			
HyFRC-S-6.75-0.70		6.75				10	142			
HyFRC-S-6.75-1.25		6.75				13	258			
HyFRC-S-6.75-1.90		6.75				16	398			
HyFRC-C-4.06-0.70	CLB	4.06	130	180	160	10	142	3	16	75
HyFRC-C-4.06-1.25		4.06				13	258			
HyFRC-C-4.06-1.90		4.06				16	398			
HyFRC-C-6.75-0.70		6.75				10	142			
HyFRC-C-6.75-1.25		6.75				13	258			
HyFRC-C-6.75-1.90		6.75				16	398			

SSB = Simply supported beam

CLB = Cantilever beam

3.2.2 Material Models, Properties, and Analysis Parameters

To investigate the effect of tensile strength on HPFRCC deformation capacity, the mechanical properties of three materials found in the literature were used in the simulations, namely UHPC, an Engineered Cementitious Composite (ECC), and a Hybrid Fiber Reinforced Concrete (HyFRC). Each of these materials have unique mechanical properties and material constituents that may be desirable for various structural applications. UHPC, which is increasingly used in bridge construction for improving durability and enhancing accelerated construction techniques [36], is an ultra high strength material with tensile and compressive strengths in the range of 5-11 MPa [77] and 120-210 MPa [77], respectively. ECC, which has tensile and compressive strengths in the range of 2.5-5.0 MPa [39] and 30-90 MPa [81], respectively, typically does not contain coarse aggregate. It was developed by Li and Leung [80] with principles of micromechanics such that it exhibits multiple fine cracking and tensile ductility. HyFRC uses a hybridization of fibers across various length scales for durability and seismic applications [74, 84], and has tensile and compressive strengths in the range of 1.5-3.1 MPa [82, 83] and 30-45 MPa [50, 82], respectively. Additionally, the strain capacity of each of these materials varies between approximately 0.5% and to 5%, depending on the experimental tension setup [77, 82]

The three materials were chosen for this study because of the range of their mechanical properties, and their wide use in various large-scale experimental programs. The mechanical properties selected used in the simulations were based on the tension and compression tests conducted by Wille and Naaman [78], Russell and Graybeal [36], and Moreno-Luna [82]. A total strain-based fixed-crack model was used as the constitutive model to simulate the behavior of these materials [105]. A constant shear retention factor (β_s) of 1% [82] was used to simulate the transfer of shear stress across the cracks. The HPFRCC materials were modeled using an eight-noded quadratic plane stress element. The size of each element was 10 × 10 mm and the thickness was 130 mm. A 3 × 3 Gauss integration scheme and quadratic interpolation was used in the finite element numerical formulation. The material tensile response was modeled using an idealized multi-linear stress-strain curve as shown in Figure 3.3 (a). The parameters such as initial stiffness (E), maximum tensile stress (f_t), and tensile strain at the onset of softening (ε_{tp}) were obtained from uniaxial tensile test data [78, 82] and are summarized in Table 3.2. The ultimate tensile strain (ε_{tu}) was based on the experimentally observed tensile fracture energy and was calculated using a linear softening model as shown in Equation (3.1) [82].

$$\varepsilon_{tu} = 2\frac{G_f}{h}\frac{1}{f_t} + \varepsilon_{tp} \tag{3.1}$$

In Equation (3.1), h is the crack bandwidth which is equal to $\sqrt{A}$, where A is the area of an individual plane stress element. As only one mesh discretization is presented in this chapter, crack-band approach was used to eliminate the problem related with mesh dependency [43, 82, 108]. Other mesh sizes were explored, but were not shown to influence the results due to the crack-band approach. The compressive behavior of the HPFRCC material was modeled using a parabolic stress-strain curve as defined in Equation (3.2) [111].

$$f_c = \begin{cases} \frac{f_c'}{3}\frac{\varepsilon_c}{\varepsilon_{co}} & \text{for } 0 \leq \varepsilon_c < \varepsilon_{co} \\ \frac{f_c'}{3}[1 + 4(\frac{\varepsilon_c - \varepsilon_{co}}{\varepsilon_{cc} - \varepsilon_{co}}) - 2(\frac{\varepsilon_c - \varepsilon_{co}}{\varepsilon_{cc} - \varepsilon_{co}})^2] & \text{for } \varepsilon_{co} \leq \varepsilon_c < \varepsilon_{cc} \\ f_c'[1 - (\frac{\varepsilon_c - \varepsilon_{cc}}{\varepsilon_{cu} - \varepsilon_{cc}})^2] & \text{for } \varepsilon_{cc} \leq \varepsilon_c < \varepsilon_{cu} \\ 0 & \text{for } \varepsilon_{cu} \leq \varepsilon_c \end{cases} \tag{3.2}$$

Where the characteristic strain values such as initial compressive strain (ε_{co}), strain at maximum compressive strength (ε_{cc}), and the ultimate compressive strain (ε_{cu}) were calculated using Equation (3.3) [111].

$$\begin{aligned}
\varepsilon_{co} &= \tfrac{1}{3}\tfrac{f_c'}{E} \\
\varepsilon_{cc} &= \tfrac{5}{3}\tfrac{f_c'}{E} \\
\varepsilon_{cu} &= \tfrac{3}{2}\tfrac{G_c}{h}\tfrac{1}{f_c'} + \varepsilon_{cc}
\end{aligned} \tag{3.3}$$

In Equation (3.2) and 3.3, the parameters such as compressive strength (f_c'), modulus of elasticity (E), compressive fracture energy (G_c), and Poisson's ratio (ν) were based on experimental data [36, 82] and are summarized in Table 3.2. The crack bandwidth, h, in Equation (3.3) is defined in the similar manner as in Equation (3.1).

Longitudinal reinforcement was modeled as a three-noded truss element with an element size of 10 mm. A three-point Gauss integration scheme was used for numerical integration of the truss element. Transverse reinforcement was modeled as a two-noded directly integrated truss elements with the same element size as longitudinal reinforcement. The uniaxial behavior of longitudinal reinforcement was modeled using the stress-strain curve defined in Equation (3.4).

$$f_s = \begin{cases} E\varepsilon_s & \text{for } 0 \le \varepsilon_s < \varepsilon_y \\ f_y & \text{for } \varepsilon_y \le \varepsilon_s < \varepsilon_{sh} \\ f_y + (f_u - f_y)(\frac{\varepsilon_s - \varepsilon_{sh}}{\varepsilon_u - \varepsilon_{sh}})^{1/3} & \text{for } \varepsilon_{sh} \le \varepsilon_s < \varepsilon_u \end{cases} \tag{3.4}$$

In Equation (3.4), the tensile stress-strain curve parameters such as modulus of elasticity (E), yield stress (f_y), ultimate stress (f_u), strain at onset of hardening (ε_{sh}) and ultimate strain (ε_u) of the longitudinal reinforcement were based on the uniaxial tensile test conducted by Bandelt and Billington [53], and are listed in Table 3.2. Von Mises yield criterion was used to model the multi-axial plastic stress state of the reinforcement [112]. The uniaxial behavior of transverse reinforcement was modeled using elastic-perfectly plastic model with Von Mises yield criterion [112], where the tensile stress-strain curve parameters such as modulus of elasticity (E) and yield stress (f_y) were taken from experimental data of Bandelt and Billington [53] and are tabulated in Table 3.2.

A recent study has shown that modeling of bond-slip mechanism can improve the simulated component level response in terms of strength, stiffness, deformation capacity and damage pattern in reinforced HPFRCC members [75]. Thus, the longitudinal reinforcing elements were connected to the HPFRCC elements through a six-noded line interface element. A three-point Newton-Cotes integration scheme was used for the line interface element. Bond-slip constitutive relationship (Figure 3.3 (b)) proposed by Bandelt and Billington [75] was used to model the interaction between longitudinal reinforcement and HPFRCC. This constitutive relationship was developed based on extensive bond-slip experimental testing under monotonic and cyclic loading for ECC material [46, 47], and can be extended for other classes of HPFRCC material (e.g., UHPC and HyFRC) by changing parameters such as maximum bond strength (u_{max}), slip at onset of softening (s_{max}), bond-slip softening stiffness (k), and residual friction bond strength (u_f). These parameters were obtained from bond-slip test data of Yoo and Yoon [62] for UHPC, and similarly for ECC and HyFRC these parameters were obtained from the test data of Bandelt and Billington [53]. The bond-slip parameters are summarized in Table 3.2, and the values of coefficients α and β in the bond-slip model were taken as 1.17 and 0.28, respectively, from the experimental data of Bandelt and Billington [53].

A nonlinear static analysis with an incremental displacement-based loading of 0.25 mm was applied until fracture was observed in the reinforcement. Fracture was assumed to occur when the strain over a 30 mm gage length of the longitudinal reinforcement exceeded 18% strain based on the approach outlined in Bandelt and Billington [75]. A regular Newton-Raphson scheme was used for equilibrium criteria and a line search algorithm was used for numerical convergence. Convergence was

Table 3.2 HPFRCC and Steel Material Properties

Property	Notation	Unit	UHPC	ECC	HyFRC	Longitudinal Steel	Transverse Steel
Maximum bond strength	u_{max}	[MPa]	10.4	8.20	7.60	-	-
Slip at onset of softening	s_{max}	[mm]	1.0	1.0	1.0	-	-
Bond-slip softening stiffness	k	[MPa/mm]	1.0	1.0	1.0	-	-
Residual friction bond strength	u_f	[MPa]	3.8	3.0	2.8	-	-
Tensile strength	f_t	[MPa]	8.0	2.9	1.8	-	-
Strain at crack initiation	ε_{t0}	[%]	0.0191	0.0169	0.0104	-	-
Strain at onset of softening	ε_{tp}	[%]	0.20	0.75	0.30	-	-
Tensile fracture energy	G_f	[MPa-mm]	19	6.1	5.3	-	-
Compressive strength	$f_c^{'}$	[MPa]	120	55	45	-	-
Compressive fracture energy	G_c	[MPa-mm]	180	53	61	-	-
Young's modulus of elasticity	E	[Gpa]	42	17	17	200	205
Poisson's ratio	ν	[mm/mm]	0.18	0.15	0.15	0.30	0.30
Shear retention factor	β_s	[%]	1.0	1.0	1.0	-	-
Yield strength	f_y	[MPa]	-	-	-	455	690
Ultimate strength	f_u	[MPa]	-	-	-	675	-
Strain at onset of hardening	ε_{sh}	[%]	-	-	-	1.36	-
Strain at ultimate strength	ε_u	[%]	-	-	-	16	-

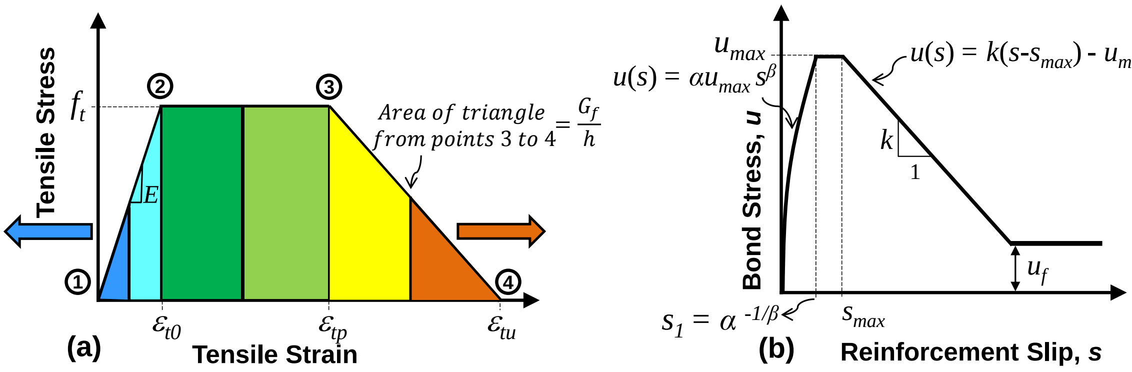

Figure 3.3 (a) Multilinear tensile property and contours of principal tensile strain (b) Bond slip constitutive relationship.
Source: [75].

assumed to have occurred at each iteration if either energy, displacement, or force norm did not exceed limiting values of 0.01%, 0.1% and 1%, respectively.

The modeling technique (i.e., total strain-based model) employed in this study has been used by several researchers in the past to accurately predict the experimental response, particularly force-deformation response and crack patterns, in reinforced concrete structural members [42, 105, 110, 113, 114], and recently it has been used for the simulation of reinforced HPFRCC structural members [75, 85, 108]. The total strain-based modeling approach including crack bandwidth and bond-slip effects, used herein, has been shown to have a high level of accuracy in predicting flexural strength and deformation capacity due to reinforcement fracture across a range of reinforcement ratios, deformation histories, and boundary conditions without the need for calibration [75]. For these reasons, the numerical models are assumed to provide reliable data that can help researchers interpret trends that have not yet been fully investigated through physical experimentation.

3.3 Effect of Variation in Tensile Strength

3.3.1 Initial Stiffness, Strength, and Drift

The simulation results of several simply supported beams with two different shear span-to-depth ratios (4.06 and 6.75) and three different reinforcement ratios (0.70%, 1.25%, and 1.90%) are discussed in this section. The beams with shear span-to-depth ratios of 4.06 will be referred to as short beams and the beams with shear span-to-depth ratio equal to 6.75 will be referred to as long beams in this study. The response of the simply supported reinforced HPFRCC beams with different tensile strengths is investigated in this section. The applied moment versus drift response of short and long beams for different reinforcement ratios are shown in Figure 3.4. Drift is expressed in percentage terms and is calculated by normalizing vertical deformation at midspan by shear span length (i.e., $\Delta/L_{shear-span}$).

The initial elastic response (i.e., before yielding occurs) of the UHPC beams is different than the elastic behavior of ECC and HyFRC beams as seen from the moment-drift response in Figure 3.4 and quantified in Table 3.3. For purposes of discussion within this dissertation, yielding of a component is defined when the average longitudinal reinforcement strain exceeds the yield strain over a gage length of 30 mm [75]. This gage length corresponds to three integration points in the finite element model. Beams were assumed to yield and undergo inelastic deformation once the strain in longitudinal reinforcement reached 0.2275% strain based on the yield stress and modulus of elasticity of the longitudinal reinforcement listed in Table 3.2.

Yield moment, stiffness, and drift at yield all increased as a function of tensile strength. The moment at yield was most highly affected by the simulated tensile strength, followed by the stiffness, and finally the drift at yield. For example, it can be observed in Table 3.3 that for a reinforcement ratio of 0.70%, the initial stiffness of UHPC-S-4.06 beam was 11.7 kN/mm with a yield moment of 24.5 kN-m which was significantly higher than the initial stiffness of ECC-S-4.06 which had a stiffness 7.80 kN/mm and yield moment of 15.2 kN-m, and furthermore, the initial stiffness of HyFRC-S-4.06 was lowest at 6.90 kN/mm with a yield moment of 13.4 kN-m. The difference in the values of initial elastic stiffness and yield moment is due to the difference in modulus of elasticity and tensile strength of the HPFRCC materials as shown in Table 3.2. The yield moment and stiffness of the simulated flexural specimens increased with tensile strength in a similar fashion to tension stiffening experiments with varying tensile strengths [50]. At yield, the tension force, T, of the flexural force couple is made up of a steel tension force T_s, and the tension force in the HPFRCC T_{hpfrcc}. High strength HPFRCCs, such as UHPC, can have a large T_{hpfrcc} force when the reinforcement yields which then results in a larger resisting moment at yield.

Drift at yield for a given shear span and reinforcement ratio was similar among materials as the drift at yield depends primarily on the amount of longitudinal reinforcement. For example, it can be seen in Table 3.2 that for a reinforcement ratio of 0.70%, the drift at yield for UHPC-S-6.75, ECC-S-6.75 and HyFRC-S-6.75 ranged between 0.91 and 0.96%.

The post-yield behavior of UHPC beams was significantly different than the ECC and HyFRC beams as shown in Figure 3.4. The post-yield stiffness of the UHPC beams was initially positive, but once the maximum moment capacity was reached, stiffness and strength degradation began, and the beams failed due to fracture of longitudinal reinforcement. Unlike the UHPC beams, most of the ECC and HyFRC beams showed positive post-yield stiffness without any strength degradation until the reinforcement fractured. The difference in the post-yield behavior, in particular the increased moment capacity at collapse, is due to the higher tensile strength of UHPC (8 MPa) in comparison to ECC (2.9 MPa) and HyFRC (1.8 MPa). A drop in flexural strength was indicative of a loss of tensile capacity that was provided by the HPFRCC material. The HPFRCC contributes more to the total tensile response of the member when the reinforcement ratio is low and when the HPFRCC tensile strength is high. Thus, drops in flexural strength were primarily limited to $\rho = 0.70\%$ simulations and UHPC simulations. Similar observations in drops in strength after yielding have been reported in studying the tension stiffening effect of HPFRCCs with varying reinforcement ratios [115] and tensile strengths [50]. This phenomenon will be further explained by illustrating crack patterns, relative slip of longitudinal reinforcement and strain in longitudinal reinforcement of different beams in Sections 3.3.2 - 3.3.3. The moment capacity of the ECC and HyFRC beams were nearly equal for each reinforcement ratio. Similar moment capacities for ECC and HyFRC beams are attributed to their similar tensile strengths, and that their flexural response when the

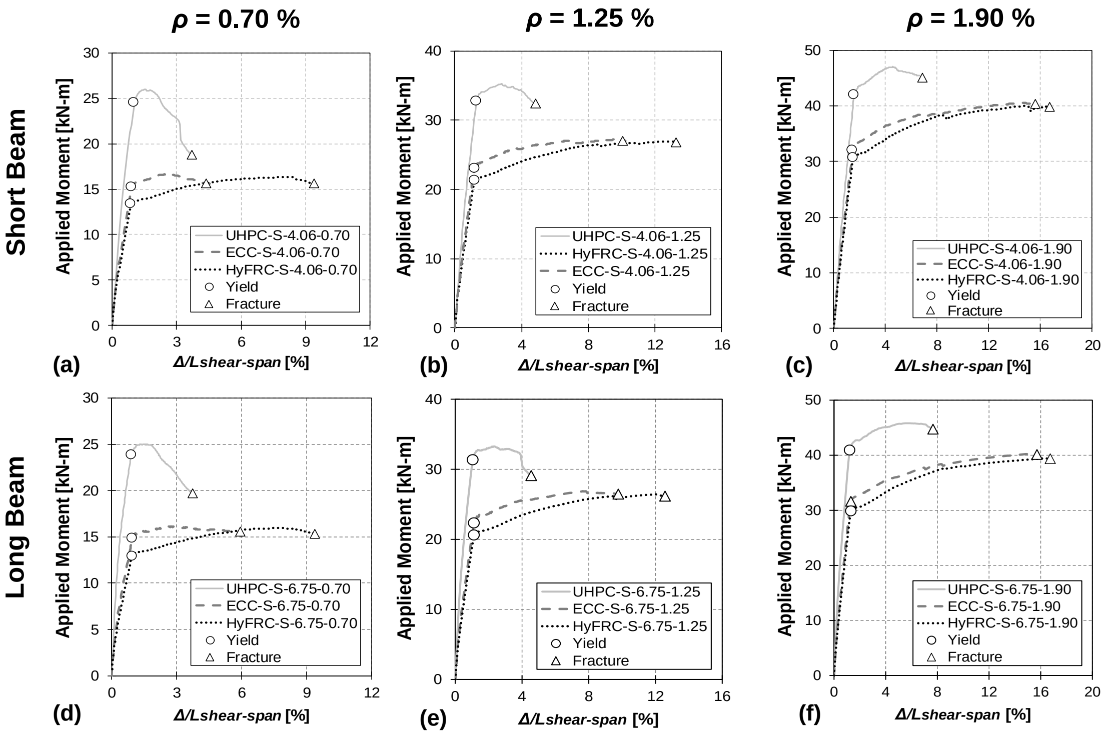

Figure 3.4 Applied moment vs. drift response of simply supported HPFRCC beams with variation in material tensile strength.

moment capacity was reached was dominated by the response of the fully hardened bar [50, 53].

The simulation response of short and long cantilever beams with different reinforcement ratios were found to follow similar pre-yield and post-yield behavior as simply supported beams. The results of long cantilever beams are discussed in Section 3.4 in the context of the influence of test setup whereas the results of short cantilever beams have not presented for the purpose of brevity, but follow the same trends as the short simply supported beams.

3.3.2 Damage Pattern

Principal tensile strain contours, indicative of damage and cracking in the beams, are associated with varying levels of strain in Figure 3.3 (a). The contours are based on the stress-strain relationship of the HPFRCC in tension, and represent

Table 3.3 Initial Stiffness, Strength and Deformation Capacity of Simply Supported Beams

Beam Notation	Initial stiffness [kN/mm]			Moment at yield [kN-m]			Drift at yield [%]		
Reinforcement Ratio	0.70%	1.25%	1.90%	0.70%	1.25%	1.90%	0.70%	1.25%	1.90%
UHPC-S-4.06	11.7	12.9	13.7	24.5	32.7	42.0	1.03	1.30	1.59
ECC-S-4.06	7.80	9.60	11.1	15.2	23.1	32.0	0.93	1.19	1.45
HyFRC-S-4.06	6.90	9.00	10.4	13.4	21.3	30.8	0.89	1.19	1.53
UHPC-S-6.75	4.50	5.30	6.20	23.9	31.3	40.9	0.91	1.05	1.21
ECC-S-6.75	2.70	3.60	4.40	14.8	22.3	31.6	0.96	1.12	1.30
HyFRC-S-6.75	2.40	3.30	4.20	12.9	20.6	29.9	0.93	1.12	1.30

elastic behavior, pseudo-strain hardening, softening, and dominant crack formation. Simulated flexural performance of beams made with each material are plotted at varying levels of deformation in beams with reinforcement ratios of 0.70% and 1.9% in Figure 3.5. The tensile strain contours are shown at different deformation levels to show the progression of damage and final damage state before fracture of the longitudinal reinforcement.

In Figure 3.5, damage patterns are shown at 1% and 2% drift for the 0.70% reinforcement ratio simulations, and at 2% and 4% drift for the 1.9% reinforcement ratio simulations. Contours of principal tensile strains are also shown at the drift associated with impending reinforcement fracture for each simulation.

At smaller deformation levels (i.e., 1% and 2% drift for the 0.70% reinforcement ratio simulations), close observation indicates that the UHPC beam has the longest region associated with softening (yellow region) of the HPFRCC material, followed by HyFRC, and then ECC. The length of the softening region is dependent upon the strain at the onset of softening (ε_{tp}), which is lowest for UHPC at 0.2%, followed by HyFRC at 0.3%, and ECC at 0.75% as summarized in Table 3.2. The simulation results show that the length of the softening region is dependent upon ε_{tp} at low reinforcement ratio. However, when the reinforcement ratio is increased (i.e., at 1.90%), the simulation results at lower deformations levels (i.e., 2% and 4% drift), exhibit the longest softening region for HyFRC material, followed by ECC, and then UHPC. With the increase in longitudinal reinforcement, softening of HPFRCC matrix is controlled by the maximum tensile strength (f_t) rather than ε_{tp}. The increased tensile reinforcement attracts higher tensile stress around HPFRCC matrix, which results into longer softening region in low tensile strength material compared to high tensile strength material. The tensile stress in HPFRCC material is transferred through the steel reinforcement via bond-slip interaction between steel and HPFRCC matrix. A sensitivity test was also carried out to study any additional effect of change in the strain at softening (ε_{tp}) (±50%) on the collapse level deformation capacity of reinforced HPFRCC beams. The result showed that the variation of deformation capacity due to change in ε_{tp} was insignificant compared to the tensile strength, so in this study, the discussion will be limited to the effect of the single most important tensile property, that is tensile strength, among others.

Contours of principal tensile strain in Figure 3.5 at impending fracture can be used to understand the deformation that causes fracture. For the $\rho = 0.70\%$ simulations, it can be seen that UHPC and ECC beams form a single dominant flexural crack whereas HyFRC beam forms two dominant flexural cracks. Since, HyFRC has two cracks, the damage in the reinforcement was distributed to two cracks which resulted in a total deformation that was 2.5 times higher than the UHPC beam and 2.1 times higher than the ECC beam. The low tensile strength and fracture energy of HyFRC, relative to ECC and UHPC, allows the formation of a dominant crack to occur more easily. As multiple dominant cracks form, the reinforcement can strain and slip over a longer length (i.e., at multiple locations), resulting in higher component deformation capacity.

Similar trends in crack localization can be observed in Figure 3.5 at the deformation causing fracture in the $\rho = 1.9\%$ simulations as well. Many dominant flexural cracks formed in the HyFRC simulation, followed by slightly fewer in the ECC simulation, and finally the UHPC simulation. The number of dominant cracks resulted in ECC and HyFRC beam deformation capacity that was more than 2 times higher than that of the UHPC beam.

In addition to flexural cracks, diagonal tension cracks (i.e., shear) also formed in ECC and HyFRC simulations as reinforcement ratio increased. Diagonal cracking was expected in the simulations since the moment capacity increased with reinforcement ratio, and thus the shear demand increased without any increase in shear capacity. Shear cracks were not observed in the UHPC simulations because flexural failure occurred before the shear cracks could develop. The effect of shear are discussed in more detail in Section 3.5.1.

The crack patterns in some of the beams, such as UHPC and ECC beams ($\rho = 0.70\%$), are non-symmetric because of the asymmetry provided by the boundary condition (i.e., lateral and vertical springs at the right support simulating pin and a single vertical spring at the left support simulating roller). The effect of complete change in boundary condition is further discussed in Section 3.4.

3.3.3 Strain in Reinforcement

Data from several experimental studies shows that the failure of reinforced HPFRCC beams occurs due to fracture of longitudinal reinforcement rather than crushing of compression zone material, unlike ordinary reinforced concrete [23, 27, 53, 63, 104]. The fracture of the reinforcement occurred due to concentration of inelastic strain at dominant cracks in HPFRCC members as seen in the tension stiffening experiment conducted by Moreno et al. [50]. In this study, strain in the longitudinal reinforcement was extracted at various component level deformations to understand

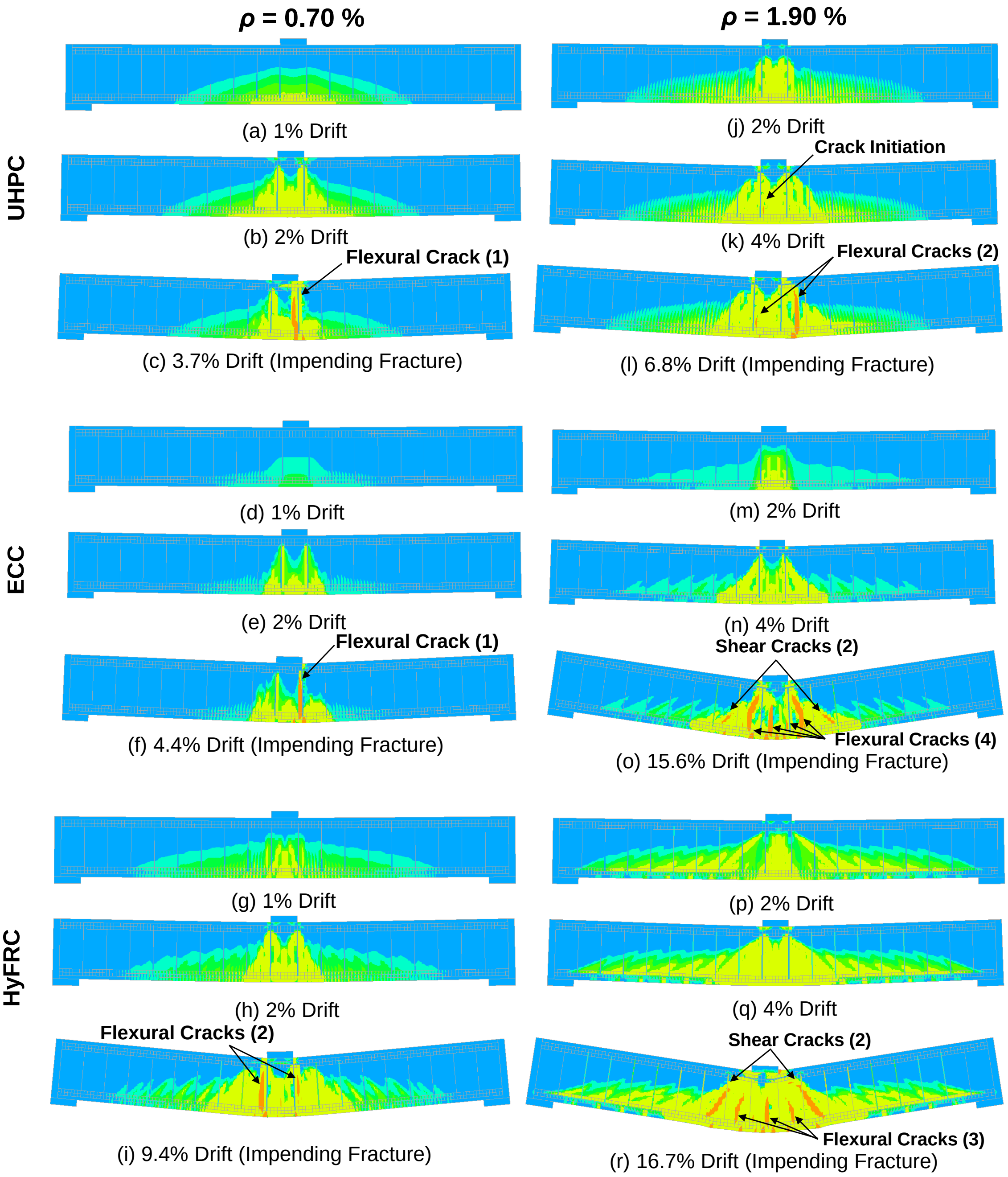

(a) 1% Drift

(j) 2% Drift

(b) 2% Drift

(k) 4% Drift

(c) 3.7% Drift (Impending Fracture)

(l) 6.8% Drift (Impending Fracture)

(d) 1% Drift

(m) 2% Drift

(e) 2% Drift

(n) 4% Drift

(f) 4.4% Drift (Impending Fracture)

(o) 15.6% Drift (Impending Fracture)

(g) 1% Drift

(p) 2% Drift

(h) 2% Drift

(q) 4% Drift

(i) 9.4% Drift (Impending Fracture)

(r) 16.7% Drift (Impending Fracture)

Figure 3.5 Principal tensile strain contour of simply supported short (a-c) UHPC beams (d-f) ECC beams (g-i) HyFRC beams with $\rho = 0.70\%$ and (j-l) UHPC beams (m-o) ECC beams (p-r) HyFRC beams $\rho = 1.90\%$ at different drift levels.

how reinforcement strain varied near dominant cracks. Figure 3.6 shows the longitudinal reinforcement strain profile along the span of simply supported HPFRCC beams.

The length of the damage can be quantified by measuring the length of plastic deformation of the reinforcement, L_p, which is defined here as the length over which strain in the reinforcing steel exceeded the yield strain for a given component deformation level. It can be seen in Figure 3.6, that for the same drift level, the UHPC beams have the smallest plastic deformation length, followed by ECC beams, and lastly, the HyFRC beams have the longest plastic deformation length. For example, longitudinal reinforcement in short beams with $\rho = 0.70\%$ (Figure 3.6 (a)) undergoes plastic deformation for a length of 160 mm with the use of UHPC, 250 mm with the use of ECC, and 370 mm with the use of HyFRC at 4% drift. This means that inelastic strain is distributed over a longer length in the material with lowest tensile strength compared to the material with highest tensile strength. Thus, the reinforcement in HyFRC beams experienced inelastic deformation over a longer length, which therefore resulted in a higher deformation capacity than the UHPC beams. In-addition to the tensile strength, the bond-slip mechanism also plays a significant role in understanding this trend of inelastic strain distribution in different HPFRCC materials as discussed in Section 3.3.4. The peaks in strain plots are locations of strain localization at a dominant crack location, as previously discussed, and the beams failed by fracture of longitudinal reinforcement at the dominant crack locations.

As the reinforcement ratio increased the length of plasticity also increased in both short (Figure 3.6 (a)-(c)-(e)) and long beams (Figure 3.6 (b)-(d)-(f)) for all three materials. The higher length of plasticity with reinforcement ratio resulted in a higher deformation capacity as observed experimentally by Bandelt and Billington [53]. As the length of plasticity increased, strain was distributed over a longer length, avoiding early reinforcement fracture and resulting in increased deformation capacity of the structural member.

A comparison of the length of plasticity between short (Figure 3.6 (a)-(c)-(e)) and long (Figure 3.6 (b)-(d)-(f)) beams for the same reinforcement shows that the plasticity length is always higher in long beams due to flexural deformation. The higher length of plasticity generally resulted in higher deformation capacity in long beams than short beams. The difference in the damage pattern and deformation capacity in short beams and long beams is discussed in more detail in Section 3.5.

3.3.4 Reinforcement Slip

Modeling the interaction between steel and HPFRCC matrix is crucial to predict the component level response of reinforced HPFRCC structural members as shown by several recent studies [75, 85, 108]. Figure 3.7 shows the relative slip between the tensile reinforcement and HPFRCC matrix in terms of reinforcement slip along the length of the simply supported HPFRCC beams. The length of reinforcement slip, L_{rs}, is defined here as the length over which the relative slip between the reinforcing steel and HPFRCC matrix exceeded the value of 0.01 mm. The impact of bond-slip mechanism on the deformation capacity of reinforced HPFRCC members with different tensile properties can be illustrated by investigating the relative slip between the reinforcement and HPFRCC matrix.

It can be seen in Figure 3.7 that the length of reinforcement slip, L_{rs}, for the same drift level is smallest for the UHPC beams, followed by ECC beams, and HyFRC beams. The trend is similar to that of the plastic deformation length as seen in Section 3.3.3. For example, longitudinal reinforcement in short beams with $\rho = 0.70\%$ (Figure 3.7 (a)) undergoes slip for a length of 150 mm with the use of UHPC, 230 mm with the use of ECC, and 360 mm with the use of HyFRC at 4% drift. Since, the bond strength of a material is associated with it's tensile properties [46, 48, 49],

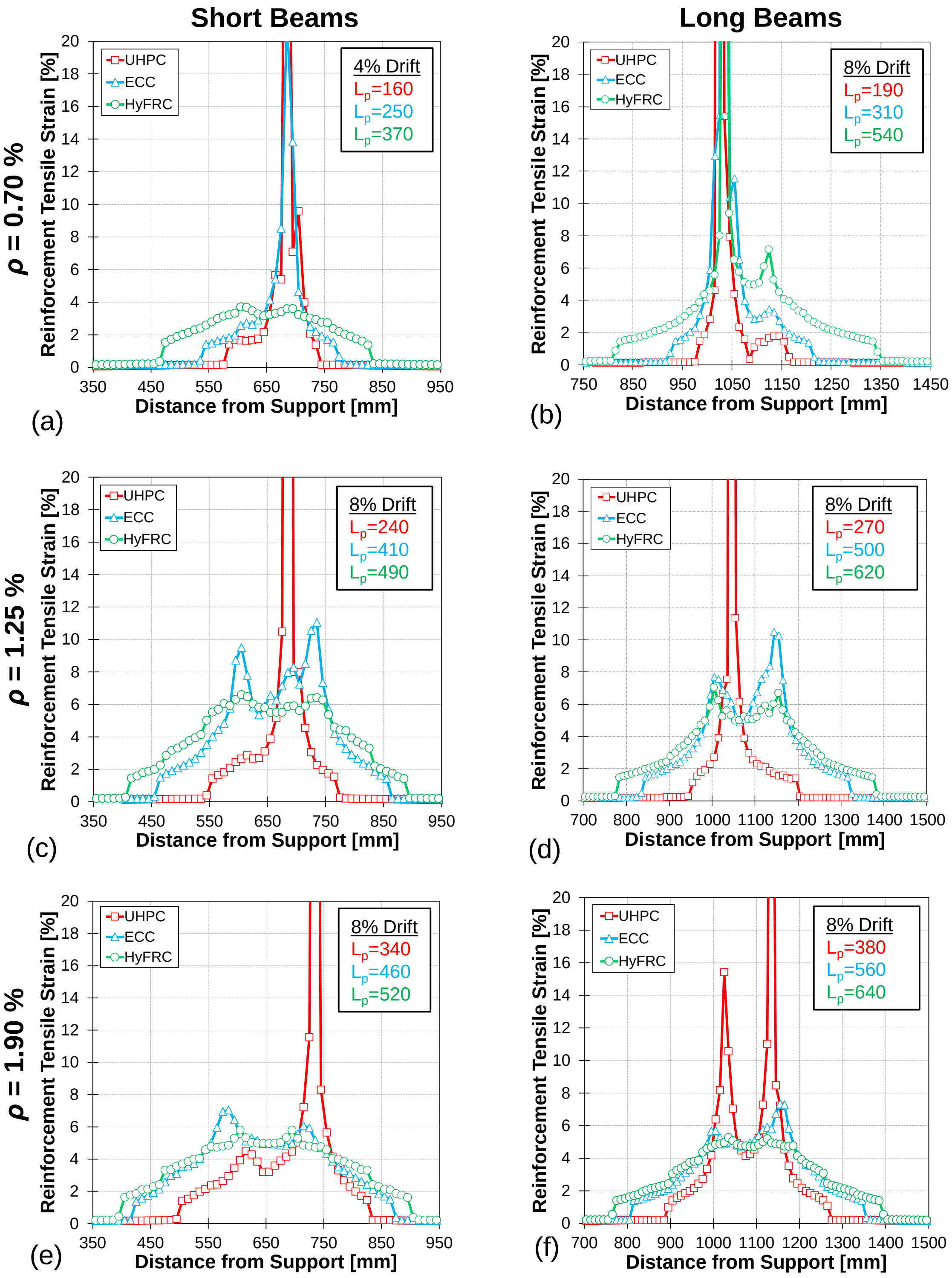

Figure 3.6 Longitudinal reinforcement strain vs. distance from support in simply supported (a-c-e) short beams and (b-d-f) long beams with different reinforcement ratios.

UHPC has the highest bond strength among the three HPFRCC materials used in this study, which resulted in the smallest relative slip between the reinforcement and HPFRCC matrix. This means that the longitudinal reinforcement gets strained over shorter length resulting into high strain concentration in beams with higher bond strength as compared to the beams with lower bond strength. Lower slip contributes to fracture of reinforcement at lower deformation levels in UHPC beams compared to ECC and HyFRC beams. The peaks in reinforcement slip plots are the locations of reinforcement strain and crack localization where the beams ultimately failed by fracture of longitudinal reinforcement.

The length of relative slip of reinforcement, L_{rs}, increased with increasing reinforcement ratio in both short (Figure 3.7 (a)-(c)-(e)) and long beams (Figure 3.7 (b)-(d)-(f)) for all three materials. Slip increased with reinforcement ratio because more tensile demand was placed on the interface with a larger area of steel. The longer length of slip with increasing reinforcement ratio resulted in a higher length of plasticity as discussed in Section 3.3.3, which increased the deformation capacity of reinforced HPFRCC beams.

3.3.5 Deformation Capacity

The deformation causing reinforcement fracture was determined by computing the average strain in the longitudinal reinforcement over three integration points, corresponding to a gage length of 30 mm using the approach described in Bandelt and Billington [75]. Beams were assumed to have lost load carrying capacity once the strain in longitudinal reinforcement reached an 18% strain value. An 18% threshold value was assumed to be a fracture strain because mild steel (f_y = 420 MPa) usually fractures at the strains between 10% to 20% under uniaxial tensile load [56]. The simulated beams did not fail by the crushing of the compression zone in all three types of HPFRCC materials due to higher damage tolerance capacity

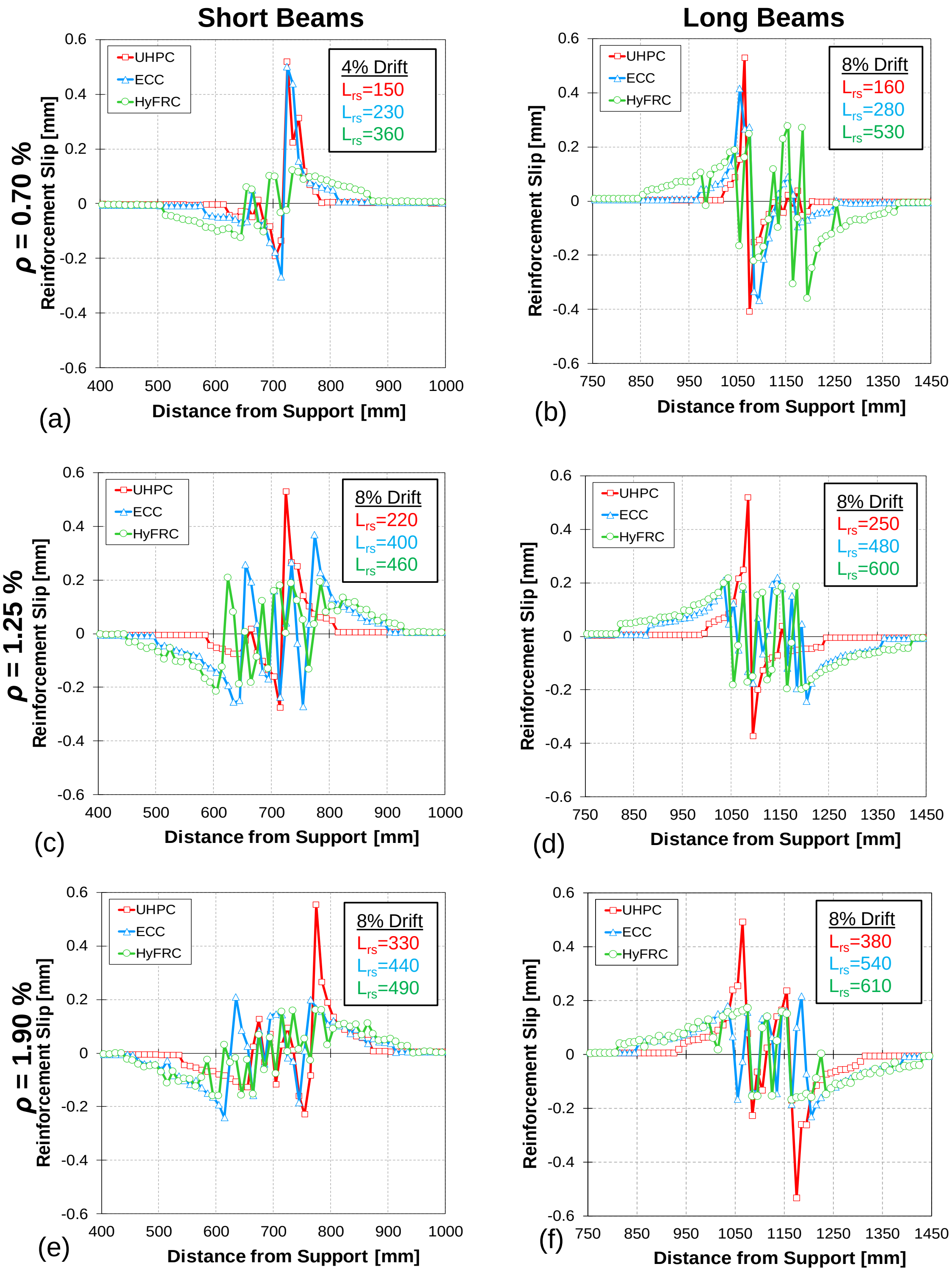

Figure 3.7 Longitudinal reinforcement slip vs. distance from support in simply supported (a-c-e) short beams and (b-d-f) long beams with different reinforcement ratios.

under compression, however; diagonal tension or shear cracks were observed as reinforcement ratio increased (Figure 3.5(o) & (r)). Deformation capacity decreased as tensile strength increased such that $(\Delta/L_{shearspan})_{HyFRC} > (\Delta/L_{shear-span})_{ECC} > (\Delta/L_{shear-span})_{UHPC}$, as shown in Figure 3.8. The trend in deformation capacity decreasing as a function of tensile strength was observed for members with the same shear span-to-depth ratio, reinforcement ratio, cross section, and boundary conditions.

The reduction in deformation capacity was due to the combined effects of crack patterns and length of plasticity that were previously discussed. Specifically, increasing tensile strength resulted in a smaller number of dominant cracks (Figure 3.5), which in turned lowered the length of plasticity of the reinforcement. With a smaller length of plasticity (Figure 3.6), the strain in the reinforcement concentrated at a dominant crack location, leading to early reinforcement fracture in comparison to the simulated specimens with lower tensile strength. The damage pattern and strain localization phenomenon under large deformations have been reported in previous experimental studies [50, 53, 63, 104].

The deformation capacity of all HPFRCC beams increased with reinforcement ratio for both short beams and long beams; for example, the deformation capacity of the short ECC beams was 4.4%, 10.1% and 15.6% for reinforcement ratios of 0.70%, 1.25% and 1.90%, respectively. The numerical simulations of deformation capacity as a function of reinforcement ratio were in agreement with recent experimental research which showed that deformation capacity of ECC beams tend to increase with increases in reinforcement ratio under monotonic and cyclic loading [53].

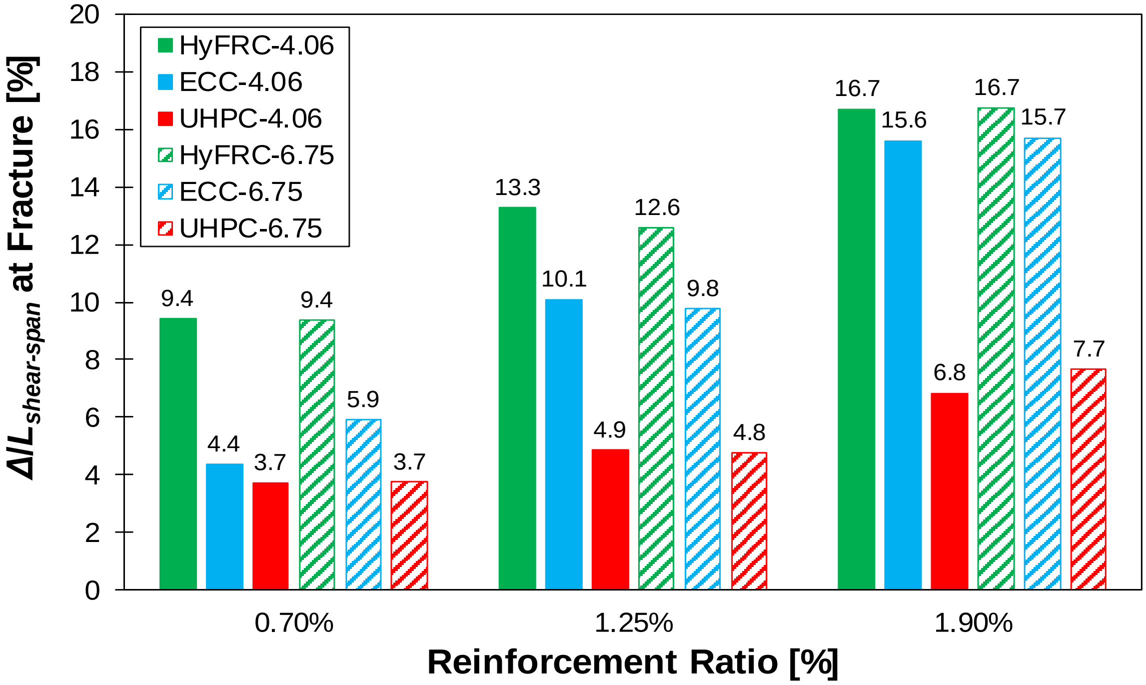

Figure 3.8 Variation in deformation capacity due to change in tensile strength in simply supported beams.

3.4 Effect of Variation in Test Setup

3.4.1 Initial Stiffness, Strength, and Drift

The simulation results of several long span ($L_{shear-span}/d = 6.75$) cantilever and simply supported beams with three different reinforcement ratios (0.70%, 1.25%, and 1.90%) are discussed in this section. The applied moment versus drift response of cantilever and simply supported beams for different reinforcement ratios are shown in Figure 3.9. The initial elastic response of cantilever beams was similar to simply supported beams for all types of HPFRCC materials. Both types of members were assumed to yield and undergo inelastic deformation after the strain in longitudinal reinforcement reached 0.2275% strain as discussed in Section 3.3.1.

The initial elastic stiffness of all cantilever HPFRCC beams are lower than that of simply supported beams (Table 3.4). This difference in the stiffness is due to the change in boundary conditions. Simply supported beams were supported by

Table 3.4 Initial stiffness, Strength and Deformation Capacity of Long Span Beams with Different Setup

Beam Notation	Initial stiffness [kN/mm]			Moment at yield [kN-m]			Drift at yield [%]		
Reinforcement Ratio	0.70%	1.25%	1.90%	0.70%	1.25%	1.90%	0.70%	1.25%	1.90%
UHPC-S-6.75	4.5	5.3	6.2	23.9	31.3	40.9	0.91	1.05	1.21
UHPC-C-6.75	1.9	2.4	2.7	22.9	31.4	39.8	1.07	1.30	1.44
ECC-S-6.75	2.7	3.6	4.4	14.8	22.3	31.6	0.96	1.12	1.30
ECC-C-6.75	1.1	1.5	1.8	14.5	22.0	31.2	1.21	1.48	1.85
HyFRC-S-6.75	2.4	3.3	4.2	12.9	20.6	29.9	0.93	1.12	1.30
HyFRC-C-6.75	1.0	1.3	1.6	12.8	20.4	29.2	1.21	1.58	2.04

compresssion-only springs, whereas the cantilever beams were connected in continuum with the foundation beam. For example, it can be observed in Table 3.4 that for a reinforcement ratio of 0.70%, the initial stiffness of UHPC-S-6.75 beam was 4.5 kN/mm which was significantly higher than the initial stiffness of UHPC-C-6.75 which is 1.9 kN/mm. A similar trend is seen for ECC and HyFRC beams with different test setups.

As expected, for a given HPFRCC material, the moment and drift at yield were similar regardless of the boundary conditions. Yield moment and drift were similar because they primarily depend on the amount of longitudinal reinforcement and the HPFRCC mechanical properties as discussed in 3.3.1. For example, it can be seen in Table 3.4 that for UHPC beams with a reinforcement ratio of 0.70%, the yield moments for UHPC-S-6.75 and UHPC-C-6.75 were 23.9 kN-m and 22.9 kN-m, respectively. Similarly, the drift capacity at yield for UHPC-S-6.75 and UHPC-C-6.75 were 0.91% and 1.07%, respectively.

For a given HPFRCC material, the post-yield behavior of long span cantilever and simply supported beams were similar as shown in Figure 3.9. In the case of the

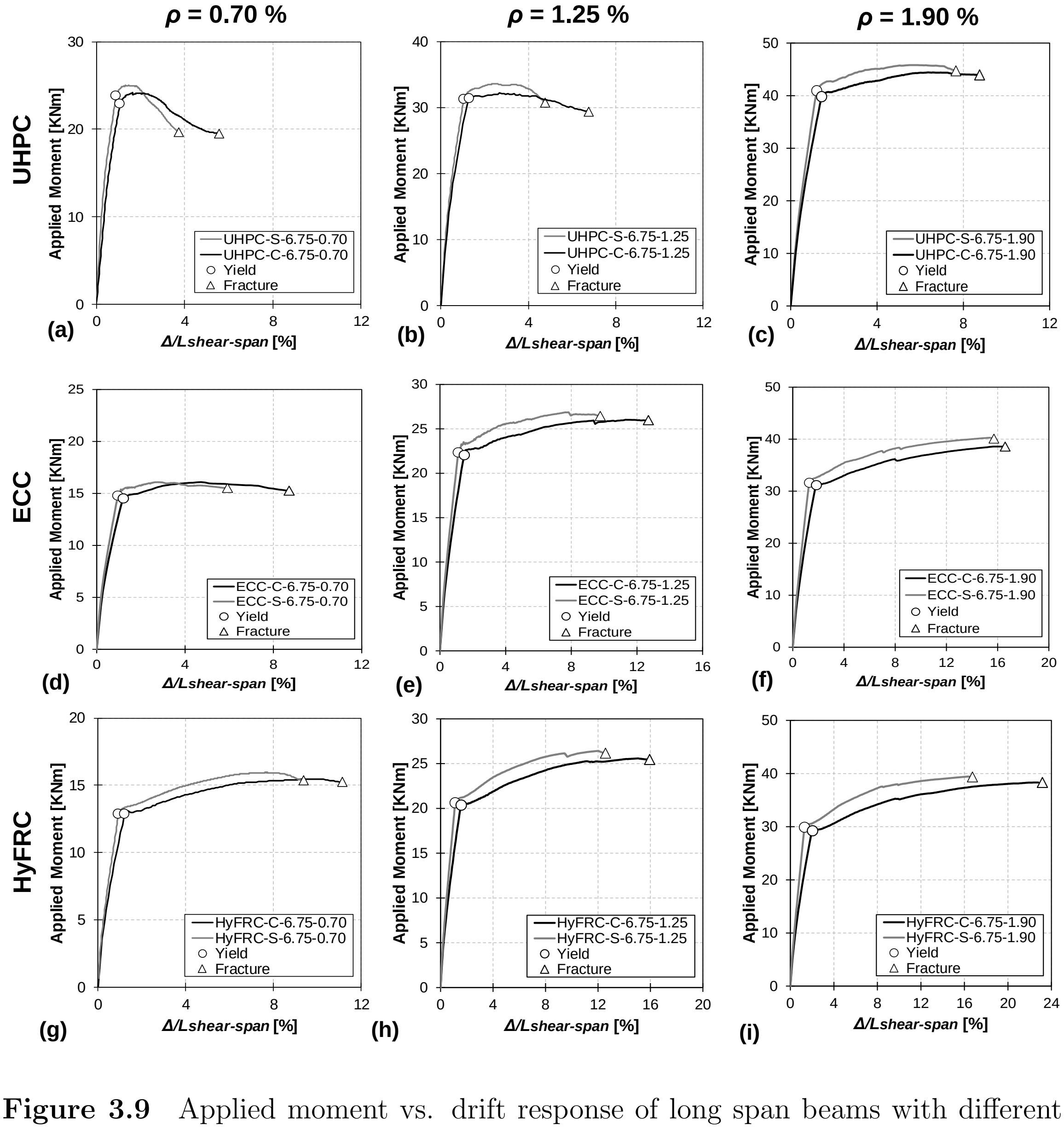

Figure 3.9 Applied moment vs. drift response of long span beams with different setup.

UHPC beams, both the cantilever and simply supported beams showed positive post-yield stiffness followed by negative stiffness and strength degradation until fracture of reinforcement was simulated. However, the ECC and HyFRC simulations primarily had positive post-yield stiffness, without loss in stiffness or strength, regardless of the boundary condition.

The nominal moment capacity for a given HPFRCC material was similar regardless of the boundary conditions. The drift at simulated reinforcement fracture was higher in cantilever members than simply supported bembers for all HPFRCC materials and reinforcement ratios considered in this study. The higher drift capacity in cantilever beams is explained based on the spread of plasticity in the longitudinal reinforcement of both types of beams in Section 3.4.4.

3.4.2 Deformation Capacity

The deformation capacity at reinforcement fracture was determined by noting the drift at which the reinforcement strain over 30 mm gage length reached the fracture strain of 18% as described in Section 3.3.5. As shown in Figure 3.10, the deformation capacity of the cantilever beam was greater than simply supported beam for all nine scenarios (three reinforcement ratios and three HPFRCC materials). Therefore, simply supported beams had lower deformation capacity than cantilever beams provided that the material and structural properties were the same. For example, for $\rho = 1.25\%$ simulations, the deformation capacity of the cantilever UHPC beam was 6.8%, and the simply supported UHPC beam had a drift capacity of 4.8%, which was 29.4% lower. Similarly, the simply supported ECC beam had a drift capacity which was 29.6% lower than that of the cantilever beam, and the HyFRC simply supported beam had a drift capacity which is 20.7% lower than the cantilever beam.

The higher deformation capacity in cantilever beams was due to penetration of longitudinal reinforcement strain into the joint which allowed the cantilever to

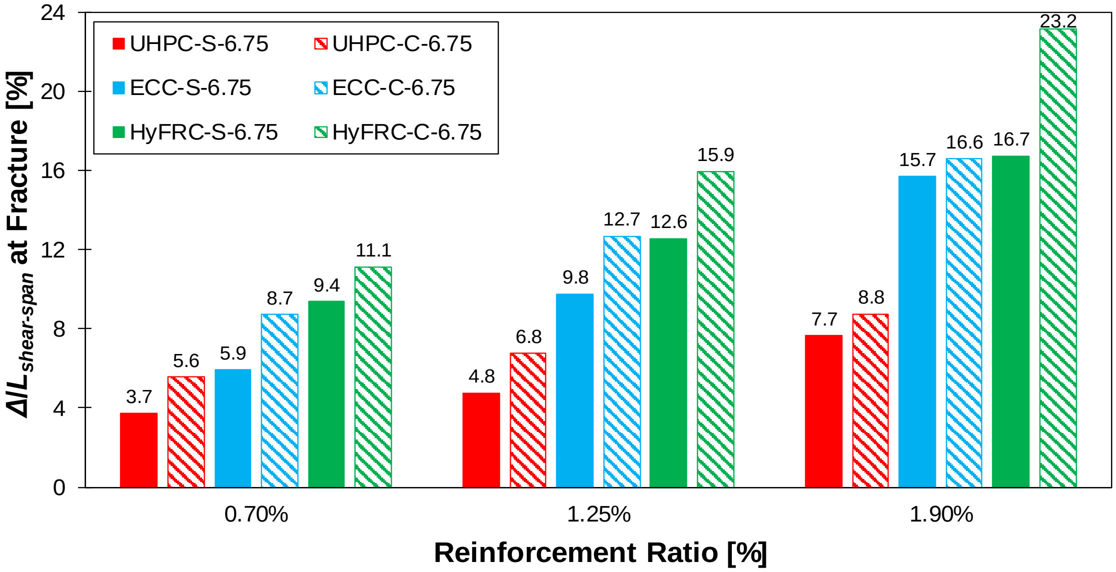

Figure 3.10 Variation in deformation capacity due to change in beam setup in long span beams.

have additional deflection as described in Section 3.4.3. The tensile stress in the longitudinal reinforcement was unable to end abruptly at the base of cantilever beam, and as a result, the reinforcement experienced plastic deformation over a long length. The spread of damage (i.e., cracking) into foundation beams, or joints, under large deformations for HPFRCC cantilever beams has been reported in previous experimental studies by Fischer and Li [23] and Frank et al. [104], among others.

3.4.3 Strain Penetration

The bond-slip mechanism between reinforcement and the foundation beam transfers reinforcement strain to the foundation beam until the bond stress reduces to zero. This phenomena is known as tensile strain penetration and is known to increase deflection and rotation capacity in ordinary reinforced concrete members [56]. To illustrate this phenomena, contours of principal tensile strains in the three types of HPFRCC long span cantilever beam with $\rho = 1.25\%$ at collapse level drift are shown in Figure 3.11. It can be observed that the damage propagates into the foundation through the longitudinal reinforcement leading to foundation softening with multiple distributed cracks (green region). The length of the damage propagating into the foundation increased from UHPC to HyFRC because the stronger matrix in UHPC beam does not allow the strain to be penetrated to longer depth compared to softer matrix of HyFRC beam. The dominant flexural cracks were simulated just above the joint region in all three types of beams, which confirms experimental observation of reinforced HPFRCC cantilever beams in past studies [23, 104].

To quantify the length of strain penetration inside the foundation beam, a plot of longitudinal reinforcement strain vs. distance from the base at the collapse level in UHPC (6.8% drift level), ECC (12.7% drift level) and HyFRC (15.9% drift level) cantilever beams with $\rho = 1.25\%$ is shown in Figure 3.12. The length of plasticity, L_p, in UHPC beam was 140 mm and the length of strain penetration in the foundation beam, L_{sp}, was 50 mm which is about 35.7% of the total plasticity length. Similarly, ECC and HyFRC beams had 32.2% and 31% strain penetration. This additional length of plasticity allows extra rotation of cantilever beams compared to the simply supported beams as will be discussed in Section 3.4.4.

3.4.4 Length of Plasticity

Damage, in the form of flexural and shear cracks, occurred in the length of the beam where longitudinal reinforcement yielded. The deformation capacity was higher when the length of plasticity, defined in this study as the length over which the reinforcement has yielded, increased as discussed in Section 3.3.3. Table 3.5 shows that the length of plasticity increases with increasing reinforcement ratio, and decreases with increasing tensile strength in the cantilever and simply supported HPFRCC beams.

For the same reinforcement ratio, the plasticity length in simply supported beam was longer than in cantilever beams; however, the deformation capacity of the

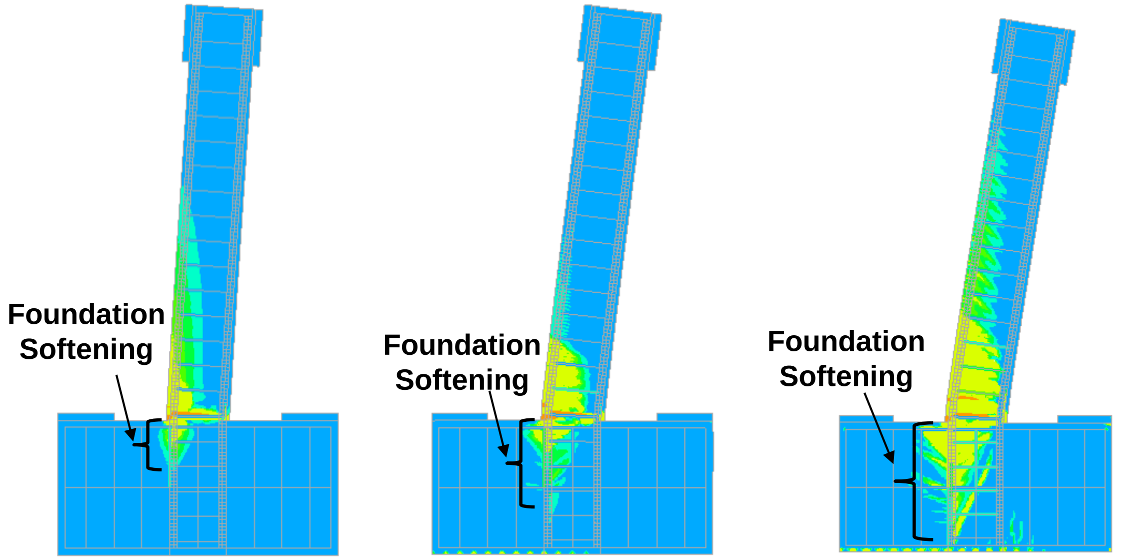

(a) UHPC-C-6.75-1.25 (b) ECC-C-6.75-1.25 (c) HyFRC-C-6.75-1.25

Figure 3.11 Principal tensile strain contour of cantilever long (a) UHPC beam (b) ECC beam (c) HyFRC beam with $\rho = 1.25\%$ at impending collapse level drift.

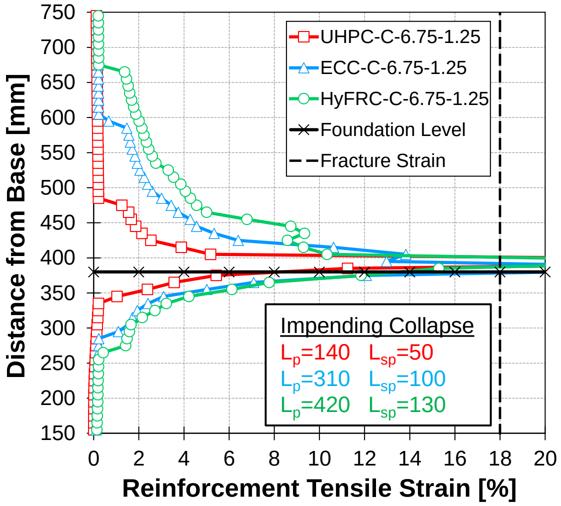

Figure 3.12 Longitudinal reinforcement strain vs. distance from base in cantilever long beams with $\rho = 1.25\%$ at impending collapse level drift.

cantilever beam was more than simply supported beam. Simply supported beams had a longer length of plasticity due to the test setup conditions. There are effectively two equivalent plastic hinges on either side of the centerline of a simply supported beam, whereas at the cantilever only forms one near the joint. To make direct comparisons between lengths of plasticity, the reader is referred to the ratio of the length of plasticity of the simply supported beam to the length of plasticity in the cantilever beam ($L_{p,S}/L_{p,C}$), reported in Table 3.5. Because of the boundary conditions of the setup, a value less than 2.0 indicates that the simply supported beam effectively has a smaller length of plasticity than the cantilever, whereas values greater than 2.0 indicate that the cantilever beam effectively has a longer length of plasticity, for the setup conditions. Table 3.5 shows that $L_{p,S}/L_{p,C}$ was less than 2.0 for all simulations.

Deformation capacity in cantilever beams was higher than simply supported beams due to tensile strain penetration as demonstrated in Section 3.4.3. The cantilever beam transfers the flexural stress at the base of the foundation beam (i.e., the joint) through the continuous embedded longitudinal reinforcement with the aid of bond-slip mechanism. The longitudinal reinforcement inside the foundation provides additional capacity to rotate under large deformations without fracture of the longitudinal reinforcement. The tensile strain of the longitudinal reinforcement was distributed to the HPFRCC material in the joint. As a result, cracks were simulated in the HPFRCC material within the joint region, which has been observed in experimental studies of reinforced HPFRCC cantilever beams [23, 85].

It can be observed from Table 3.5 that the $L_{p,S}/L_{p,C}$ ratio in the HyFRC sets were found to be the lowest whereas UHPC beams had the highest values among three different HPFRCC materials. This indicates that the tensile strain penetration is significantly higher in low tensile strength HPFRCC material (softer matrix) than in high tensile strength HPFRCC material (tougher matrix). Reinforcement strain penetration decreases with increasing HPFRCC tensile strength because fewer cracks

Table 3.5 Length of Plasticity in HPFRCC Long Span Beams

Notation	Length of Plasticity [mm]		
Reinforcement Ratio	0.70%	1.25%	1.90%
UHPC-S-6.75	190	270	380
UHPC-C-6.75	100	140	220
$L_{p,S}/L_{p,C}$	1.90	1.93	1.73
ECC-S-6.75	310	500	640
ECC-C-6.75	210	310	410
$L_{p,S}/L_{p,C}$	1.48	1.61	1.56
HyFRC-S-6.75	550	650	720
HyFRC-C-6.75	330	420	510
$L_{p,S}/L_{p,C}$	1.67	1.55	1.41

are able to form in the joint, and instead cracks, and therefore reinforcement strain, localize in the beam rather than the joint.

3.5 Effect of Variation in Shear Span-to-Depth Ratio

3.5.1 Damage Pattern

Contours of principal tensile strains of the ECC beams with $\rho = 0.70\%$ and 1.90% are shown in Figure 3.13 (a)-(f) and (g)-(l), respectively. Each figure shows strain contours in the short beams ($L_{shear-span}/d = 4.06$) at 1%, 2% and 4% drift levels, and in the long beams ($L_{shear-span}/d = 6.75$) at 4%, 8% and 12% drift levels to illustrate the damage progression and type of crack pattern induced. The strain contours are representative of the behavior across the three materials investigated in this study for the two different beam lengths. The deformation capacity and damage pattern in the short beams were controlled by a combination of flexure-shear interactions, whereas the long beam simulations were dominated more by flexural behavior.

For the low reinforcement ratio simulations ($\rho = 0.70\%$), the region of ECC softening (yellow region) remained nearly constant between 2 and 4% drift; however, at 4% drift, the short beam had one dominant crack (Figure 3.13 (c)) while the long beam had two dominant cracks (Figure 3.13 (f)). In the case of high reinforcement ratio ($\rho = 1.90\%$), both short and long beam softened at 4% drift level; however, damage progressed steadily in the long beam where the number of dominant cracks increased from three to five at 8 and 12% drift levels, respectively, as shown in Figure 3.13 (k)-(l). Similarly, in the short beam (Figure 3.13 (h)-(i)), two cracks appear at 8% drift which transformed to five large cracks at 12% drift level. Although, the number of cracks at 12% drift was the same in both beam lengths, the short beam had two diagonal tension (i.e., shear) cracks along with three flexural cracks, while the long beam had five flexural cracks.

Thus, increasing the length of an HPFRCC beam, and thereby reducing the shear demand on the member, increases the number of dominant cracks at low reinforcement ratios, and changes the type of cracking from a combination of flexure and shear cracking to primarily flexure at high reinforcement ratios. The change in cracking behavior from altering the beam length (i.e., V/M ratio) also influenced the deformation capacity, as discussed in Section 3.5.2.

3.5.2 Deformation Capacity

In seven out of nine sets of simulations (three HPFRCC materials and three reinforcement ratios), long beams had higher or nearly equal deformation capacity than short beams as shown in Figure 3.14. The deformation in long beams was due to bending (flexural deformation), whereas the deformation in short beams was due to a combination of distortion (shear deformation) and bending. Although, the simulations showed a trend that flexure dominated beams tended to have marginally higher deformation capacity than beams influenced by flexure and shear stresses, the

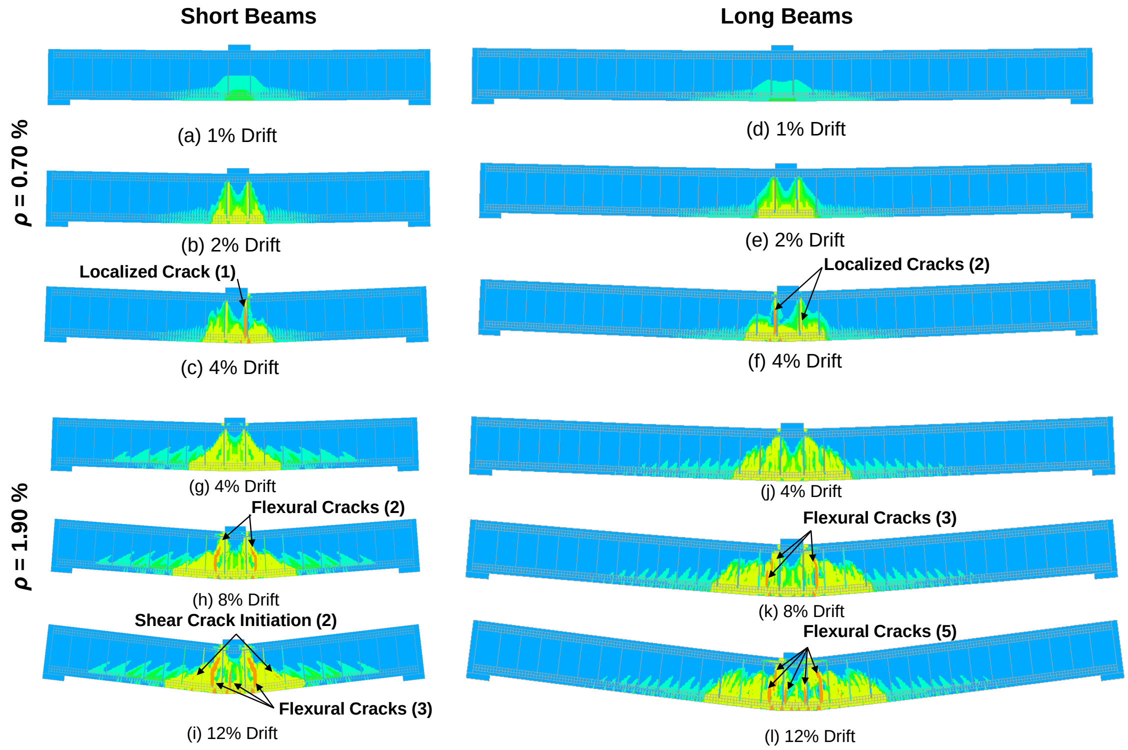

Figure 3.13 Principal tensile strain contour of simply supported (a-c) short ECC beam (ECC-S-4.06-0.70) (d-f) long ECC beam (ECC-S-6.75-0.70) with $\rho = 0.70\%$ and (g-i) short ECC beam (ECC-S-4.06-1.90) (j-l) long ECC beam (ECC-S-6.75-1.90) with $\rho = 1.90\%$ at different drift levels.

difference was smaller than what might be expected. For example, the largest increase in drift capacity observed by moving from a short beam to a long beam was 1.5% drift.

The short ECC and HyFRC beams at 1.25% reinforcement ratio had higher deformation capacity than the long beams, and therefore did not follow the same trend as the other seven pairs of simulations where higher deformation capacity was predicted in the long beams. The reverse trend of deformation capacity at 1.25% reinforcement ratio in these two sets of simulations (ECC and HyFRC) was found to be associated with the number of dominant cracks in these beams. In the case of the ECC beams, three dominant cracks were observed in both the short and long beams. Based on the other simulations, more number of dominant crack was expected in long beams compared to short beam, so that the damage is distributed in more number of cracks avoiding early fracture of reinforcement in long beams. In the case of the HyFRC beams, the long beam had fewer cracks than the short beam (3 vs. 4, respectively). Fewer cracks in the long beam subsequently led to an increment of inelastic damage in three major cracks rather than damage being distributed in more number of smaller cracks which led to early collapse of long beam.

3.6 Relative Influence of Material Properties and Structural Characteristics on Deformation Capacity

To quantify the relative influence of material properties and structural characteristics on deformation capacity of HPFRCC beams, a four-factor two-level full factorial design was completed using Minitab Version 18.1 [116]. Full factorial design analysis is often used to identify the variable with the highest impact in a multi-variable study. Further, it has the ability to demonstrate whether the combined effect of two or more variables is significant in an analysis or not. The current study has four factors (tensile strength, reinforcement ratio, setup, and shear span-to-depth ratio). One factor, tensile strength, contained three levels (8.0, 2.9, & 1.8 MPa), while the other

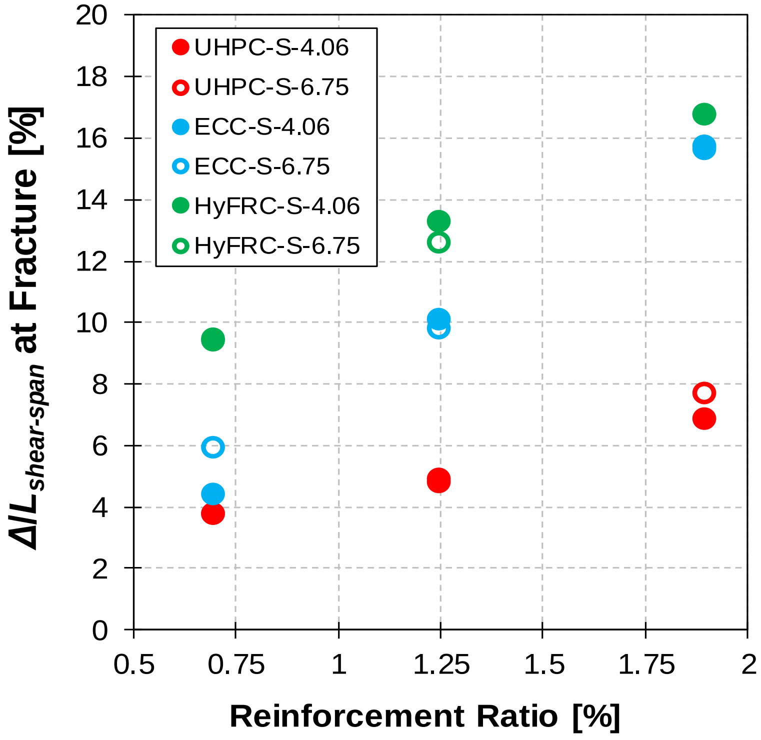

Figure 3.14 Variation in deformation capacity due to change in shear span-to-depth ratio.

factors, such as shear span-to-depth ratio, contained two levels (e.g., 4.06 & 6.75). The factorial design was carried out at the 95% confidence level using a two-sided confidence interval.

The output of the statistical analysis in the form of a Pareto chart (Figure 3.15(a)) shows that tensile strength, reinforcement ratio, boundary condition, and a combination of tensile strength and reinforcement ratio cross the reference line. Therefore, these factors produce statistically significant effects on the response quantity, which was set as the deformation capacity in this study. Figure 3.15(a) shows the magnitude or degree to which a factor is statistically significant based on absolute value of the standardized effect (t-value on X-axis) of the factors. It can be observed that tensile strength had the strongest affect followed by reinforcement ratio, and then test setup. The effect due to a change of shear span-to-depth ratio (or combination of tensile strength & shear span-to-depth ratio) were not significant as the t-value was less than the reference value (< 2.1).

The normal probability plot of the standardized effects shows whether the effect increases or decreases the response (i.e., deformation capacity) as shown in Figure 3.15(b). The normal plot shows positive standardized effect towards the right side and negative standardized effect towards the left side of the fitted-line. In other words, positive values tend to increase deformation capacity, while negative values tend to decrease deformation capacity. The effect of tensile strength is negative meaning that the deformation capacity decreases with increasing tensile strength. In contrast, deformation capacity increases with increasing reinforcement ratio as shown in the strong positive effect seen in the plot. Similarly, the combined effect of tensile strength and reinforcement ratio leads to a net decrease in deformation capacity (negative side of the fitted-line). The cantilever test setup was assigned a numeric value of -1 in the statistical analysis, while the simply supported beam was assigned a value of $+1$. As a result, the effect of test setup was also negative, meaning as the boundary condition changes from cantilever to simply supported beam, deformation capacity decreases.

The factors whose effects are not significant are near zero and are fitted in a line, while the factors shown away from the fitted-line have statistically significant effects on the response (i.e., deformation capacity). The rate at which these factors affect the response can be determined by observing the distance between the variable and the fitted line. For example, tensile strength causes a sharp decrease in deformation capacity and is therefore furthest away from the fitted line with a negative standardized effect. Reinforcement ratio has a slightly smaller effect, and is therefore closer to the line on the positive side because higher reinforcement ratio results in an increase in deformation capacity. The influence of tensile strength is so high that the combined response of tensile strength and reinforcement ratio is skewed to the negative direction. The change of test setup from cantilever to simply supported condition has the smallest effect that was deemed significant.

The statistical analysis distinctly shows the magnitude of influence, significance, and the direction of influence of each of the variables considered in this study. Based on these observations, contour plots of reinforcement ratio vs. tensile strength were developed and are shown in Figure 3.16 to predict deformation capacity for both simply supported and cantilever HPFRCC beams. The range of deformation capacity obtained using the contour plot for simply supported beam are in agreement with the monotonic experimental data of Bandelt and Billington [53]. ECC beams with a tensile strength of 2.2 MPa (based on inverse analysis of unreinforced bending specimens) were tested with reinforcement ratios of 0.70%, 1.3%, and 2.0% under three point bending. The 0.70% reinforcement ratio specimen fractured at a deformation of 8.4%, and the contour plot shown in Figure 3.16(b) predicts a drift capacity between 8 and 10%. Similarly, the 1.3% reinforcement ratio experimental specimen failed at a deformation of 12%[53], and the contour plot shown in Figure 3.16(b) developed based on numerical simulation presented in this chapter predicts a deformation capacity between 12 and 14%. Finally, the 2.0% experimental specimen had a drift capacity of 16% [53], and Figure 3.16(b) predicts a deformation capacity between 16 and 18%. A cantilever beam tested by Frank et al. [91] with a reinforcement ratio of 1.3% and a tensile strength of approximately 3.5 MPa [85] had an experimental deformation capacity of 16%, which is slightly above the contour predicted value in Figure 3.16(a) of 14%. The discrepancy in the contour predicted value is likely because the specimen tested by Frank et al. [91] was flexure-dominated, while the contours assume a behavior that is between the “flexure-” and “flexure-shear” stress states associated with variations in span-to-depth ratio. Contour plots can also be developed based on a sensitivity analysis of cyclically loaded specimens; however, the results from this study provide a

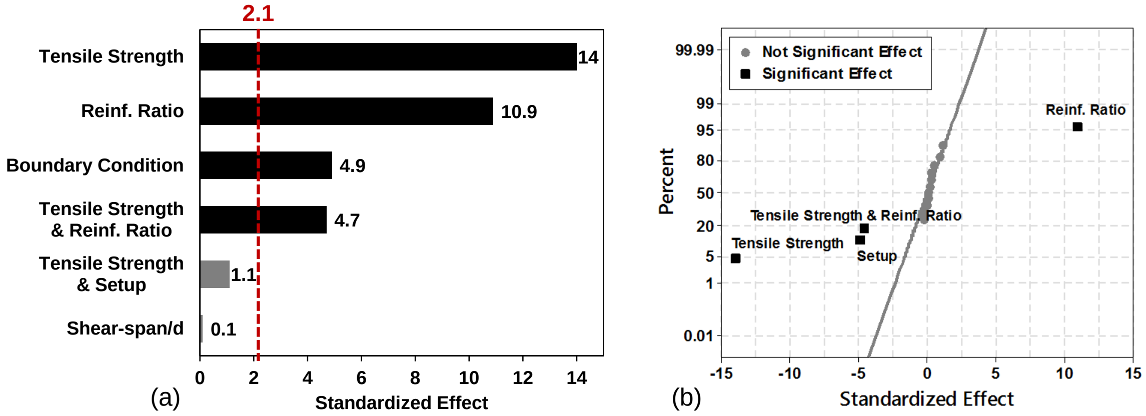

Figure 3.15 Influence of different factors on deformation capacity based on (a) Pareto chart of standardized effects (b) Normal distribution plot of standardized effects.

starting part for estimating deformation capacity of HPFRCC members over a range of tensile strengths and reinforcement ratios.

3.7 Conclusions

This chapter involved a numerical investigation of material properties and structural characteristics that influence deformation capacity of reinforced HPFRCC members. The motivation for the research presented was to identify sources of variability in deformation capacity that have been observed in the literature, but not yet fully understood. Thirty-six two-dimensional finite element models of reinforced HPFRCC beams with different material properties, shear span-to-depth ratios, test setups, and reinforcement ratios were subjected to monotonic loading until fracture of the reinforcement was simulated. Material properties were varied through the use of three types of HPFRCCs characterized predominantly by their tensile strengths (UHPC, ECC, and HyFRC). Similarly, long- and short-span beams were considered for variation in shear span-to-depth ratio. Simply supported and cantilever beams were used to vary the test setup, and three different reinforcement ratios (0.70%,

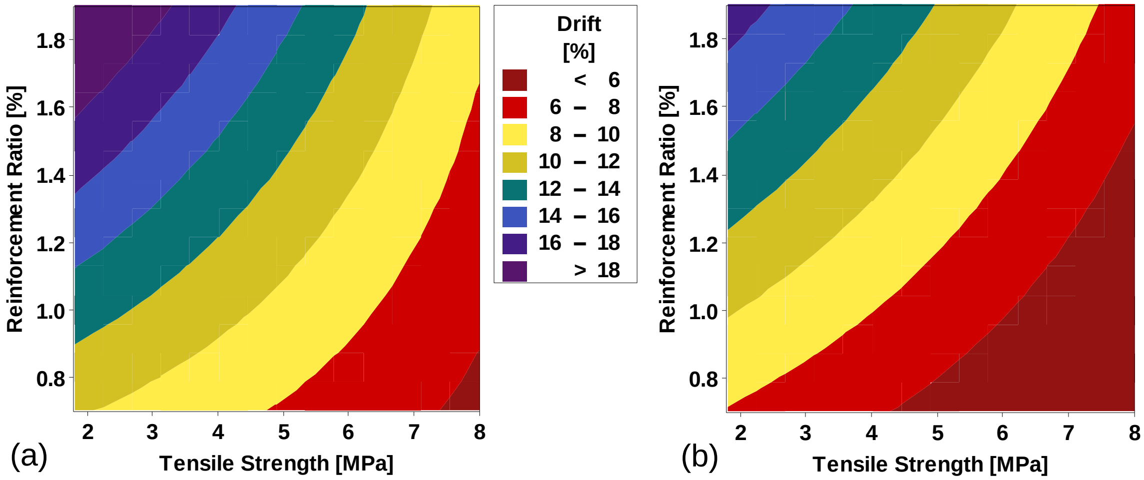

Figure 3.16 Contour diagram of reinforcement ratio vs. tensile strength for predicting drift capacity of (a) Cantilever HPFRCC beam and (b) Simply supported HPFRCC beam.

1.25%, and 1.90%) were used to see the variation in deformation capacity across a range of reinforcement ratios.

The simulation results showed that there was a reduction in deformation capacity, by as much as 63%, by increasing the HPFRCC tensile strength from 1.8 MPa (HyFRC) to 8 MPa (UHPC) in simply supported beams. The influence of tensile strength was more pronounced at the low reinforcement ratio and short span beam simulations. The reduction in deformation capacity was mainly due to the resistance of the high tensile strength material which prevented multiple dominant cracks from forming compared to the low tensile strength material, which allowed multiple dominant cracks to form. A lower number of cracks and low rebar slip resulted in strain concentration over a smaller gage length of longitudinal reinforcement, and thereby early fracture of the reinforcement occurred. As the reinforcement ratio increased, the number of cracks and length of plasticity increased in all three types of beams (UHPC, ECC, and HyFRC) which is consistent with experimental results [53].

Changing the boundary conditions from cantilever to simply-supported resulted in a reduction of deformation capacity between 5.3% and 43.3% for reinforced HPFRCC beams. UHPC beams were significantly affected (28.6% average reduction in deformation capacity) by the change in test setup whereas HyFRC beams were least affected. The difference in the deformation capacity between cantilever beams and simply supported beams is mainly because of a higher spread of plasticity in the reinforcement as cracking occurs in the joint of a cantilever beam, effectively lengthening the gage length over which fracture occurs. The strain penetration phenomenon observed in the simulations has also been observed for reinforced concrete cantilever members [56]

Shear span-to-depth ratio, which had the least impact on deformation capacity than the other factors, was also investigated. Numerical simulations of simply supported beams showed a reduction in deformation capacity between 1% and 26% as the shear span-to-depth ratio decreased from 6.75 to 4.06. Short span beams tended to have lower deformation capacity due to flexure-shear deformations. The discrepancy in the deformation capacity between long and short span beam was due to the number of cracks and type of cracks as seen from the principal tensile strain contours. Flexure-shear dominated short beams had fewer cracks with inelastic deformation localized over a small length of the beam. Cracking patterns of short span beams included diagonal tension cracks along with vertical flexural cracks, which aided in early fracture compared to flexure dominated long span beams which only experienced flexural cracking.

Finally, statistical analysis was conducted to understand the relative impact of material properties and structural characteristics on deformation capacity. It was shown that, in descending order of importance, tensile strength, reinforcement ratio, and boundary conditions were the most influential characteristics in predicting deformation capacity. Contour plots of predicted deformation capacity were developed and found to agree with experimental results [53]. The framework used for the development of the contour plots can be extended for cyclically loaded specimens and other material or structural characteristics to better understand their impact on component-level behavior.

CHAPTER 4

PLASTIC HINGE BEHAVIOR AND ROTATION CAPACITY IN REINFORCED DUCTILE CONCRETE FLEXURAL MEMBERS

4.1 Introduction and Background

In recent years, there has been a gradual shift in seismic design philosophy from traditional force-based seismic design (FBSD) to alternative seismic design principles based on deformation capacity known as performance-based seismic design (PBSD) [87]. In PBSD, a structure is designed to achieve a target performance level under a specified intensity of seismic loading. The performance level of a structure is explicitly defined in terms of metrics such as material strain or inelastic component rotation that corresponds to physical damage such as yielding, crushing, or fracture of tensile reinforcement [97, 117]. PBSD also requires inelastic modeling of structural components to measure these performance metrics which cannot be completed using elastic modeling techniques typically applied in FBSD approach. Therefore, it is important to accurately quantify inelastic structural component response in order to calculate displacements and rotation demands for performance assessment of structures subjected to different intensities of seismic loading. In reinforced concrete structural elements, numerous experimental and numerical studies have been used to understand inelastic behavior in terms of plastic hinge region response, which has resulted in empirical models to predict plastic hinge length as shown in Table 4.1.

As PBSD approaches have become more commonplace in analysis and design, engineers have sought out new materials and structural systems to take advantage of material and structural ductility [35, 98]. In the area of reinforced concrete, recent developments have been made to improve the mechanical response of concrete materials and have led to the emergence of high-performance fiber-reinforced cementitious composites (HPFRCCs). HPFRCCs are a class of cement-based ductile materials exhibiting a pseudo tensile strain-hardening behavior with distributed cracking under uniaxial tension[2, 18]. Under compression, these materials have increased damage tolerance with resistance to spalling [38, 74]. The improved mechanical properties of HPFRCC significantly increases ductility, energy dissipation capacity and damage tolerance of structural members, especially in expected plastic hinge locations under seismic loadings [45]. Reinforced HPFRCC structural members such as beams [22, 23, 27, 72], columns [21, 73], walls[24], and beam-column joints [28], among others, have been physically tested in laboratories under quasi-static monotonic and reversed cyclic loading, and found to be a promising alternative to improve structural performance and constructability compared to conventional reinforced concrete members. Unlike reinforced concrete, predicting the plastic hinge behavior of components using ductile concrete materials has received limited response.

Recent literature has shown that the HPFRCC flexural members reinforced with mild steel predominantly fail by fracture of tensile reinforcement which contrasts the usual compression crushing phenomenon in ordinary reinforced concrete members [53, 104]. Composite behavior of reinforced HPFRCC is characterized by higher bond strength [46–48] which helps resist the formation of splitting cracks leading to damage localization in the vicinity of a single transverse crack or few cracks as seen in tension stiffening experiments [50, 74]. Experimental investigations of reinforced HPFRCC beams conducted by Bandelt and Billington [53] shows that the number of flexural cracks and the rate of damage progression in the plastic hinge region, increases with increasing reinforcement ratio. Further, the deformation capacity of specimens under cyclic loading were found to be lower than the corresponding monotonic specimens because of a rapid accumulation of plastic strain in the localized crack region with increasing loading cycles. In another study, it was found that the presence of large pulses at the beginning of loading history could increase the accumulation rate of reinforcement strain in HPFRCC flexural members with low reinforcement ratios, and cause fracture of reinforcement at drifts lower than specimens without pulses [63].

The plastic hinge region of reinforced HPFRCCs is a complex inelastic region with a highly non-linear interaction between the reinforcement and HPFRCC matrix, characterized by multiple fine distributed crack before yielding of the reinforcement and a small number (usually one or two) of localized dominant cracks after yielding of the reinforcement [53, 62]. The formation and nature of plastic hinge regions in a structural member govern the nominal load carrying capacity, as well as the ultimate displacement, rotation, and energy dissipation capacities under extreme loadings. The *equivalent plastic hinge length*, generally referred to as “plastic hinge length”, L_p, is the length over which plastic curvature is assumed to be constant, such that the integrated area under the actual plastic curvature is equal to the area under the assumed curvature [56]. This plastic hinge length provides a simplified method to calculate total plastic rotation or deformation capacity of a member undergoing large inelastic deformation using cross-sectional curvature analysis. The physical length of a real plastic hinge region is close to the length over which the reinforcement yields, which will be referred to as reinforcement yielding zone, L_y, in this chapter [56, 59].

With availability of advance finite element modeling technique such as total strain-based models [42, 43, 105] and recent development of bond-slip constitutive model that captures the complex interaction between reinforcement and HPFRCC matrix [75]; numerical simulations are able to predict damage stages such as yielding of reinforcement, reinforcement fracture, and damage pattern similar to that of actual physical experimentation [75, 109]. In this chapter, a finite element-based approach is applied to investigate the plastic hinge region in reinforced HPFRCC members to avoid significant cost and time associated with large scale experimental programs. Numerical simulations are used as a tool to develop expressions of plastic hinge length for different HPFRCC material and structural properties, and the proposed expressions are validated on a large experimental database.

4.2 Existing Studies on Plastic Hinge Region in Reinforced HPFRCC

Table 4.1 shows numerous plastic hinge length equations developed for reinforced concrete and reinforced HPFRCCs under different loading conditions, and for various structural elements. The expressions are based on regression analysis of either experimental, numerical, or combined experimental and numerical studies carried out with variations in material and geometric properties. Researchers have identified three distinct phenomena that causes the spread of plasticity in plastic hinge region, namely: (a) moment gradient related to the increment of moment with length of shear span or flexural depth, (b) tension shift related to shear distortion which invalidates the linear strain distribution assumption in a cross-section, and (c) tensile strain penetration which refers to an increment in length of plasticity due to accumulation of significant strain inside a joint or foundation through the bond-slip mechanism between the longitudinal reinforcement and the surrounding matrix [56, 57]. Most of the primary variables that are used to define the plastic hinge length expressions in Table 4.1, explicitly take into account one or two of these phenomena. For example, length(L), shear span(z), shear span to depth (z/d), or effective depth (d) are associated with moment gradient in a flexural member. Similarly, yield stress (f_y), diameter of longitudinal reinforcement (d_b), reinforcement ratio (ρ), or compressive strength (f'_c) are related to strain penetration. Most of the expressions ignore the tension shift phenomenon, assuming its effect to be statistically insignificant, or incorporate this effect implicitly by calibrating the equation with ultimate rotation or displacement obtained through experimental or numerical studies.

In regards to HPFRCC plastic hinge length, Naaman et al. [18] conducted an early study to quantify the plastic hinge length and used it to compute plastic rotation

Table 4.1 Empirical Models of Plastic Hinge Length

Reference	Expressions	Element	Loading
Baker [118]	$k_1k_2k_3d(z/d)^{1/4}$	RC Beam	Monotonic
Sawyer [95]	$0.25d + 0.075z$	RC Beam	Monotonic
Corley [54]	$0.5d[1 + (0.4/\sqrt{d})(z/d)]$	RC Beam	Monotonic
Mattock [55]	$0.5d + 0.05z$	RC Beam	Monotonic
Paulay and Priestley [56]	$0.08L + 0.022f_yd_b$	RC Beam & Column	Monotonic
Naaman et al. [18]†	$0.5(1.06 + 0.13\rho V)d$	R-HPFRCC Beam	Monotonic
Panagiotakos and Fardis [101]	$0.18d + 0.021a_{sl}f_yd_b$	RC Beam & Column	Monotonic
	$0.12d + 0.014a_{sl}f_yd_b$	RC Beam & Column	Cyclic
Bae and Bayrak [58]	$[\,\{0.3(P/P_o) + 3(A_s/A_g) - 0.1\}\,(L/h) + 0.25]h \geq 0.25h$	RC Column	Cyclic
Berry et al. [96]	$0.05L + 0.1f_yd_b/\sqrt{f'_c}$	RC Column	Cyclic
Tariq et al. [61]	$(0.3 + 0.18\rho)d$	R-HPFRCC Beam	Cyclic
Xu et al. [60]†	$[10(f_c/f_y)^{1.5}\{E_{sh}/(E_s\rho_s)\} - 0.12]d + 0.238z$	R-HPFRCC Beam	Monotonic

†Length of reinforcement yielding region

capacity of reinforced HPFRCC flexural members through experimental testing of 12 reinforced HPFRCC beams containing steel fibers under monotonic loading, and with reinforcement ratios ranging from 0.67% to 1.89%. An empirical equation was proposed for plastic hinge length corresponding to the length of reinforcement yielding zone, L_y (Table 4.1). The plastic curvature was shown to vary non-linearly from the reinforcement yielding section to the section corresponding to ultimate strain($\varepsilon_{cu} = 0.003$). The proposed plastic hinge equation had to be multiplied by a *curvature modification factor*, $\beta (= 0.56 - 0.16V_f)$, to compute the average plastic curvature over the reinforcement yielding zone, L_y, in order to calculate plastic rotation capacity, θ_p, of the flexural member. However, the curvature modification factor was developed for steel fibers used in that particular study and it is unclear if this equation holds true for other types of fiber-reinforcing materials (e.g., polymeric fibers). Further, the failure criteria chosen (i.e., $\varepsilon_{cu} = 0.003$) for the calculation of plastic rotation capacity for reinforced HPFRCC beams is too conservative because a recent experimental study has shown that the strain in extreme compression fiber can reach a value up to 0.03

before extensive softening of cementitious matrix begins followed by the failure of the member due to fracture of the tensile reinforcement [119]. Similarly, several other studies have concluded that the reinforced HPFRCC flexural members do not lose significant load-carrying capacity and undergo considerable plastic deformation before failure occurs by the rupture of longitudinal reinforcement [53, 62, 63, 92].

Parra-Montesinos and Chompreda [27] conducted an experimental study to investigate the deformation capacity and shear strength of structural members constructed with steel fiber-reinforced cement composites (FRCC). In order to estimate the plastic rotation capacity under reversed cyclic loading, the authors used an equivalent plastic hinge length, L_p, equal to the "*effective depth*" of the cross-section; however, this was assumed based on literature by Blume et al. [120] used for the analysis of conventional reinforced concrete buildings under seismic loading.

Xu et al. [60] performed a parametric study of reinforced ECC beams under monotonic loading by varying material and cross-sectional properties, and proposed an equation to predict the length of reinforcement yielding zone, L_y (Table 4.1) . This length is close to the physical plastic hinge length over which the seismic detailing is required for the ductile performance of the plastic hinge region, but it cannot be used directly to compute plastic rotation capacity of a HPFRCC member, unless curvature distribution data is available along the reinforcement yielding zone, L_y. Further, failure of the beams were observed to be by crushing of the compression zone material as most of the beams were singly reinforced beams; however, in ductile seismic design practice, doubly reinforced symmetrical cross-sections are more common in flexural members because of the expected moment reversal under seismic loading [56, 94].

Tariq et al. [61] used a fiber-based lumped plasticity modeling technique to calibrate experimentally tested reinforced ECC beams by minimizing the error in the force-deformation backbone response and collapse level drift. An expression for equivalent plastic hinge length, L_p (Table 4.1), was proposed that could reasonably predict fracture strain at collapse drift in specimens under different types of cyclic loading; however, the equation was based on a limited database of cantilever beams with variation in cross-sectional dimensions and tensile reinforcement ratio only, and only one HPFRCC material was considered.

Pokhrel and Bandelt [65, 109] conducted an investigation with variation in mechanical properties, geometric properties, and boundary conditions to identify potential variables affecting deformation capacity and plasticity (i.e., reinforcement yielding zone, L_y) under monotonic loading. The study showed that there was a substantial decrease in the deformation capacity, length of plasticity (L_y) and length of rebar slippage with increase in tensile strength, f_t. Tensile strength influenced these factors as strain concentrated over a shorter gage length of the reinforcement, leading ultimately to early fracture of the tensile reinforcement. In addition to that, the change in boundary conditions from cantilever to simply-supported (i.e., end-hinges to center hinges) resulted in a reduction of deformation capacity in reinforced HPFRCC beams. Cantilever beams had higher deformation capacity because of a larger spread of plasticity inside the joint of the foundation due to strain penetration which increases plastic rotation capacity in ordinary reinforced concrete members as well [56, 57, 96]. This study, however, did not quantify plastic hinge length and did not consider the effect of cyclic loading on the length of plasticity in reinforced HPFRCC members.

4.3 Numerical Simulation Description and Validation

4.3.1 Finite Element Models

The finite element software DIANA FEA Version 10.2 [110] was used to create two dimensional finite element models with variation in material properties, section geometry, and boundary conditions. Representative finite element models of simply supported and cantilever beams used in the research study are shown in Figure 4.1. The test setup and specimen dimensions for the numerical simulations were selected

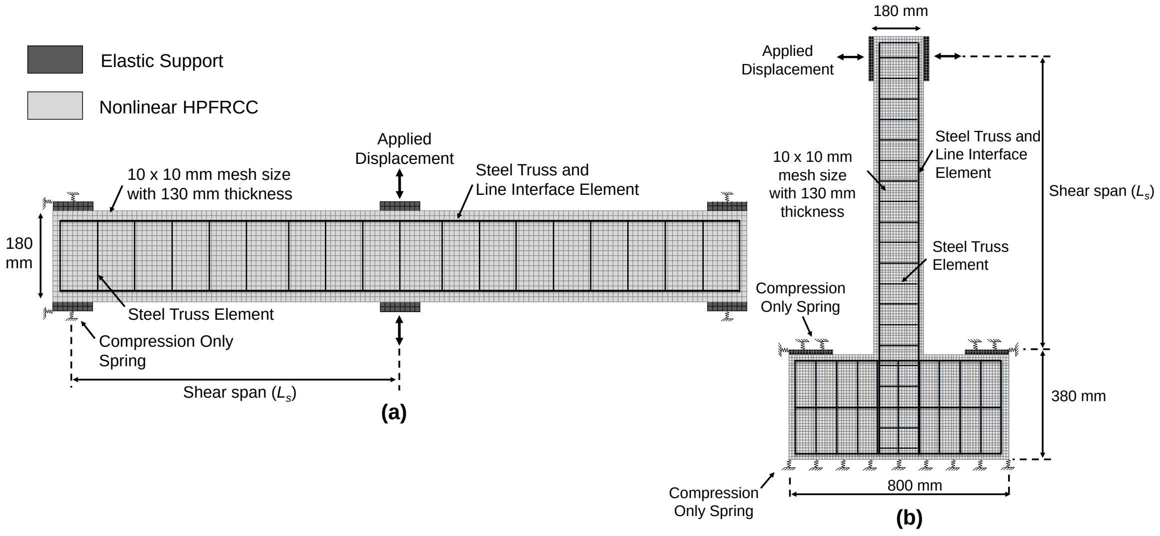

Figure 4.1 Finite element geometry of (a) simply supported beam (b) cantilever beam.

based on representative reinforced HPFRCC component experiments conducted under monotonic and cyclic loading to high deformations including fracture of the reinforcement [23, 53, 63, 93].

Elastic support and loading plates were used at both sides of the beams to prevent inelastic stress concentration at the interface between plates and HPFRCC beam elements. Vertical and lateral springs were modeled as uniaxial springs at the base of the support plates with stiffness to replicate the softness of the plate supports as in the physical experiment [75, 104]. Foundation beams with dimension ($l \times b \times h$) of 800 mm × 130 mm × 380 mm were used as the fixed base support for the cantilever beams similar to the experimental testing conducted by Frank et al. [104].

There are several potential variables that can affect the formation, spread, and length of plastic hinge region in reinforced HPFRCC members. In this study, a total of 72 finite element beam simulations with variation in shear span, reinforcement ratio, tensile and compressive property of HPFRCC, boundary condition, and loading type are considered as discussed in Sections 4.3.1.1- 4.3.1.5.

4.3.1.1 Shear Span. Shear span (L_s) of a structural member is the length between maximum moment and zero moment. Shear span is directly related to the moment gradient in a plastic hinge region of a structural element. The equations listed in Table 4.1 for reinforced concrete members show that the equivalent plastic hinge length is directly proportional to the shear span. To investigate the length of plastic hinge region in reinforced HPFRCC, shear span lengths of 650 mm and 1080 mm were chosen corresponding to shear span-to-depth ratio (L_s/d) of 4.06 and 6.75, respectively. Specimens with a shear span-to-depth ratio of 6.75 are considered to be dominated by flexural deformations; while specimens with a shear span-to-depth ratio of 4.06 are considered to have contribution in deformation from both flexure and shear stresses [94].

4.3.1.2 Reinforcement Ratio. Reinforcement ratio is directly related with the maximum moment capacity, ultimate rotation capacity and tensile strain penetration phenomenon in a reinforced concrete or HPFRCC member. Symmetrical longitudinal reinforcement on top and bottom with areas of 142 mm^2, 258 mm^2, and 398 mm^2 corresponding to reinforcement ratios of 0.70%, 1.25% and 1.90% were used. It is recognized that increasing the area of compression steel limits the potential for damage on the compression side of the members; however, symmetrical reinforcement was selected to make comparisons to results from the available database in which the members are generally symmetrically reinforced for seismic applications. All of the beams were modeled with transverse reinforcement of 16 mm^2 with uniform spacing of 75 mm.

4.3.1.3 Boundary Conditions. Two boundary conditions were considered in this investigation such that plastic hinges could form at the center of a simply supported beam and at the end of a cantilever beam integrally connected to a foundation element. Previous research studies on HPFRCCs were conducted either on simply supported or cantilever elements; however, the effects of end conditions have not been systematically studied to identify the boundary conditions effects in the spread of plasticity in reinforced HPFRCC members.

4.3.1.4 Tensile and Compressive Property. In order to investigate the effect of tensile strength and compressive strength on the length of the plastic hinges in reinforced HPFRCC members, the mechanical response of three types of materials, namely, an Ultra-High Performance Concrete (UHPC), an Engineered Cementitious Composite (ECC) and a Hybrid Fiber Reinforced Concrete (HyFRC) were used in the simulations. Each of these materials have unique mechanical properties that are promising for various structural applications. UHPC, which is increasingly used in bridge construction for improving durability and accelerated construction techniques [36], is an ultra high strength material with tensile and compressive strengths in the range of 5.5-11 MPa [77] and 112-210 MPa [77], respectively. ECC, developed by Li and Leung [80] with principles of micro-mechanics such that it exhibits ultra high tensile ductility under uniaxial test, has tensile and compressive strengths in the range of 2.5-5.0 MPa [39] and 30-90 MPa [81], respectively. HyFRC uses a hybridization of fibers across various length scales for durability and seismic applications [74, 84], and has tensile and compressive strengths in the range of 1.5-3.1 MPa [82, 83] and 30-45 MPa [50, 82], respectively.

The three materials were chosen for this study because of the range of their mechanical properties associated with their distinctive fiber compositions, and their wide use in various large-scale experimental programs. UHPC, which is also known as, Ultra-High-Performance Fiber-Reinforced Concrete (UHP-FRC), generally contains $1\%-2.5\%$ by volume fraction (V_f) of smooth, hooked, or twisted steel fibers with an aspect ratio (l_f/d_f) of $65-100$ [36, 78], whereas ECC mixtures mostly contain

2% by volume fraction of polyvinyl alcohol or polyethylene fibers with an aspect ratio of 300−350 [27, 82]. HyFRC consists of a hybrid combination of steel macro-fibers and polyvinyl alcohol micro-fibers with a volume fraction of 0.5%−1.3% and 0.2%−0.3%, respectively [82, 83]. Macro-fibers in HyFRC mixtures generally have an aspect ratio of 55−80, whereas micro-fibers have an aspect ratio of 200−250 [82, 83]. The fiber types and mixture constituents were not simulated numerically; however, the mechanical response associated with each mixture was included in the simulation. Representative tensile strengths (f_t) and compressive strengths ($f_c^{'}$) corresponding to UHPC (8 MPa & 120 MPa), ECC (2.9 MPa & 55 MPa), and HyFRC (1.8 MPa & 45 MPa) were used in the simulation. These mechanical properties were selected based on the uniaxial tension and compression tests conducted by Wille and Naaman [78], Russell and Graybeal [36], and Moreno et al. [82], whose mix compositions did not use coarse aggregates as a constituent material for UHPC and ECC.

4.3.1.5 Load Type. Two types of loading were used on the reinforced members in this study: (a) monotonic loading, and (b) reversed cyclic loading. Monotonic loading was applied using incremental displacement-based approach at a step size of 0.25 mm until the fracture of longitudinal reinforcement or crushing of HPFRCC was observed. Reversed cyclic loading was applied using the FEMA 461 [86] loading protocol such that two successive cycles with the same maximum amplitude of drift was applied. The amplitude of drift was increased by 40% for the next two successive cycles, and this process was repeated until the failure was observed. The first two cycles had maximum amplitude of 0.15% drift, where the drift was obtained by normalizing vertical deflection by shear-span (i.e., Δ/L_s). A total of 72 finite element models were simulated in this study with variability in the loading scenario, boundary condition, shear span, tensile reinforcement ratio, and HPFRCC type ($2 \times 2 \times 2 \times 3 \times 3$).

4.3.2 Material Models and Analysis Parameters

4.3.2.1 HPFRCC Material Model. A total strain-based fixed-crack model was used as the constitutive model to simulate the behavior of HPFRCC materials [105]. A constant shear retention factor (β_s) of 1% [75] was used to simulate the transfer of shear stress across the cracks. Although there are more refined approaches to simulate the shear transfer mechanism pertaining to fiber bridging action in various types of HPFRCC materials [43], same shear retention factor was used for all three types of HPFRCCs in this study because of the flexure dominant nature of most of the simulated beams [121], and to avoid numerical convergence issue and severe stress locking associated with constant high shear retention factor under large inelastic deformation [113]. The HPFRCC materials were modeled using eight-noded quadratic plane stress elements. The size of each element was 10 × 10 mm and the thickness was 130 mm. A 3 × 3 Gauss integration scheme and quadratic interpolation was used in the finite element numerical formulation. The material tensile response was modeled using an idealized multi-linear stress-strain curve (Figure 4.2 (a)), as it has been successfully used by researchers to simulate composite action between steel reinforcement and HPFRCC material [82], and component level response of reinforced HPFRCC flexural members [61, 63, 65, 75].

Parameters such as initial stiffness (E), maximum tensile stress (f_t), and tensile strain at the onset of softening (ε_{tp}) were obtained from uniaxial tensile test data [78, 82] and are summarized in Table 4.2. The ultimate tensile strain (ε_{tu}) was based on the experimentally observed tensile fracture energy and was calculated using a linear softening model as shown in Equation (3.1) [82].

$$\varepsilon_{tu} = 2\frac{G_f}{h}\frac{1}{f_t} + \varepsilon_{tp} \tag{4.1}$$

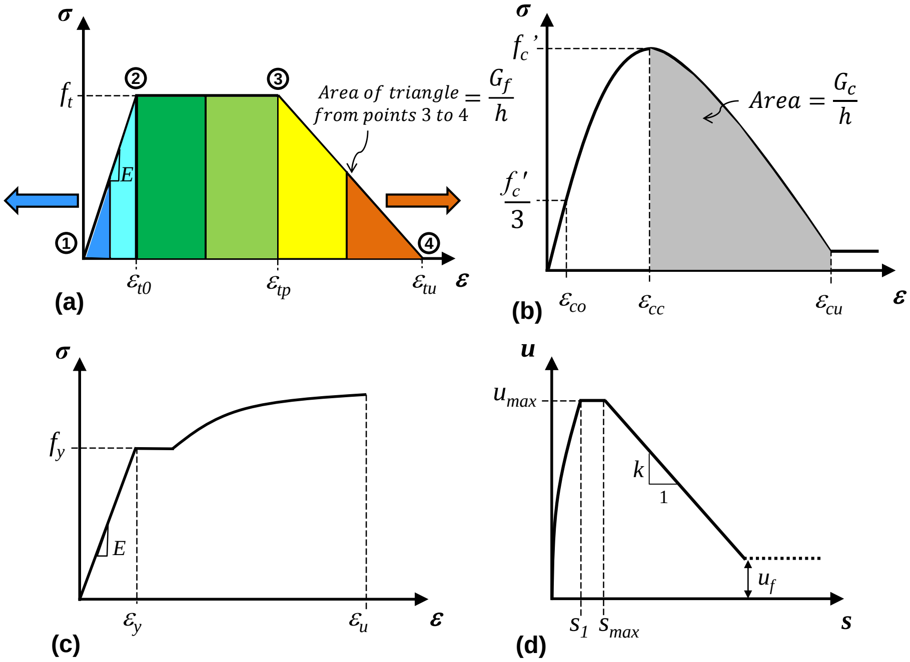

Figure 4.2 (a) Multilinear tensile stress-strain parameters of HPFRCC and contours of principal tensile strains (b) parabolic compressive stress-strain parameters of HPFRCC (c) uniaxial tensile stress-strain parameters of steel (d) Bond-slip parameters.

The compression response of the HPFRCC materials was modeled using a parabolic stress-strain curve based on compressive fracture energy [111] as shown in Figure 4.2 (b). The compression stress-strain parameters such as compressive strength ($f_c^{'}$), compressive fracture energy (G_c), and Poisson's ratio (ν) were based on experimental data [36, 82] and are summarized in Table 4.2. The initial compressive strain (ε_{co}), compressive strain at maximum compressive strength (ε_{cc}) and the ultimate compressive strain (ε_{cu}) were calculated using the parabolic model as shown in Equation (4.2) [110].

$$\begin{aligned}\varepsilon_{co} &= \tfrac{1}{3}\tfrac{f_c^{'}}{E}\\ \varepsilon_{cc} &= \tfrac{5}{3}\tfrac{f_c^{'}}{E}\\ \varepsilon_{cu} &= \tfrac{3}{2}\tfrac{G_c}{h}\tfrac{1}{f_c^{'}} + \varepsilon_{cc}\end{aligned} \tag{4.2}$$

In Equation (4.1) and 4.2, h is the crack bandwidth which is equal to $\sqrt{A}$, where A is the area of an individual plane stress element. As only one mesh discretization is presented in this chapter, crack-band approach was used to eliminate the problem related with mesh dependency [43, 82, 108]. Other mesh sizes were explored, but were not shown to influence the results due to the crack-band approach. The cyclic tensile and compressive behavior of HPFRCC was represented by secant unloading and reloading path through origin. There are more refined approaches as well [42, 43], but the secant path approach has less convergence issue, and has been previously used by researchers in simulating component level response of reinforced concrete [114] and reinforced HPFRCC [75] with sufficient accuracy. Kesner et al. [38] conducted an experimental investigation to characterize uniaxial cyclic response of HPFRCC material and found out that there was 50% to 80% reduction in tensile fracture energy of HPFRCC material under cyclic loading compared to monotonic loading. Therefore, to accurately simulate inelasticity and damage in HPFRCC under cyclic loading, a *damaged fracture energy* equal to 50% of the monotonic fracture energy (G_f) was utilized for simulations under cyclic loading.

4.3.2.2 Steel Material Model. Longitudinal reinforcement was modeled as a three-noded truss element with an element size of 10 mm. A three-point Gauss integration scheme was used for numerical integration of the truss element. Transverse reinforcement was modeled as a two-noded directly integrated truss elements with the same element size as longitudinal reinforcement. The constitutive behavior of longitudinal reinforcement was modeled using the Von Mises plasticity strain hardening model [112] for monotonic loading. The longitudinal reinforcement under cyclic loading was modeled using a modified two-surface plasticity model [122] which includes the Bauschinger effect essential to capture the hysteretic response in beams under cyclic loading [85, 114] as discussed in Section 4.3.3. The tensile stress-strain curve parameters such as modulus of elasticity (E), yield stress (f_y), ultimate stress (f_u), and ultimate strain (ε_u) of the longitudinal reinforcement were based on representative uniaxial tensile tests of steel reinforcement conducted by Bandelt and Billington [53] as shown in Figure 4.2 (c) and are listed in Table 4.2. The constitutive behavior of the transverse reinforcement was modeled using the Von Mises plasticity model without strain hardening [112], and the tensile stress-strain curve parameters such as modulus of elasticity (E) and yield stress (f_y) were taken from experimental data of Bandelt and Billington [53] and are tabulated in Table 4.2.

4.3.2.3 Bond-Slip Model. The modeling of a bond-slip mechanism can improve the simulated component level response in terms of strength, stiffness, deformation capacity and damage pattern in reinforced HPFRCC members [75]. The longitudinal reinforcing elements were connected to the HPFRCC elements through a six-noded line interface element. A three-point Newton-Cotes integration scheme was used

Table 4.2 Bond-slip, HPFRCC, and Steel Material Properties

Property	Notation	Unit	UHPC	ECC	HyFRC	Longitudinal Steel	Transverse Steel
Maximum bond strength	u_{max}	[MPa]	10.4	8.20	7.60	-	-
Slip at onset of softening	s_{max}	[mm]	1.0 (0.6)	1.0 (0.6)	1.0 (0.6)	-	-
Bond-slip softening stiffness	k	[MPa/mm]	1.0 (5.0)	1.0 (5.0)	1.0 (5.0)	-	-
Residual friction bond strength	u_f	[MPa]	3.8 (2.2)	3.0 (1.8)	2.8 (1.6)	-	-
Tensile strength	f_t	[MPa]	8.0	2.9	1.8	-	-
Strain at crack initiation	ε_{t0}	[%]	0.0191	0.0169	0.0104	-	-
Strain at onset of softening	ε_{tp}	[%]	0.20	0.75	0.30	-	-
Tensile fracture energy	G_f	[MPa-mm]	19 (9.5)	6.1 (3.1)	5.3 (2.7)	-	-
Compressive strength	$f_c^{'}$	[MPa]	120	55	45	-	-
Compressive fracture energy	G_c	[MPa-mm]	180	53	61	-	-
Young's modulus of elasticity	E	[GPa]	42	17	17	200	205
Poisson's ratio	ν	[mm/mm]	0.18	0.15	0.15	0.30	0.30
Shear retention factor	β_s	[%]	1.0	1.0	1.0	-	-
Yield strength	f_y	[MPa]	-	-	-	455	690
Ultimate strength	f_u	[MPa]	-	-	-	675	-
Strain at ultimate strength	ε_u	[%]	-	-	-	16	-

Note: The values inside parenthesis are only used for simulation under cyclic loading.
All the other values are same for simulations under either monotonic or cyclic loading.

for the line interface element. The bond-slip model (Figure 4.2 (d)) proposed by Bandelt and Billington [75] was used to simulate the interaction between longitudinal reinforcement and HPFRCC. The bond-slip constitutive relationship was developed based on extensive bond-slip experimental testing under monotonic and cyclic loading for ECC material [46, 47], and was extended for other classes of HPFRCC material (e.g., UHPC and HyFRC) by changing parameters such as maximum bond strength (u_{max}), slip at onset of softening (s_{max}), bond-slip softening stiffness (k), and residual friction bond strength (u_f). These parameters were obtained from bond-slip test data of Dagenais and Massicotte [123] for UHPC, and similarly for ECC and HyFRC these parameters were obtained from the test data of Bandelt and Billington [53].

4.3.2.4 Analysis Parameters. A nonlinear static analysis with an incremental displacement-based loading was used for the simulation. The details about monotonic and cyclic loading have already been discussed in Section 4.3.1.5. There were two types of failure observed in this study: (a) fracture of longitudinal reinforcement, and (b) crushing of HPFRCC material. Fracture was assumed to occur when the strain over a 30 mm gage length of the longitudinal reinforcement exceeded an 18% assumed fracture strain based on the approach outlined in Bandelt and Billington [75]. Crushing of compression zone was assumed to occur when the compressive strain in a single HPFRCC element reached the ultimate compressive strain (ε_{cu}) based on compression model shown in Figure 4.2 (b). A regular Newton-Raphson scheme was used for equilibrium criteria and a line search algorithm was used for numerical convergence. Convergence was assumed to have occurred at each iteration if either energy, displacement, or force norm did not exceed limiting values of 0.01%, 0.1% and 1%, respectively.

4.3.3 Finite Element Model Verification

Using the finite element modeling technique described in Section 4.3.2, two reinforced HPFRCC beams were simulated under monotonic loading (M-1.3 and ECC-M-1.3) and two were simulated under reversed cyclic loading (C-1.3 and ECC-0.95-F). While detail description of the specimens can be found in the literature [53, 63, 91], some important material and geometric properties of the specimens are summarized in Table 4.3. Specimens M-1.3 and C-1.3 were simply supported test specimens, whereas ECC-M-1.3 and ECC-0.95-F were tested under cantilever test setup. It can be observed from Figure 4.3 that the initial stiffness, load carrying capacity, and drift capacity at two damage levels (i.e., yield and collapse) are captured reasonably well through the numerical simulation for all the cases. However, there is over prediction of load at reinforcement fracture in specimen ECC-M-1.3 because the necking region

Table 4.3 Material and Geometrical Properties of Validation Specimens

Notation	Loading	Test	L_s	Cross Section			HPFRCC		Longitudinal Reinforcement ($\rho = \rho^{'}$)			
	Type	Setup	[mm]	b[mm]	d[mm]	h[mm]	f_t[MPa]	$f_c^{'}$[MPa]	f_y[MPa]	d_b[mm]	n	A_s[mm^2]
M-1.3 [53]	Monotonic	SSB	690	130	160	180	2.2	46	455	13	2	258
ECC-M-1.3 [91]	Monotonic	CLB	760	130	160	180	4.0	45	455	13	2	258
C-1.3 [53]	Cyclic	SSB	690	130	160	180	2.2	46	455	13	2	258
ECC-0.95-F [63]	Cyclic	CLB	810	170	170	200	4.0	45	455	13	2	258

SSB = Simply supported beam and CLB = Cantilever beam

of steel reinforcement was not modeled in the numerical simulation due to numerical convergence issues [61, 63, 75]. The failure mode in all of the numerically simulated members was due to the fracture of the longitudinal reinforcement which is in agreement with the experimental observations (Figure 4.4). Under monotonic loading, fracture was observed at one major flexural crack location in the physical specimen M-1.3 (Figure 4.4 (a)), whereas fracture was simulated at two major flexural cracks in finite element model (Figure 4.4 (b)) because of the nearly symmetrical damage localization on either side of mid-span in the numerical simulation.

Since the plastic hinge region is associated with a high level of inelastic damage and cracking, it is important to closely simulate the damage pattern. Figure 4.4 shows the comparison of damage pattern observed in test specimens and the principal tensile strain contours obtained through numerical simulation, just before failure. Principal tensile strain contours, indicative of damage and cracking in the beams, are associated with varying levels of strain as shown in Figure 4.2 (a). The contours are based on the stress-strain relationship of the HPFRCC in tension, and represents elastic behavior, pseudo-strain hardening, softening, and dominant crack formation. In the case of monotonically loaded test specimen M-1.3 (Figure 4.4 (a) and (b)), the primary crack patterns (i.e., major flexural cracks and flexure-shear cracks) are in good agreement with the numerical simulation crack patterns, indicating the capability of the finite element modeling technique to simulate damage patterns.

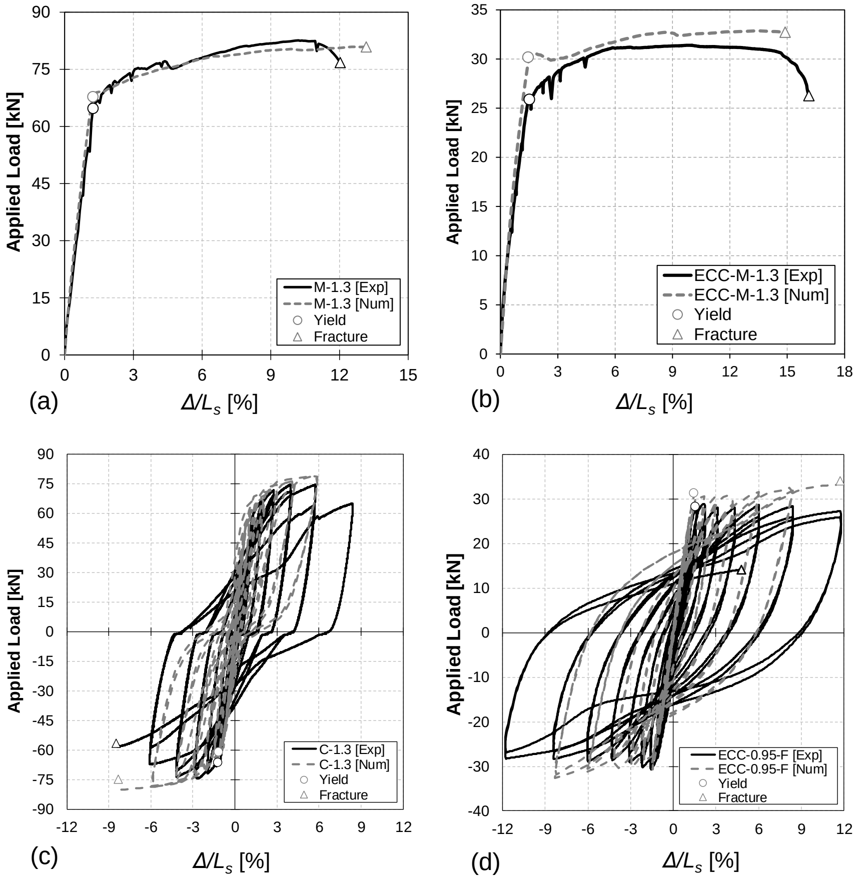

Figure 4.3 Experimental and simulated applied force vs drift response of (a) M-1.3 (b) ECC-M-1.3 (c) C-1.3 and (d) ECC-0.95-F.
Source: [53, 63, 91].

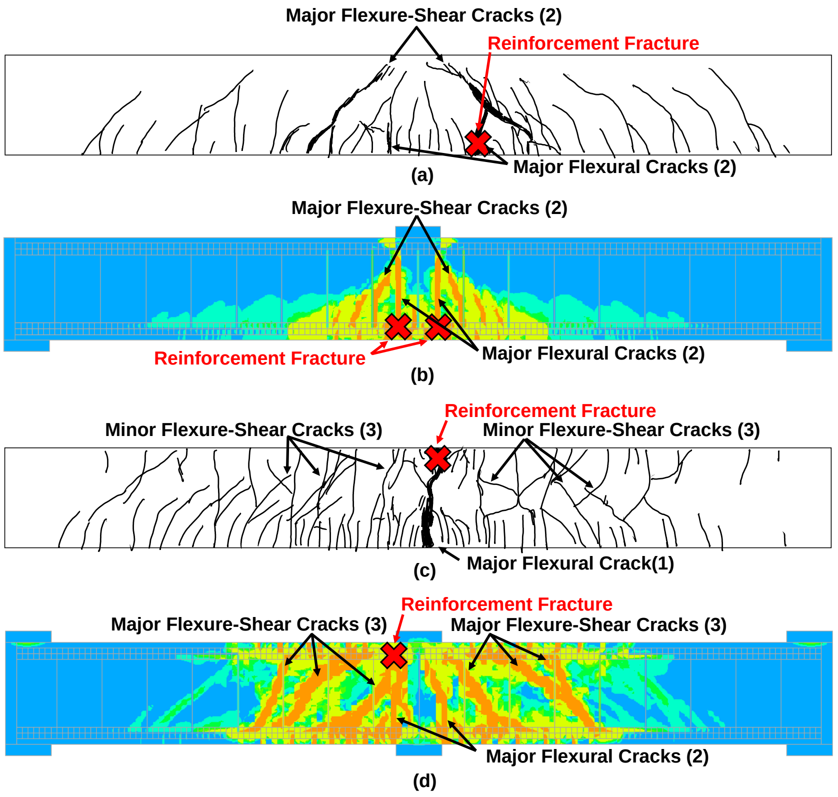

Figure 4.4 (a) Experimental damage pattern in M-1.3 [53] (b) simulated principal tensile strain contours in M-1.3 (c) experimental damage pattern in C-1.3 [53] and (d) simulated principal tensile strain contours in C-1.3 before the failure.

Under reversed cyclic loading, it can be seen that the amount of damage increased in both test specimen and simulation compared to the monotonically loaded specimen. There was a single major flexural crack in the test specimen C-1.3 (Figure 4.4 (c)), whereas there were two major flexural crack in the simulated crack pattern (Figure 4.4 (d)) because of the nearly symmetrical response on either side of the mid-span in the numerical simulation. However, reinforcement fracture was only simulated at one side of the beam because of the increased effect of the asymmetric boundary condition on the accumulation of reinforcement strain under large cyclic drifts. The flexure-shear crack widths were over predicted in Figure 4.4 (d) and is one of the limitations of this numerical simulation technique; however, the location and type of cracks (flexure-shear) and reinforcement rupture location were closely simulated under reversed cyclic loading.

4.4 Plastic Hinge Region in Reinforced HPFRCC

The plastic hinge region in ordinary reinforced concrete structural element consists of the reinforcement yielding zone, concrete crushing zone, and curvature localization zone [102]; however, in reinforced HPFRCC structural member, the plastic hinge region comprises of reinforcement yielding zone, tensile strain concentration zone, and curvature localization zone. HPFRCC compression crushing was observed in two finite element models out of seventy-two finite element simulations carried out in this study, which is significantly less than what would be expected in reinforced concrete members. The failure of seventy simulated HPFRCC specimens occurred due to fracture of the tensile reinforcement due to concentration of inelastic strain at dominant cracks in HPFRCC members as explained experimentally in the tension stiffening experiments conducted by Moreno et al. [50]. Additionally, under monotonic or cyclic flexural loading, several experimental studies have shown that the failure of reinforced HPFRCC beams occurs due to fracture of longitudinal reinforcement rather than crushing of compression zone material, unlike ordinary reinforced concrete [23, 27, 53, 63, 104]. The details of reinforcement yielding zone and tensile strain concentration zone are discussed in Section 4.4.1 and discussion regarding curvature localization zone is provided in Section 4.4.2.

4.4.1 Strain Distribution

Tensile strain in the longitudinal reinforcement was extracted at collapse level drifts to understand how reinforcement strain varied along the shear-span of the structural member. The collapse level drift is the drift level at which the strain in the longitudinal reinforcement exceeded the assumed fracture strain of 18% as previously discussed for finite element verification purposes in Section 4.3.3. Figure 4.5 shows a plot of reinforcement tensile strain in UHPC, ECC, and HyFRC under monotonic and cyclic loading along the length of the members. The tensile strain plot for both simply supported beams (Figure 4.5 (a) & (b)) and cantilever beams (Figure 4.5 (c) & (d)) have been shown for representative simulations with a shear-span (L_s) equal to 650 mm and reinforcement ratio (ρ) equal to 1.25%.

The length of the tensile longitudinal reinforcement over which the strain exceeded the yield strain of steel is defined here as the reinforcement yielding zone (L_y). It can be observed from the numerical simulation results , that regardless of the loading type, L_y increased with a decrease in tensile strength and matrix toughness (i.e., $(L_y)_{HyFRC} > (L_y)_{ECC} > (L_y)_{UHPC}$) at the collapse level for both types of boundary conditions. Comparisons between the length of reinforcement yielding under monotonic and cyclic loading for the same setup and HPFRCC material shows that L_y is longer under cyclic loading than monotonic loading in eight out of twelve simulation results. The experimental study carried out by Bandelt and Billington [53] also showed similar results (i.e., large number of distributed cracks and longer length of damage) under cyclic loading compared to monotonic loading for identical simply supported beam specimens.

Reinforcement tensile strain plots at various drift levels revealed that the strain increment was higher along reinforcement hardening length ($\varepsilon_s > \varepsilon_{sh}$) compared to the other regions. The length of this hardening region is defined herein as tensile strain concentration zone (L_{sc}). Plots of reinforcement strain (Figure 4.5 (a) & (b)) shows that the tensile strain concentration length, L_{sc}, is shorter under cyclic loading compared to monotonically loaded simply-supported beam specimens. Investigation of principal tensile strain contour revealed that the number of dominant cracks were lower under cyclic loading such that damage localized more rapidly, and reinforcement strain increased exponentially within a short length in cyclically loaded simply supported beams. In the case of cantilever beams (Figure 4.5 (c) & (d)), analysis shows that the region of tensile strain concentration was found to be marginally higher for monotonically loaded specimens compare to those cyclically loaded. The reason for a longer L_{sc} under monotonic loading in the cantilever beam setup was due to a higher number of dominant cracks as compared to specimens loaded cyclically.

4.4.2 Curvature Distribution

The curvature of a cross-section was calculated using Equation (4.3). This equation is based on the assumption that the plane section perpendicular to the axis of bending will remain perpendicular after the flexural bending.

$$\phi = \frac{\varepsilon_s}{d - c} \tag{4.3}$$

where, ε_s is the strain in tensile longitudinal reinforcement, d is the distance from tensile longitudinal reinforcement to the extreme compression fiber, and c is the

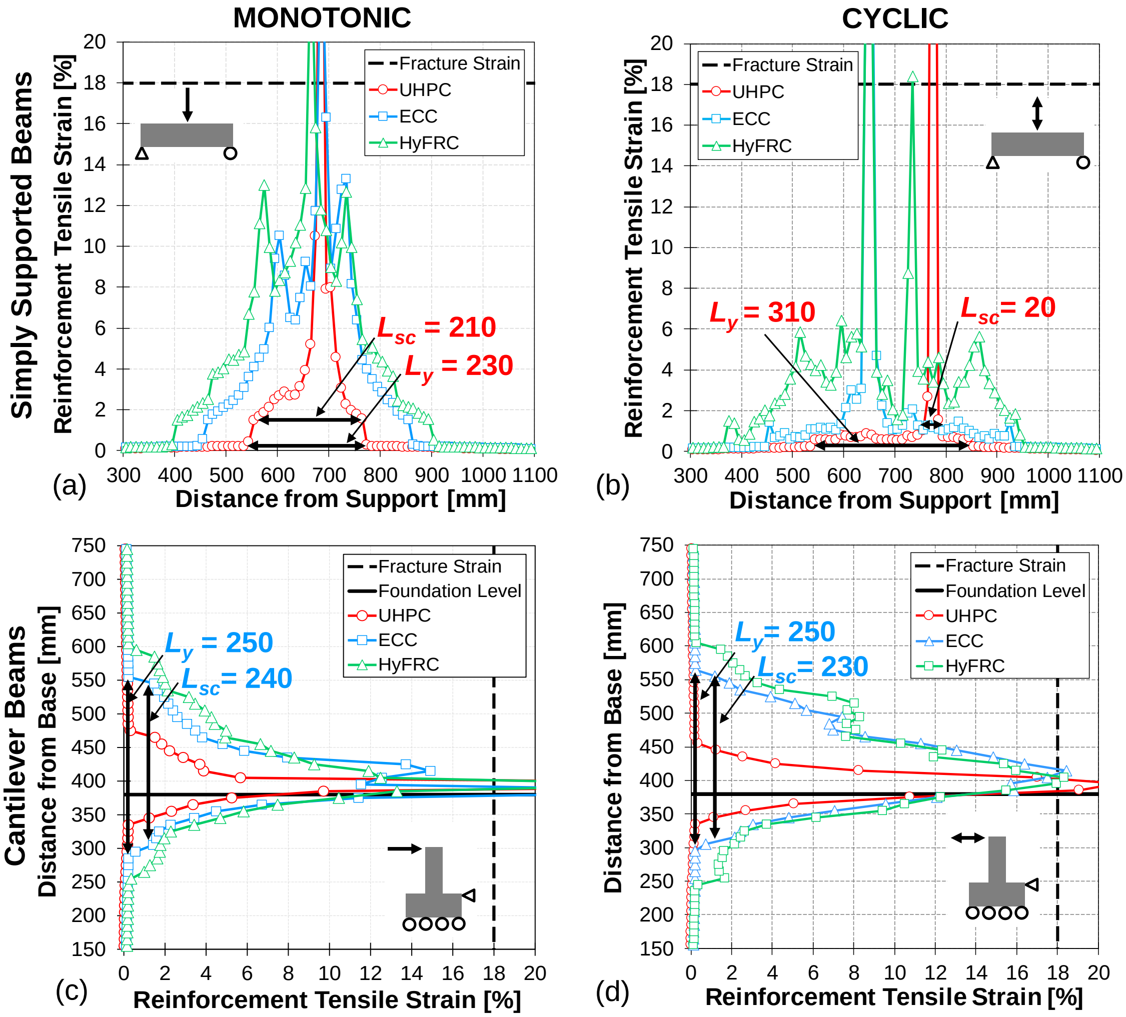

Figure 4.5 Longitudinal reinforcement strain vs. distance from support in simply supported beams under (a) monotonic and (b) cyclic loading; distance from base vs. longitudinal reinforcement strain in cantilever under (c) monotonic and (d) cyclic loading for simulations with $L_s = 650$ mm & $\rho = 1.25\%$ at collapse level.

distance from neutral axis to the extreme compression fiber. Figure 4.6 shows plots of curvature distribution in UHPC, ECC, and HyFRC under monotonic and cyclic loading just prior to collapse (i.e., reinforcement fracture). The curvature distribution plot for both simply supported beams (Figure 4.6 (a) & (b)) and cantilever beams (Figure 4.6 (c) & (d)) have been shown for representative simulations with shear-span (L_s) equal to 650 mm and reinforcement ratios (ρ) equal to 1.25%. After yielding of the tensile reinforcement, section curvatures along a small region near the dominant crack section increases exponentially compared to other regions of the shear-span. This region of sharp curvature increase contributes more towards plastic deflection of the member and is referred to as curvature localization zone (L_{cl}). The curvature localization phenomenon has been observed experimentally in reinforced HPFRCC beams [18]. For the purposes of the discussion in this study, curvature localization length, L_{cl}, is defined as the length over which a curvature value of $2.5\times10^{-4}\text{mm}^{-1}$ was exceeded as shown in Figure 4.6. The curvature localization phenomenon was found to be most pronounced in UHPC, followed by ECC, and finally HyFRC under both types of loading and boundary conditions. This is due to relatively shorter length of strain concentration zone, L_{sc}, in UHPC followed by a longer L_{sc} in ECC and the longest L_{sc} in HyFRC as discussed in Section 4.4.1.

Figure 4.6 (a) & (b) show that the curvature distribution in two sets of simply supported beams (UHPC and ECC) are highly localized under cyclic loading than under monotonic loading (i.e., $L_{cl,cyclic} < L_{cl,monotonic}$). However, all sets of cantilever beams (Figure 4.6 (c) & (d)) subjected to cyclic loading, exhibit a more uniform curvature distribution compared to the monotonically loaded beams (i.e., $L_{cl,cyclic} > L_{cl,monotonic}$). The difference between curvature localization in the two boundary conditions is due to the transfer of post-yield strain into the foundation through bond-slip mechanism between longitudinal reinforcement and HPFRCC matrix. This phenomenon results into a more uniform plastic curvature distribution aided by foundation softening due to large cyclic load reversal, which allows the damage to propagate inside the foundation region of the cantilever beam. This causes the formation of longer curvature localization zone in cantilever beams under cyclic loading compared to the monotonic loading. Yuan and Wu [103] conducted an extensive study to investigate the effect of different loading scenarios on the plastic hinge length of reinforced concrete flexural member with foundations and found that the length of curvature localization zone was longer in members under cyclic loading compared to the monotonic loading scenario due the effect of reversed load cycling.

4.5 Equivalent Plastic Hinge Length (L_p)

The ultimate displacement, rotation, or ductility capacity of a reinforced HPFRCC structural member can be calculated using linear strain distribution assumptions (i.e., pure flexural behavior) and the concept of equivalent plastic hinge length. This mathematical approach has been extensively used for the analysis of conventional reinforced concrete member [56]. For example, if the equivalent plastic hinge length (L_p) is known, the total (or ultimate) rotation capacity of a reinforced concrete or HPFRCC structural element can be calculated using Equation (4.4).

$$\theta_u = \theta_y + \theta_p = \frac{1}{2}\phi_y L_s + (\phi_u - \phi_y)L_p \tag{4.4}$$

In Equation (4.4), ϕ_y and ϕ_u are the curvatures at the critical section of the structural member at yield and collapse. The equivalent plastic hinge length, L_p, is defined as the fictitious length near the critical section of a structural member over which the plastic curvature is assumed to be constant, such that the integrated area under the actual plastic curvature is equal to the area under the idealized plastic curvature [56]. This mathematical approach of concentrating the inelasticity in a small region is analogous to a mechanical hinge, and therefore, widely used in

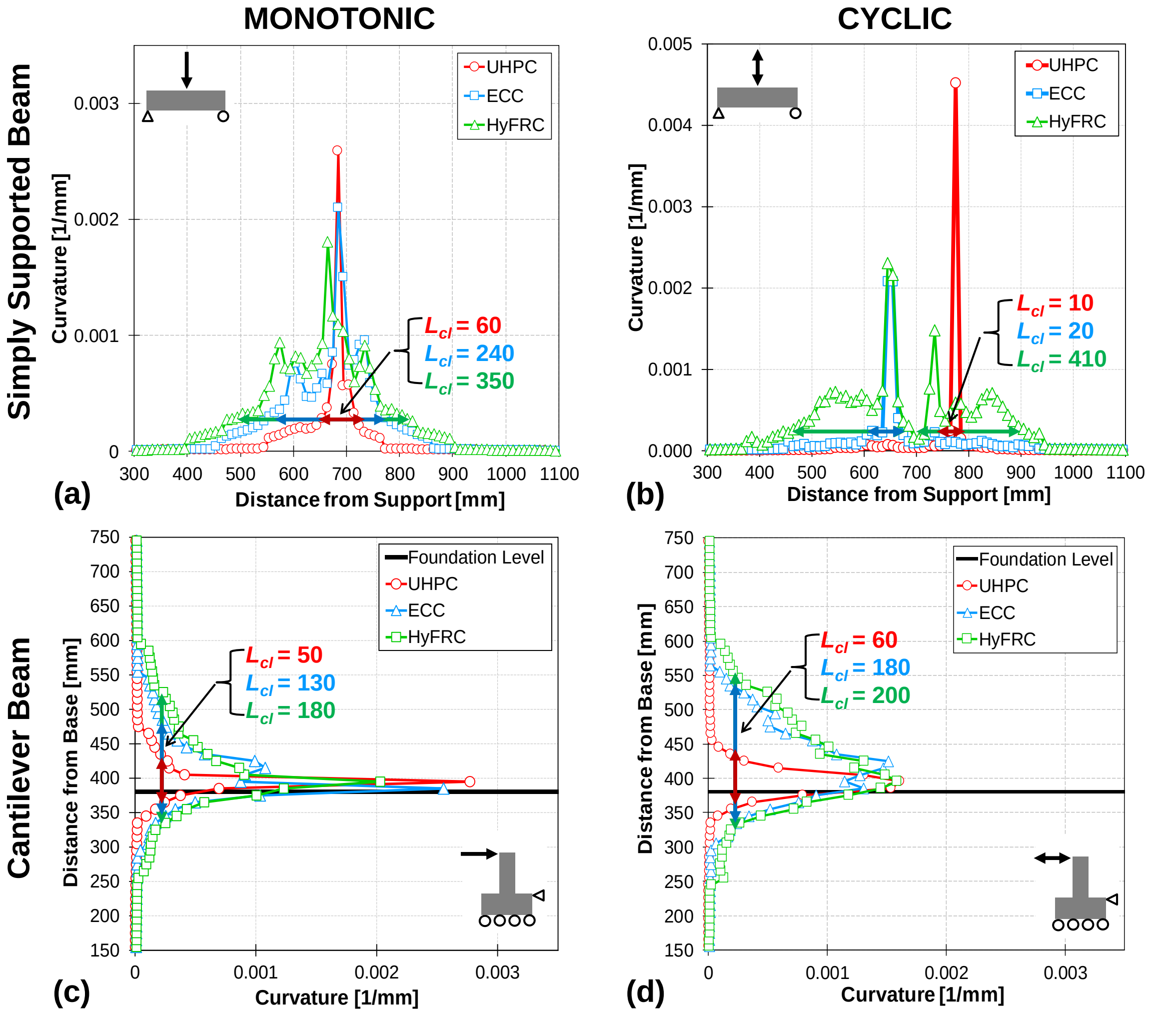

Figure 4.6 Curvature vs. distance from support in simply supported beams under (a) monotonic and (b) cyclic loading; curvature vs. distance from base in cantilever under (c) monotonic and (d) cyclic loading for simulations with L_s = 650 mm & $\rho = 1.25\%$ at collapse level.

industry for lumped plasticity based modeling of structural components in buildings and bridges [98, 99]. Further, the equivalent plastic hinge length lumps the effects of tension shift due to shear cracking, bond-slip phenomenon and tension-stiffening in the plastic hinge region implicitly and is the conventional way of calculating displacement parameters at collapse level through hand calculations [56, 101].

4.5.1 Theoretical Formulation

Equivalent plastic hinge length was computed by numerical integration and structural mechanics. The theoretical formulation can be understood using a cantilever beam with shear-span, L_s, subjected to a lateral load, P, as shown in Figure 4.7 (a). The collapse level curvature distribution of the cantilever would be highly non-linear (Figure 4.7 (b)) with a significant portion of longitudinal reinforcement near the section of maximum moment exceeding the yield stress. This curvature distribution at collapse can be idealized and divided into two regions: elastic curvature and plastic curvature (Figure 4.7 (c)). Thus, the total rotation capacity of the cantilever can be calculated as the sum of the yield rotation, θ_y, and plastic rotation, θ_p, as shown in Figure 4.7(d). Using numerical simulation, the yield rotation can be calculated by integrating the curvature distribution, at the yielding of the reinforcement, along the shear-span and length of the reinforcement embedded inside the foundation (area below the elastic curvature in Figure 4.7 (b)). The plastic rotation can be calculated by integrating the plastic curvature ($\phi_p(z) = \phi_u(z) - \phi_y(z)$) along the reinforcement yielding zone using Equation (4.5) (shaded region in Figure 4.7 (b)).

$$\theta_p = \int_0^{L_y} [\phi_u(z) - \phi_y(z)]dz \tag{4.5}$$

where $\phi_u(z)$ and $\phi_y(z)$ are the section curvatures of the beam at the collapse and yield levels. Using the equal area principle, equivalent plastic hinge length can be calculated

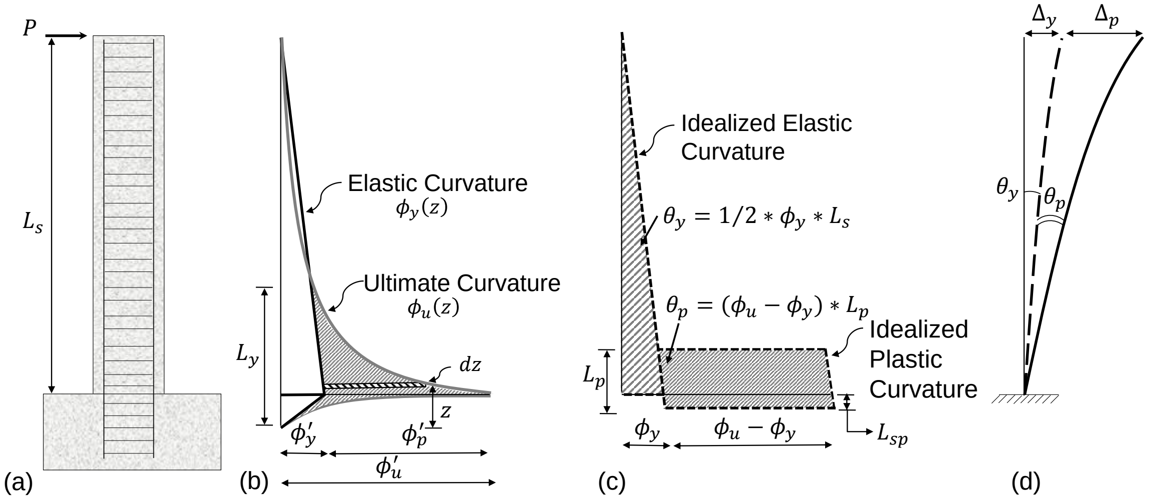

Figure 4.7 Theoretical basis of equivalent plastic hinge length (a) cantilever beam with lateral load (b) actual curvature distribution (c) idealized elastic and plastic curvature (d) yield and plastic rotation or deflection.

by dividing the plastic rotation (obtained from Equation (4.5) by a constant plastic curvature (i.e., $\phi_p = \phi_u - \phi_y$) as shown in Equation (4.6).

$$L_p = \frac{\theta_p}{(\phi_u - \phi_y)} \tag{4.6}$$

where ϕ_u and ϕ_y are the curvatures at the critical section of the beams at collapse level and yield level, which were calculated using Equation (4.7) and (4.8) based on the *plane section hypothesis, uniaxial stress-strain relationship, equilibrium of forces, and strain compatibility* as described in Section 4.6.1 and 4.6.2.

$$\phi_u = \frac{\varepsilon_{su}}{d - c_u} \tag{4.7}$$

$$\phi_y = \frac{\varepsilon_{sy}}{d - c_y} \tag{4.8}$$

In Equations (4.7) and (4.8), ε_{sy} is the yield strain in tensile longitudinal reinforcement, ε_{su} is the ultimate strain in tensile longitudinal reinforcement, d is the distance from tensile longitudinal reinforcement to the extreme compression fiber, c_u and c_y are the distances from neutral axis to the extreme compression fiber at collapse level and yield level, respectively. Unlike ordinary concrete which is analyzed based on crushing of the cementitious material, the collapse level curvature, ε_{su}, of HPFRCC members are calculated based on reinforcement fracture strains as this is the common failure mechanism.

4.5.2 Expression for L_p in Reinforced HPFRCC

An new expression was developed based on the 72 numerical simulations. The developed expression proposed in this study is based on existing expressions (Table 4.1) for reinforced concrete and reinforced HPFRCC, and a previous study carried out by Pokhrel and Bandelt [65, 109] to identify variables controlling deformation capacity of reinforced HPFRCC flexural members at collapse. The new equivalent plastic hinge length, L_p (mm), expression combines four predictor variables: shear-span (L_s) in, tensile longitudinal reinforcement ratio (ρ), tensile strength of HPFRCC material (f_t), and yield stress of reinforcement (f_y) as given in Equation (4.9).

$$L_p = \alpha L_s + \beta \frac{\rho f_y}{f_t} \tag{4.9}$$

where α and β are the model coefficients determined through regression. The first term in the expression shows the dependence of plastic hinge length on moment gradient with changing shear-span. The second term shows the dependence of plastic hinge length on (1) tensile strain penetration inside the foundation or joint (L_{sp} shown in Figure 4.7 (c)), and (2) strain concentration and curvature localization within a shear-span due to change in tensile strength of the HPFRCC material and reinforcement ratio. It can be observed from the new plastic hinge length expression that among all the variables associated with the mechanical property of HPFRCCs, tensile strength (f_t) is the primary variable governing the equivalent plastic hinge length in reinforced HPFRCC members and other factors such as tensile strain at onset of softening (ε_{tp}) do not primarily impact the equivalent plastic hinge length.

The model coefficients α and β in Equation (4.9) were obtained by minimizing the sum of the squares of residuals using regression analysis for four scenarios, considering variation in boundary conditions and loading scheme. Two main sets of equations were developed to account for load variation; one set under monotonic loading scenario and another set under cyclic loading scenario. Equation (4.10) was formulated using numerical results for one-half of the simply supported beams ($L_{p,center}$) and the full length of cantilever beams ($L_{p,joint}$) under monotonic loading. Equation (4.11) was similarly developed under cyclic loading. The numerical simulation results of simply supported models were used to formulate center hinge equations and the simulation results of cantilever models were used to formulate joint hinge equations, which incorporate post-yield strain penetration inside the joint.

$$\text{Monotonic Loading} \begin{cases} L_{p,center} = 0.02L_s + 0.24\frac{\rho f_y}{f_t} \\ L_{p,joint} = 0.03L_s + 0.27\frac{\rho f_y}{f_t} \end{cases} \tag{4.10}$$

$$\text{Cyclic Loading} \begin{cases} L_{p,center} = 0.01L_s + 0.11\frac{\rho f_y}{f_t} \\ L_{p,joint} = 0.03L_s + 0.39\frac{\rho f_y}{f_t} \end{cases} \tag{4.11}$$

4.5.3 Comparison with Existing L_p

Figure 4.8 shows the comparison of numerically simulated plastic hinge length values with the values obtained through the different equations. It can be seen that statistical parameters such as the mean ratio (μ_{RATIO}) of derived expression-to-numerically simulated L_p value is greater than 1.44 (i.e., most of the values lie above and/or left of the mean line) Figure 4.8 (a-h). This implies that the existing L_p expressions overestimate the equivalent plastic hinge length, which can result in over-prediction of plastic rotation capacity in reinforced HPFRCC structural members as demonstrated in Section 4.6.3 when the proposed expression is validated against a large database of experiments. Further, there is large dispersion in the L_p values predicted by the existing empirical models as indicated by the coefficient of variation values ($47\% \leq CoV \leq 69\%$). The over-prediction and scatter can be attributed to the following: (1) six of the empirical equations (Figure 4.8 (a-f)) were developed using reinforced concrete experimental data rather than reinforced HPFRCC specimens; (2) most of the expressions were developed considering only one type of loading scheme (e.g., Figure 4.8 (a-d) & (g) were developed using monotonically loaded specimens); (3) L_p expression for reinforced HPFRCC members developed by Naaman et al. [18] was based on reinforcement yielding zone which is larger than equivalent plastic hinge length and cannot be used for computation of displacement parameters at collapse level; and (4) L_p expression for reinforced HPFRCC members proposed by Tariq et al. [61] was based on a limited database of six reinforced ECC specimens without variation in HPFRCC type, boundary condition and loading scheme. The new equation developed in this study predicts equivalent plastic hinge length with high accuracy ($\mu_{RATIO} = 1.0$) and significantly less prediction scatter ($15\% \leq CoV \leq 29\%$) compared to the existing models under both type of loading as shown in Figure 4.8 (i). However, it should be noted that the proposed plastic hinge length expression is valid at the collapse level and that the plastic rotation capacity of structural element at intermediate damage states (e.g., between yield and collapse), if calculated using this equation, would provide an nonconservative estimate.

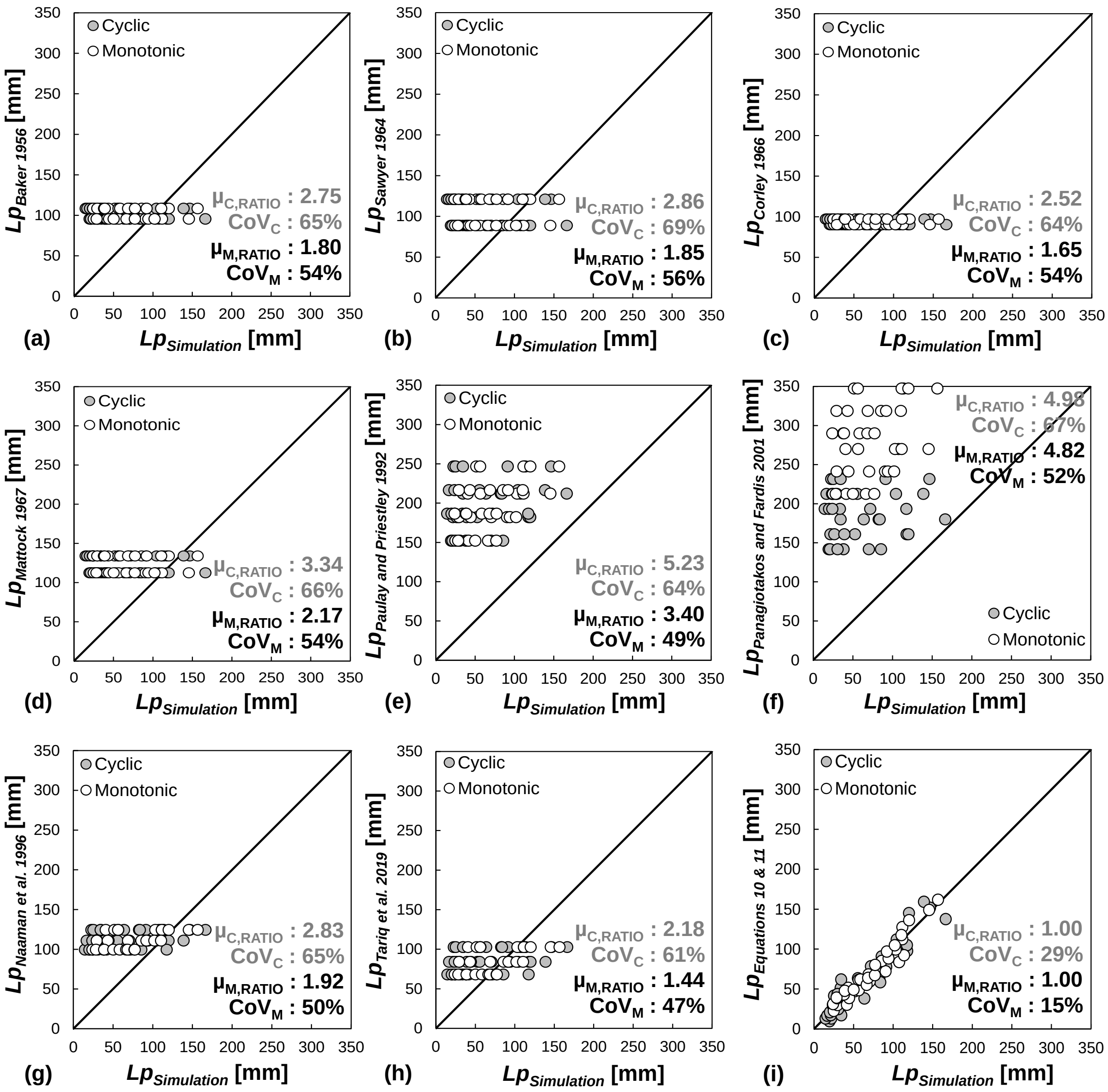

Figure 4.8 Comparison of simulated plastic hinge length with expressions from (a) Baker (b) Sawyer (c) Corley (d) Mattock (e) Paulay and Priestley (f) Panagiotakos and Fardis (g) Naaman et al. (h) Tariq et al. (i) current study (Equations (4.10) & (4.11)).
Source: [18, 54–56, 61, 95, 101, 118].

4.6 Section Analysis

4.6.1 Chord Rotation and Moment at Yield

The analytical model to calculate chord rotation and moment at yield using cross-section analysis is based on the extension of commonly used Euler-Bernoulli beam theory used in the analysis of reinforced concrete members. The assumptions of the analytical formulation are listed below:

1. The distribution of strain across the cross-section is assumed to be linear *(Euler-Bernoulli hypothesis)*.
2. The strain in the reinforcement and HPFRCC are assumed to be equal at the same layer *(perfect bond assumption)*.
3. The internal stresses are computed from the strain through the uniaxial stress-strain relationship for both steel and HPFRCC *(uniaxial material model)*.

The analytical model with the cross-section parameters required to calculate chord rotation and moment at yield is shown in Figure 4.9 (a-c). The internal stress distribution shown in Figure 4.9 (c) is based on principal stresses at the integration points across the critical section of the finite element models at yield level. The flowchart shown in Figure 4.10 (a) shows the procedure to calculate yield curvature and moment of the member using simplified mechanics. The cross-section and material properties are used as the input parameters for the analytical framework. The section is assumed to have reached its yield capacity when the strain in the tensile reinforcement reaches the yield strain. Using the assumptions stated earlier, cross-sectional forces are computed and the neutral axis depth is iterated until the section equilibrium condition is satisfied. It can be observed in Figure 4.9 (c), HPFRCC contributes significantly to the tensile component (i.e., $T_{to} + T_t$) of the section forces, which is ignored in the analysis of reinforced concrete. Once the neutral axis depth of the critical section is found, the section yield curvature can be determined using Equation (4.8). The yield rotation, θ_y (rad), of the member can be computed using one of the several elastic-beam deflection procedure such as moment-area method as defined in Equation (4.12).

$$\theta_y = \frac{1}{2}\phi_y L_s \tag{4.12}$$

The yield moment capacity, M_y ($\times 10^{-3}$ kNm), can be computed through moment equilibrium of the cross-section as shown in Equation (4.13).

$$M_y = (f_s^{'} - E_h\varepsilon_s^{'})A_s^{'}(d - d^{'}) + \frac{1}{2}f_c bc(d - \frac{c}{3}) - \frac{1}{2}f_t b d_{to}(d - c - \frac{2d_{to}}{3}) - f_t b(h - c - d_{to})(\frac{(h - c - d_{to})}{2} - c_e) \tag{4.13}$$

where $f_s^{'}$ (MPa) is the stress in compressive reinforcement, E_h (MPa) is modulus of elasticity of HPFRCC, $\varepsilon_s^{'}$ (mm/mm) is the strain in compressive reinforcement, $A_s^{'}$ (mm^2) is the area of compressive reinforcement, d (mm) is the effective depth of cross section, $d^{'}$ (mm) is the distance from top compressive fiber to center of compressive reinforcement, f_c (MPa) is the stress at top compressive fiber, b (mm) is the width of cross section, h (mm) is the height of cross section, c (mm) is the neutral axis depth, f_t (MPa) is the tensile strength of HPFRCC, d_{to} (mm) is the distance from neutral axis to the strain layer corresponding to ε_{to} (mm/mm), and c_e (mm) is the distance from bottom tensile fiber to center of tensile reinforcement.

To validate the proposed analytical formulation, alternate values of chord rotations were calculated using the numerical simulation results, where the strain data at integration points on the tension and compression sides were extracted to compute curvature values along the shear-span of the beams at yield. The chord rotation was calculated by numerically integrating curvature distribution along the length of the beam and in the case of cantilever setup, the contribution of pre-yield strain penetration was taken into account by integrating curvature inside the joint as stated in Equation (4.14).

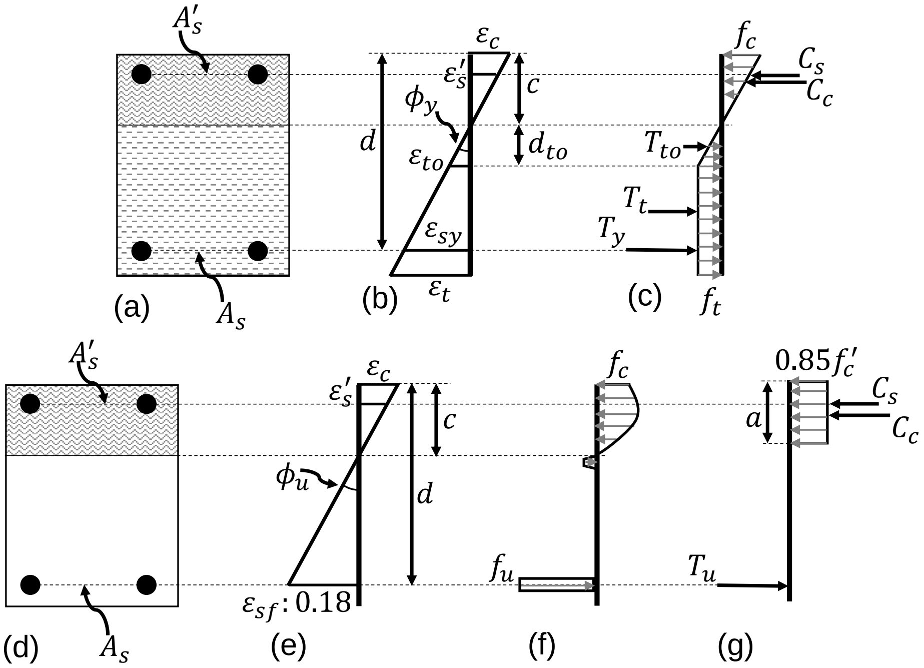

Figure 4.9 Analytical model at yield level (a) cross section (b) strain distribution (c) stress distribution with section forces; and at collapse level (d) cross section (e) strain distribution (f) stress distribution (g) equivalent Whitney's stress block and sectional forces.

$$\theta_y = \int_0^{L_s} [\phi_y(z)] dz \tag{4.14}$$

The yield moment was calculated from numerical simulation by extracting the load carrying capacity at yield and using principles of statics (i.e., $M_{y,CLB} = P_y L_s$ or $M_{y,SSB} = (P_y/2)L_s$). Figure 4.11 (a-b) shows the comparison of the yield rotation and moment computed using the analytical framework in comparison to the numerical simulation results. It can be observed that the mean ratio (μ_{RATIO}) of analytical-to-numerically simulated value of θ_y is equal to 0.85 under cyclic loading and 0.90 under monotonic loading (i.e., most of the values lie below or right of the mean line). This implies that the rotation values are marginally under-predicted using the proposed analytical model which can be attributed to pre-yield strain penetration which has not been incorporated into the analytical model, as L_s has been used to

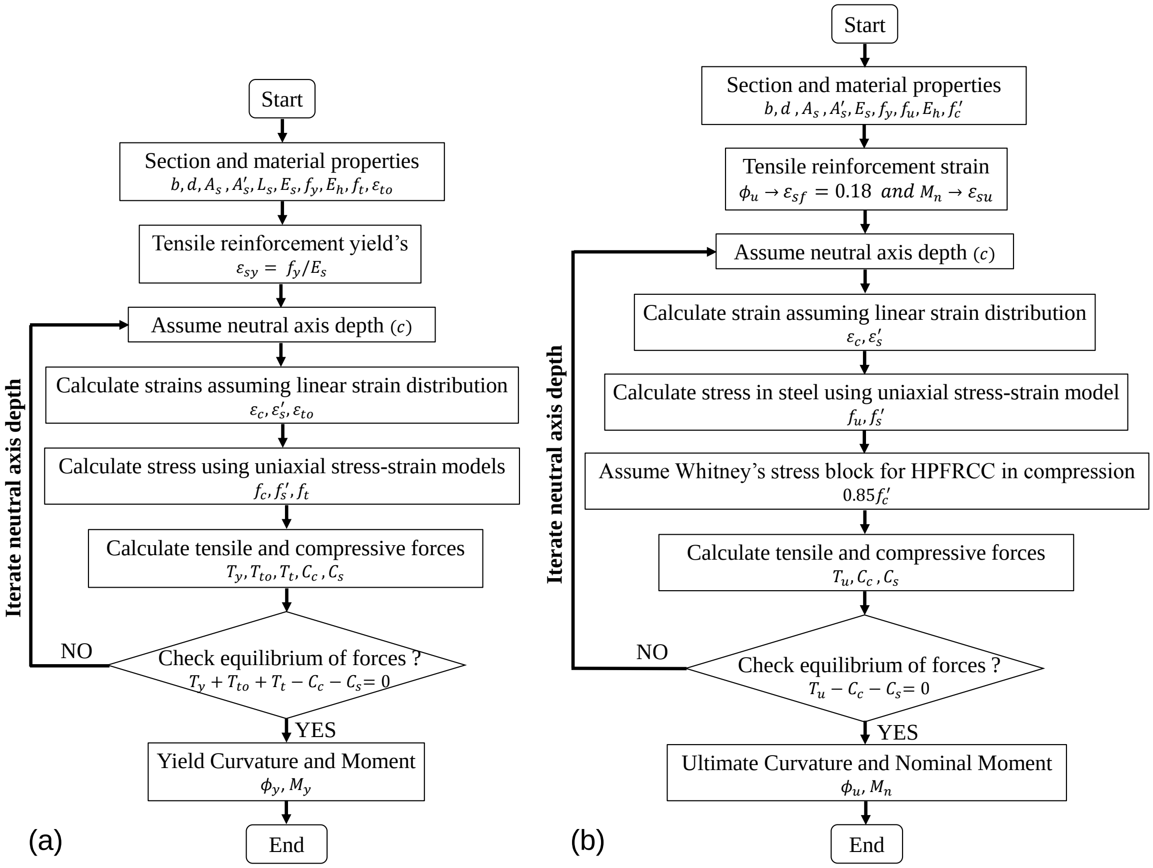

Figure 4.10 Flowchart to calculate sectional (a) yield curvature and yield moment (b) ultimate curvature and nominal moment.

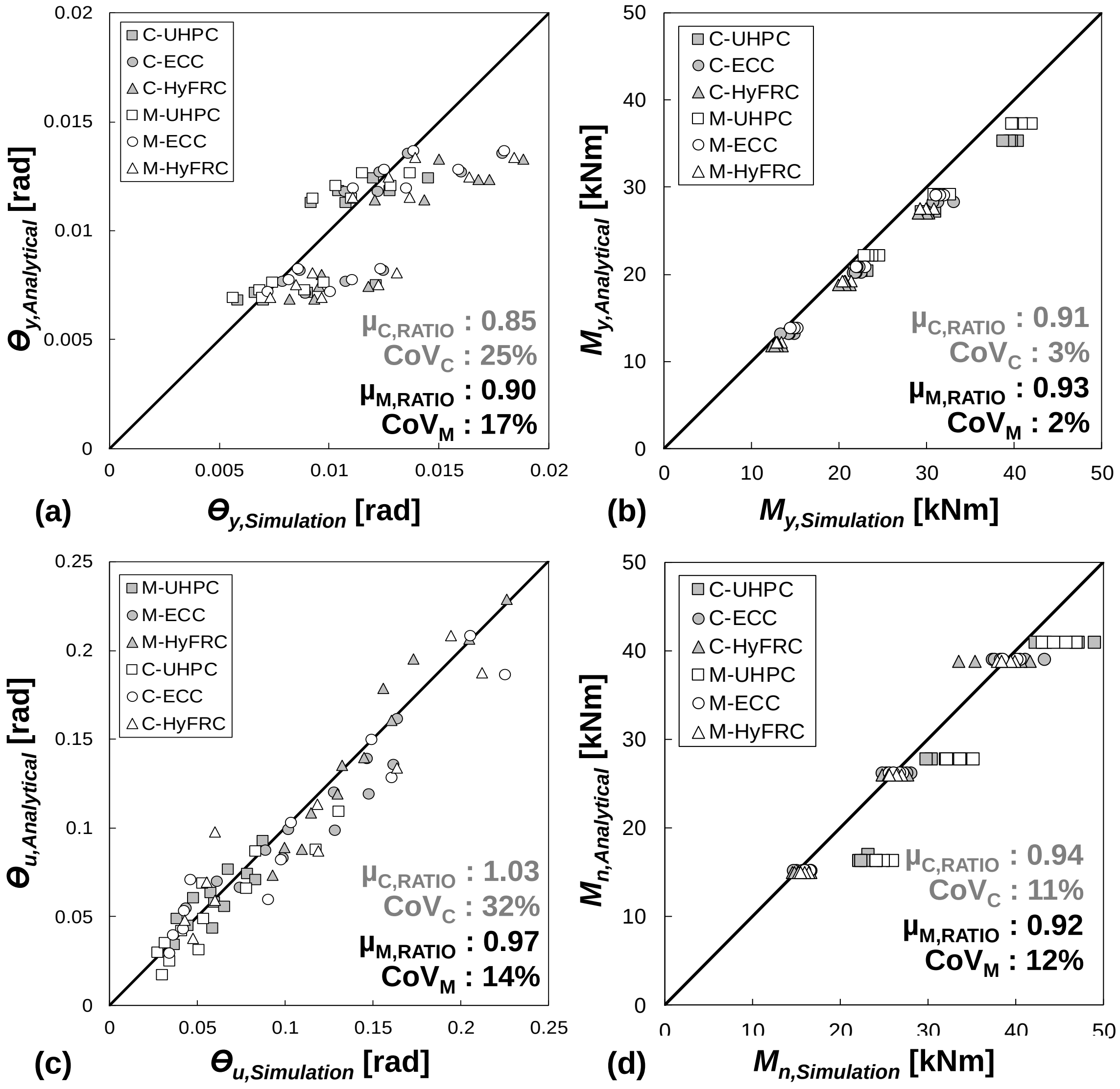

Figure 4.11 Comparison of analytical vs. simulated (a) yield rotation (b) yield moment (c) ultimate rotation and (d) nominal moment.

calculate the yield rotation without including the additional length inside the joint. This was done to generalize the analytical formulation based on shear-span length for any location of plastic hinge (i.e., center hinge or joint hinge connected). The yield moment was found to be well predicted using the analytical model with the mean ratio (μ_{RATIO}) of analytical-to-numerically simulated value of M_y equal to 0.91 under cyclic loading and 0.93 under monotonic loading, and with minimal prediction scatter ($CoV \leq 3\%$). The analytical model predicts yield rotation and moment with reasonable accuracy and can be useful to estimate the yield point of a moment-rotation curve (i.e., M_y, θ_y) through hand calculations for reinforced HPFRCC flexural members. It should be noted that the tensile strength of HPFRCC material is not assessed through a standard test procedure and subsequently its value can vary widely based on the type of test specimen or setup used [38, 79]. The plastic hinge length expression and analytical equation of yield moment requires the value of HPFRCC tensile strength as an input parameter, therefore a sensitivity analysis was carried out to evaluate the impact of such variation. It was found that a 10% change in tensile strength resulted in a 6% change in plastic hinge length, and a 2% change in yield moment.

4.6.2 Chord Rotation at Collapse and Nominal Moment

The chord rotation at the collapse level will be referred herein as the ultimate rotation (θ_u) and the maximum moment capacity of the reinforced HPFRCC beams will be referred to as nominal moment (M_n). To calculate ultimate rotation and nominal moment, a simplified mechanics-based approach was used with the same underlying assumptions as used in Section 4.6.1 (i.e., *plane section hypothesis, strain compatibility, and uniaxial material model*). The analytical model with the cross-section parameters required to calculate ultimate chord rotation is shown in Figure 4.9 (d-g). The analytical model to compute nominal moment is similar to

Figure 4.9 (d-g), except that the controlling strain criteria in the tensile steel is equal to ultimate strain ($\varepsilon_s = \varepsilon_{su}$). This criteria is based on the experimental study which suggest that at the peak load (corresponding to nominal moment), crack localization and inelastic strain concentration leads to fully hardened tensile reinforcement [53, 63]. The internal stress distribution shown in Figure 4.9 (f) is based on principal stresses at the integration points across the critical section of the finite element models. The sequential algorithm to calculate ultimate curvature at a critical section and nominal moment capacity of the member is shown in Figure 4.10 (b). The input parameters required for the framework includes cross-sectional and material properties. The cross-section is assumed to have reached the collapse level when the strain in tensile reinforcement reaches the fracture strain (ε_{sf}) of 18% and nominal level when the strain in tensile reinforcement reaches the ultimate strain (ε_{su}). The finite element simulation was able to predict experimental collapse at 18% fracture strain under both monotonic and cyclic loading in Section 4.3.3. Thus, a constant strain of 18% has been adopted in both finite element simulation and the analytical framework to calculate the ultimate chord rotation. The fixed strain criterion provides simplicity and consistency for hand calculation under different loading scheme, similar to the ultimate compressive failure strain of 0.003 used in reinforced concrete to calculate nominal flexural strength [33]. One of the significant differences of the sectional stress distribution in Figure 4.9 (f) with that of Figure 4.9 (c), is nearly zero contribution of HPFRCC in tensile component of section stresses in Figure 4.9 (f) due to the formation of localized flexural cracks at the critical section. The internal parabolic compressive stress block at the critical section shown in Figure 4.9 (f) is simplified using an equivalent Whitney's stress block, which is defined as a uniformly distributed compressive stress of $0.85f_c'$ applied along the depth "a" from extreme compression fiber as shown in Figure 4.9 (g). The equivalent Whitney's stress block has been previously used in computation of nominal flexural strength of steel fiber reinforced concrete [124, 125] with reasonable agreement to physical experimentation result. Using the three fundamental assumptions stated in Section 4.6.1, cross-section forces were computed and the neutral axis depth was iterated until the sectional equilibrium condition is satisfied. The nominal moment, M_n ($\times 10^{-3}$ kNm), can be computed using Equation (4.15) through the equilibrium of sectional moment.

$$M_n = (f_s^{'} - 0.85 f_c^{'}) A_s^{'} (d - d^{'}) + 0.85 f_c^{'} b a (d - \frac{a}{2}) \tag{4.15}$$

where $f_s^{'}$ (MPa) is the stress in compressive reinforcement, $A_s^{'}$ (mm^2) is the area of compressive reinforcement, d (mm) is the effective depth of cross section, $d^{'}$ (mm) is the distance from top compressive fiber to center of compressive reinforcement, $f_c^{'}$ (MPa) is the maximum compressive stress of HPFRCC material, b (mm) is the width of cross section, and $a = \beta_1 c$ (mm) is the height of the equivalent Whitney's stress block. The value of β_1 depends on the maximum compressive stress of HPFRCC used; with a minimum value of 0.65 (if $f_c^{'} \geq 56$ MPa), a maximum value of 0.85 (if $f_c^{'} \leq 28$ MPa) and linear variation between the two extreme values (if 28 MPa $< f_c^{'} < 56$ MPa) [33]. The equation to calculate nominal moment (M_n) is similar to that of doubly reinforced concrete, but there will be significant numerical difference in M_n due to the higher force associated with the hardened tensile reinforcement (T_u) which substantial increases the sectional moment arm. There are several versions of the analytical model (Figure 4.9) proposed by researchers to calculate nominal flexural strength (M_n) in reinforced steel fiber reinforced concrete (SFRC) [124, 125] and UHPC [126] with variations in internal stress distribution and failure criteria; however, in this study a common formulation of nominal flexural strength is being proposed for broad variants of HPFRCC with a wide range tensile and compressive properties.

Ultimate rotation capacity of a reinforced HPFRCC flexural member can be expressed as the sum of yield (θ_y) and plastic rotation (θ_p) as defined in Equation (4.4) [56]. The elastic rotation (θ_y) of the member can be computed using Equation (4.12) by following the procedure described in Section 4.6.1. After determining the neutral axis depth at the collapse drift, ultimate curvature (ϕ_u) of a critical section can be determined using Equation (4.7). Finally, using the new expression of equivalent plastic hinge length (i.e., Equation (4.10) & Equation (4.11)) and section curvatures (ϕ_y and ϕ_u) determined earlier, the plastic rotation was calculated by re-arranging Equation (4.6).

To verify the proposed analytical formulation, values of ultimate chord rotations were calculated based on the numerical simulation results. Strain data at integration points on tension and compression sides were extracted to compute curvature values along the shear-span of the beams at collapse level. The chord rotation was calculated by numerically integrating curvature distribution along the shear span of the beam (in the case of cantilever setup, the contribution of post-yield strain penetration was taken into account by integrating curvature inside the joint) at the collapse level, θ_u (rad), using Equation (4.16).

$$\theta_u = \int_0^{L_s} \phi_u(z)dz \tag{4.16}$$

The nominal moment was calculated from numerical simulation by extracting the maximum load carrying capacity and using the principle of statics (i.e., $M_{n,CLB} = P_n L_s$ or $M_{n,SSB} = (P_n/2)L_s$). Figure 4.11 (c-d) shows the comparison of the ultimate rotation and nominal moment computed using the analytical framework and the numerical simulation technique. It can be observed that the mean ratio (μ_{RATIO}) of the analytical-to-numerically simulated value of θ_u is equal to 1.03 under cyclic loading and 0.97 under monotonic loading, indicating a very accurate estimation of ultimate rotation. However, there is slightly higher scatter in the rotation values as indicated by the coefficient of variation values ($CoV_C = 32\%$ and $CoV_M = 14\%$). The nominal moment was found to be well predicted using analytical model with the mean ratio (μ_{RATIO}) of analytical-to-numerically simulated value of M_n equal to 0.94 under cyclic loading and 0.92 under monotonic loading with significantly less scatter as indicated by the low coefficient of variation ($CoV \leq 12\%$). This simplified mechanics-based analytical framework can be utilized to estimate maximum moment capacity and collapse level rotation capacity of reinforced HPFRCC flexural members through hand calculations.

4.6.3 Verification with Experimental Database

To validate the proposed analytical framework, a database of experimentally tested HPFRCC beams was compiled, whose failure mode was due to fracture of tensile longitudinal reinforcement. The database is composed of 37 cyclically tested HPFRCC beams and 13 monotonically tested HPFRCC beams, with cantilever and simply supported test setups. Due to nature of the evaluation process, experimental data was limited to reinforced ductile concrete specimens which reached their full displacement capacity and failed in flexure due to reinforcement fracture. Validation of the analytical framework was completed using 12 UHPC specimens, 33 ECC specimens and five High-Performance Fiber-Reinforced Concrete (HPFRC) specimens. HPFRC is another class of HPFRCC which generally contains 1.5% by volume fraction of steel fibers and coarse aggregates of maximum 1/2” size [26, 90]. The important material and cross-section properties required for the sectional analysis are listed in Table 4.4. The experimental yield moment (M_y), nominal moment (M_n) and ultimate drifts (Δ_u/L_s) of beams are presented in the last three columns of the table, which are used to verify the accuracy of the analytical framework.

To calculate flexural strength at yield, the section models and flowchart shown in Figure 4.9 (a-c) & 4.10 (a) were used along with Equation (4.13) as discussed in Section 4.6.1. Similarly, to compute nominal flexural strength, the section models and flowchart shown in Figure 4.9 (e-f) & 4.10 (b) were used along with Equation (4.15) as discussed in Section 4.6.2.

Figure 4.12 (a) shows the comparison of analytically calculated moment with the experimental moment at yield level. The statistical metrics ($\mu_{C,RATIO} = 0.89$ and $\mu_{M,RATIO} = 0.95$) show that the analytical method marginally under-predicts the yield moment values with small dispersion ($CoV \leq 10\%$) in the estimated values. The under-prediction of yield moment, even when considering the tensile stress component of HPFRCC, is hypothesized due to localized early strain hardening in the tensile reinforcement (at the critical section) of the reinforced HPFRCC test specimens, before the occurrence of global yielding at the component level [50]. The under-prediction will be more pronounced in sections with multiple layers of tensile reinforcement because the outermost layer of tensile steel yields early and starts to harden before yielding of the inner layer of tensile steel. Figure 4.12 (b) shows the comparison of analytically calculated nominal moment with the experimental values. The nominal moment was found to be well predicted using the analytical model with the mean ratio (μ_{RATIO}) of analytical-to-experimental value of M_n equal to 1.02 under cyclic loading and 1.05 under monotonic loading with less scatter as indicated by the low coefficient of variation ($CoV \leq 15\%$). The proposed analytical formulation was compared with the standard code-based approach (i.e., ACI Committee 318 [33]) to calculate the moment capacity at both damage levels (i.e., yield and nominal) and it was found to improve the prediction capability by more than 25%.

Figure 4.13 shows the comparison of analytically computed ultimate rotation capacity (e.g., $\theta_{u,Baker1956}$) with experimentally observed ultimate rotation ($\theta_{u,Experimental}$) of the reinforced HPFRCC database compiled in Table 4.4. The analytical framework described in Section 4.6.2 along with Equation (4.4) was used to calculate the ultimate rotation, using various existing expressions for equivalent plastic hinge length (e.g., $\theta_{u,Baker1956}$ was calculated using $L_{p,Baker}$) listed in Table 4.1. The experimental value of ultimate rotation ($\theta_{u,Experimental}$) was computed through the ultimate drifts (Δ_u/L_s) listed in the last column of Table 4.4. The mean ratio (μ_{RATIO}) of analytical-to-experimentally observed θ_u value is greater than 1.41 for monotonic specimens and 1.38 for cyclic specimens (Figure 4.13 (a-h)). This suggests that the use of the existing equations of L_p into the proposed analytical framework tend to overestimate the ultimate rotation capacity in reinforced HPFRCC flexural members. Further, there is significant scatter in the prediction as indicated by the coefficient of variation values (CoV) ranging from 31% to 51% under both types of loading scenario. The possible reasons of over-prediction and scatter can be attributed to the limitation of existing plastic hinge length expressions as described in Section 4.5.3.

The proposed analytical framework with the incorporation of new equivalent plastic hinge length expression exhibits better prediction capability ($\mu_{C,RATIO} = 0.96$ and $\mu_{M,RATIO} = 0.75$) and less scatter ($CoV_C = 22\%$ and $CoV_M = 29\%$) as indicated by the statistical measures under both types of loading scheme (Figure 4.13 (i)). The improvement in the estimation is due to the use of new L_p equation tailored for reinforced HPFRCC under different loading scenarios, boundary condition, shear span, tensile strength, reinforcement ratio and yield strength. The use of the L_p expression proposed by Tariq et al. [61] provides the least over-prediction under cyclic loading, among the existing equations, because it was developed based on cyclically loaded reinforced ECC test specimens whose failure occurred through fracture of tensile reinforcement, which is the dominant failure mechanism observed in reinforced HPFRCC members. Further, the current database contains 35 cantilever specimens out of a total 50 specimens, which is the same type of test setup used by Tariq et al.

[61] to formulate the L_p expression. The use of the new L_p expression proposed in this study can give marginally conservative ultimate rotation capacity of reinforced HPFRCC which is good for practical purposes.

Table 4.4 Experimental Database with Yield Moment, Nominal Moment, and Ultimate Drifts (Continued)

References	Specimen Name	HPFRCC Type	Fiber Type	Setup Type	Load Type	Failure Mode	L_s [mm]	Height [mm]	Width [mm]	Depth [mm]	L_s/d [mm/mm]	E [MPa]	f_c' [MPa]	f_t [MPa]	$f_y = f_y'$ [MPa]	f_u [MPa]	ρ [%]	ρ' [%]	f_{ys} [MPa]	ϕ_v [mm]	s_v [mm]	M_y [kNm]	M_n [kNm]	Δ_u/L_s [%]
Fischer and Li [23]*	ECC-0.57-0	ECC	PE	CL	C	RF	500	100	100	82.0	6.10	18000	80	6.0	410	620	1.73	1.73	315	3	25	6.0	8.0	14.0
	ECC-0-0	ECC	PE	CL	C	RF	500	100	100	85.0	5.88	18000	80	6.0	410	620	1.67	1.67	316	0	0	6.0	8.3	15.0
Parra-Montesinos† and Chompreda [27]	PE2.0-0-0.6	ECC	PE	DCL	C	RF	685	250	100	230.0	2.98	10026	56	3.5	440	670	0.62	0.62	-	0	0	22.1	22.8	7.0
	PE2.0-0-1.1	ECC	PE	DCL	C	RF	685	250	100	230.0	2.98	7992	44	3.5	440	730	1.12	1.12	-	0	0	33.1	34.7	10.0
Olsen and Billington [26]	No. 2 P-Bar	HPFRC	SF	CL	C	RF	914	457	70	416.9	2.19	33794	52	4.0	662	745	0.19	0.19	696	3	76	31.0	33.4	2.7
	V-Bar-2	HPFRC	SF	CL	C	RF	914	457	70	415.4	2.20	33794	52	4.0	469	634	0.33	0.33	696	3	76	42.1	42.3	3.8
	Taper	HPFRC	SF	CL	C	RF	914	457	70	415.4	2.20	33794	52	4.0	469	634	0.33	0.33	696	3	76	43.9	44.7	2.5
Yuan et al. [89]*	S-4	ECC	PVA	CL	C	RF	1400	400	200	344.5	4.06	18500	50	5.0	359	542	1.37	1.37	408	8	100	139.6	179.9	6.4
	S-5	ECC	PVA	CL	C	RF	1400	400	200	344.5	4.06	18500	50	5.0	359	542	1.37	1.37	408	8	100	136.6	175.8	6.0
	S-6	ECC	PVA	CL	C	RF	1400	400	200	344.5	4.06	18500	50	5.0	359	542	1.37	1.37	408	8	100	135.1	167.6	5.3
Tavallali et al. [90]†	UC4-F	HPFRC	SF	DCL	C	RF	610	254	406	203.0	3.00	31176	44	4.4	669	807	1.23	1.23	469	10	51	160.3	173.7	12.0
	UC2-F	HPFRC	SF	DCL	C	RF	610	254	406	203.0	3.00	30095	41	4.1	669	807	1.23	1.23	469	10	102	149.4	164.6	11.0
Yoo and Yoon [62]*	S13-0.94%	UHPC	SSF	4P-SSB	M	RF	900	220	150	179.1	5.02	46733	212	5.8	495	743	0.94	0.53	491	10	80	36.3	39.3	5.8
	S13-1.50%	UHPC	SSF	4P-SSB	M	RF	900	220	150	177.5	5.07	46733	212	5.8	510	765	1.49	0.54	491	10	80	49.5	55.8	5.7
	S19-0.94%	UHPC	SSF	4P-SSB	M	RF	900	220	150	179.1	5.02	46881	210	8.5	495	743	0.94	0.53	491	10	80	35.1	42.0	5.6
	S19-1.50%	UHPC	SSF	4P-SSB	M	RF	900	220	150	177.5	5.07	46881	210	8.5	510	765	1.49	0.54	491	10	80	46.5	56.3	7.3
	S30-0.94%	UHPC	SSF	4P-SSB	M	RF	900	220	150	179.1	5.02	46773	210	8.0	495	743	0.94	0.53	491	10	80	36.0	43.2	8.9
	S30-1.50%	UHPC	SSF	4P-SSB	M	RF	900	220	150	177.5	5.07	46773	210	8.0	510	765	1.49	0.54	491	10	80	47.4	56.1	8.1
	T30-0.94%	UHPC	TSF	4P-SSB	M	RF	900	220	150	179.1	5.02	46972	232	9.5	495	743	0.94	0.53	491	10	80	35.1	43.5	7.3
	T30-1.50%	UHPC	TSF	4P-SSB	M	RF	900	220	150	177.5	5.07	46972	232	9.5	510	765	1.49	0.54	491	10	80	50.4	60.3	9.1
Frank et al. [91]†	ECC-1.30-M	ECC	PVA	CL	M	RF	760	178	127	149.3	5.09	7000	44	4.0	455	675	1.36	1.36	690	3	75	19.7	23.9	16.0
	ECC-1.30-MF	ECC	PVA	CL	C	RF	760	178	127	149.3	5.09	7000	44	4.0	455	675	1.36	1.36	690	3	75	19.8	23.2	11.9
Bandelt and Billington [53]†	M-0.54	ECC	PVA	4P-SSB	M	RF	457	230	130	209.5	2.18	16000	47	2.2	395	620	0.52	0.52	690	3	75	15.9	17.1	11.0
	C-0.54	ECC	PVA	4P-SSB	C	RF	457	230	130	209.5	2.18	16000	47	2.2	395	620	0.52	0.52	690	3	75	15.8	16.4	3.4
	M-0.70	ECC	PVA	3P-SSB	M	RF	685	180	130	159.5	4.29	16000	47	2.2	445	690	0.68	0.68	690	3	75	14.4	17.4	8.4
	C-0.70	ECC	PVA	3P-SSB	C	RF	685	180	130	159.5	4.29	16000	47	2.2	445	690	0.68	0.68	690	3	75	14.4	15.5	4.8
	M-1.3	ECC	PVA	3P-SSB	M	RF	685	180	130	158.0	4.34	16000	47	2.2	455	675	1.26	1.26	690	3	75	22.2	28.3	12.0
	C-1.3	ECC	PVA	3P-SSB	C	RF	685	180	130	158.0	4.34	16000	47	2.2	455	675	1.26	1.26	690	3	75	22.7	25.6	8.5
	M-2.0	ECC	PVA	3P-SSB	M	RF	685	180	130	156.5	4.38	16000	47	2.2	440	625	1.96	1.96	690	3	75	30.8	41.1	16.0

Table 4.4 (Continued) Experimental Database with Yield Moment, Nominal Moment, and Ultimate Drifts

References	**Specimen Name**	**HPFRCC Type**	**Fiber Type**	**Setup Type**	**Load Type**	**Failure Mode**	L_s [mm]	**Height** [mm]	**Width** [mm]	**Depth** [mm]	L_s/d [mm/mm]	**E** [MPa]	$f_c^{'}$ [MPa]	f_t [MPa]	$f_y = f_y^{'}$ [MPa]	f_u [MPa]	ρ [%]	$\rho^{'}$ [%]	f_{ys} [MPa]	ϕ_v [mm]	s_v [mm]	M_y [kNm]	M_n [kNm]	Δ_u/L_s [%]
Hung and Chueh [92]	B-2R-1SF	UHPC	SF	CL	C	RF	1850	350	250	309.5	5.98	33300	148	6.2	703	907	1.98	1.98	477	13	75	342.3	351.5	8.0
	B-2R-2SF	UHPC	SF	CL	C	RF	1850	350	250	309.5	5.98	34110	152	6.2	703	907	1.98	1.98	477	13	75	342.3	360.8	9.0
	B-1.4R-2SF	UHPC	SF	CL	C	RF	1850	350	250	309.5	5.98	33030	147	6.2	703	907	1.32	1.32	477	13	75	259.0	240.5	7.0
	B-1.4R-2LF	UHPC	SF	CL	C	RF	1850	350	250	309.5	5.98	32220	143	8.0	703	907	1.32	1.32	477	13	75	259.0	249.8	8.0
Frank et al. [63]†	ECC-0.73-F	ECC	PVA	CL	C	RF	760	178	127	150.8	5.04	7000	44	4.0	445	690	0.74	0.74	690	3	75	11.8	13.3	11.9
	ECC-0.95-F	ECC	PVA	CL	C	RF	813	203	165	161.3	5.04	7000	44	4.0	455	675	0.97	0.97	690	3	38	23.6	24.2	11.9
	ECC-1.00-F	ECC	PVA	CL	C	RF	813	203	165	162.8	4.99	7000	44	4.0	445	690	1.06	1.06	690	3	38	27.2	27.6	11.9
	ECC-1.30-F	ECC	PVA	CL	C	RF	760	178	127	149.3	5.09	7000	44	4.0	455	675	1.36	1.36	690	3	75	19.8	23.4	11.9
	ECC-1.40-F	ECC	PVA	CL	C	RF	813	203	165	161.3	5.04	7000	44	4.0	455	675	1.45	1.45	690	3	38	32.9	33.9	16.9
	ECC-1.50-F	ECC	PVA	CL	C	RF	813	203	165	159.8	5.09	7000	44	4.0	440	625	1.51	1.51	690	3	38	31.5	34.7	16.7
	ECC-0.73-SP	ECC	PVA	CL	CSP	RF	760	178	127	150.8	5.04	7000	44	4.0	445	690	0.74	0.74	690	3	75	12.2	13.4	8.5
	ECC-0.95-SP	ECC	PVA	CL	CSP	RF	813	203	165	161.3	5.04	7000	44	4.0	455	675	0.97	0.97	690	3	38	24.4	24.6	11.9
	ECC-1.00-SP	ECC	PVA	CL	CSP	RF	813	203	165	162.8	4.99	7000	44	4.0	445	690	1.06	1.06	690	3	38	28.5	28.5	11.9
	ECC-1.30-SP	ECC	PVA	CL	CSP	RF	760	178	127	149.3	5.09	7000	44	4.0	455	675	1.36	1.36	690	3	75	20.5	23.7	16.9
	ECC-1.40-SP	ECC	PVA	CL	CSP	RF	813	203	165	161.3	5.04	7000	44	4.0	455	675	1.45	1.45	690	3	38	34.1	34.6	16.9
	ECC-1.50-SP	ECC	PVA	CL	CSP	RF	813	203	165	159.8	5.09	7000	44	4.0	440	625	1.51	1.51	690	3	38	33.7	35.5	16.7
	ECC-0.73-LP	ECC	PVA	CL	CLP	RF	760	178	127	150.8	5.04	7000	44	4.0	445	690	0.74	0.74	690	3	75	13.7	14.1	6.1
	ECC-0.95-LP	ECC	PVA	CL	CLP	RF	813	203	165	161.3	5.04	7000	44	4.0	455	675	0.97	0.97	690	3	38	25.2	26.1	11.9
	ECC-1.00-LP	ECC	PVA	CL	CLP	RF	813	203	165	162.8	4.99	7000	44	4.0	445	690	1.06	1.06	690	3	38	27.6	28.7	11.9
	ECC-1.30-LP	ECC	PVA	CL	CLP	RF	760	178	127	149.3	5.09	7000	44	4.0	455	675	1.36	1.36	690	3	75	20.5	23.3	16.9
	ECC-1.50-LP	ECC	PVA	CL	CLP	RF	813	203	165	159.8	5.09	7000	44	4.0	440	625	1.51	1.51	690	3	38	32.5	36.1	16.7

Note: SF = Steel fibers, SSF = Smooth Steel Fibers, TSF = Twisted Steel Fibers

CL = Cantilever, DCL = Double cantilever, 3P-SSB = 3 Point-Simply supported beam, 4P-SSB = 4 Point-Simply supported beam

C = Cylic load, M = Monotonic load, CSP = Cyclic load with initial small pulse, CLP = Cyclic load with initial large pulse

RF = Reinforcement Fracture, †Yield load computed based on load deflection response in the reference, *Yield load value provided in the reference

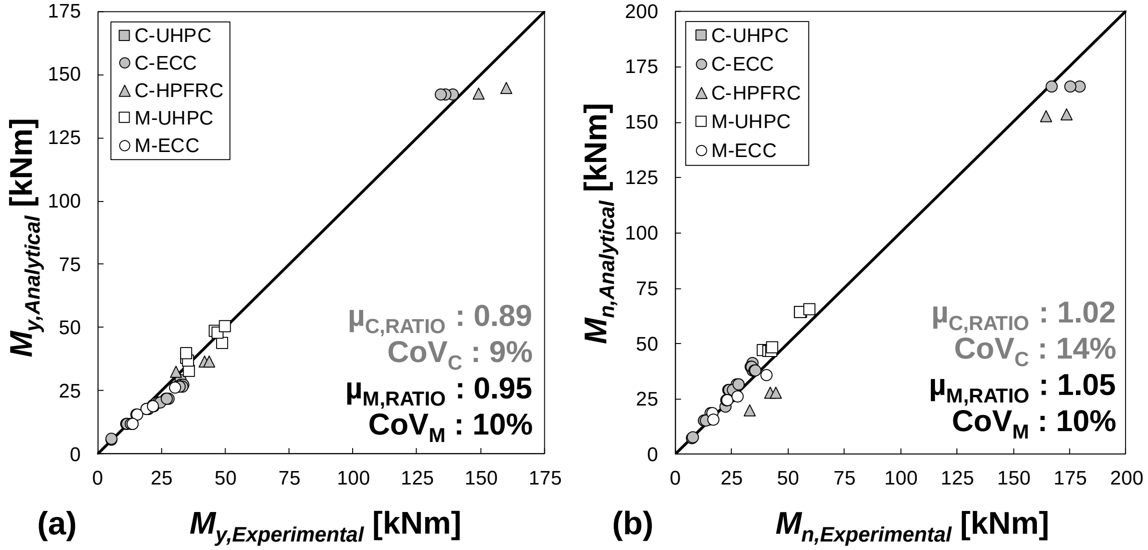

Figure 4.12 Comparison of analytical vs. experimental (a) yield moment (b) nominal moment.

4.7 Conclusions

The unique characteristics of reinforced HPFRCC structural member under flexural loading, such as high resistance to splitting cracks, less rebar slippage, damage localization in a single or few flexural cracks, inelastic strain concentration within a small region of rebar, and failure by the fracture of tensile longitudinal reinforcement in the plastic hinge region [53, 62, 63, 65, 75] motivated the research presented in this chapter. A detailed numerical investigation of the plastic hinge region in reinforced HPFRCC flexural members with variations in mechanical properties, geometric properties, and loading scheme was conducted.

The strain distribution along the length of HPFRCC flexural members showed that the length of reinforcement yielding zone, L_y, increased with decrease in tensile strength of HPFRCC material, and L_y was longer under cyclic loading compared to monotonic loading in majority of simulations. The length of tensile strain concentration zone, L_{sc}, was found to be shorter under cyclic loading compared to monotonic loading in simply supported beams, whereas L_{sc} was found to be marginally longer under cyclic loading compared to monotonic loading in cantilever

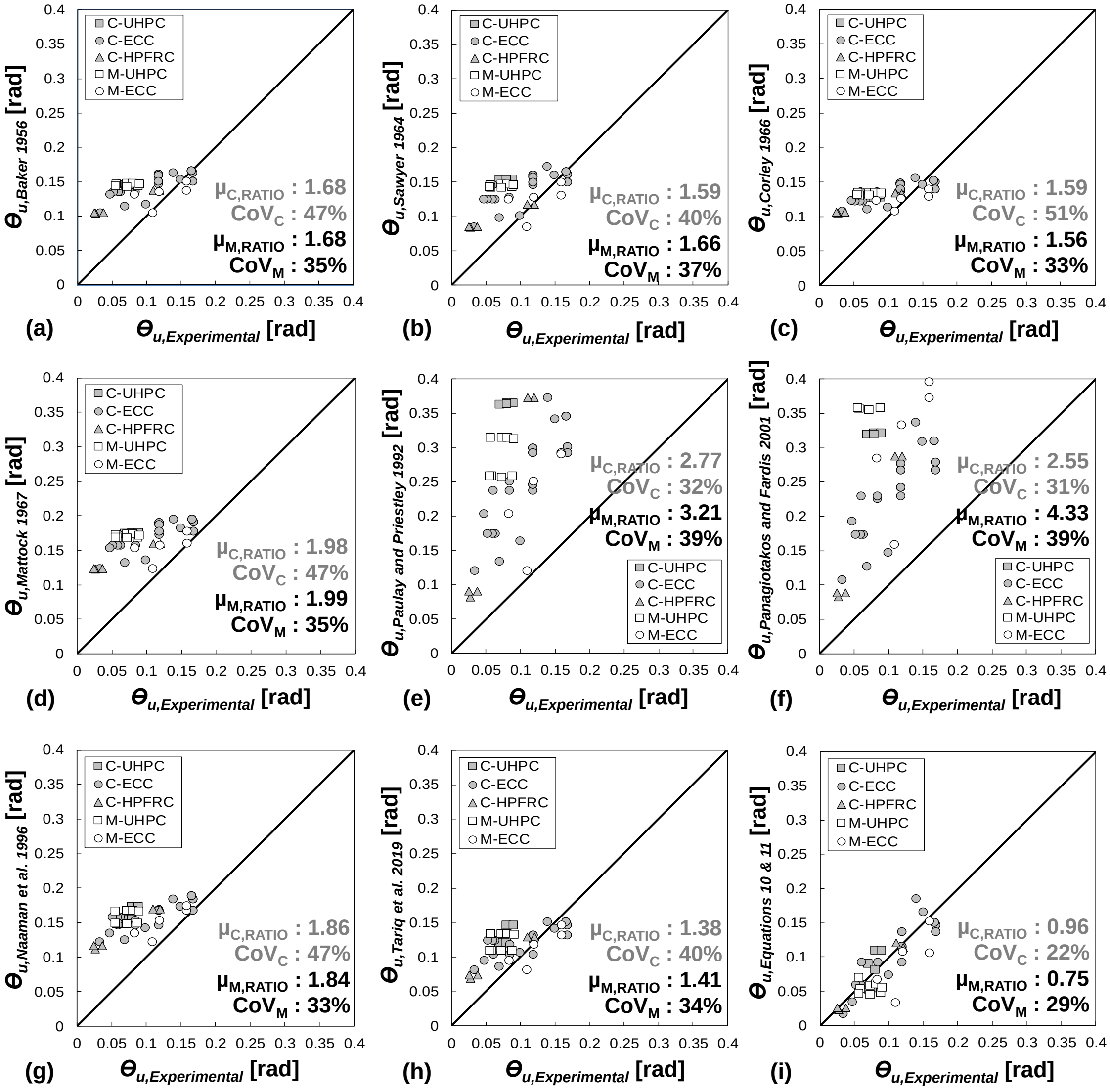

Figure 4.13 Comparison of analytical vs. experimental ultimate rotation capacity using equivalent plastic hinge expressions of (a) Baker [118] (b) Sawyer [95] (c) Corley [54] (d) Mattock [55] (e) Paulay and Priestley [56] (f) Panagiotakos and Fardis [101] (g) Naaman et al. [18] (h) Tariq et al. [61] (i) Equations 4.10 & 4.11.

beams. The investigation of curvature localization zone, L_{cl}, revealed that under cyclic loading, the length of curvature localization zone was less compared to monotonic loading in simply supported beams, whereas in cantilever beams the trend of L_{cl} was found to be reverse (i.e., $L_{cl,monotonic} < L_{cl,cyclic}$).

An improved expression for equivalent plastic hinge length for reinforced HPFRCC flexural members was proposed, which explicitly takes into account the change in moment gradient, strain penetration effect and influence of inelastic strain concentration. The effectiveness of new expression was evaluated through comparison with existing expressions and in combination with the analytical method to estimate rotation capacity at collapse level.

An analytical framework based on section analysis and component level structural analysis was developed to calculate flexural strength and rotational parameters at multiple damage levels for reinforced HPFRCC flexural members. The proposed framework was validated through an experimental database of 50 reinforced HPFRCC test specimens subjected to monotonic and cyclic loading. The ultimate chord rotation computed using the analytical framework and new plastic hinge length expression showed better prediction capability ($\mu_{C,RATIO} = 0.96$ and $\mu_{M,RATIO} = 0.75$) compared to the use of existing plastic hinge length equations. The flexural strength prediction under both types of loading scenario were found to be well predicted ($0.89 \leq \mu_{C,RATIO} \leq 1.02$ and $0.95 \leq \mu_{M,RATIO} \leq 1.05$) with prediction scatter not higher than 15%.

The proposed equivalent plastic hinge length expression for reinforced HPFRCC flexural members can be conveniently used by practicing engineers to model structural components employing “fiber-based fixed length hinge model” in commercial analysis/design softwares such as ETABS, STAAD Pro, SAP2000, Perform 3D, OpenSEES, etc. The developed framework provides an effective tool to determine moment capacity at yield and nominal levels for steel reinforced

HPFRCC section, irrespective of the class of HPFRCC used. Further, the analytical model can be effectively used to calculate rotation values of the backbone curve of “concentrated plastic hinge models” such as rigid plastic hinge or non-linear spring hinge of structures constructed with HPFRCC in plastic hinge region.

CHAPTER 5

EFFECT OF FIBER CONTENT VARIATION IN PLASTIC HINGE REGION OF REINFORCED UHPC FLEXURAL MEMBERS

5.1 Introduction and Background

Ultra-high performance concrete (UHPC) is an advanced cement-based composite material designed with optimal particle packing density, such that, it possesses extremely high compressive strength ($>$ 120 MPa without heat treatment) and enhanced durability properties [77]. When combined with short discontinuous fibers, UHPC materials have high tensile strength ($>$ 5 MPa), tensile fracture toughness, and ductile strain-hardening behavior under uniaxial tension tests [77]. The mechanical properties of UHPC have led researchers and engineers to perform a large number of proof-of-concept investigations under extreme loading conditions such as blast, impact, earthquake, and fire [127]. In high seismic zones, researchers are especially interested in the applicability of UHPC in plastic hinge regions of structural components undergoing large inelastic deformations [128]. Various classes of high performance fiber reinforced cementitious composites (HPFRCCs) have already been effectively used in plastic hinge region of structural components such as coupling beams, columns, and bridge piers in recent years [129]. The use of UHPC in the plastic hinge regions of structural components can enhance the load carrying capacity, ductility, and energy absorption capacity because the mechanical properties of UHPC can prevent premature failure associated with damage in plastic hinge regions, as is typically observed in structural components made with conventional concrete (e.g., spalling of cover, buckling of rebar, shear cracks, etc.).

Structural components can be engineered to improve the damage tolerance of structures by using UHPC in plastic hinge region, while using conventional concrete in the remaining portions of the component [128]. Such an approach can minimize the high cost associated with UHPC while reducing the overall life cycle cost (i.e., maintenance and repair cost) of the structure. To optimize the initial construction cost, the fiber volume fraction used in a UHPC material can be reduced; however, the influence of such a reduction on structural ductility and performance of plastic hinge regions is not well understood. A previous numerical study conducted using a wide range of HPFRCC materials indicated that the tensile strength and ductility of the matrix can significantly alter the amount of damage and the length of the plastic hinge region in reinforced HPFRCC flexural members [65, 130]. Therefore, the use of low fiber content in regions undergoing large displacement reversals may result in an undesired failure mechanism (e.g., shear cracking) without the formation of a ductile plastic hinge mechanism.

Other experimental and numerical studies have shown that the flexural behavior of reinforced HPFRCCs (including UHPC) in terms of crack progression, reinforcement plasticity, and failure mechanism is significantly different than conventional reinforced concrete structural components [53, 62, 75, 131]. Specifically, the failure mode of flexural members is found to be predominantly through the fracture of longitudinal reinforcement rather than compression crushing of an HPFRCC matrix. This is due to a crack localization phenomenon observed in reinforced HPFRCC structural components, wherein the plastic damage concentrates in the vicinity of a single or few flexural cracks. Several bond experiments with lap splice beam specimens have shown that higher bond strength of HPFRCC matrix restraints the formation of splitting cracks which leads to such a phenomenon [46, 123, 132]. Further, tension stiffening experiments of reinforced HPFRCC prisms have shown that there is localized strain hardening in longitudinal reinforcement at such localized cracks [50, 52]. Localized hardening of steel reinforcement can provide a strengthening mechanism at the critical section of reinforced HPFRCC flexural members, until the member loses its load-carrying capacity by reinforcement fracture.

Shao and Billington [133] recently conducted an experimental study with reinforced UHPC beams consisting of two different reinforcement ratios ($\rho = 0.96\%$ and 2.10%). The study showed that there can be two different failure paths in reinforced UHPC beams depending on the amount of longitudinal reinforcement used. The use of low reinforcement ratio led to failure after crack localization failure path in which there were three major damage states: yielding, crack localization, and rebar fracture. The use of a high reinforcement ratio led to failure after gradual strain hardening failure path in which the intermediate damage state changed from crack localization to compression crushing (or softening). The flexural failure paths and various damage states are seen to be pre-dominantly dependent on longitudinal reinforcement and matrix property based on similar experimental studies carried out on other HPFRCC materials [119, 131].

Although several experimental studies have been conducted to understand the flexural behavior of reinforced UHPC beams, there is a lack of experimental investigation to understand and quantify the spread of plasticity in plastic hinge regions of reinforced UHPC beams. As a part of this initial experimental study, two reinforced UHPC beams with 1% and 2% fiber volume fraction (V_f) were tested under a four-point bending test setup. The flexural response, length of reinforcement yielding, inelastic curvature distribution, crack distribution, and strain variation within the maximum moment region were investigated. Analytical models and a recently proposed equivalent plastic hinge length equation for ductile concrete composites were used to predict flexural strengths and rotation values at various damage states.

Table 5.1 Mixture Proportions (per m^3)

Specimen	Premix Blend [kg]	Water [kg]	Fibers [% Vol.]	Admix. A [kg]	Admix. B [kg]	Admix. C [kg]
UHPC-1%	1939	194	1.0	20	26	28
UHPC-2%	1960	196	2.0	20	26	28

5.2 Experimental Program

5.2.1 Materials, Mixture proportions, and Mechanical Tests

Two types of mixture proportions were used in the experiment as listed in Table 5.1. The propriety pre-mix blend contained a mixture of cement, quartz, and silica fume. There were three types of admixtures used to improve the workability of UHPC during the casting period. Standard smooth steel fibers with a diameter of 0.2mm and length of 13 mm were used in both mixtures. The naming convention of the beam specimens were based on the percentage of fiber volume fraction used in each specimen. Therefore, UHPC-1% denotes the specimen with a fiber volume fraction of 1% and UHPC-2% indicates the specimen containing a fiber volume fraction of 2%. The materials were mixed in a horizontal shear mixer and poured from one end of the beam mold until the mold was filled up to the full height.

All UHPC specimens were moist cured and tested at 56 ± 3 days of casting. The representative results of mechanical tests have been tabulated in Table 5.2. Both compression and flexural tests of the two types of UHPC mixtures were conducted in accordance with ASTM C1856−17 [134]. Cylindrical specimens of diameter 75 mm and height 150 mm were prepared and tested to obtain compressive strength and modulus of elasticity. Four-point bending tests were performed on UHPC prisms with a cross section dimension of 75 × 75 mm and a length of 300 mm to obtain the equivalent bending stress versus displacement response as shown in Figure 5.1.

Table 5.2 Mechanical Properties

Description	f_t^1 [MPa]	G_f^1 [MPa-mm]	$f_c^{'}$ [MPa]	E [GPa]	f_y [MPa]	f_u [MPa]	ε_u [%]	ε_f [%]
UHPC-1%	5.2	6.4	170	41.6	-	-	-	-
UHPC-2%	9.2	6.7	180	42.5	-	-	-	-
Longitudinal Rebar (#6)	-	-	-	190	470	780	10	18^2
Transverse Rebar (#3)	-	-	-	200^3	510^3	-	-	-

^{1}Obtained using inverse analysis, ^{2}Extrapolated value, ^{3}Manufacturer listed value

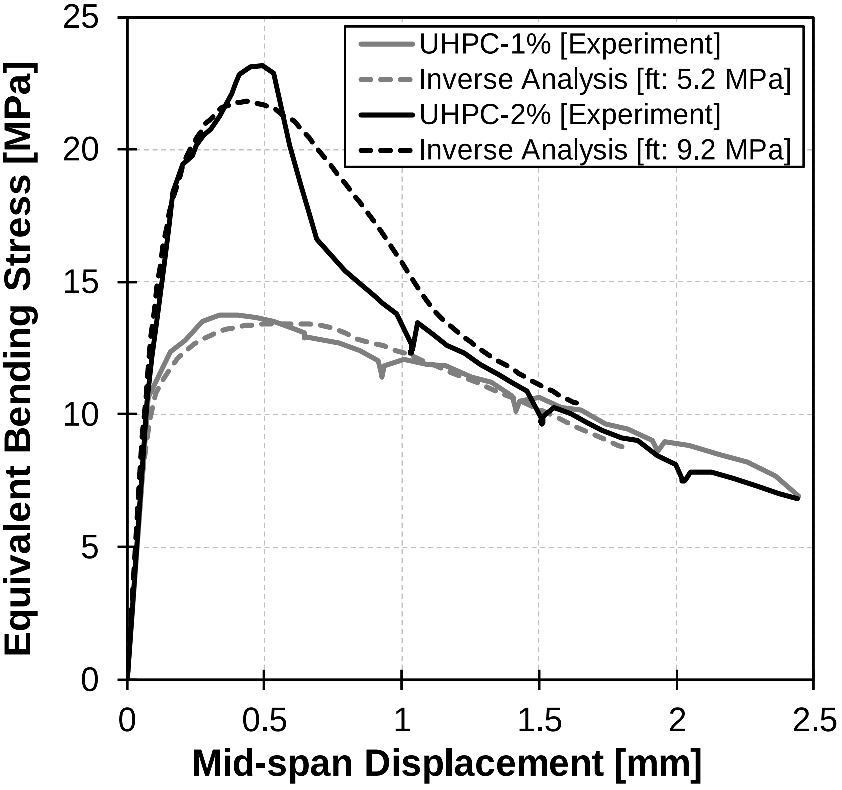

Figure 5.1 Equivalent bending stress vs. mid-span displacement of unreinforced UHPC beams.

An inverse analysis was conducted using two-dimensional finite element simulations to estimate the tensile strength (f_t) and tensile fracture energy (G_f) of the two UHPC mixtures. It can be observed from Figure 5.1 that the simulated flexural response from inverse analysis closely approximates the experimental flexural behavior of unreinforced UHPC prisms. Therefore, the estimated tensile strengths of the mixtures listed in Table 5.2 were used in lieu of tensile strength values obtained from direct tension test to investigate the flexural behavior and plastic hinge region of reinforced UHPC beams tested in this study. ASTM A615 Grade 60 steel with a diameter of 19 mm was used as longitudinal reinforcing bar in both UHPC-1% and UHPC-2% specimens. A uniaxial tension test was conducted using an extensometer of gage length 50 mm to obtain characteristic tensile properties of the longitudinal reinforcement as listed in Table 5.2. Transverse reinforcement of Grade 60 steel with manufacturer listed yield strength of 510 MPa was used in both specimens.

5.2.2 Test Specimens, Setup and Instrumentation

Two reinforced UHPC beam specimens were tested using a four-point bending setup as shown in Figure 5.2. A digital image correlation (DIC) system was used to assess variations in strain in the constant moment region of 200 mm between the two point loads. Since the DIC system could not be extended further due to laboratory constraints, a series of linear variable displacement transducers (LVDTs) were used to measure the vertical displacement along one side of the beam to a distance of 200 mm from the center line of the right point load towards the roller support.

Figure 5.3 shows the design of the beam with longitudinal reinforcement layout, transverse reinforcement layout, location of strain gages, and cross-section details. The strain in the bottom longitudinal reinforcement was measured at five locations by attaching post-yield strain gages (YEFLA-2-3LJC-F from Tokyo Measuring Instruments Lab) with a maximum measurement capacity of 10%. Two

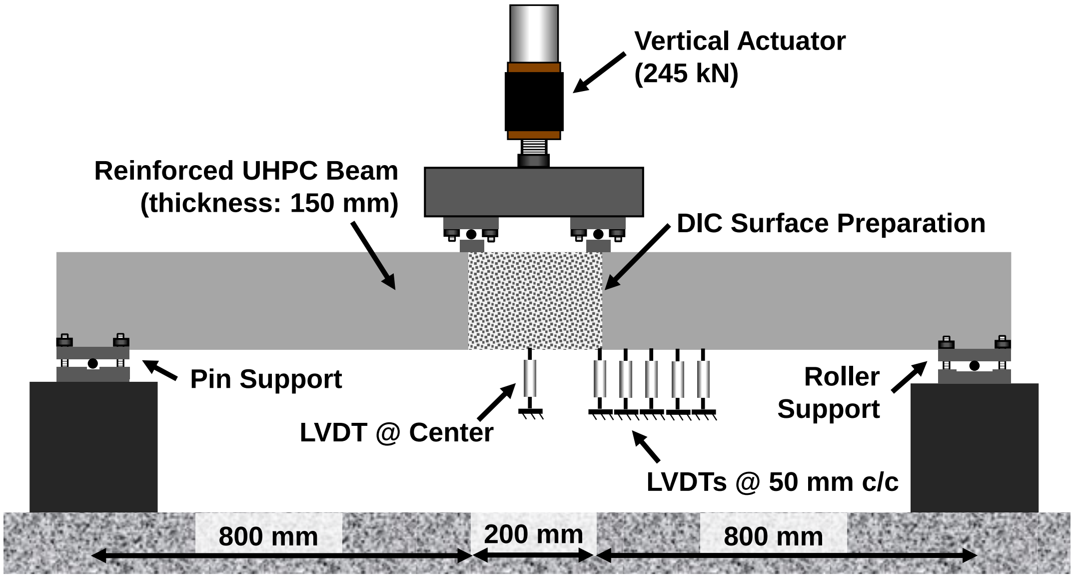

Figure 5.2 (a) Test setup of reinforced UHPC beams with location of DIC surface and LVDTs.

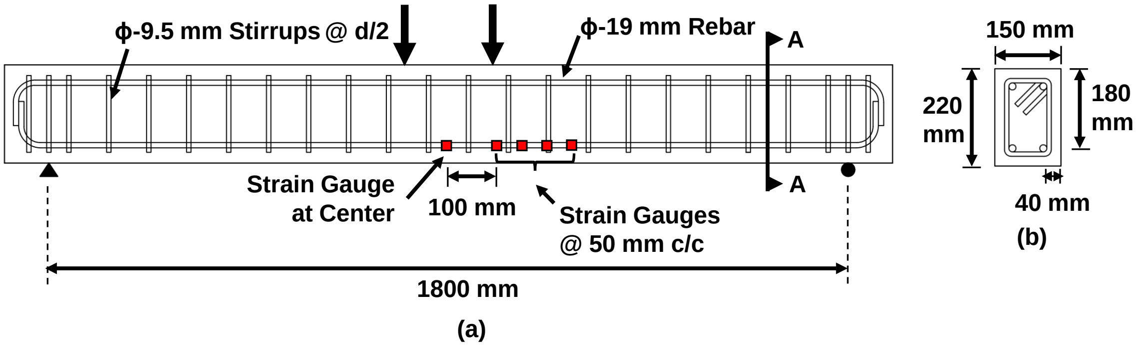

Figure 5.3 (a) Specimen design detail with location of strain gages (b) cross section at A-A.

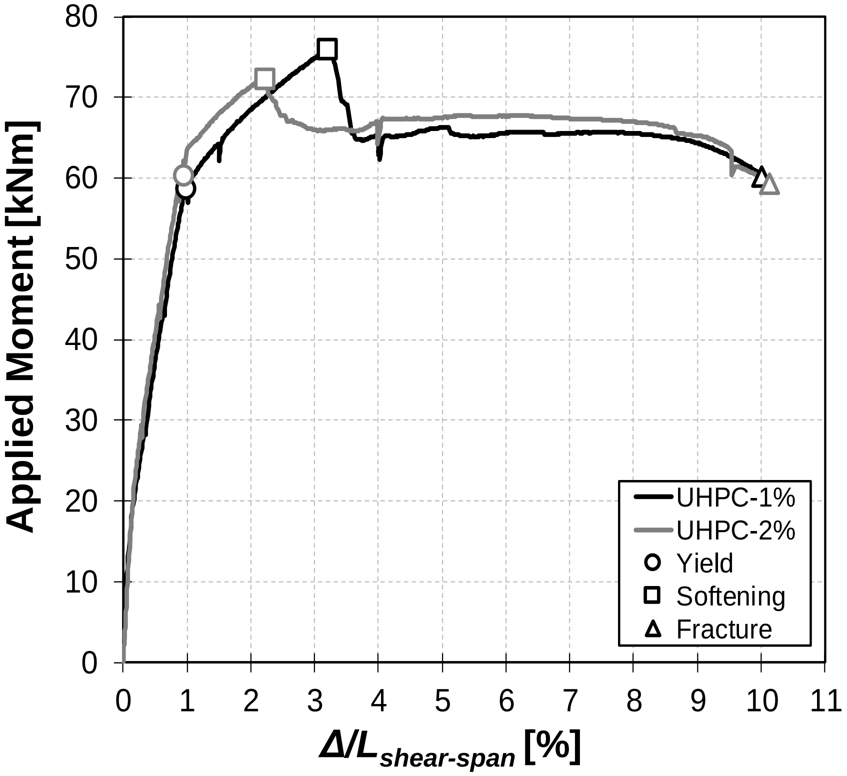

Figure 5.4 Applied moment vs. drift response of two reinforced UHPC beams with different damage states.

longitudinal reinforcing bars of diameter 19 mm were used in the top and bottom sides of the cross section resulting into a tensile longitudinal reinforcement ratio of 2.10%. Transverse reinforcement was provided at a spacing of one-half of the effective depth (i.e., d/2) with bars of diameter 9.5 mm. The specimens were subjected to a monotonic loading at the rate of 0.097 mm/s until they lost their load carrying capacity by fracture of the tensile longitudinal reinforcement.

5.3 Result and Discussion

5.3.1 Moment vs. Drift Response

The applied moment versus drift response of the two specimens with various damage states is shown in Figure 5.4. Drift is expressed in percentage (%) and is calculated by normalizing the vertical displacement at mid-span by the shear-span length

$(\Delta/L_{shear-span})$. The initial elastic response of both beams including stiffness, moment at yield and drift at yield are similar. The beams were assumed to yield when the strain in the tensile reinforcement at mid-span reached the yield strain (ε_y) of 0.2772%. At yield, the moment and drift capacities are similar because of the use of the same reinforcement ratio $(\rho = 2.10\%)$ in both beams. The strength and drift capacities at yield are less sensitive to variations in tensile strength of the matrix (or fiber volume fraction) in specimens with higher reinforcement ratios compared to specimens with lower reinforcement ratios [65].

After yield, the flexural load carrying capacity increased in both specimens due to the combination of fiber bridging action and localized hardening of the tensile reinforcement. The post-yield stiffness of both beams were similar; however, the nominal moment (M_n) capacity (i.e., peak moment capacity) of UHPC-2% (72.2 kNm) was found to be lower than UHPC-1% (75.9 kNm). It was anticipated that the UHPC-2% specimen, which has twice the fiber content and a higher tensile strength than UHPC-1% beam, would have a higher nominal moment capacity than UHPC-1% specimen. However, a higher rate of post-yield strain accumulation in the compression zone of UHPC-2% specimen was observed (Figure 5.8 (a)). This led to earlier softening of the compression matrix and a lower flexural load carrying capacity in UHPC-2% specimen than in UHPC-1% specimen. The drift of UHPC-2% specimen at the nominal level is lower than the drift of UHPC-1% by 31% because of the rapid strain concentration in the compression zone of the UHPC-2% specimen. For example, at 2.2% drift level, the compression zone strain (ε_c) in UHPC-2% beam was found to be 35% higher than in UHPC-1% beams (i.e., $(\varepsilon_c)_{UHPC-2\%} = 0.42\%$ whereas $(\varepsilon_c)_{UHPC-1\%} = 0.31\%$ as shown in Figure 5 (a)) as further discussed in Section 5.3.5.

Both specimens were able to achieve large deformations without significantly losing load carrying capacity because the hardened bottom longitudinal reinforcement acted as the tensile component of the flexural couple before reaching the fracture point. This failure mechanism with gradual strain hardening of tensile reinforcement is mostly found in reinforced HPFRCC flexural members with high reinforcement ratios [17]. It is interesting to note that the variation of fiber content did not influence the value of ultimate drift capacity $((\Delta/L_{shear-span})_{UHPC-1}\% = 10.02\%$ and $((\Delta/L_{shear-span})_{UHPC-2}\% = 10.15\%)$. The results indicates that the ultimate rotation or drift capacity of reinforced UHPC beams with high longitudinal reinforcement (i.e., $\rho > 2\%$) is not sensitive to variation in fiber volume fraction compared to the beams with low to moderate reinforcement ratio (i.e., $1\% < \rho < 2\%$).

5.3.2 Strain Distribution

Figure 5.5 presents the variation of reinforcement tensile strain from mid-span to the right side of the specimens (up to 250 mm). At 1% drift, it can be observed that the UHPC-1% specimen had a reinforcement yielding length, L_{py}, of 50 mm, whereas the longitudinal reinforcement yielded over a length of 90 mm in UHPC-2% specimen. However, L_{py} in the UHPC-1% specimen increased at higher drift level compared to UHPC-2% specimen because of the opening of flexural cracks along a longer span length as shown in Figure 4.5. The fiber bridging action and matrix tensile strength of UHPC-1% specimen is lower than the UHPC-2% specimen. The lower strength of UHPC-1% allowed cracks top easily open at high drift levels and plasticity distributed uniformly over a longer length of reinforcement. The length of reinforcement yielding remained constant at higher drifts in both specimens as the inelastic strain concentration mostly occurred near a dominant crack location as was observed in previous studies involving reinforced HPFRCC flexural members [9,19]. At 8% drift level, the length of reinforcement yielding region in UHPC-1% specimen ($L_{py} = 290$ mm) was longer than UHPC-2% specimen ($L_{py} = 230$ mm). These results suggest that the plastic hinge length in beams with higher fiber content (or higher

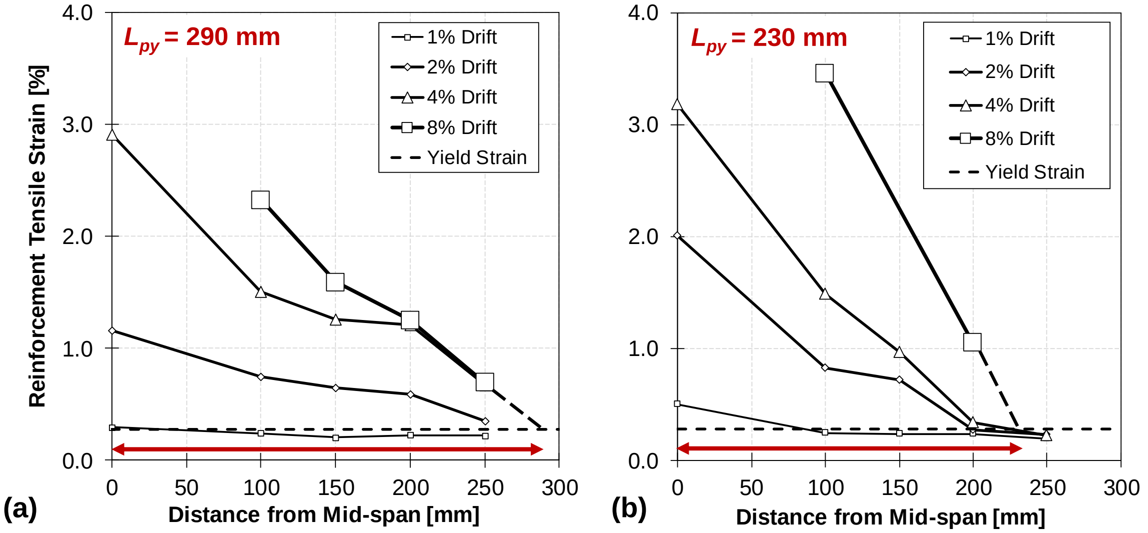

Figure 5.5 Longitudinal reinforcement tensile strain vs. distance from mid-span at various drift levels for (a) UHPC-1% specimen and (b) UHPC-2% specimen.

tensile strength and matrix toughness) are shorter than those with lower fiber content (or lower tensile strength and matrix toughness). This is also in agreement with the length and type of cracking pattern shown in Figure 5.7 and further discussed in Section 5.3.4.

5.3.3 Curvature Distribution

Curvature distribution along the span of the specimens were calculated using the vertical displacements data obtained from the six LVDTs. Mathematically, curvature at a section can be approximated using the elastic deflection theory as shown in Equation (5.1).

$$\theta_u = \theta_y + \theta_p = \frac{1}{2}\phi_y L_s + (\phi_u - \phi_y) L_p \tag{5.1}$$

where θ_i and θ_{i+1} are the angles at sections i and i+1. These angles can be computed using the vertical displacements obtained from LVDTs along the span of the beam. Due to the opening of localized cracks at higher drifts, the recorded vertical displacement data at some locations were estimated using a trendline. Figure 5.6

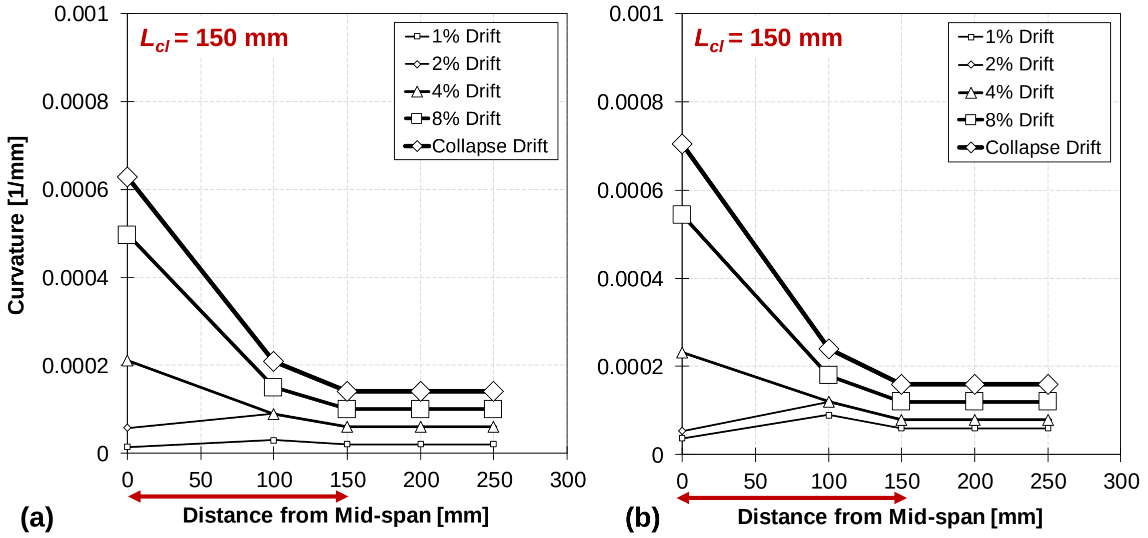

Figure 5.6 Curvature vs. distance from mid-span at various drift levels for (a) UHPC-1% and (b) UHPC-2% specimens.

shows curvature distribution from mid-span to the right side of the specimens at incremental drift levels. At a lower drift level (1% or 2%), the curvature is maximum below the point load, which is the assumed hinge location under four-point bending setup. However, at larger drift levels (4% or more) the curvature is larger at mid-span because of the opening of a major crack at mid-span, such that the section at mid-span deforms more than the section below the point load as seen from the crack pattern at in Figure 4. The overall trend of the curvature is similar to the theoretical curvature under four-point bending test where the curvature is maximum near the mid-span and sharply decreasing away towards the support. The curvature localization region (L_{cl}) was 150 mm in both the specimens indicating there was no substantial effect of fiber content variation in curvature distribution of reinforced UHPC flexural members with high reinforcement ratios.

5.3.4 Crack Pattern in Plastic Hinge Region

Figure 5.7 shows the crack pattern and location of reinforcement fracture in UHPC specimens at impending collapse level drift (i.e., $(\Delta/L_{shear-span})_{UHPC-1}\% = 10.02\%$

and $(\Delta/L_{shear-span})_{UHPC-2}\% = 10.15\%$). Both specimens contained multiple fine distributed cracks without any flexural crack localization up to 1% drift level. However, after yielding of tensile reinforcement, flexural cracks slowly began to open as the fiber-bridging action declined in some of the cracks. Four major flexural cracks widened in both specimens, but the major cracks were evenly spaced in UHPC-1% specimen compared to UHPC-2% specimen (Figure 5.7).

Major cracks widened in the region away from maximum moment in the UHPC-1% specimen because the cracks could open at lower flexural load due to a lower tensile strength and fracture energy of UHPC-1% matrix. In UHPC-2% specimen, major cracks were confined to the maximum moment region and damage was predominantly localized in a single crack (i.e., crack number 3). As crack number 3 widened, rebar plastic strain in the vicinity of that crack concentrated at a higher rate in the UHPC-2% specimen as compared to the UHPC-1% specimen (Figure 5.8 (b)) as further discussed in Section 5.3.5. The maximum sizes of major and minor cracks were found to be larger in the UHPC-2% specimen ($\omega_{(majorcracks)} = 19$ mm and $\omega_{(minorcracks)} = 0.13$ mm) compared to the UHPC-1% specimen ($\omega_{(majorcracks)} = 13$ mm and $\omega_{(minorcracks)} = 0.11$ mm) at collapse level. In higher tensile strength UHPC, there is tendency of damage accumulation in existing cracks, instead of opening of the new cracks because of tougher matrix and higher degree of fiber-bridging action. Furthermore, the distance between the extreme minor and major cracks were found to be longer in UHPC-1% specimen ($L_{(minorcracks)} = 1350$ mm and $L_{(majorcracks)} = 420$ mm) compared to UHPC-2% ($L_{(minorcracks)} = 935$ mm and $L_{(majorcracks)} = 240$ mm) which can be attributed to the comparatively weaker matrix and lower fiber-bridging action in UHPC-1% specimen compared to UHPC-2% specimen.

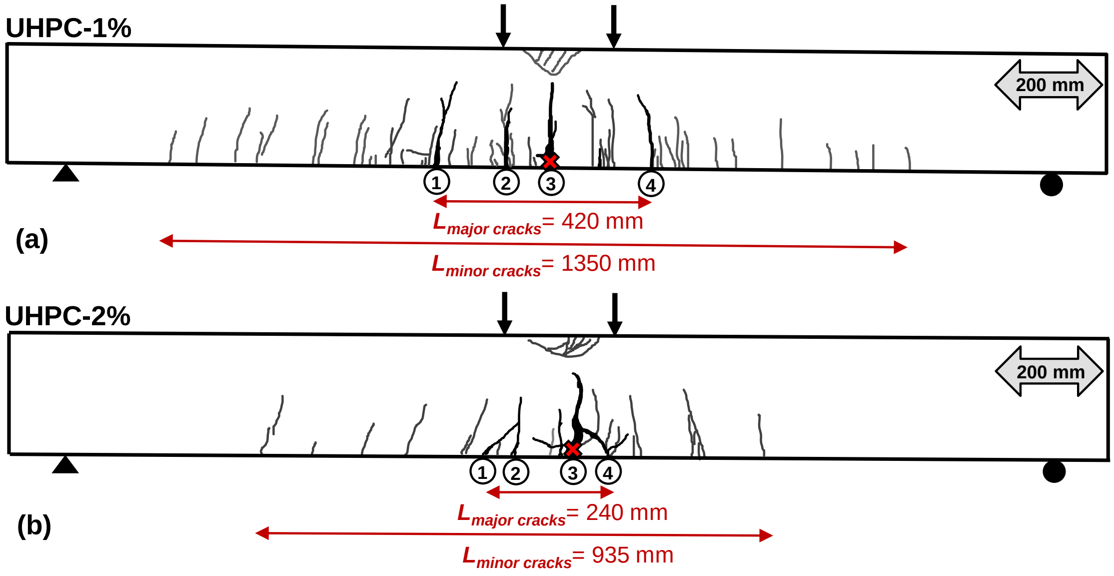

Figure 5.7 Crack pattern in (a) UHPC-1% and (b) UHPC-2% specimens at impending collapse.

5.3.5 Variation of Strain in Maximum Moment Region

Figure 5.8 shows the variation of compression and tension strain at mid-span with incremental drift levels. The slope of the lines indicates the rate of strain accumulation in the compression zone (Figure 5.8 (a)) or in the tensile reinforcement (Figure 5.8 (b)) at mid-span. After yielding of the specimens, the rate of compression strain accumulation in the UHPC-2% specimen became marginally higher compared to the UHPC-1% specimen because the high tensile strength matrix attracts larger forces at smaller deformation level. Further, higher bond strength in UHPC-2% specimen restricted the formation of splitting cracks, causing early rebar hardening over a small de-bonded length. The hardening led to widening of a mid-span crack and rapid strain concentration in the tensile longitudinal reinforcement in UHPC-2% specimen at a lower drift level as shown in Figure 5.8 (b). For example, the strain in the tensile reinforcement at 2% drift level in UHPC-2% specimen was 2.00% and that in UHPC-1% specimen was 1.16%. The effect of this rapid strain variation caused softening of UHPC-2% beam at a lower drift level compared to

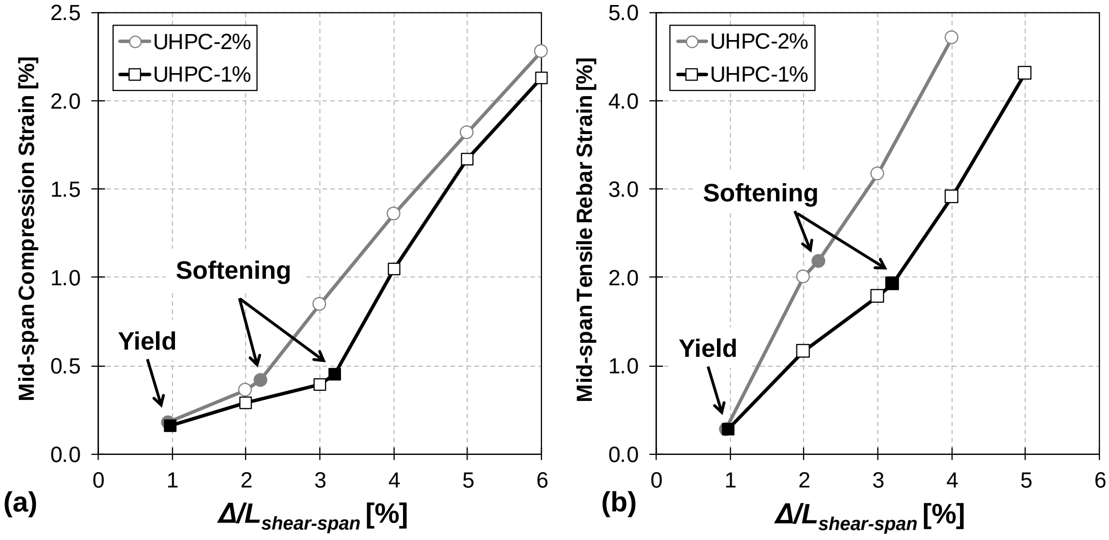

Figure 5.8 (a) Mid-span compression strain vs. drift and (b) mid-span longitudinal tensile reinforcement strain vs. drift.

UHPC-1% beam ($(\Delta/L_{shear-span})_{UHPC-1}\% = 3.2\%$ and $(\Delta/L_{shear-span})_{UHPC-2}\% = 2.2\%$). After softening of the specimens, the compression strain accumulation rate in the UHPC-1% specimen increased compared to the UHPC-2% specimen. The difference in compression strain at the same drift level decreased progressively at higher drift levels. The localized hardening strain in tensile reinforcement at mid-span of the UHPC-2% specimen was much higher compared to the UHPC-1% specimen at the same drift levels. For instance, the strain in tensile reinforcement at 4% drift level in UHPC-2% specimen was 4.72% and that in UHPC-1% specimen was 2.91%. It was anticipated that the UHPC-2% would fail earlier by fracture of reinforcement based on this trend. However, UHPC-2% had a similar deformation capacity as UHPC-1% as discussed in Section 5.3.1. Further investigation is required to understand the failure mechanism at higher strain levels using post-yield strain gages of a larger strain capacity.

5.3.6 Prediction of Flexural Strength and Rotation Capacity

The flexural behavior and failure mechanism of reinforced HPFRCC is significantly different than the conventional reinforced concrete as demonstrated by several experimental studies [7-10]. A recently proposed analytical model was used to predict flexural strength and rotation capacity at different damage states (Figure 5.9) [10,20]. The predictability of the analytical model was measured by comparison with the experimentally obtained values. The flexural strengths and curvatures at various damage states were computed assuming linear strain distribution and using cross section properties of the specimens. The beams were assumed to reach the yield level when the tensile reinforcement strain reached the yield value (i.e., ε_y). The analytical model shown in Figure 5.9 (b) considers a tensile stress block contribution which is ignored in the flexural calculation of conventional concrete components. Elastic deflection theory was used to compute yield rotation using the yield curvature value as shown in Equation (5.2). It can be observed from Table 5.3 that the prediction ratio of both the parameters are close to 1.00, which indicates that the analytical formulation can be successfully used to compute yield rotation and moment capacity of reinforced UHPC flexural members.

Two analytical models were used to estimate the nominal moment capacity: one with modified Hognestad compression stress block (Figure 5.9 (c)) and the second with simplified Whitney compression stress block (Figure 5.9 (d)). Both models considered localized hardening of the reinforcement bar as observed in tension stiffening experiments [50, 52]. The beams were assumed to the reach nominal level when the strain in the compression zone reached 3% [131] or tensile reinforcement strain reached ultimate value (ε_u) [66]. It can be observed from Table 5.4 that the nominal moment predictability using a modified Hognestad stress block is better compared to the use of simplified rectangular Whitney stress block; however, both give reasonable estimates of strength.

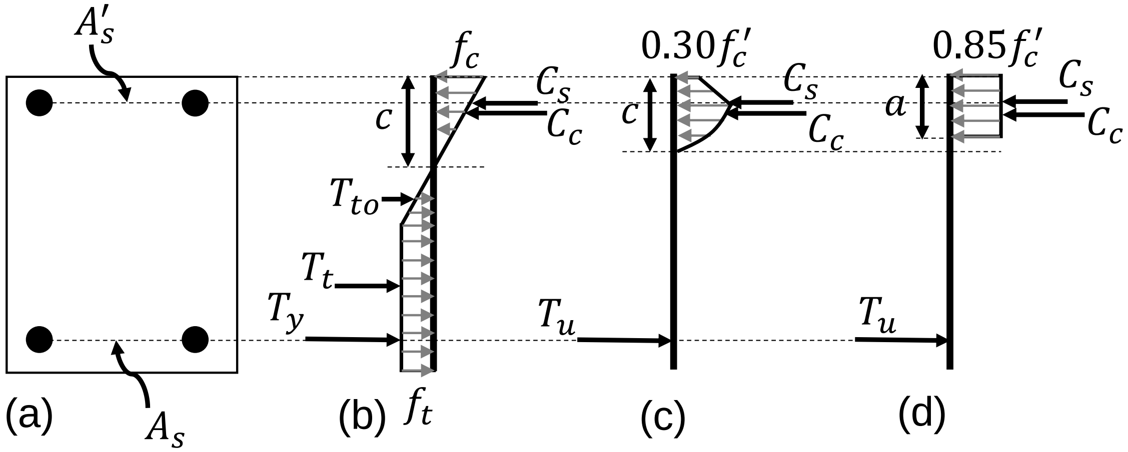

Figure 5.9 Analytical model for section analysis (a) cross-section (b) stress distribution at yield level (c) stress distribution at nominal level using modified Hognestad stress block (d) simplified stress distribution at nominal and ultimate level using Whitney stress block.
Source: [66, 131].

Table 5.3 Comparison of Experimental and Analytical Results at Yield Level

Specimen	Yield Rotation [rad]			Yield Moment [kNm]		
	Ana.	Exp.	Ana./Exp.	Ana.	Exp.	Ana./Exp.
UHPC-1%	1939	194	1.0	20	26	28
UHPC-2%	1960	196	2.0	20	26	28

Table 5.4 Comparison of Experimental and Analytical Results at Nominal and Ultimate Level

Specimen	Nominal Moment [kNm]					Ultimate Rotation [rad]		
	Exp.	Ana.^{1}	Ana.^{2}	Ana./Exp.^{1}	Ana./Exp.^{2}	Exp.	Ana.	Ana./Exp.
UHPC-1%	76	75	80	0.98	1.06	0.1002	0.083	0.83
UHPC-2%	72	75	81	1.03	1.12	0.1015	0.060	0.59

^{1}Figure 5.9 (c), ^{2}Figure 5.9 (d)

The ultimate rotation capacity was computed using Equation (4.4).

$$\theta_u = \theta_y + \theta_p = \frac{1}{2}\phi_y L_s + (\phi_u - \phi_y)L_p \tag{5.2}$$

where L_s is the shear span length (mm), ϕ_y and ϕ_u are the section curvatures of the structural member at yield level (mm^{-1}) and collapse level (mm^{-1}), respectively. In the above equation, L_p is the equivalent plastic hinge length (mm), which was computed using a recently developed expression based on a range of HPFRCC materials as shown in Equation (5.3) [20].

$$L_p = 0.02L_s + 0.24\frac{\rho f_y}{f_t} \tag{5.3}$$

where ρ is the longitudinal reinforcement (%), f_y is the yield stress (MPa), and f_t is the tensile strength of UHPC mixture (MPa). The analytical framework underestimated the ultimate rotation capacity in both specimens (Table 5.4). The reason for this discrepancy is the underestimation of equivalent plastic hinge length values for reinforced UHPC specimens tested in this experiment. The expression shown in Equation (5.3) was developed using reinforced HPFRCC beams with typical reinforcement ratio (i.e., $0.70\% < \rho < 1.90\%$) and a maximum tensile strength of 8 MPa. As such, the majority of the specimens followed the failure after crack localization path with damage localization in a dominant crack. In the current experiment, both the specimens followed failure after gradual strain hardening failure path due to the use of a high reinforcement ratio. The damage was uniformly distributed over longer length as seen from the crack patterns. Therefore, there is a need to further improve the plastic hinge length expression for highly reinforced UHPC beams (i.e., $\rho > 2.0\%$) using a more rigorous parametric investigation.

5.4 Conclusions

The study presented in this chapter provides valuable insight about the formation of plastic hinges with variation in fiber volume fraction. The following conclusions can be drawn from this study:

- The variation in fiber content does not impact ultimate rotation capacity in reinforced UHPC beams with high longitudinal reinforcement ratio ($\rho > 2.0\%$).
- The length of plasticity in the longitudinal reinforcement increases with a decrease in fiber volume fraction because of the formation of multiple distributed flexural cracks along the plastic hinge region.
- No significant difference in the curvature distribution was observed due to variation in the fiber content.
- Distribution of visible cracks in the specimens indicated that the damage is much more localized in specimens with higher fiber content ($L_{(majorcracks)} =$ 240mm) than those with low fiber content ($L_{(majorcracks)} =$ 420mm) because the UHPC matrix with high fiber content had higher tensile strength, bond strength, and fracture energy which restrained the formation of splitting cracks and prevented widening of flexural cracks.
- Experimental flexural strength and rotation at yield and nominal level were well predicted using the recently developed analytical methods.
- A parametric study with a wider variation in fiber content at high reinforcement ratios is necessary to further improve a recently developed plastic hinge length expression such that ultimate rotation capacity can be computed with higher accuracy.

CHAPTER 6

EXPERIMENTAL PROGRAM TO INVESTIGATE PLASTIC HINGE BEHAVIOR IN REINFORCED HPFRCC FLEXURAL MEMBERS

6.1 Introduction

The behavior of plastic hinge regions in conventional reinforced concrete members has been extensively studied through experimental research conducted on various types of structural components such as beams, columns, and shear walls [54–58, 95, 135]. These studies consider variations in material, cross-section, and loading properties to identify the fundamental variables impacting the plastic hinge region and associated deformation capacity of the structural component. This enabled researchers and practicing engineers to design new concrete structures and retrofit old concrete structures using displacement based design approaches rather than force based approaches [97, 136, 137].

Although extensive numerical studies to understand the variability in deformation capacity and plastic hinge behavior of HPFRCC structural components have been presented in the preceding chapters, conducting additional experiments with large scale HPFRCC structural components is important to complement the numerical and analytical studies. A review of the existing literature indicates that there have been considerable research efforts in the past to formulate analytical techniques to compute the nominal flexural strength of reinforced HPFRCC members through physical tests [125, 131, 138, 139]; however, very few studies have been conducted to study the plastic hinge behavior through physical experimentation [18, 93].

This chapter outlines an experimental program to investigate the plastic hinge behavior in reinforced HPFRCC flexural members. To reduce the number of physical tests, statistical observations made in Chapter 3 were used. Statistical analysis using full factorial design method indicated that the tensile strength of HPFRCC is the most statistically significant factor influencing deformation capacity (see Figure 3.15). Further, regression analysis carried out to develop the equivalent plastic hinge length expression in Chapter 4 showed that the *p-value* associated with the HPFRCC tensile strength was less than 0.001, indicating high statistical significance of the variable.

Apart from tensile strength of HPFRCC, the deformation capacity and plastic hinge behavior in reinforced HPFRCC components, as well as conventional reinforced concrete, varies significantly under monotonic and cyclic loading conditions [53, 103, 140, 141]. Therefore, loading criteria is another significant factor taken into consideration for physical experimentation.

Based on the statistical analysis, construction cost, and time associated with large scale experimentation, it was decided that a total of four tests (2 × 2) with variation in loading scenario (2) and HPFRCC material (2) would provide important data on the behavior of plastic hinge region. Each specimen will be subjected to monotonic and reversed cyclic loading conditions. Two variants of HPFRCCs with the upper bound and lower bound tensile strengths will be used for the experiment (i.e., UHPC ($f_t = 8.0$ MPa) and HyFRC ($f_t = 1.8$ MPa)). A larger shear-span-to-depth ratio ($L_{shear-span}/d = 7.15$) will be used for the experiment to limit shear deformations in the plastic hinge region. Cantilever beams will be cast instead of simply supported beams to investigate the influence of tensile strain penetration inside the joint. The moment-drift response, strains on longitudinal reinforcement and HPFRCC surface, maximum crack widths at incremental drift levels, crack patterns at different damage states, and component failure mode will be investigated. The details and expected outcomes of the experimental program are discussed in Sections 6.2 and 6.3.

6.2 Design of Experimental Program

6.2.1 Material and Mixture Proportions

Three types of materials will be used for the experimentation: an Ultra High Performance Concrete (UHPC), a Self-Consolidating Hybrid Fiber Reinforced Concrete (SC-HyFRC), and a Self-Consolidating Concrete (SC-C). Self-Consolidating type of mixtures will be used to avoid the problem associated with *fiber clumping*, to improve the workability, and to eliminate the use of external vibration techniques. SC-C is used in the foundation beam to reduce the cost of the experimental program as described in Section 6.2.3. The mixture proportion per cubic meter of each material are presented in Table 6.1 and the properties of fibers are listed in Table 6.2.

Table 6.1 Mixture Proportion of HPFRCCs and Concrete (per m^3)

Mixture	Binder [kg]				Aggregate [kg]		Water [kg]	Chemical Admixtures [wt. % of Binder]			Fibers [% Vol.]		
	C	FA	SF	GQ	Coarse	Fine		HRWR	A	VMA	SS	SH	PVA
UHPC	712	-	231	211	-	1020	109	3.26	3.18	-	2	-	-
SC-HyFRC	397	131	-	-	418	1044	237	0.93	-	2.21	-	1.3	0.2
SC-C	397	131	-	-	497	1006	237	0.42	-	0.40	-	-	-

C = Cement, FA = Fly ash, SF = Silica fume, GQ = Ground quartz

VMA = Viscosity modifying admixture, HRWR = High range water reducing admixture, A = Accelerator

Table 6.2 Fiber Properties

Notation	Material	Form	Length [mm]	Diameter [mm]	Strength [MPa]	Stiffness [GPa]
SS	Steel	Smooth	13	0.20	2600	205
SH	Steel	Hooked end	30	0.55	1100	200
PVA	Polyvinyl alcohol	Smooth	8	0.04	1600	43

The UHPC mixture used in the experiment will be a pre-mix blend (Ductal JS1000) with typical composition shown in Table 6.1 [77]. A high range water reducing admixture and an accelerator, supplied with the pre-mix blend, will be used during the mixing action to ensure workable and flowable UHPC mix. The mixture contains 2% by volume fraction (V_f) of smooth steel fibers with an aspect ratio (l_f/d_f) of 65, which provides UHPC with the characteristic "pseudo strain hardening" tensile behavior.

The SC-HyFRC mixture will contain Type I/II Portland Cement, Class F fly ash, coarse aggregate with nominal maximum size of 9.5 mm, fine aggregate with a fineness modulus of 3.2, a high range water reducing admixture (e.g., BASF Glenium 3030NS), and a viscosity modifying admixture (e.g., BASF Rheomac VMA 362). The SC-HyFRC mixture consists of a hybrid combination of steel macro-fibers and polyvinyl alcohol micro-fibers with a volume fraction of 1.3% and 0.2%, respectively. The aspect ratio of macro-fibers is 55 and that of micro-fibers is 200. The SC-C mixture will be designed to have a similar compressive strength as that of the SC-HyFRC mixture. The SC-C mixture will contain the same constituents as that of the SC-HyFRC mixture, with the only difference being in the absence of fibers [46, 74].

6.2.2 Mixing and Mechanical Properties

The mixing and casting of the beam specimens will be done in two stages with the use of two types of concrete mixers. In the first stage, SC-C will be mixed in a tilted rotary drum mixer and poured on the two sides of the foundation beam mold (i.e., 150 mm on each side as shown in Figure 6.2). The SC-C will then be cured inside the mold for 7 days using wet burlap and plastic sheets. After 7 days, the inner surface of SC-C sections in the foundation will be prepped. This will be done to ensure strong bond between the existing SC-C section and new HPFRCC section. In the second stage of casting, the HPFRCC material (UHPC or SC-HyFRC) will be mixed in a horizontal shear mixer and poured from the far-end of the cantilever side until the mixture fills up the mold at the foundation end. This pouring mechanism guarantees

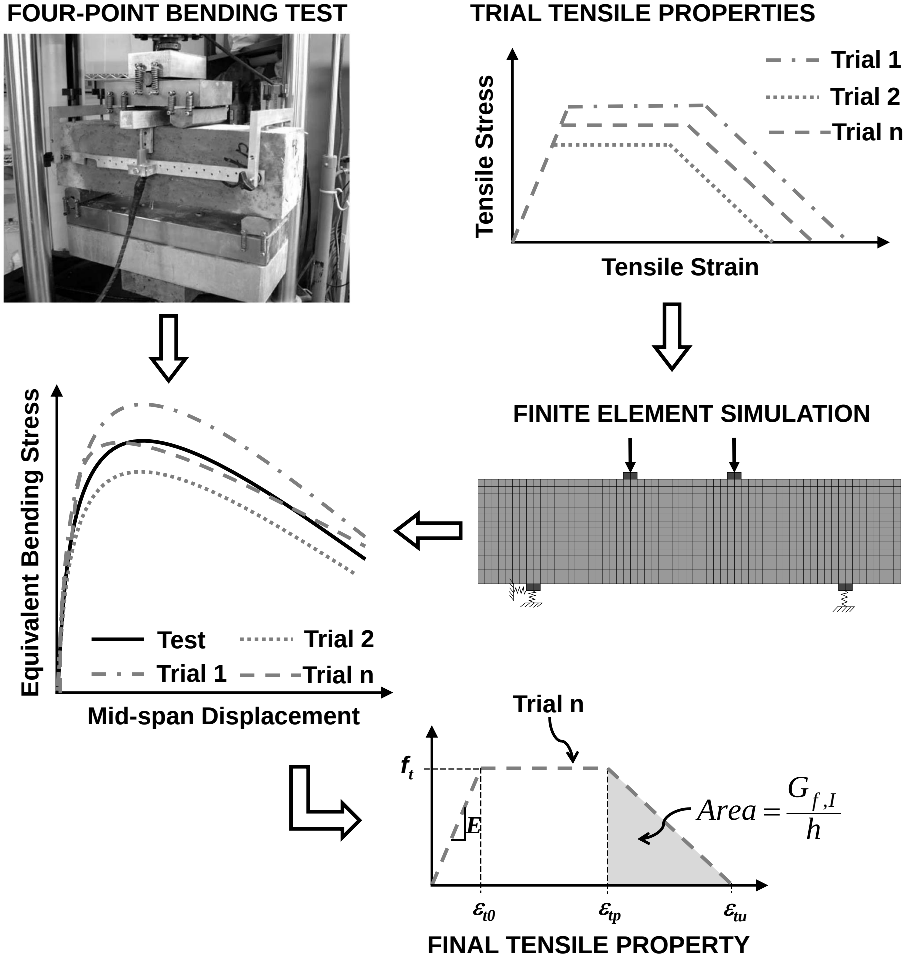

Figure 6.1 Framework of inverse analysis.

that the fibers are oriented along the longitudinal axis of the cantilever portion of the beam.

The rheology of the freshly mixed UHPC mixture will be measured using a modified flow table test as reported in the study conducted by FHWA [77, 142]. The flow-ability of the self-consolidating mixtures will be measured following the ASTM C1611−18 standard [143]. The unit weight and temperature of freshly mixed HPFRCCs and concrete will be measured in accordance with appropriate ASTM standards [144, 145]. To characterize the compression behavior, three UHPC cylinders with a diameter of 75 mm and a height of 150 mm, per cantilever specimen, will be cast following ASTM C1856−18 standard [134]. The same number of SC-HyFRC cylinders with a diameter of 100 mm and a height of 200 mm, per cantilever specimen, will be cast conforming to ASTM C39−15a standard [146]. For each cantilever specimen, the flexural behavior will be characterized by fabricating two prisms with a cross-section of 152 mm × 152 mm and a length of 533 mm [147].

All the specimens will be removed from the molds after 24 ± 8 hours of casting and moist cured. The specimens will be tested at 28 days ± 20 hours of casting [148]. The cylinders will be end ground before performing the tests. Compression tests of UHPC cylinders will be conducted at a loading rate of 4.5 kN/s ± 0.2 kN/s and that of SC-HyFRC cylinders will be conducted at a loading rate of 2 kN/s ± 0.4 kN/s in accordance with the appropriate ASTM standards [134, 146]. The flexural prism specimens will placed on a simply-supported setup and loaded at the third point. The UHPC prisms will be loaded at a rate of 0.025 mm/min to 0.075 mm/min and SC-HyFRC prisms will be loaded at the rate of 0.035 mm/min to 0.1 mm/min in accordance with ASTM C1609 standard [147].

An inverse analysis technique will be used to characterize the tensile behavior of UHPC and SC-HyFRC mixtures. The inverse analysis technique is an indirect method used to assess the uniaxial tension behavior of fiber reinforced concrete. It has been successfully used by the researchers in the past to obtain the full tensile stress-strain curve without resorting to the actual direct tension test [75, 82, 131, 149]. The framework of inverse analysis that will be adapted in this study is shown in Figure 6.1. The average equivalent bending stress and mid-span deflection response obtained from the four-point bending tests will be used as the test reference curve. Trial multi-linear tensile stress-strain curves will be used as an input tensile material model in a two-dimensional finite element model, with cross-section and boundary conditions similar to that of the test specimen. An incremental displacement-based loading of 0.01 mm will be applied to get the flexural response from the simulated specimen. Trial simulations will be continued until the numerical model with the closest flexural behavior to that of the test specimen is obtained. The final tensile stress-strain curve will be extracted from this numerical model and can be used as the substitute for direct tensile behavior.

The longitudinal reinforcement steel, conforming to ASTM A615 Grade 60 specification, will be used in the beam specimens. A uniaxial tension test will be conducted using an extensometer of gage length 50 mm to obtain the characteristic tensile properties of the deformed rebar used in the experiment. A displacement controlled loading rate of 0.015 mm/s to 0.003 mm/s will be used in accordance with ASTM E8−16a standard [150]. Transverse reinforcing steel conforming to ASTM A108 specification will be used in both the cantilever and foundation portion of the beam specimens. The transverse reinforcement will be a smooth round bar with a diameter of 6 mm and manufacturer specified yield strength of 370 MPa.

6.2.3 Test Setup, Matrix, and Specimen Details

Cantilever beam specimens with an enlarged foundation beam will be tested using the setup shown in Figure 6.2. HSS sections will be clamped to the strong floor using threaded rods to restraint the lateral movement of the foundation beam. Two HSS sections, one on each side, are placed on top of the foundation beam and connected to the strong floor using threaded rod to prevent the vertical movement of the foundation beam. The hydraulic actuator is connected to the top of the cantilever, using steel plates and threaded rods, on one side, and connected to the reaction wall, on the other side. The force will be applied to the cantilever and recorded through a load cell of the 490 kN hydraulic actuator.

A composite foundation beam will be cast to minimize the cost of construction. Conventional concrete will be used on the two sides of the foundation beam over a length of 150 mm, away from the joint region. HPFRCC will be used in the mid-region over a length of 510 mm, where the effect of strain penetration is expected. A speckle pattern will be created using hydrated lime and black spray paint over a length of 950 mm (i.e., 570 mm along cantilever and 380 mm along foundation). This surface preparation is required to measure strain using the digital image correlation (DIC) technique. A displacement transducer will be connected to the center-point of load plate to monitor displacement as further discussed in Section 6.2.4.

Table 6.3 Test Matrix

Notation	Loading Type	Material Type	$L_{shear-span}$ [mm]	Cross Section		Depth	Longitudinal Steel		Transverse Steel		
				b [mm]	h [mm]	d [mm]	d_b [mm]	Area [mm^2]	d_s [mm]	Area [mm^2]	Spacing [mm]
UHPC-M	Monotonic	UHPC	1140	130	180	160	13	258	6	32	75
UHPC-C	Cyclic										
HyFRC-M	Monotonic	SC-HyFRC	1140	130	180	160	13	258	6	32	75
HyFRC-C	Cyclic										

A total of four specimens will be tested as summarized in Table 6.3. The naming convention adopted in the study is based on the type of HPFRCC and loading scenario. For example, UHPC-M refers to a monotonic test specimen constructed with UHPC material. The shear span of the cantilever portion was increased to 1140 mm, from the original 1080 mm in the numerical specimens, to accommodate the position of the hydraulic actuator in the laboratory. The cross-section and longitudinal reinforcement area is the same as that of numerical cantilever specimen used in Chapters 3 and 4. Figure 6.3 shows the design of the experimental specimen with longitudinal reinforcement layout, transverse reinforcement layout, cross-section details, and location of strain gages. Two longitudinal reinforcing bars of 13 mm diameter in each side of the cross-section will be used in the cantilever portion (ρ = 1.25%), whereas six longitudinal reinforcing bars of 16 mm diameter will be used in the foundation. Transverse reinforcement will be provided at a spacing of 75 mm in both the cantilever and foundation. The cross-section width of the foundation

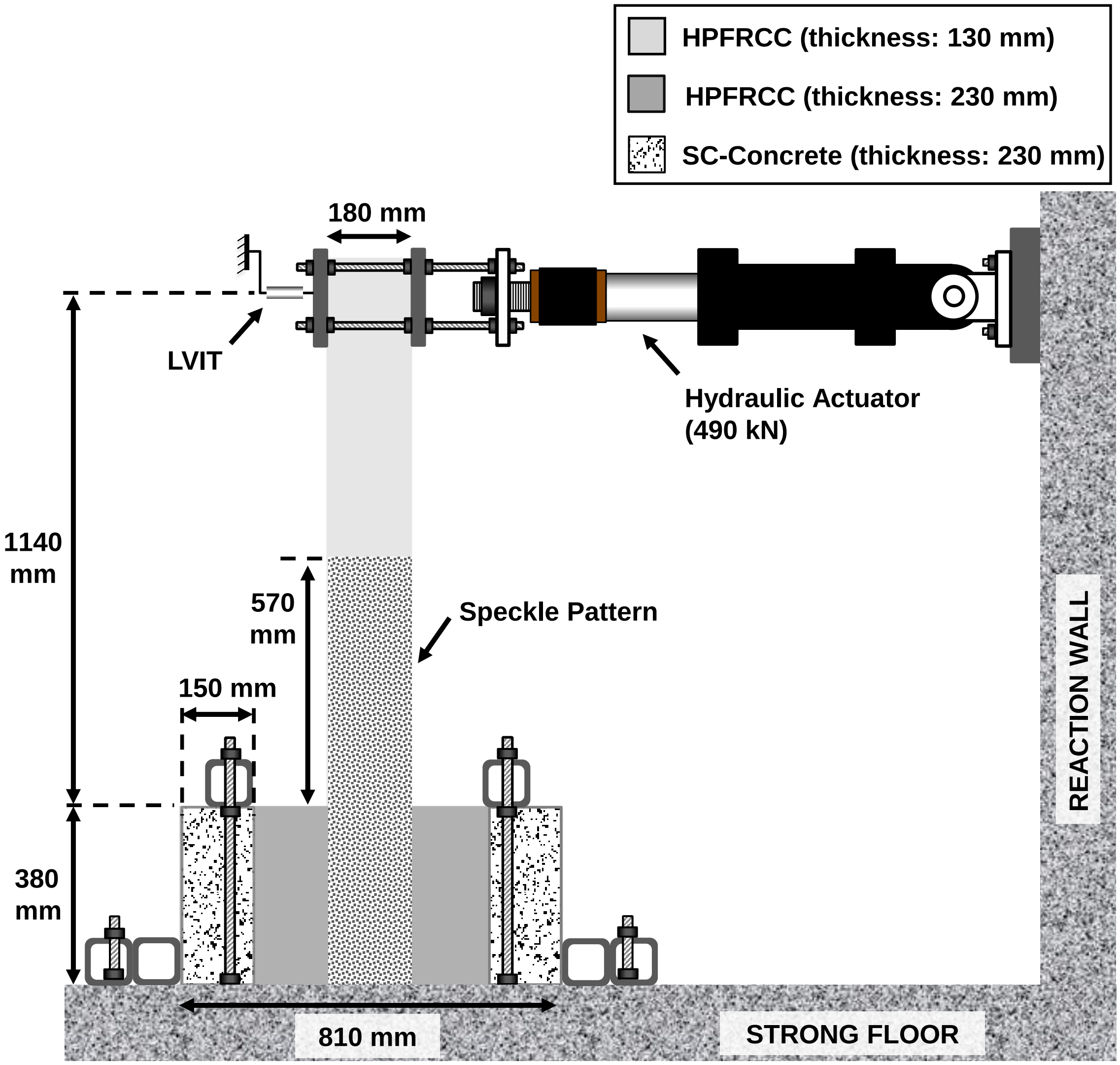

Figure 6.2 Test setup of reinforced HPFRCC beam with location of DIC surface and LVIT.

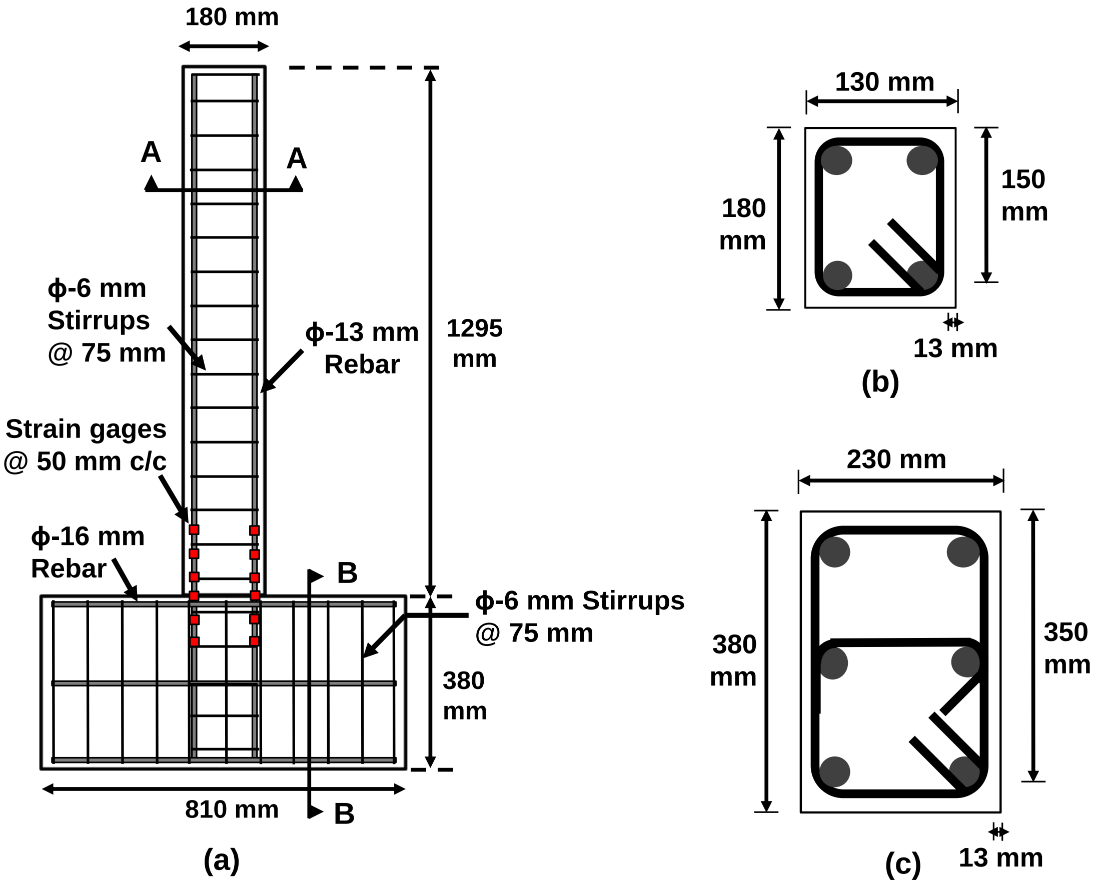

Figure 6.3 (a) Specimen design detail with location of strain gages (b) cross section at A-A (c) cross section at B-B.

was made larger to imitate framing of a cantilever beam inside a strong column (i.e., structural member with a higher flexural rigidity).

6.2.4 Data Acquisition System

Four types of data will be acquired from each test: applied load data, displacement data from the tip of the cantilever, strain data of reinforcement, and strain data of the HPFRCC surface near the joint region. The data will be collected using the data acquisition system plan as described below.

- *Load cell*: The applied load at every time step will be directly measured from the load cell of the hydraulic actuator. The description about the loading machine and protocol is discussed in Section 6.2.5
- *Linear variable inductive transducer*: A linear variable inductive transducer (LVIT) with a stroke length of 200 mm (LDI-119-200-A010A from OMEGA Instruments) will be used to measure the linear displacement of the tip of the cantilever beam. A single LVIT will be connected to the center-point of the load plate to measure the lateral displacement under monotonic load and two LVITs will be used, one on each side of the load plate, to measure the displacement under reversed cyclic loading condition.
- *Strain gage*: A total of twelve strain gages (KFH-6-120-C1-11L3M3R from OMEGA Instruments) will be used to measure the strain from the longitudinal reinforcement. Strain gages will be attached in two longitudinal bars located on the opposite bending sides (Figure 6.3). The gages in the rebar will be spaced 50 mm apart with two gages inside the foundation, one at the joint location, three in the cantilever portion. At strain gage locations, the ribs present in the deformed bars will be removed using an angle grinder before attaching the strain gages. Appropriate waterproofing and mechanical protection will be provided at the location of all the strain gages.
- *Digital Image Correlation*: A digital image correlation (DIC) system will be used to assess the strain from the bottom of foundation beam to half-span of cantilever beam as shown in Figure 6.2. DIC is an image-based data acquisition system, which is useful to measure displacement and strain fields in test specimens under different loading conditions. This technique requires the specimen surface to be prepared with a high-contrast speckle pattern to trace the displacement field. A digital camera can be used to capture images of the prepared surface, while the specimen is being loaded. The captured images will be analyzed using correlation algorithm developed in MATLAB based software, known as, Ncorr [151]. DIC is an emerging technology and is

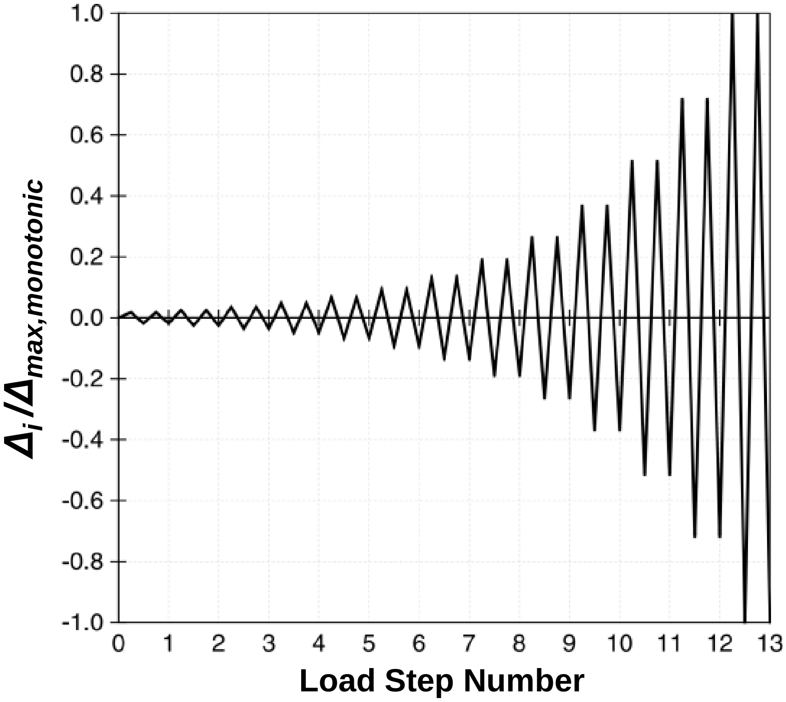

Figure 6.4 Cyclic loading protocol.

being increasingly used to investigate engineering behavior. In this study, the use of multiple LVITs to measure linear displacement and curvature near the critical section would require substantially more resource and budget; however, virtual extensometers of 50 mm length can be created inside the DIC system to measure the strain and curvature at two extreme fibers (tension zone and compression zone) of the cantilever specimen.

6.2.5 Loading Protocol

The beams will be tested under two types of loading conditions: monotonic and reversed cyclic loading. Each specimen will be tested under monotonic loading in the first phase of testing. A hydraulic actuator (MTS system) with a maximum load capacity of 490 kN will be used to apply the load. The specimens will be subjected to a quasi-static displacement controlled load rate of 0.097 mm/s [133, 152], until the specimen completely fails by achieving a damage state (e.g., fracture of rebar) or loses more than 50% of the peak load carrying capacity [53].

In the second phase of testing, the specimens will be subjected to cyclic loading history based in accordance with FEMA 461 report [86]. The cyclic loading history is a function of maximum monotonic deformation capacity, $\Delta_{\text{max,monotonic}}$, as shown in Figure 6.4. The specimens will be cycled two times at each amplitude, after which the displacement amplitude will be increased by 40%. The application of load will be stopped after the specimen reaches a failure state or if it loses 50% of the load carrying capacity [53].

6.3 Experimental Outcomes

The expected outcomes from this experimental study will be the global load-deformation response, reinforcement strain, HPFRCC surface strain, crack pattern at incremental drift levels, and validation of analytical methods. The discussion regarding each of these outcomes is given below.

- *Global response*: The global component-level response in terms of load vs. deformation will be obtained through the data acquisition system used in testing. The difference between monotonic and cyclic load-deformation response in two different classes of HPFRCC will be investigated. Further, the parameters such as initial stiffness, yield strength, yield drift, collapse strength, and collapse drift of specimens will be quantified and used to validate the numerical findings. The failure path and final failure mode of two types of reinforced HPFRCC cantilever specimens will be explored and compared with the numerical study.
- *Rebar strain*: The strain from the rebar surface at 12 locations will be collected in each specimen. The distribution of strain along the reinforcement bar under monotonic and cyclic loading will be compared. The length of reinforcement yield region, strain penetration length, and strain concentration region (i.e., rebar hardening region) will be quantified. The cyclic evolution of strain at various locations near the critical section will be investigated to under the impact of strain reversal on crack pattern and failure mode.
- *HPFRCC surface strain*: The principal tensile strain variation on the surface of HPFRCC will be investigated through DIC system. The phenomenon such as crack localization can be investigated and quantified using DIC technique. Furthermore, strain at the extreme fibers (tension and compression side) of the cantilever will be measured by creating virtual extensometers of 50 mm at every load step. Curvature values at various damage states can be computed based

on these measured strains. The strain distribution and curvature distribution along the plastic hinge region will be investigated.

- *Crack pattern*: The crack pattern will be recorded using a digital camera at 1% increments in the drift level. Crack characteristics such as maximum and minimum crack width at major damages states (e.g., rebar yielding, crack localization, rebar fracture, etc.) of four specimens will be quantified and investigated to understand the plastic hinge behavior. Longitudinal splitting crack will also be recorded at various damage states to understand its impact on flexural crack distribution and crack localization in the plastic hinge region of reinforced HPFRCC structural components.

- *Validation of analytical method*: The experimental equivalent plastic hinge length of the four specimens can be computed using Equation 4.6, by utilizing curvature distribution data obtained from DIC system. The robustness of the numerically developed equivalent plastic hinge length expressions proposed in Chapter 4 (Equation 4.11 and 4.10) will then be checked by comparing numerical values with the experimental calculated values. Similarly, the simplified analytical method presented in Chapter 4 can be used to compute the flexural strength and rotation capacity at different damage states. The mechanical properties of HPFRCCs and reinforcement can be used as input to perform the calculations. The analytical values can then be compared with the experimentally obtained values to validate and supplement the numerical findings of Chapter 4.

CHAPTER 7

CONCLUSIONS

7.1 Summary

This dissertation focused on understanding the behavior of steel reinforced HPFRCC structural components, which are being increasingly used as primary structural members in new buildings and bridges. The initial motivation behind this research was to understand the reason behind wide variability observed in deformation capacity of physically tested reinforced HPFRCC beams, at a specific reinforcement ratio [53]. To understand this variation in deformation capacity and plastic hinge behavior (*plastic hinge behavior is closely associated with deformability of structural components*), extensive numerical, statistical, and analytical studies in three major classes of HPFRCCs were performed. To supplement the numerical study, an experimental study with two steel reinforced UHPC specimens was conducted. Further, a detailed experimental program, with variation in mechanical properties and loading condition, has been outlined as a further research extension.

The influence of factors affecting component-level deformation capacity and plasticity in three types of HPFRCC materials (a Ultra High Performance Concrete, an Engineered Cementitious Composite, and a Hybrid Fiber Reinforced Concrete) were identified. A statistical analysis was carried identify the relative impact of various factors on component deformation capacity and bi-variate contour plots were developed to predict ultimate deformation capacity.

The plastic hinge behavior of reinforced HPFRCC components under monotonic and cyclic loading were investigated using numerical simulations. A recently proposed bond-slip constitutive relationship was incorporated in the numerical models to capture strain concentration and crack localization behavior in the plastic hinge region, as observed in physical experiments [53, 62, 131, 153]. Further, regression analysis was carried out to develop new equivalent plastic hinge length equations and a simplified analytical approach was proposed to compute flexural strengths and rotation capacities at different damage levels for a wide range of HPFRCC materials.

An experimental study with two steel reinforced UHPC beams under four-point bending setup was conducted. The UHPC matrix had variations in tensile strength and tensile fracture energy due to the use of fibers with different volume fractions (1% and 2%). The test was conducted under monotonic displacement based loading with both the beams having high reinforcement ratios ($\rho = 2.10\%$). An emphasis was placed on examining strain distribution and crack pattern in the plastic hinge region. The ability of the analytical method to compute flexural strengths and rotation capacities was also examined.

7.2 Conclusions and Contributions

7.2.1 Deformation Capacity and Plasticity

A series of two dimensional finite element simulations were conducted with variation in material and structural properties. Mechanical properties of HPFRCCs, steel reinforcement, and bond-slip parameters available in the literature were used to model the numerical specimens. A nonlinear static analysis using DIANA FEA Version 10.2 [110] was conducted to understand the influence of HPFRCC tensile strength, boundary condition, and shear span-to-depth ratio on the deformation capacity of reinforced HPFRCC components. Parameters such as moment-drift response, reinforcement strain distribution, reinforcement slip distribution, principal tensile strain contours, and drift at collapse were investigated to understand the cause of variability in the deformation capacity and plasticity.

The results of the study indicated that the component-level deformation capacity is inversely associated with the tensile strength of HPFRCC matrix. This relationship was observed consistently across a range of reinforcement ratios, test setups, and shear span-to-depth ratios. For example, simply supported beams with 0.70% reinforcement ratio had a reduction in the deformation capacity by 63% by increasing the tensile strength from 1.8 MPa (HyFRC) to 8 MPa (UHPC). In general, the simulated beams with small shear span-to-depth ratio ($L_{shear-span}/d = 4.06$) and low reinforcement ratio ($\rho = 0.70\%$) had a more pronounced effects due to variation in tensile strength of HPFRCCs.

The crack patterns showed that the reduction in deformation capacity are associated with the *crack localization phenomenon*. The HPFRCC with high tensile strength (UHPC) tends to form a single dominant flexural crack where the entire inelastic damage concentrates as observed in physical experiments [53, 62, 131, 153]. The tough matrix and high tensile fracture energy resists the formation of multiple dominant flexural cracks compared to the low tensile strength HPFRCCs (HyFRC), which allows the formation of multiple dominant cracks along the shear span of the beams.

A comparison of reinforcement slippage length in the specimens with different tensile strengths indicated that the slip length decreased, on average by 60%, when the tensile strength of HPFRCC increased from 1.8 MPa (HyFRC) to 8 MPa (UHPC). This indicates that the low rebar slip resulted in strain concentration over a smaller gage length of longitudinal reinforcement, and thereby early fracture of the reinforcement occurred in UHPC compared to HyFRC specimens.

The change in the boundary condition from cantilever to simply-supported resulted in a reduction of deformation capacity by as much as 43%, in reinforced HPFRCC beams. The UHPC beams were most significantly affected whereas HyFRC beams were least affected. The difference in the deformation capacity between cantilever beams and simply supported beams was mainly due to the ability of the cantilever beams to undergo additional rotation due to transfer of tensile strain into the foundation beam through a bond-slip mechanism between longitudinal reinforcement and HPFRCC matrix. Further, cantilever beams with HyFRC had 2.5 to 3 times longer length of plasticity inside the joint compared to UHPC beams.

The influence of shear span-to-depth ratio on deformation capacity was lower compared to the other factors investigated. The simulated results showed that there was reduction in deformation capacity, up to 26%, due to change in shear span-to-depth ratio in simply supported beams. The beams with short shear span were dominated by flexure-shear stress compared to long shear span beams with flexural stress. The crack patterns in long span beams were mostly transverse flexural crack near a critical section, whereas short span beams had a combination of transverse flexural cracks and diagonal shear cracks.

A multi-variate statistical analysis was carried out, at 95% confidence level, to quantify the magnitude of influence, statistical significance, and the direction of influence of the variables affecting the deformation capacity. It was found that the tensile strength of HPFRCC, reinforcement ratio, and boundary condition were the main factors impacting deformation capacity, in descending order of statistical significance. Further, bi-variate contour plots were generated to predict the component-level deformation capacity in cantilever and simply-supported setups. The contour plots had agreement with the existing experimental results [53] and can serve as a tool to estimate deformation capacity of reinforced HPFRCC members over a range of tensile strength and reinforcement ratios.

7.2.2 Plastic Hinge Behavior and Rotation Capacity

An advanced finite element based study was carried out to study the complex behavior of plastic hinge regions in HPFRCC structural components under monotonic and reversed cyclic loading conditions. A total strain based fixed crack model, plasticity model, and a recently proposed bond-slip model were incorporated in the numerical study to accurately simulate the strain distribution and damage patterns in plastic hinge region of HPFRCC members. The adopted numerical modeling technique was first shown to predict the moment-drift response, control points of backbone curve, and crack pattern in the plastic hinge region of physically tested reinforced HPFRCC beam specimens under monotonic and reversed cyclic loading conditions.

To understand the plastic hinge behavior in reinforced HPFRCC beams, tensile reinforcement strain profile was investigated along the length of beams. The results indicated that the length of reinforcement yielding region increased with a decrease in tensile strength of HPFRCC material (i.e., $(L_y)_{HyFRC} > (L_y)_{ECC} > (L_y)_{UHPC}$). Further, due to the effect of cyclic load reversal, the length of reinforcement yielding region increased under cyclic loading compared to monotonic loading. The tensile strain concentration region (i.e., rebar hardening region) was shortest in HPFRCC with the highest tensile strength and vice-versa. This was caused by accumulation of strain over a short de-bonded rebar length in a single dominant crack formed in HPFRCC with high tensile strength and tough matrix.

Similarly, the investigation of curvature distribution profile along the length of beams revealed that curvature localization was most noticeable in HPFRCCs with the highest tensile strength (UHPC) and least in HPFRCCs with the lowest tensile strength (HyFRC). This trend was observed across all loading and boundary conditions. Further, in simply supported beams, the length of curvature localization region was less under cyclic loading conditions compared to monotonic loading, whereas in cantilever beams the trend of curvature localization region was found to be reverse. This was caused due to increased post-yield strain penetration into the foundation under large cyclic load reversal in case of cantilever beams.

A new expression of equivalent plastic hinge length for reinforced HPFRCC flexural members was developed using numerical integration, structural mechanics, and regression analysis. The improved expression explicitly considers the effect of change in moment gradient, strain penetration effect, and influence of inelastic strain concentration. The existing empirical expressions over predicted plastic hinge length by more than 44% as compared to the new plastic hinge length expression because most of the existing empirical expressions were developed based on physical tests on traditional reinforced concrete. Further, the average simulated plastic hinge length values normalized by effective depth are listed in Table 7.1 to approximately calculate the equivalent plastic hinge length for the three types of HPFRCCs considered in this dissertation.

Table 7.1 Approximate Normalized Value of Plastic Hinge Length (L_p/d)

HPFRCC	Loading	Center Hinge			Joint Hinge		
Type	Type	$\rho = 0.70\%$	$\rho = 1.25\%$	$\rho = 1.90\%$	$\rho = 0.70\%$	$\rho = 1.25\%$	$\rho = 1.90\%$
UHPC	Monotonic	0.15	0.20	0.30	0.25	0.30	0.35
	Cyclic	0.10	0.15	0.20	0.25	0.35	0.55
ECC	Monotonic	0.20	0.45	0.70	0.35	0.55	0.70
	Cyclic	0.15	0.20	0.30	0.45	0.70	1.00
HyFRC	Monotonic	0.45	0.60	0.75	0.50	0.70	0.95
	Cyclic	0.20	0.25	0.40	0.65	0.80	1.35

A simple framework based on section analysis and a new plastic hinge length expression were developed to calculate flexural strengths and rotation values at multiple damage levels for reinforced HPFRCC flexural members. The framework was validated using an extensive experimental database of 50 reinforced HPFRCC test specimens with different boundary conditions, materials, and loading scenarios. The ultimate rotation value was computed using the analytical framework and the new plastic hinge length expression showed better prediction capability ($\mu_{C,RATIO} = 0.96$ and $\mu_{M,RATIO} = 0.75$) compared to the use of existing plastic hinge length equations. The flexural strength prediction under both types of loading scenario were found to be well predicted ($0.89 \leq \mu_{C,RATIO} \leq 1.02$ and $0.95 \leq \mu_{M,RATIO} \leq 1.05$) with low prediction scatter (CoV $\leq$ 15%).

7.2.3 Effect of Fiber Content Variation

Two reinforced UHPC beams with variation in fiber volume fraction were tested under a four-point bending setup. Both of the beams had high reinforcement ratio ($\rho >$ 2.0%) such that the compression capacity of UHPC was fully utilized under pure bending. The test was primarily conducted to understand the impact of using lower fiber content (V_f = 1%) on component-level ductility and stability of plastic hinge region.

The findings of the study show that reduction in fiber content by as much as 50% did not influence the yield and ultimate rotation capacity of reinforced UHPC beams having a high reinforcement ratio (i.e., ρ = 2.10%). This indicates that the structural component deformation capacity is less sensitive to fiber content (*or tensile strength of HPFRCC matrix*) in beams with high reinforcement ratio ($\rho >$ 2.0%). Both the tested beams failed through fracture of the longitudinal reinforcement after undergoing gradual strain hardening. The sensitivity of component response to the type of reinforcing bars used should be further explored.

The length of reinforcement yielding increased by 26% with a decrease in fiber volume fraction by 50%. This may be attributed to the formation of multiple distributed flexural cracks along the plastic hinge region due to decrease in fiber bridging action and a decrease in tensile strength of HPFRCC matrix. The distribution of plastic curvature in both specimens was not influenced by the change in fiber volume fraction.

The length of beam over which minor visible cracks appeared, increased by 75%, in the specimen with 1% fiber content compared to the specimen with 2% fiber content. This is due to lower fiber-bridging action and weaker matrix strength in specimens with lower fiber content. Furthermore, the dominant cracks widened over a longer length in the specimen with 1% fiber content compared to 2% specimen. The damage was much more localized in specimens with higher fiber content than those with low fiber content because the UHPC matrix with high fiber content had higher tensile strength which restrained the formation of splitting cracks and prevented widening of transverse cracks.

The post-yield rate of compression strain accumulation was found to be higher in the specimen with 2% fiber content compared to the specimen with 1% fiber content. Similarly, the rate of tensile strain accumulation in the mid-span rebar location was found to be higher in specimen with 2% fiber content. This shows that higher tensile strength matrix in specimen with 2% fiber content attracted larger stress and strain at lower deformation level.

Two different analytical models were used to successfully estimate the flexural strengths at yield and nominal level with less than 12% prediction error. The yield rotation values could be predicted with less than 3% error. However, the ultimate rotation capacity of the test specimens were underestimated by the analytical model. It is hypothesized that the ultimate rotation capacity of highly reinforced UHPC beams is not sensitive to tensile strength of HPFRCC matrix and that the collapse level response is governed by the mechanical behavior of longitudinal reinforcing bar.

7.3 Research Limitations

7.3.1 Deformation Capacity and Plasticity

The influence of various factors on deformation capacity and plasticity in reinforced HPFRCC were presented in Chapter 3. One of the limitation of the study was that the impact of the use of high strength steel and change in rebar hardening modulus (E_{sh}) were not considered as the part of the numerical study. The change in the rebar properties might influence the deformation capacity and plasticity in HPFRCC beams because of the change in the bond transfer mechanism between steel and HPFRCC matrix. This can ultimately lead to a significant difference in the formation of splitting cracks and transverse flexural cracks along the length of the structural member.

One of the other limitations of the study is that only a monotonic loading condition was used; however, the study can be extended to reversed cyclic loading as well to quantify the component-level deformation capacity in reinforced HPFRCC members.

7.3.2 Plastic Hinge Behavior and Rotation Capacity

In Chapter 4, the inelastic strain distribution and curvature distribution along the shear span of the simulated specimens were investigated to develop an equivalent plastic hinge length expression. Further, simplified analytical models were proposed to compute strength and rotation capacity of reinforced HPFRCC flexural members. The main limitation of this study is that physical experiments were not conducted to strengthen the numerical and analytical formulations. Although physical tests in large number of beams is not possible due to the high cost and long time associated with experiments, several large scale component-level tests will be conducted as future research extension. The detail experimental program has been outlined in Chapter 6.

Recently published ACI 318-19 building code [64] removed the provision for the use of Grade 40 steel for seismic applications. It recommends the use of either mild steel (Grade 60) or high strength steel (Grade 80 and 100) in girders, columns, and shear walls for seismic applications. The use of high strength steel in combination with HPFRCC can be ideal because of the ability of HPFRCC to restrict crack widths, limit the development length to a lower value, and withstand higher shear attracted by higher yield strength rebar. In light of this new recommendation from the building code, it is also necessary to understand the plastic hinge behavior in reinforced HPFRCC with the use of high strength rebar and make any improvements to the equivalent plastic hinge length expression, if needed.

7.3.3 Effect of Fiber Content Variation

The influence of change in fiber volume fraction in reinforced UHPC flexural member is presented in Chapter 5. Only two fiber contents (i.e., V_f =1% and 2%), were used for the investigation; however, additional fiber content variation should be considered to understand the impact in plastic hinge behavior of reinforced UHPC structural components. There is also a necessity to consider testing specimens under reversed cyclic loading and investigating the effect due to load reversals. Further, this study should be extended to other classes of HPFRCCs (e.g., ECC and HyFRC) to investigate the change in plastic hinge behavior and rotation capacity.

One of the other limitations of this study is that the DIC region should be extended to the entire shear-span length instead of the maximum moment region, if the conditions in the laboratory permits. This will help to measure the strain distribution along the shear-span of the beam, even if, the post-yield strain gage attached to the reinforcement fails at large drift level due to electro-mechanical issues.

7.4 Future Research Extensions

This dissertation focused on numerical, statistical, and experimental methods to predict the flexural deformation, strength, and plastic hinge length of structural components constructed with a wide range of HPFRCC materials. However, there are many important areas pertinent to physical experimentation, modeling, and design of HPFRCC components which need further research considerations. The following is a list of such areas that the author believes require investigation.

- More physical experiments have to be conducted with a wider variability in material and structural properties using linear displacement transducers and post-yield strain gages near the maximum moment region to further validate the numerical and analytical findings of this dissertation.

- Damage states (e.g., yielding and fracture) of reinforced HPFRCC flexural members can be numerically predicted using smeared crack approach at the continuum level; however, there is still a need to develop numerically efficient and robust constitutive models for both 2D and 3D finite element analysis to fully capture the hysteretic response under reversed cyclic loading. Material characterization tests under bi- and tri-axial conditions, for major classes of HPFRCCs (e.g., UHPC, ECC, and HyFRC), should be conducted to aid the development of such models.

- The research presented in this dissertation can serve as a framework to conduct research study in order to identify factors affecting deformation capacity and plasticity in columns constructed with HPFRCCs. A study to quantify the plastic hinge length and rotation capacity by varying factors such as, axial load ratio, is necessary to advance the use of HPFRCCs in plastic hinge region of bridge piers in seismically active zones. Furthermore, it is also necessary to quantify hysteretic parameters to accurately and efficiently model nonlinearity in bridge piers, enabling the strategic use of HPFRCCs in potential plastic hinge regions.

- Recent experimental studies [119, 131, 153] indicate that the compression capacity of HPFRCCs can be fully utilized in the flexural members by using mild steel (Grade 60) with high reinforcement ratio ($\rho > 2.0\%$) or high strength steel (Grade 80 or Grade 100) with moderate reinforcement ratio ($1.0\% < \rho < 2.0\%$). However, to quantify the plastic rotation capacity in such members, there is a need to conduct a parametric study to identify dominant variables affecting the plastic hinge region and rotation capacity.

- Experimental studies with variation in fiber content and longitudinal reinforcement in flexural members constructed with other classes of HPFRCCs, such as ECC and HyFRC, should also be done to investigate any changes in overall flexural behavior due to differences in fiber bridging action.

REFERENCES

[1] U. Riedel and J. Nickel. Natural fibre-reinforced biopolymers as construction materials–new discoveries. *Macromolecular Materials and Engineering*, 272(1):34–40, 1999.

[2] V.C. Li. On engineered cementitious composites (ECC) a review of the material and its applications. *Journal of Advanced Concrete Technology*, 1(3):215–230, 2003.

[3] J. R. Correia, L. Valarinho, and F. A. Branco. Post-cracking strength and ductility of glass-GFRP composite beams. *Composite Structures*, 93(9):2299–2309, 2011.

[4] H. M. Jonkers, A. Thijssen, G. Muyzer, O. Copuroglu, and E. Schlangen. Application of bacteria as self-healing agent for the development of sustainable concrete. *Ecological Engineering*, 36(2):230–235, 2010.

[5] A. Palomo, M. W. Grutzeck, and M. T. Blanco. Alkali-activated fly ashes: a cement for the future. *Cement and Concrete Research*, 29(8):1323–1329, 1999.

[6] P. K. Mehta and P. M. Monteiro. *Concrete: Microstructure, Properties, and Materials*. New York, NY: McGrawHill, third edition, 2006.

[7] M. G. Juenger, F. Winnefeld, J. L. Provis, and J. H. Ideker. Advances in alternative cementitious binders. *Cement and Concrete Research*, 41(12):1232–1243, 2011.

[8] L. Burris, K. Kurtis, and T. Morton. Novel alternative cementitious materials for development of the next generation of sustainable transportation infrastructure. Technical Report Publication No. FHWA-HRT-16-017, Federal Highway Administration, McLean, Virginia, USA, 2015.

[9] G. P. Gonzalez and H. K. Moo-Young. Transportation applications of recycled concrete aggregate. *FHWA state of the Practice National Review*, 2004.

[10] M. S. Winfield and A. Taylor. Rebalancing the load: the need for an aggregate conservation strategy for Ontario. Technical report, Pembina Institute, Toronto, ON, 2005.

[11] X. Li. Recycling and reuse of waste concrete in china: Part ii. structural behaviour of recycled aggregate concrete and engineering applications. *Resources, Conservation and recycling*, 53(3):107–112, 2009.

[12] J. F. Bonacci and M. Maalej. Externally bonded fiber-reinforced polymer for rehabilitation of corrosion damaged concrete beams. *Structural Journal*, 97(5):703–711, 2000.

[13] A. S. Debaiky, M. F. Green, and B. B. Hope. Carbon fiber-reinforced polymer wraps for corrosion control and rehabilitation of reinforced concrete columns. *Materials Journal*, 99(2):129–137, 2002.

[14] J. Li, J. Gong, and L. Wang. Seismic behavior of corrosion-damaged reinforced concrete columns strengthened using combined carbon fiber-reinforced polymer and steel jacket. *Construction and Building Materials*, 23(7):2653–2663, 2009.

[15] M. Badawi and K. Soudki. Control of corrosion-induced damage in reinforced concrete beams using carbon fiber-reinforced polymer laminates. *Journal of composites for construction*, 9(2):195–201, 2005.

[16] D. R. Lankard. Properties, applications: slurry infiltrated fiber concrete (sifcon). *Concrete International*, 6(12):44–47, 1984.

[17] L. E. Hackman, M. B. Farrell, and O. O. Dunham. Slurry infiltrated mat concrete (simcon). *Concrete International*, 14(12):53–56, 1992.

[18] A. E. Naaman, P. Paramasivam, G. Balazs, and ... G. Lohrmann. Reinforced and prestressed concrete using HPFRCC matrices. In A. E. Naaman and H. W. Reinhardt, editors, *Proceedings of the Second International RILEM Workshop - High Performance Fiber Reinforced Cement Composites 2 (HPFRCC-2)*, pages 291–347, London, UK, 1996. London, UK: E&FN Spon.

[19] A. Bentur and S. Mindess. *Fibre Reinforced Cementitious Composites.* New York, NY: CRC Press, second edition, 2006.

[20] V. C. Li. From micromechanics to structural engineering-the design of cementitous composites for civil engineering applications. *Journal of Structural Mechanics and Earthquake Engineering*, 10(2):37–48, 1993.

[21] S. L. Billington and J. K. Yoon. Cyclic response of unbonded posttensioned precast columns with ductile fiber-reinforced concrete. *ASCE Journal of Bridge Engineering*, 9(4):353–363, 2004.

[22] B. A. Canbolat, G. J. Parra-Montesinos, and J. K. Wight. Experimental study on seismic behavior of high-performance fiber-reinforced cement composite coupling beams. *ACI Structural Journal*, 102(1):159–166, 2005.

[23] G. Fischer and V. C. Li. Effect of matrix ductility on deformation behavior of steel-reinforced ECC flexural members under reversed cyclic loading conditions. *ACI Structural Journal*, 99(6):781–790, 2002.

[24] K. Kim and G. J. Parra-Montesinos. Behavior of HPFRCC Low-Rise Walls Subjected to Displacement Reversals. In A. E. Naaman and H. W. Reinhardt, editors, *Proceedings of the High Performance Fiber Reinforced Cement Composites 4 (HPFRCC-4)*, pages 505–515, Cachan Cedex, France, 2004. Bagneux, France: RILEM Publications S.A.R.L.

[25] K. E. Kesner and S. L. Billington. Investigation of infill panels made from engineered cementitious composites for seismic strengthening and retrofit. *Journal of Structural Engineering*, 131(11):1712–1720, 2005.

[26] E. C. Olsen and S. L. Billington. Cyclic response of precast high-performance fiber-reinforced concrete infill panels. *ACI Structural Journal*, 108(1):51–60, 2011.

[27] G. J. Parra-Montesinos and P. Chompreda. Deformation capacity and shear strength of fiber-reinforced cement composite flexural members subjected to displacement reversals. *Journal of Structural Engineering*, 133(3):421–431, 2007.

[28] G. J. Parra-Montesinos, S. W. Peterfreund, and S. H. Chao. Highly damage-tolerant beam-column joints through use of high-performance fiber-reinforced cement composites. *ACI Structural Journal*, 102(5):487–495, 2005.

[29] S. Sritharan. Design of uhpc structural members: Lessons learned and astm test requirements. *Advances in Civil Engineering Materials*, 4(2):113–131, 2015.

[30] L. Hou, R. Xu, D. Chen, S. Xu, and F. Aslani. Seismic behavior of reinforced engineered cementitious composite members and reinforced concrete/engineered cementitious composite members: A review. *Structural Concrete*, 21(1):199–219, 2020.

[31] V. C. Li and H. Stang. Elevating FRC material ductility to infrastructure durability. In M. Prisco, R. Felicetti, and G. A. Plizzari, editors, *Proceedings of the Sixth RILEM Symposium on Fiber-Reinforced Concretes (BEFIB 2004)*, pages 171–186, Varenna, Italy, 2004. Bagneux, France: RILEM Publications S.A.R.L.

[32] C. P. Ostertag and J. Blunt. Use of fiber reinforced concrete in bridge approach slabs. Technical Report CA09-0632, Caltrans Division of Research & Innovation, California Department of Transportation Engineering Services Center, Sacramento, California, USA, 2008.

[33] ACI Committee 318. Building code requirements for structural concrete (ACI 318-14) and commentary. Technical Report ACI 318-14, American Concrete Institute, Farmington Hills, Michigan, USA, 2014.

[34] R. Lequesne, M. Setkit, C. Kopczynski, J. Ferzli, M. Y. Cheng, G. J. Parra-Montesinos, and J. K. Wight. Implementation of high-performance fiber reinforced concrete coupling beams in high-rise core-wall structures. *ACI Special Publication*, SP-280(7):1–12, 2011.

[35] V. C. Li. Can concrete be bendable? *American Scientist*, 100(6):484–493, 2012.

[36] H. G. Russell and B. A. Graybeal. Ultra-high performance concrete: A state-of-the-art report for the bridge community. Technical Report Publication No. FHWA-HRT-13-060, Federal Highway Administration, McLean, Virginia, USA, 2013.

[37] Z. B. Haber, I. D. Varga, B. A. Graybeal, B. Nakashoji, and R. El-Helou. Properties and behavior of uhpc-class materials. Technical Report Publication No. FHWA-HRT-18-036, Federal Highway Administration, McLean, Virginia, USA, 2018.

[38] K. E. Kesner, S. L. Billington, and K. S. Douglas. Cyclic response of highly ductile fiber-reinforced cement-based composites. *ACI Materials Journal*, 100(5):381–390, 2003.

[39] V. C. Li, S. Wang, and C. Wu. Tensile strain-hardening behavior of polyvinyl alcohol engineered cementitious composite (pva-ecc). *ACI Materials Journal*, 98(6):483–492, 2001.

[40] A. E. Naaman and H. W. Reinhardt. Proposed classification of hpfrc composites based on their tensile response. *Materials and Structures*, 39(5):547–555, 2006.

[41] B. Gencturk and A. S. Elnashai. Numerical modeling and analysis of ecc structures. *Materials and structures*, 46(4):663–682, 2013.

[42] T. S. Han, P. H. Feenstra, and S. L. Billington. Simulation of highly ductile fiber-reinforced cement-based composite components under cyclic loading. *ACI Structural Journal*, 100(6):749–757, 2003.

[43] C. C. Hung and S. El-Tawil. Hybrid Rotating/Fixed-Crack Model for High-Performance Fiber-Reinforced Cementitious Composites. *ACI Materials Journal*, 107(6):568–576, 2010.

[44] C. C. Hung and S. H. Li. Three-dimensional model for analysis of high performance fiber reinforced cement-based composites. *Composites Part B: Engineering*, 45(1):1441–1447, 2013.

[45] G. J. Parra-Montesinos. High-performance fiber-reinforced cement composites: An alternative for seismic design of structures. *ACI Structural Journal*, 102(5):668–675, 2005.

[46] M. J. Bandelt and S. L. Billington. Bond behavior of steel reinforcement in high-performance fiber-reinforced cementitious composite flexural members. *Materials and Structures*, 49(1):71–86, 2016.

[47] M. J. Bandelt, T. E. Frank, M. D. Lepech, and S. L. Billington. Bond behavior and interface modeling of reinforced high-performance fiber-reinforced cementitious composites. *Cement and Concrete Composites*, 83:188–201, 2017.

[48] S. H. Chao, A. E. Naaman, and G. J. Parra-Montesinos. Bond behavior of reinforcing bars in tensile strain-hardening fiber-reinforced cement composites. *ACI Structural Journal*, 106(6):897–906, 2009.

[49] M. H. Harajli. Bond Stress Slip Model for Steel Bars in unconfined or Steel , FRC , or FRP confined concrete. *Journal of Structural Engineering*, 135(5):509–518, 2009.

[50] D. M. Moreno, W. Trono, G. Jen, C. Ostertag, and S. L. Billington. Tension stiffening in reinforced high performance fiber reinforced cement-based composites. *Cement and Concrete Composites*, 50(2014):36–46, 2014.

[51] G. Fischer and V. C. Li. Influence of matrix ductility on tension-stiffening behavior of steel reinforced engineered cementitious composites (ECC). *ACI Structural Journal*, 99(1):104–111, 2002.

[52] C. C. Hung, H. S. Lee, and S. Nga. Tension-stiffening effect in steel-reinforced UHPC composites : Constitutive model and effects of steel fibers. *Composites Part B: Engineering*, 158(August 2018):269–278, 2019.

[53] M. J. Bandelt and S. L. Billington. Impact of reinforcement ratio and loading type on the deformation capacity of high-performance fiber-reinforced cementitious composites reinforced with mild steel. *Journal of Structural Engineering*, 142(10):04016084, 2016.

[54] W. Corley. Rotational capacity of reinforced concrete beams. *Journal of the Structural Division*, 92(5):121–146, 1966.

[55] A. H. Mattock. Discussion of rotational capacity of reinforced concrete beams. *Journal of the Structural Division*, 93(2):519–522, 1967.

[56] T. Paulay and M. J. N. Priestley. *Seismic Design of Reinforced Concrete and Masonry Buildings*. New York, NY: John Wiley & Sons, 1992.

[57] E. M. Hines, J. I. Restrepo, and F. Seible. Force-displacement characterization of well-confined bridge piers. *ACI Structural Journal*, 101(4):537–548, 2004.

[58] S. Bae and O. Bayrak. Plastic hinge length of reinforced concrete columns. *ACI Structural Journal*, 105(3):290–300, 2008.

[59] I. Kazaz. Analytical study on plastic hinge length of structural walls. *Journal of Structural Engineering*, 139(11):1938–1950, 2012.

[60] L. Xu, J. Pan, C. Lu, and W. Yin. Development mechanism of plastic hinge in reinforced engineered cementitious composite beams under monotonic loading. *Structural Concrete*, pages 1–15, 2018.

[61] H. Tariq, E. A. Jampole, and M. J. Bandelt. Fiber-hinge modeling of engineered cementitious composite flexural members under large deformations. *Engineering Structures*, 182:62–78, 2019.

[62] D. Y. Yoo and Y. S. Yoon. Structural performance of ultra-high-performance concrete beams with different steel fibers. *Engineering Structures*, 102:409–423, 2015.

[63] T. E. Frank, M. D. Lepech, and S. L. Billington. Experimental testing of reinforced ecc beams subjected to various cyclic deformation histories. *Journal of Structural Engineering*, 144(6):04018052, 2018.

[64] ACI Committee 318. Building code requirements for structural concrete (ACI 318-14) and commentary. Technical Report ACI 318-19, American Concrete Institute, Farmington Hills, Michigan, USA, 2019.

[65] M. Pokhrel and M. J. Bandelt. Material properties and structural characteristics influencing deformation capacity and plasticity in reinforced ductile cement-based composite structural components. *Composite Structures*, 224:111013, 2019.

[66] M. Pokhrel and M. J. Bandelt. Plastic hinge behavior and rotation capacity in reinforced ductile concrete flexural members. *Engineering Structures*, 200:109699, 2019.

[67] A. M. Brandt. Fibre reinforced cement-based (frc) composites after over 40 years of development in building and civil engineering. *Composite structures*, 86(1-3):3–9, 2008.

[68] J. P. Romualdi and G. B. Batson. Mechanics of crack arrest in concrete. *Journal of Engineering Mechanics Division*, 89(3):147–168, 1963.

[69] J. P. Romualdi and J. A. Mandel. Tensile strength of concrete affected by uniformly distributed and closely spaced short lengths of wire reinforcement. *Journal of ACI*, 61(6):657–671, 1964.

[70] P. Balaguru and J. Kendzulak. Mechanical properties of slurry infiltrated fiber concrete (sifcon). *Special Publication*, 105:247–268, 1987.

[71] N. K. Opara and S. Malak. Tensile behavior of slurry infiltrated mat concrete (simcon). *Materials Journal*, 94(1):39–46, 1997.

[72] R. D. Lequesne, G. J. Parra-Montesinos, and J. K. Wight. Seismic Behavior and Detailing of High-Performance Fiber-Reinforced Concrete Coupling Beams and Coupled Wall Systems. *Journal of Structural Engineering*, 139(8):1362–1370, 2013.

[73] M. Panagiotou, W. Trono, G. Jen, P. Kumar, and C. Ostertag. Experimental seismic response of hybrid fiber-reinforced concrete bridge columns with novel longitudinal reinforcement detailing. *ASCE Journal of Bridge Engineering*, pages 1–12, 2014.

[74] G. Jen, W. Trono, and C. P. Ostertag. Self-consolidating hybrid fiber reinforced concrete : Development , properties and composite behavior. *Construction and Building Materials*, 104:63–71, 2016.

[75] M. J. Bandelt and S. L. Billington. Simulation of deformation capacity in reinforced high-performance fiber-reinforced cementitious composite flexural members. *Journal of Structural Engineering*, 144(10):04018188, 2018.

[76] P Richard and M. H. Cheyrezy. Reactive powder concrete. *Cement and Concrete Research*, 25(7):1501–1511, 1995.

[77] B. A. Graybeal. Material property characterization of ultra-high performance concrete. Technical Report Publication No. FHWA-HRT-06-103, Federal Highway Administration, McLean, Virginia, USA, 2006.

[78] K. Wille and A. E. Naaman. Fracture energy of uhpfrc under direct tensile loading. In et al. B.H. Oh, editor, *Proceedings of the Fracture Mechanics of Concrete and Concrete Structures (FraMCoS-7)*, pages 65–72, Jeju, Korea, 2010.

[79] B. A. Graybeal and F. Baby. Development of direct tension test method for ultra-high-performance fiber-reinforced concrete. *ACI Materials Journal*, 110(2), 2013.

[80] V. C. Li and C .Y. Leung. Steady-state and multiple cracking of short random fiber composites. *Journal of Engineering Mechanics*, 118(11):2246–2264, 1992.

[81] V. C. Li. *Engineered Cementitious Composites (ECC) - Material, Structural, and Durability Performance*, chapter 24. London,UK: CRC Press, 2008.

[82] D. Moreno-Luna. *Tension stiffening in reinforced high performance fiber reinforced cement based composites.* PhD. Dissertation, Stanford University, 2014.

[83] J. Blunt and C. P. Ostertag. Performance-based approach for the design of a deflection hardened hybrid fiber-reinforced concrete. *Journal of Engineering Mechanics*, 135(9):978–986, 2009.

[84] P. Kumar, G. Jen, W. Trono, D. Lallemant, M. Panagiotou, and C. P. Ostertag. Self compacting hybrid fiber reinforced concrete composites for bridge columns. Technical Report PEER Report 2011/106, Pacific Earthquake Engineering Research Center, University of California, Berkeley, California, USA, 2011.

[85] T. E. Frank. *Response of reinforced engineered cementitious composite flexural members subjected to various cyclic deformation histories.* PhD. Dissertation, Stanford University, 2017.

[86] FEMA. Interim testing protocols for determining the seismic performance characteristics of structural and nonstructural components. Technical Report FEMA 461, Federal Emergency Management Agency, Washington D.C., USA, 2007.

[87] M. J. N. Priestley. Performance based seismic design. *Bulletin of the New Zealand Society for Earthquake Engineering*, 33(3):325–346, 2000.

[88] A. Ghobarah. Performance-based design in earthquake engineering: state of development. *Engineering structures*, 23(8):878–884, 2001.

[89] F. Yuan, J. Pan, Z. Xu, and C. Y. Leung. A comparison of engineered cementitious composites versus normal concrete in beam-column joints under reversed cyclic loading. *Materials and structures*, 46(1-2):145–159, 2013.

[90] H. Tavallali, A. Lepage, J. M. Rautenberg, and S. Pujol. Concrete beams reinforced with high-strength steel subjected to displacement reversals. *ACI Structural Journal*, 111(5):1037–1048, 2014.

[91] T. E. Frank, M. D. Lepech, and S. L. Billington. Effect of deformation history on steel-reinforced hpfrcc flexural member behavior. In H. W. Reinhardt, G. J. Parra-Montesinos, and H. Garrecht, editors, *Proceedings of the Seventh International Workshop on High Performance Fiber Reinforced Cement Composites (HPFRCC-7)*, Stuttgart, Germany, June 01–03, 2015. Bagneux, France: RILEM Publications S.A.R.L.

[92] C. C. Hung and C. Y. Chueh. Cyclic behavior of uhpfrc flexural members reinforced with high-strength steel rebar. *Engineering Structures*, 122:108–120, 2016.

[93] A. Hemmati, A. Kheyroddin, and M. K. Sharbatdar. Plastic hinge rotation capacity of reinforced hpfrcc beams. *Journal of Structural Engineering*, 141(2):04014111, 2013.

[94] J. K. Wight. *Reinforced Concrete: Mechanics and Design.* Hoboken, NJ: Pearson, seventh edition, 2015.

[95] H. A. Sawyer. Design of concrete frames for two failure stages. *ACI Structural Journal*, pages 405–437, 1964.

[96] M. P. Berry, D. E. Lehman, and L. N. Lowes. Lumped-plasticity models for performance simulation of bridge columns. *ACI Structural Journal*, 105(3):270, 2008.

[97] ASCE. Seismic evaluation and retrofit of existing buildings. Technical Report ASCE/SEI 41-13, American Society of Civil Engineers, Reston, Virginia, USA, 2014.

[98] J. Moehle, Y. Bozorgnia, N. Jayaram, P. Jones, M. Rahnama, and N. Shome. Case studies of the seismic performance of tall buildings designed by alternative means. Technical Report PEER Report 2011/05, Pacific Earthquake Engineering Research Center, Berkeley, California, USA, 2011.

[99] M. L. Marsh, I. G. Buckle, and Jr. Edward Kavazanjian. LRFD Seismic Analysis and Design of Bridges Reference Manual. Technical Report FHWA-NHI-15-004, Federal Highway Administration, Washington, DC, USA, 2014.

[100] M. Pokhrel, P. Warnitchai, and T. Ornthammarath. The effect of ground motion selection procedure and hazard spectra on design seismic demand of near-fault reinforced concrete tall buildings. In Liang-Jenq Leu and Kung-Chun Lu, editors, *Proceedings of the Fifth Asia Conference on Earthquake Engineering (5ACEE)*, Taipei, Taiwan, October 16–18, 2014.

[101] T. B. Panagiotakos and M. N. Fardis. Deformations of reinforced concrete members at yielding and ultimate. *ACI Structural Journal*, 98(2):135–148, 2001.

[102] X. M. Zhao, Y. F. Wu, and A. T. Leung. Analyses of plastic hinge regions in reinforced concrete beams under monotonic loading. *Engineering Structures*, 34:466–482, 2012.

[103] F. Yuan and Y. F. Wu. Effect of load cycling on plastic hinge length in rc columns. *Engineering Structures*, 147:90–102, 2017.

[104] T. E. Frank, M. D. Lepech, and S. L. Billington. Experimental testing of reinforced concrete and reinforced ECC flexural members subjected to various cyclic deformation histories. *Materials and Structures*, 50(5):232, 2017.

[105] P. H. Feenstra, J. G. Rots, A. Arnesen, J. G. Teigen, and K. V. Hoiseth. A 3D constitutive model for concrete based on a con-rotational concept. In De Borst, Bicanic, Mang, and Meschke, editors, *Proceedings of the Computational Modeling of Concrete Structures, (Euro-C 1998)*, pages 13–22, Rotterdam, Netherlands, 31 March–03 April, 1998. Leiden,Netherlands: Balkema.

[106] M. Z. Cohn and S. K. Ghosh. The flexural ductility of reinforced concrete sections. *Publications of the International Associate of Bridge and Structural Engineers*, 32(2):86–83, 1972.

[107] M. J. Bandelt and S. L. Billington. Simulating bond-slip effects in high-performance fiber-reinforced cement based composites under cyclic loads. In René de Borst Nenad Bícanić, Herbert Mang, Günther Meschke, editor, *Proceedings of the Computational Modeling of Concrete Structures (EURO-C 2014)*, pages 1059 – 1066, St. Anton am Arlberg, Austria, March 24–27, 2014. London,UK: CRC Press.

[108] S. L. Billington, Y. Shao, T. E. Frank, M. J. Bandelt, and D. M. Moreno. Simulation of reinforced ductile cement-based composite beams under cyclic loads. In *Proceedings of the Computational Modeling of Concrete and Concrete Structures (Euro-C 2018)*, pages 805–812, Bad Hofgastein, Austria, 26 February–01 March, 2018. London,UK: CRC Press.

[109] M. Pokhrel and M. J. Bandelt. Simulation of reinforced HPFRCC deformation capacity under flexure- and shear-dominated stress states. In *Proceedings of the Computational Modeling of Concrete and Concrete Structures (Euro-C 2018)*, pages 633–640, Bad Hofgastein, Austria, 26 February–01 March, 2018. London,UK: CRC Press.

[110] DIANAFEA. Diana release 10.2. http://www.dianafea.com, 2017 (accessed on September 1, 2017).

[111] P. H. Feenstra. *Computational aspects of biaxial stress in plain and reinforced concrete*. PhD. Dissertation, Delft University of Technology, 1993.

[112] R. V. Mises. Mechanics of solid bodies in the plastically-deformable state. *Göttin Nachr Math Phys*, 1:582–592, 1913.

[113] J. G. Rots and J. Blaauwendraad. Crack models for concrete: discrete or smeared ? fixed, multi-directional or rotating ? *HERON*, 34(1):1–59, 1989.

[114] W. P. Kwan and S. L. Billington. Simulation of structural concrete under cyclic load. *Journal of Structural Engineering*, 127(12):1391–1401, 2001.

[115] W. Nguyen, G. Jen, W. D. Trono, D. M. Moreno, S. L. Billington, and C. P. Ostertag. Tension stiffening effect of reinforced high-performance fiber-reinforced cementitious composites. In H. W. Reinhardt, G. J. Parra-Montesinos, and H. Garrecht, editors, *Proceedings of the Seventh International Workshop on High Performance Fiber Reinforced Cement Composites (HPFRCC-7)*, Stuttgart, Germany, June 01–03, 2015. Bagneux, France: RILEM Publications S.A.R.L.

[116] Minitab Inc. Minitab release 18.1. http://www.minitab.com, 2017 (accessed on December 1, 2017).

[117] ATC. Seismic performance assessment of buildings (volume 1-methodology). Technical Report FEMA-P-58-1, Federal Emergency Management Agency, Washington, DC, USA, 2012.

[118] A. L. Baker. *The Ultimate Load Theory Applied to the Design of Reinforced & Prestressed Concrete Frames*. Concrete Publications Ltd., London, 1956.

[119] Y. Shao and S. L. Billington. Predicting the two predominant flexural failure paths of longitudinally reinforced high-performance fiber-reinforced cementitious composite structural members. *Engineering Structures*, 199:109581, 2019.

[120] J. A. Blume, N. M. Newmark, and L. H. Corning. *Design of Multistory Reinforced Concrete Buildings for Earthquake Motions*, volume 4. Portland Cement Association Chicago, 1961.

[121] N. Mitra and L. N. Lowes. Factors influencing analytical continuum simulation of three-point bend test of a concrete notched beam. In *Proceedings of the Fourteenth World Conference of Earthquake Engineering (WCEE-14)*, Beijing, China, October 12–17 2008.

[122] C. Shen, E. Mizuno, and T. Usami. A generalized two-surface model for structural steels under cyclic loading. *Doboku Gakkai Ronbunshu*, 10(2):23–33, 1993.

[123] M. Dagenais and B. Massicotte. Cyclic behavior of lap splices strengthened with ultra high performance fiber-reinforced concrete. *Journal of Structural Engineering*, 143(2):04016163, 2017.

[124] R. N. Swamy and A. A. Saad. Deformation and ultimate strength in flexure of reinforced concrete beams made with steel fiber concrete. *Journal of ACI*, 78(5):395–405, 1981.

[125] ACI Committee 544. Design considerations for steel fiber reinforced concrete. Technical Report ACI 544.4R-88, American Concrete Institute, Farmington Hills, Michigan, USA, 1988.

[126] S. Aaleti, B. Petersen, and S. Sritharan. Design guide for precast uhpc waffle deck panel system, including connections. Technical Report Publication No. FHWA-HIF-13-032, Federal Highway Administration, Washington, DC, USA, 2013.

[127] D. Y. Yoo and Y. S. Yoon. A review on structural behavior , design , and application of Ultra-High-Performance Fiber-Reinforced concrete. *International Journal of Concrete Structures and Materials*, 10(2):125–142, 2016.

[128] S. Ichikawa, H. Matsuzaki, A. Moustafa, M. A. Elgawady, and K. Kawashima. Seismic-resistant bridge columns with ultrahigh-performance concrete segments. *Journal of Bridge Engineering*, 21(9):04016049, 2016.

[129] K. Rokugo, T. Kanda, H. Yokota, and N. Sakata. Applications and recommendations of high performance fiber reinforced cement composites with multiple fine cracking (HPFRCC) in Japan. *Materials and Structures*, 42(9):1197–1208, 2009.

[130] M. Pokhrel and M. J. Bandelt. Plastic hinge region and rotation capacity in reinforced HPFRCC flexural members at collapse level. In N. Banthia and V. Kodur, editors, *Proceedings of the Seventh International Colloquium on Performance, Protection & Strengthening of Structures under Extreme Loading & Events (PROTECT 2019)*, Whistler, Canada, September 16–17, 2019.

[131] Y. Shao and S. L. Billington. Flexural performance of steel-reinforced engineered cementitious composites with different reinforcing ratios and steel types. *Construction and Building Materials*, 231:117159, 2020.

[132] J. K. Lee. Bonding Behavior of Lap-spliced Reinforcing Bars Embedded in Ultra-High Strength Concrete with Steel Fibers. *KSCE Journal of Civil Engineering*, 20(1):273–281, 2016.

[133] Y. Shao and S. L. Billington. Utilizing full UHPC compressive strength in steel reinforced UHPC beams. In Eric Steinberg, Sriram Aaleti, and Green Brian, editors, *Proceedings of the Second International Interactive Symposium on Ultra-High Performance Concrete (2IIS-UHPC)*, Albany, New York, USA, June 2–5, 2019.

[134] American Society for Testing and Materials. Standard practice for fabricating and testing specimens of ultra-high performance concrete. *ASTM C1856/C1856M-17*, pages 1–4, 2017.

[135] M. J. N. Priestley, F. Seible, and G. M. Calvi. *Seismic Design and Retrofit of Bridges.* New York, NY: John Wiley & Sons, 1996.

[136] F. Seible, M. J. N. Priestley, G. A. Hegemier, and D. Innamorato. Seismic retrofit of RC columns with continuous carbon fiber jackets. *Journal of Composites for Construction*, 1(2):52–62, 1997.

[137] M. J. N. Priestley, G. M. Calvi, and M. J. Kowalsky. Direct displacement-based seismic design of structures. In *Proceedings of the New Zealand Society for Earthquake Engineering Conference (2007 NZSEE)*, Pavia, Italy, 2007. IUSS Press.

[138] B. Mobasher, Y. Yao, and C. Soranakom. Analytical solutions for flexural design of hybrid steel fiber reinforced concrete beams. *Engineering Structures*, 100:164–177, 2015.

[139] M. Shafieifar, M. Farzad, and A. Azizinamini. A comparison of existing analytical methods to predict the flexural capacity of Ultra High Performance Concrete (UHPC) beams. *Construction and Building Materials*, 172:10–18, 2018.

[140] M. Pokhrel and M. J. Bandelt. Predicting UHPC structural response at ultimate limit state through numerical simulation technique. In Eric Steinberg, Sriram Aaleti, and Green Brian, editors, *Proceedings of the Second International Interactive Symposium on Ultra-High Performance Concrete (2IIS-UHPC)*, Albany, New York, USA, June 2–5, 2019.

[141] S. Grammatikou, D. Biskinis, and M. N. Fardis. Ultimate strain criteria for rc members in monotonic or cyclic flexure. *Journal of Structural Engineering*, 142(9):04016046, 2016.

[142] American Society for Testing and Materials. Standard test method for flow of hydraulic cement mortar. *ASTM C1437/C1437M-17*, pages 1–2, 2017.

[143] American Society for Testing and Materials. Standard test method for slump flow of self-consolidating concrete. *ASTM C1611/C1611M-18*, pages 1–4, 2018.

[144] American Society for Testing and Materials. Standard test method for density (unit weight), yield, and air content (gravimetric) of concrete. *ASTM C138/C138M-16*, pages 1–4, 2016.

[145] American Society for Testing and Materials. Standard test method for temperature Of freshly mixed hydraulic-cement concrete. *ASTM C1064/C1064M-12*, pages 1–3, 2012.

[146] American Society for Testing and Materials. Standard test method for compressive strength of cylindrical concrete specimens. *ASTM C39/C39M-15a*, pages 1–7, 2015.

[147] American Society for Testing and Materials. Standard test method for flexural performance of fiber-reinforced concrete (using beam with third-point loading). *ASTM C1609/C1609M-12*, pages 1–9, 2012.

[148] American Society for Testing and Materials. Standard practice for making and curing concrete test specimens in the laboratory. *ASTM C192/C192M-16a*, pages 1–8, 2016.

[149] F. Baby, B. Graybeal, P. Marchand, and F. Toutlemonde. UHPFRC tensile behavior characterization: inverse analysis of four-point bending test results. *Materials and Structures*, 46(8):1337–1354, 2013.

[150] American Society for Testing and Materials. Standard test methods for tension testing of metallic materials. *ASTM E8/E8M-16a*, pages 1–30, 2016.

[151] J. Blaber, B. Adair, and A. Antoniou. Ncorr: open-source 2d digital image correlation matlab software. *Experimental Mechanics*, 55(6):1105–1122, 2015.

[152] W. Nguyen, M. J. Bandelt, W. Trono, S. L. Billington, and C. P. Ostertag. Mechanics and failure characteristics of hybrid fiber-reinforced concrete (hyfrc) composites with longitudinal steel reinforcement. *Engineering Structures*, 183:243–254, 2019.

[153] U. Hasgul, K. Turker, T. Birol, and A. Yavas. Flexural behavior of ultra-high-performance fiber reinforced concrete beams with low and high reinforcement ratios. *Structural Concrete*, 19(6):1577–1590, 2018.